Developing Laboratory-Based X-ray Spectroscopies for Energy and Materials Research spectroscopy

Evan P. Jahrman

A dissertation

submitted in partial fulfillment of the

requirements for the degree of

Doctor of Philosophy

University of Washington

2019

Reading Committee:

Gerald T. Seidler, Chair

Marjorie Olmstead

Subhadeep Gupta

Program Authorized to Offer Degree:

Physics

University of Washington

Abstract

Developing Laboratory-Based X-ray Spectroscopies for Energy and Materials Research spectroscopy

Evan P. Jahrman

Chair of the Supervisory Committee:
Professor Gerald T. Seidler
Physics

Advanced x-ray spectroscopies interrogate a material's electronic structure in an element-specific manner. Traditionally, X-ray absorption fine structure (XAFS) and X-ray emission spectroscopy (XES) studies are performed at synchrotron X-ray light sources. These facilities serve to push the forefront of science and, thus, operate under an access model which necessarily excludes projects requiring routine analytical characterization, rapid feedback for prototyping, or regular access.

In response to this deficit, my dissertation presents a laboratory-based XAFS and XES spectrometer of high energy resolution, reproducibility, and efficiency, along with other improvements in instrumentation, especially as pertains to the utilized crystal analyzer. A range of basic and applied materials problems were addressed with this and similar instrumentation. Select applied research studies include *operando* XAFS analysis of a prototype lithium-ion battery's state-of-charge and state-of-health and an XES-based method for the quantification of

hexavalent chromium in manufactured plastics that is being developed into a standard test method. Basic research spanned a study of photoexcitation dynamics in Ni metal and time-dependent density functional theory interpretations of valence-to-core XES spectra collected from a series of vanadium oxide and vanadyl phosphate energy storage materials candidates.

This thesis provides strong evidence that laboratory-based X-ray spectroscopy instrumentation can serve as a powerful tool for increasing productivity and understanding in the fields of chemistry and materials science.

Table of Contents

List of Figures xii

List of Tables xxxi

Chapter 1. The Photoelectric Effect and its Associated Spectroscopies 1

1. Context and Motivation 1

2. Photoelectric Processes 2

2A. Overview of photoelectric effects 2

2B. X-ray Photoelectron Spectroscopy (XPS) 4

2C. X-ray Absorption Fine Structure (XAFS) Analysis 7

2C. I. X-ray Absorption Near-Edge Structure (XANES) 9

2C. II. Extended X-ray Absorption Fine Structure (EXAFS) 21

3. X-ray Emission Spectroscopy (XES) 30

3A. Overview 30

3B. Kα ($KL_{II,III}$) XES 32

3C. Kβ mainlines ($KM_{II,III}$) XES 34

3D. Kβ valence-to-core (nominally $KM_{IV,V}$) XES 36

4. Perturbations on two state transitions 39

4A. Origin of Natural Line Width 39

4B. Raman and Auger Effects 42

4C. Multielectron Excitation Satellites 45

5. References 50

Chapter 2. Practical Considerations for Experiments and Simulations 58

1. Experiment Design 58

a. Measurement modes 58

b. Source Selection 59

c. Monochromator Considerations 63

d. Sample Considerations 68

e. Data Collection and Analysis 70

2. Theoretical Calculations 73

3. References 80

Chapter 3. An Improved Laboratory-Based X-ray Absorption Fine Structure and X-ray Emission Spectrometer for Analytical Applications in Materials Chemistry Research 86

1. Introduction 87

2. Experimental 89

a. Monochromator Design 89

b. Sample Preparation Details 97

c. Synchrotron XAS Measurement Details 98

3. XAFS and EXAFS Results and Discussion 99

a. Basic Instrument Performance 99

b. XAFS Demonstration Studies 105

c. XES Demonstration Studies 114

4. Summary and Conclusions 123

5. Acknowledgements 123

6. References 125

..... Vacuum Formed Temporary Spherical and Toroidal Bent Crystal Analyzers for X-ray Absorption and Emission Spectroscopy 133

Chapter 4. 133

1. Introduction 134

2. Methods 135

3. Results 143

4. Conclusions 153

5. Acknowledgements 154

6. References 154

Chapter 5. Spherically Bent Mica Analyzers as Universal Dispersing Elements for X-ray Emission Spectroscopy 158

1. Introduction 160

2. Methods 163

3. Results and Discussion 165

4. Conclusions 172

5. Acknowledgements 172

6. References 173

Chapter 6. Overview of Energy Storage Research and the Contributions of X-ray Spectroscopy176

1. Historical Context and Societal Impact 176

2. Research strategies to achieve improvements 182

3. Summary of Recent X-ray Spectroscopy Investigations of Energy Storage Materials ... 196

4. References 197

Chapter 7. A Mail-in and User Facility for X-ray Absorption Near Edge Structure: The CEI-XANES laboratory x-ray spectrometer at the University of Washington 202

1. Introduction 203

2. Instrument Design and Operation 204

3. Experimental 209

4. Results 210

5. Use Landscapes in a Future with Ubiquitous Laboratory XAFS and XES 214

6. Conclusion 218

7. Acknowledgements 219

8. Funding Information 219

9. References 219

Chapter 8. Laboratory-based X-ray Absorption Spectroscopy on a Working Pouch Cell Battery at Industrially-Relevant Charging Rates 223

1. Introduction 224
2. Experimental Details 227
3. Results and Discussion 230
4. Conclusion 238
5. Acknowledgments 239
6. References 240

Chapter 9. Valence-to-core X-ray Emission Spectroscopy of Vanadium Oxide and Lithiated Vanadyl Phosphate Materials 243

1. Introduction 244
2. Methodology 248
3. Results and Discussion 252
4. Conclusion 258
5. Acknowledgements 259
6. References 259

Chapter 10. Determination of Hexavalent Chromium Fractions in Plastics Using Laboratory-Based, High-Resolution X-Ray Emission Spectroscopy 265

1. Introduction 266
2. Methods 269
3. Results and Discussion 275
4. Conclusion 284

5. Acknowledgments 284

6. References 285

Chapter 11. Double-Ionization Satellites in the X-ray Emission Spectrum of Ni Metal 288

1. Introduction 289

2. Experimental Procedure 292

3. Results and Discussion 299

4. Conclusion 304

5. Acknowledgements 305

6. References 305

List of Figures

Fig. 1-1: Reproduced from Hubbell et al.5 The total cross section of Cu for photon interactions shown with its individual components: the atomic photoeffect, τ; coherent scattering, σCOH; incoherent scattering, $\sigma INCOH$; nuclear photoabsorption, $\sigma PH.N.$; and total pair production, κ. 2

Fig. 1-2: Reproduced from de Groot et al.[7] X-ray absorption cross-sections of two transition metals. The L-edges are visible at around 1 keV and the K-edges for each element are visible between 6 and 9 keV. 4

Fig. 1-3: Reproduced from Bi et al.[17] XPS of V $2p_{3/2}$ spectra of V_2O_5 nanocables with a gradient of oxygen vacancies introduced by surface polymerization with poly(3,4-ethylenedioxythiophene), G-V_2O_5/PEDOT, and V_2O_5-based nanocables, V_2O_5-NF. The V^{3+}, V^{4+}, and V^{5+} oxidations states are represented by V_2O_3, VO_2, and V_2O_5, respectively. 6

Fig. 1-4: Reproduced from Powell.[15] The calculated inelastic mean free path of an electron is shown as a function of energy for a few materials. 7

Fig. 1-5: Reproduced from Newville.[30] XAFS spectrum taken at the Fe K-edge on FeO. The XANES and EXAFS regions are shown. 9

Fig. 1-6: From Jahrman et al.[31] A comparison of measurements performed at APS 9-BM (Synchrotron) and with laboratory-based instrumentation at the University of Washington (Lab-based). XANES spectra were collected at the V K-edge of an epsilon phase vanadyl phosphate lithium ion battery cathode. The following XANES features are labeled: (a) a pre-edge peak, (b) a shoulder feature, (c) the edge, (d) a white line feature, (e) a series of scattering peaks from atoms neighboring the absorbing V atom. 10

Fig. 1-7: From Jahrman et al.[39] The pre-edge peaks of the XANES spectra of (a) potassium chromate, a hexavalent reference, and (b) CRM 8113a, a standard reference material. Also shown is the fit along with its components as calculated in Athena.[40] 13

Fig. 1-8: From Gaur and Shrivastava.[46] The Cu K-edge XANES spectra of a collection of mono- and divalent Cu species. A variety of spectral features are designated, including Peak S and Shoulder S, which are collectively referred to as shoulder features in this work. 15

Fig. 1-9: From Mundy et al.[46] Co K-edge XANES spectra of CoP and Co_2P produced by a novel synthesis procedure, $CoCl_2$ and Co metal commercial standards, and a second CoP compound produced by an established literature procedure.[45] 15

Fig. 1-10: From Jahrman et al.[56] The Ni K-edge XANES spectra of a layered oxide cathode material at different states of charge. Results were acquired *operando* at the reported charging rates. 18

Fig. 1-11: From Jahrman et al.[56] The position of the Ni K-edge of the XANES spectrum collected at each charge state for a variety of charging and discharging rates. A few of the corresponding XANES spectra are shown in Fig. 1-10. 19

Fig. 1-12: From Piao et al.[62] The Au M_3-edge XANES spectra of Au and two Au-Al alloys collected in total electron yield (TEY). 20

Fig. 1-13: From Sayers et al.[86] Fourier transformation of the oscillatory part of χ from crystalline and amorphous Ge, *i.e.* a radial structure function providing a measure of bond lengths in these two systems. 24

Fig. 1-14: From Sevillano *et al.*[97] First shell mean-square vibrational amplitudes for Cu as a function of temperature. A variety of force-constant models are considered and compared to experimental data in the literature. The theoretical models are (A) that of Svensson *et al.*,[100] (B)

that of Nicklow *et al.*,[101] (C) that of Sevillano *et al.*,[97] (D) the Debye model, and (E) the Einstein model. 28

Fig. 1-15: Reproduced from Podgoršak.[120] Depiction of two popular schemes, IUPAC and Siegbahn notation, for naming X-ray transition lines involving a K-shell core hole in the initial state. 31

Fig. 1-16: Reproduced from Glatzel and Bergmann.[123] Mn K-shell emission lines in MnO. The Kβ main and satellite lines are shown with the specified magnifications. 32

Fig. 1-17: Reproduced from Glatzel and Bergmann.[123] $K\alpha_1$ FWHM in Fe compounds measured by XES; (a) full boxes: nominal number of unpaired 3d electrons, (b) empty boxes: the effective number of unpaired 3d electrons in the ground state, (c) circles: the effective number of unpaired 3d electrons in the 1s core hole excited state. The shown linear regression is for (c). 33

Fig. 1-18: Reproduced from Koster.[132] The Kβ emission spectra of some heme proteins: iron(III) protoporphyrin chloride (Hemin), desoxyhemoglobin (Hb), oxyhemoglobin (HbO_2), carbonmonoxidehemoglobin (HbCO), methemoglobin (metHb), and metmyoglobin (metMb). The main Kβ is subtracted from the spectrum and the bare shoulder is shown in the inset. 35

Fig. 1-19: Reproduced from Messinger et al.[131] The Kβ mainline XES measurements of several Mn oxides. A pictorial representation is given for the fluorescence transition. 36

Fig. 1-20: Reproduced from Rovezzi et al.[136] Cr-based empirical references. Experimental data is shown in the top panel following removal of the tail from the lower energy Kβ main line and then peak normalization. Theoretical simulations are shown in the bottom panel. Vertical dashed lines compare the main features in simulation and experiment. 38

Fig. 1-21: Reproduced from MacMillan et al.[135] For the case of Cr VTC-XES, the above data points display the average, experimentally calibrated, energies of DFT-calculated Kβ'' features

for ligands grouped by donor atom. Error bars represent two standard deviations. Gray bars indicate experimental values with error bars acquired from fitting analyses. Bolded ligands contribute strongly to the Kβ'' intensity, while non-bolded ligands are expected to be difficult to resolve. 39

Fig. 1-22: From Taguchi et al.[140] The LS-term dependence of the lifetime of states with a 3p core hole in a free Mn^{2+} ion. The dashed line represents the linear model and the solid vertical lines represent calculated lifetimes. 41

Fig. 1-23: From Taguchi et al.[140] Mn Kβ XES of MnF_2 using a constant (a) and term-dependent (b) broadening of the lifetime of the 3p core hole state. 42

Fig. 1-24: From Enkisch et al.[143] The effect of the electronic density of states on the final emission spectrum. Schematics (a) through (d) will be discussed in the text. 44

Fig. 1-25: From Valenza et al.[165] The measured XES from Ni foil in the valence-to-core region. The data is fit to a sum of pseudo-Voigt functions representing phenomenological multielectron satellites and the diagram line. Not shown are the fit components representing the Ni $Kβ_{1,3}$ and radiative Auger effect features. 46

Fig. 2-1: Reproduced from Newville.[8] An incident beam of photons, I_0, passing through a material with thickness t. A final beam of photons, I, escapes the material. 59

Fig. 2-2: Reproduced from Maio.[12] Historical growth of source brilliance for several institutions compared to a conventional X-ray tube source. Note that SR refers to synchrotrons, while the acronyms are Stanford synchrotron radiation lightsource (SSRL), national synchrotron light source (NSLS), advanced photon source (APS), European synchrotron radiation facility (ESRF), the linac coherent light source (LCLS), self-amplified spontaneous emission (SASE), and X-ray free electron laser (XFEL). 60

Fig. 2-3: Reproduced from Seidler.[11] Simulated Co K-edge XANES data for a Co metal foil. Poisson noise was applied to a spectrum measured at a synchrotron by assuming a given number of counts per point..... 61

Fig. 2-4: Reproduced from Seidler.[11] The measured spectrum from a Moxtek X-ray tube source operated at 10 W tube power. 62

Fig. 2-5: Reproduced from Goodsell with minor modification.[42] Sketch of Johann and Johansson style crystal on the Rowland circle of a wavelength dispersive spectrometer. 66

Fig. 2-6: Figure and caption reproduced from Jahrman.[43] "(a) CAD rendering front view of the vacuum formed bent crystal analyzer (VF-BCA). (A) Bent wafer; (B) front flange with polyimide film (not shown); (C) pumping line; (D) aluminum alloy vertical support plate; (E) support bolts to define the position of the outer diameter of the VF-BCA body. (b) CAD rendering section view of the VF-BCA. (F) CNC-machined vacuum form; (G) steel backing plate for magnetic mounting, where magnets (not shown) are attached alongside part (D). (c) Photograph of the VF-BCA; note the flexible orange polyimide film that allows air pressure to force the wafer into the shape of the form machined into part (F). A second, similar VF-BCA instead has a simple recess in part (F) to accept a 1-m radius of curvature concave glass lens. (d) Photograph of a commercial, anodically bonded 10-cm diameter SBCA with 1-m radius of curvature."..... 67

Fig. 2-7: Reproduced from Pickering with minor modification.[64] S K-edge XANES measurements of S_8 particles prepared at various particle sizes..... 70

Fig. 2-8: Reproduced from Bunker.[77] The concept of a chemical filter is outlined. 72

Fig. 2-9: Reproduced from Behne.[78] A compact, focusing spatial filter made from interleaved W sheets. The entrance is shown in the top and exit on bottom. 73

Fig. 2-10: (a) Reproduced from Smolentsev.[128] Mn VTC-XES spectra of hydrated Mn^{2+} ions measured experimentally (top, black) and calculated by DFT according to a cluster of six water molecules coordinated to a Mn^{2+} ion (bottom, red). (b) Reproduced from Zhang.[93] Mn VTC-XES spectra of hydrated Mn2+ ions measured experimentally (top, blue) and calculated by TDDFT (bottom, red)..... 79

Fig. 2-11: Reproduced from the supporting information provided by Zhang.[93] Mn VTC-XES spectra of hydrated Mn2+ ions measured experimentally (top, blue), TDDFT result in the FCH procedure (middle, red), TDDFT result without relaxation of the excited state (bottom, green). 80

Fig. 3-1: (a) Corner perspective of spectrometer in XANES configuration. The SBCA and source are mechanically coupled to the center carriage. The two-axis tilt is no longer utilized. Source and detector are at $\alpha = 40°$ (see Fig. 3-2). (b) CAD rendering of the helium box (removed from frame (a)) enclosing the x-ray beampath. The slots on the left and right faces are oriented at the height of source and detector, while a rectangular cutout on the far face permits transit of x-rays to the SBCA. Each slot is typically covered by a polyimide film attached to the frame of the helium box..... 90

Fig. 3-2: (a) Illustration depicting the parameter α and θB. The SBCA resides at the bottom of the Rowland circle while the carriage coupling the SBCA location and the source as represented by the hollow dot is at the center of the Rowland circle. The diagonal line represents the travel range of the source with dots at its end points. (b) The magnitude of the SBCA's displacement from its location, $d(\theta_B)$, at $\theta B = 85°$ is plotted as a function of θ_B for various values of α..... 93

Fig. 3-3: (a) While holding the source fixed at $\theta B = 84°$, the detector was scanned from 83.5 to 84.5°. Scans were taken at various rotations of the SBCA about its center with the optimum position designated as 0°. Data was taken off the 444 harmonic of a Ge SBCA using a x-ray

tube source with a Pd anode operated at 52.5 W tube power. The duration of each scan was approximately 45 seconds. (b) The total number of counts, as integrated over the range from 83.5 to 84.5° for each scan, is shown as a function of the analyzer's angular rotation. The solid line is a quadratic fit. 95

Fig. 3-4: An I_0 scan spanning the entire range of the instrument. Data was collected using the 444 harmonic of a Ge SBCA. An x-ray tube source with a Pd anode was operated at 100 W power. Fluorescence lines can be seen from Cu Kα and Kβ lines as well as a small W line around 8400 eV. This last line is likely due to some small number of W atoms from the filament being deposited onto the surface of the target anode as has been discussed elsewhere.[31] 101

Fig. 3-5: Six consecutive scans are shown of a transmission mode measurement across the K-edge of the Mn foil. Measurements were collected using a Si (440) SBCA. An x-ray tube source with a W anode was operated at 25 W with a 10 μm thick Zn foil acting as an absorber to suppress the W fluorescence line observed on the Si (660) harmonic in accordance with methods previously reported, although done here without a slit system.[50] The residuals between subsequent scans are shown at the bottom of the figure (magnified five times) with a Poisson envelope enclosing two standard deviations. 102

Fig. 3-6: (a) XANES spectra of the V foil collected using an x-ray tube source with a W anode and operated at 50 W power. Comparison was made to synchrotron results and offset for clarity, see the text for discussion. (b) An enlarged view of the pre-edge feature at ~5464 eV including comparison with synchrotron results with the indicated Gaussian broadening. Laboratory-based measurements used either a masked or unmasked Ge (422) SBCA. Spectra are offset for clarity. 104

Fig. 3-7: (a) The V K-edge XANES spectra of a vanadyl phosphate-based battery laminate. Spectra were acquired with the present instrumentation (Lab-Based) and at APS 9-BM (Synchrotron). The spectra are offset for clarity of presentation. The full range of scans was chosen to extend from 5390 eV out to 10 $Å^{-1}$ to ensure proper normalization and background removal for comparison to the synchrotron. (b) XANES spectra of uncharged and charged battery laminates of NMC composition. Data was again acquired out to 10 $Å^{-1}$ and data was collected at lower energies to aid background removal. (c) XES spectra of a charged and uncharged NMC laminate. The residual of the two spectra is displaced below the main results. Peak count rates were around 12,000 counts per second for the uncharged laminate and 6,000 for the charged laminate. 108

Fig. 3-8: (a) XANES spectra of $CePO_4$ and CeO_2, representative Ce^{3+} and Ce^{4+} compounds, respectively. Reference spectra were acquired on beamline X23-A2 of the National Synchrotron Light Source (NSLS). (b) Comparison of synchrotron (endstation 11-2 at SSRL) and lab-based U L_3-edge XANES for $(PPh_4)_2UCl_6$, a U^{4+} reference compound. Data was calibrated to the maximum of the first derivative of the K-edge spectrum of a yttrium foil at 17038.4 eV. 110

Fig. 3-9: EXAFS of Ni Foil collected at UW (Lab-based) compared to synchrotron results (APS 13-ID). Results are shown in energy space (a), along with the magnitude of the EXAFS in radial space (b), the real part of the EXAFS in radial space (c), and the EXAFS with quadratic weighting in k-space (d), respectively. Also shown are the fitted models acquired from Artemis.[47] Data was collected using 100 W power for a Pd anode x-ray tube and using a Si (551) SBCA. Measurement times were 1.7 and 6.9 h for I_0 and I_T, respectively..... 113

Fig. 3-10: (a) The full range of V Kβ XES from a collection of V compounds measured in the lab spectrometer. Measurement times were 12.4 h for all samples. Note that the vanadyl

phosphate data represents three scan ranges, with the main scans spanning 5395 eV to 5485 eV, this range was joined with supplemental data sets to span the entire range shown and permit equivalent background subtractions for all systems. (b) V $K\beta_{1,3}$ XES from a suite of oxides measured in the lab spectrometer..... 117

Fig. 3-11: VTC-XES spectra of Zn metal, ZnO, and $ZnCl_2$ after background subtraction and integral normalization across the full VTC energy range. 119

Fig. 3-12: (a) The As Kα XES spectra of trivalent and pentavalent arsenic oxide species (a). The intensity scale is for the $NaAsO_2$ sample; the intensity of the Na_2HAsO_4*7H20 has been scaled upward by ~30% to give it the same integral intensity for ease of comparison for the energy shift as a function of As oxidation state. The study used a Si (555) toroidally bent crystal analyzer following an in-house design.[41] (b) Collected $L\beta_1$ XES spectra of $(PPh_4)_2UCl6$ and $(NMe_4)_2UO_2Cl_4$, which are in the U^{4+} and U^{6+} state, respectively. The most intense spectral feature is the $L\beta_1$, though less intense features can be found toward lower energies. The spectra are peak normalized here for comparison. A residual is provided and spectra are offset for clarity. No change in spectrum was observed across any of the scans, indicating no radiation damage. The data was calibrated to the maximum of the Kα of a Mo foil at 17480 eV..... 122

Fig. 4-1: (a) CAD rendering front view of the vacuum formed bent crystal analyzer (VF-BCA). (A) bent wafer; (B) front flange with polyimide film (not shown); (C) pumping line; (D) aluminum alloy vertical support plate; (E) support bolts to define the position of the outer diameter of the VF-BCA body. (b) CAD rendering section view of the VF-BCA. (F) CNC-machined vacuum form; (G) steel backing plate for magnetic mounting, where magnets (not shown) are attached alongside part (D). (c) Photograph of the VF-BCA, note the flexible orange polyimide film that allows air pressure to force the wafer into the shape of the form machined

into part (F). A second, similar VF-BCA instead has a simple recess in part (F) to accept a 1-m radius of curvature concave glass lens. (d) Photograph of a commercial, anodically-bonded 10-cm diameter SBCA with 1-m radius of curvature. 137

Fig. 4-2: (a) The Rowland circle implementation for the laboratory spectrometer, shown for a 70 ° Bragg angle. Note the definition of the detector plane. Also note that perfect point-to-point focusing by the optic would require that its radius of curvature out of the Rowland plane be equal to the normal distance from the source-detector arc to the optic, i.e., the sagitta of the reflexive arc from the source point on the Rowland circle to the detector point, indicated as 88.3cm on the diagram above. This motivates the use of toroidally curved forms, as discussed in the text. (b) Photograph of the laboratory spectrometer. (c) Photograph from the reverse side of a vacuum-formed bent crystal analyzer installed into the spectrometer. Note the presence of small magnets inside visible channels of the plastic 3D-printed part coupled to the steel mounting plate (part (G) in Fig. 1) to hold the analyzer in location but allow easy rotation about the azimuthal angle. .. 141

Fig. 4-3: Characterization of the spatial distribution of x-ray intensity on the detector plane from (top) a commercial Si (551) analyzer (SBCA); (second from top) VF-BCA-1 with a Si (711) wafer and (second from bottom) VF-BCA-2 with a Si (711) wafer; (bottom) VF-BCA-3 with a Si (711) wafer, a torus optimized for $\theta B = 70$ °. The orientations are defined relative to the plane of the Rowland focusing circle. The colorscale of each frame is independently normalized; for a comparison of intensities, see Fig. 4-4. 144

Fig. 4-4: (a) Comparison of beam profiles in the Rowland plane for different optics. (b) Comparison of beam profiles in the direction perpendicular to the Rowland plane different optics. The extent of the silicon SDD's active region is represented by the shaded regions..... 146

Fig. 4-5: (a) The modeled beam height as a function of θB for doubly-curved optics with a 1-m principal radius of curvature but with secondary curvatures designed for point-to-point focus as design Bragg angles $\theta*$ varying in 5° steps from 55° to 90°, the latter being for a fully spherical analyzer. (b) For a $\theta* = 70°$ toroidal optic, the modeled fraction of x-rays hitting three different circular detectors with diameters of 5 mm, 10 mm, and 15 mm. 148

Fig. 4-6: Monochromator count rate as a function of photon energy using a Si (551) or equivalent wafer. The sharp features at, e.g., ~8900 eV, are Cu Kβ fluorescence lines from the heatsink of the x-ray tube anode. The rapid roll-off for the spherical optics is due the steadily increasing out-of-plane spread upon decreasing Bragg angle, causing the beam to become taller than the 4-mm active height of the SDD. The toroidal optic shows much improved performance in the designed Bragg angle range. 149

Fig. 4-7: Representative spectra demonstrating the capability of the vacuum-clamped optics to perform high-resolution measurements. (a) Comparison of Ni XANES measured with each optic using Si (551) or equivalent wafers. (b) Comparison of Ni XANES measured with each optic using Si (444) wafers. (c) Comparison of Cu Kα XES with each optic using Si (444) wafers.. 151

Fig. 4-8: Spectra demonstrating the energy resolution achievable in the instrument given a commercial optic. (a) Ni XANES measured with the Si (551) SBCA (UW) and at the synchrotron (Synch.) as referenced in Hephaestus.[46] (b) Comparison of a small region of the Ni XANES shown in (a) along with a spectrum representing the literature results after convolution with a 0.8 eV Gaussian in Athena.[46] 152

Fig. 5-1: Discussion of the relationship between analyzer mosaicity and energy resolution. (a) The usual Rowland configuration with a perfect crystal analyzer, where a polychromatic source results in a single monochromatic refocused spot. (b) For a mosaic crystal analyzer, some small

range of Bragg angles is accessed resulting in a band of spectrally-unique refocal spots on the detector side of the Rowland circle, moving from lower energy (red) closer to backscatter to higher energy (blue) farther from backscatter..... 161

Fig. 5-2: The Ni K-edge XANES spectrum of a Ni foil. Each mica grade is separated into a separate subpanel and was tested with and without a 1-mm wide Pb detector slit ('slit' in the figure panels), so as to investigate the degradation due to the mosaic spread of the various mica samples. In each subpanel, the collected XANES spectra were compared to a spectrum collected at APS 13ID and reported in the Hephaestus package.[51] 166

Fig. 5-3: Energy dispersive x-ray spectra taken at 85 degrees Bragg angle. All intensities are in units of counts per second per unit analyzer crystal area. (a) Comparison of efficiencies for the four mica spherically bent analyzers. Several of the (0,0,*l*) reflections of mica are labeled. (b) Comparison of the mica 1 analyzer to the three indicated commercial analyzers..... 168

Fig. 5-4: X-ray emission spectra for each harmonic of the mica 1 SBCA as a function of Bragg angle, using the energy resolution of the SDD to select independent regions of interest for each of the nonvanishing harmonics from (0,0,14) to (0,0,30). The multipliers under the (0,0,*l*) label indicated the data scaling needed to bring the signal to common levels for purposes of display. The cluster of weak peaks marked 'escape' at ~75 degrees on the (0,0,14) reflection are from detector escape peaks from the high intensities on the (0,0,20) reflection. 170

Fig. 5-5: Comparison of the mica 1 SBCA with standard analyzers commercial analyzers, all applied to the Cu Kα fluorescence line. The differing apparent energy resolutions are partly due to analyzer quality and partly due to different source broadening at the three different Bragg angles used in the study. 171

Fig. 6-1: The National Renewable Energy Laboratory's traditional representation of photovoltaic efficiency records as tabulated by Green *et al.*[6]..... 178

Fig. 6-2: Reproduced from the California Independent System Operator Corporation.[7] Net load is shown as a function of time-of-day. Net load is the difference between forecasted load and expected electricity production from variable generation resources. Measurements were collected on January 11, 2012. Other years represent projected values. Four regions are visible: (1) ~ 4:00 a.m. people start to wake up and make use of electrical appliances. (2) ~ 7:00 a.m. the sun rises and solar generation resources become active. (3) ~ 4:00 p.m. the sun begins to set and people return home from their daily routines and begin using at-home electronic devices. (4) ~ 7:00 p.m. demand on the system begins to decrease as individuals retire for the evening. 179

Fig. 6-3: Reproduced from Tarascon.[14] Energy densities and specific energies of various rechargeable battery chemistries..... 181

Fig. 6-4: Reproduced from Bloomberg New Energy Finance.[15] Historical LIB pack prices are denoted by triangles with projected priced represented by a dashed line. The shaded regions show projected demand for LIBs. Note that ESS encompasses stationary energy storage applications, while E-Bus refers to electric buses..... 181

Fig. 6-5: Reproduced from Goodenough.[26] Schematic of a conventional LIB showing the flow of transport of Li ions and electrons. 183

Fig. 6-6: Reproduced from Deng.[20] The electrode potentials and achievable capacities spanned by a variety of candidate electrode materials..... 184

Fig. 6-7: Reproduced from Deng.[20] Three mechanisms for Li storage in LIBs. 185

Fig. 6-8: Reproduced from Kasnatscheew.[21] Three motifs for Li transport within the active material of an electrode. These motifs include 1D transport along channels (as in olivine

structure types), 2D transport along defined sheets (as with layered structure types), or 3D diffusion (as in spinel structure types). 186

Fig. 6-9: Reproduced from Fang.[56] (A) Optical microscope image of Li dendrites in a beaker cell as reported by Xu *et al.*[55] (B) Whisker-like Li deposited during cycling with a mix of standard solvents, electrolytes, and additives. (C) Chunky Li deposited during cycling with a high-concentration ether-based electrolyte. 189

Fig. 6-10: Reproduced from Schipper.[75] Phase diagram representing the ternary system between three transition metal oxide species along with example compositions and considerations. 191

Fig. 6-11: Reproduced from Jeong.[76] Chronological energy densities of cylindrical-18650 LIBs. 192

Fig. 6-12: Reproduced from Clément.[77] Average discharge potential and volumetric energy density vs. volumetric capacity of selected cathode materials for lithiation or sodiation. 192

Fig. 6-13: Reproduced from Noh.[78] Trend in discharge capacity, thermal stability, and capacity retention as a function of Ni concentration in Ni-rich NMC cathode materials. 194

Fig. 6-14: Reproduced from Bak.[83] Mass spectroscopy results for oxygen as a function of temperature (top) compared with the materials' phase as determined by *in situ* XRD. 194

Fig. 6-15: Reproduced from Yagi.[83] Insertion of Mg^{2+} from an aqueous or triglyme electrolyte into a host lattice. 195

Fig. 6-16: Reproduced from Hautier.[84] Average voltage of select phosphates versus achievable capacity. Each redox couple is designated by a marker unique to the given element. The red dashed line represents an upper voltage beyond which decomposition of the electrolyte may occur. 195

Fig. 6-17: Reproduced from Cuisinier.[84] Speciation distribution analysis results based on linear combination analysis of S K-edge XANES results upon cycling of a Li-S battery at a C/10 rate. Spectra are fit to a linear combination of four reference compounds: S_8, S_6^{2-}, S_4^{2-}, and Li_2S.... 197

Fig. 7-1: Diagram showing the movement of the Detector and the SBCA in a fixed-source Rowland circle in the direction of low (red) to high (blue) energy. Note that both the source position and the direction from the source to the optic are fixed due to the stationary source... 205

Fig. 7-2: CAD Rendering of CEI-XANES (top view). Labelled with red arrows are the 4 motors used in a scan (Detector, θ, 2θ, and ρ), and the turret motor which switches between optics. The key components are labelled with blue arrows and letters: A) the x-ray source, B) the detector, and C) the optic. Not shown is the helium box to reduce air absorption. 206

Fig. 7-3: Comparison of CEI-XANES (solid) and synchrotron (dashed, collected at APS 20-BM) data for both abiotic magnetite (blue) and lepidocrocite (red). Spectra are offset for clarity. 211

Fig. 7-4: Comparison of V Foil XANES spectra taken with CEI-XANES (blue) and at APS (green). Broadening the APS spectrum by 0.8 eV (orange) aligns it well with the CEI-XANES spectrum. Assuming an energy resolution 0.6 eV for the APS data, we estimate an energy resolution of 1.0 eV for CEI-XANES at the V k-edge. Spectra are offset for clarity. 212

Fig. 7-5: Ni XANES spectra of an NMC pouch cell battery before and after charging. Not shown is a scan over a longer range used to normalize these data. Measurement time was 2 minutes for each spectrum. See the text for discussion. 213

Fig. 7-6: Comparison of Nano Yb:$YLiF_4$ crystals (blue) with bulk crystals (yellow), and Yb^{III} standard Yb_2O_3 (green) measured at UW and $Yb^{II/III}$ mixed-valent Yb:CaF_2 (red) reproduced from Yoshida, et al (2005). Spectra offset for clarity. 214

Fig. 7-7: Schema outlining the different ways that synchrotron and laboratory XAS interact. See text for further details..... 216

Fig. 8-1: Measured voltage and capacity for the battery cell as a function of time from the start of the experiment. A series of dots designate the start of each XAS scan. Curves are shown for all cycles for which the cell was studied via XANES measurements at the Ni K-edge..... 231

Fig. 8-2: Ni K-edge XANES of the LIB at different degrees of lithiation. The state of charge at the start of each scan is provided in each figure. Only scans at specified intervals were provided for clarity. Spectra corresponding to a C/5 rate were truncated from scans extending over several hundred eV..... 233

Fig. 8-3: The Ni K-edge of each spectrum given as a function of state of charge at each cycle rate. Data taken faster than C/5 are offset successively by 0.5 eV..... 234

Fig. 8-4: Ni K-edge XAFS of the LIB at different degrees of lithiation for the C/5 and C/2.5 cycle rates. The state of charge at the start of each scan is provided in each figure. The horizontal axis has been converted from energy to outgoing photoelectron kinetic energy, i.e., the energy above the edge position. The peak related to scattering from the neighboring oxygen atoms is centered approximately 67 eV above the edge..... 235

Fig. 8-5: Measured voltage and capacity for the battery cell as a function of elapsed time. A series of dots designate the start of each XAS scan. Curves are shown for one full cycle during which XANES measurements were carried out at the Mn or Co K-edge..... 237

Fig. 8-6: Mn and Co K-edge XANES of the LIB at different degrees of lithiation. The state of charge at the start of each scan is provided in each figure. Only scans at specified intervals were provided for clarity..... 238

Fig. 9-1 Experimental V VTC-XES spectra of the set of V oxides and vanadyl phosphates. Spectra are shown after deadtime correction, constant background subtraction and integral normalization over the entire scan range. 253

Fig. 9-2: Representative experimental V VTC-XES results are shown for V_2O_5 (blue) along with the background fit to the low- and high-energy ranges of the VTC (orange, dashed). These two spectra are shown offset from the residual (green). The residual represents the VTC-XES without the tail from the V $K\beta_{1,3}$. 254

Fig. 9-3: V VTC-XES results for a suite of V oxides. The top spectrum in each frame is the experimental spectrum after correction for the tail from the V $K\beta_{1,3}$. The middle spectrum in each frame is the spectrum calculated by `FEFF9` using a Green's function approach. The bottom spectrum in each frame is the spectrum calculated by `NWChem` using a TDDFT approach. The sticks represent transition lines sorted into bins of 0.25 eV width. The sticks are subject to an arbitrary rescaling for clarity 255

Fig. 9-4: V VTC-XES results for a suite of vanadyl phosphates. The top spectrum in each frame is the experimental spectrum after correction for the tail from the V $K\beta_{1,3}$. The middle spectrum in each frame is the spectrum calculated by `FEFF9` using a Green's function approach. The bottom spectrum in each frame is the spectrum calculated by `NWChem` using a TDDFT approach. The sticks represent transition lines sorted into bins of 0.25 eV in width. The sticks are subject to an arbitrary rescaling for clarity 256

Fig. 9-5: Representative V VTC-XES TDDFT simulation. The relative contribution of each type of orbital to the transition lines occupying the corresponding region are shown in the histogram plot below the spectrum. 258

Fig. 10-1: Cr Kα XES of selected trivalent and hexavalent reference Cr compounds after background correction and integral normalization. Note, the spectrum of Cr(III) acetylacetonate is nearly identical to that of Cr(III) benzoylacetonate, and therefore hidden from view. 277

Fig. 10-2: Vertically offset Cr Kα XES spectra of plastics bracketed by compounds of pure-end member species (trivalent Cr_2O_3, top; hexavalent $BaCrO_4$, bottom). The measured spectrum for each plastic is shown along with the fit (dashed) provided by a least-squares regression analysis and the percent Cr(VI) determined from the fit. The first 10 eV and last 15 eV, which were collected to properly correct for background, are omitted. Note that all spectra are background corrected and integral normalized. For ease of reference, vertical dashed lines pass through the center of the Cr $K\alpha_1$ and $K\alpha_2$ peaks in $BaCrO_4$..... 279

Fig. 10-3: The near-edge region of: (a) the XAFS spectra of the hexavalent reference, potassium chromate, and (b) CRM 8113a, a certified reference material developed for heavy metal analysis with respect to RoHS directives. Also shown are the acquired fits and their components..... 282

Fig. 11-1: Experimental Diagrams for Energy Scale Reproduction — Above are standard Rowland circle geometries used in (a) x-ray emission and (b) x-ray absorption fine structure measurements. An intermediate hybrid geometry, (c), is used to establish a common energy scale across measurements. This is necessary to correct for sample absorptive effects in XES measurements..... 295

Fig. 11-2: Sample Geometry — X-ray photons of energy E_i from a source spectrum of intensity $I_o(E_i)$ are incident at an angle α relative to the face of the sample of thickness t. A detector, placed at an angle β from the sample's face, measures an emission spectrum $I(E_e)$..... 297

Fig. 11-3: Measured Spectra from Various Sample Geometries — Spectra from each of the three experimental configurations of Fig. 1 with the hybrid and XANES spectra energy corrected. An

energy shift of 8.75 eV aligned the hybrid and XANES spectra to the energy scale established at the synchrotron. A comparable energy shift was also needed to align the XES data to the new, common energy scale..... 300

Fig. 11-4: Absorption-Corrected Nickel Valence Emission — This figure shows both the uncorrected and corrected spectra of Ni valence emission. Obtaining the correct intensity of multi-electron peaks, which are identified via the *Z*+1 approximation, is critical for theory comparison..... 301

Fig. 11-5: Phenomenological Fits to Ni Multi-Electron Peaks — This figure shows the multiple pseudo-Voigt functions that were used to fit to each of the multi-electron emission peaks. These peaks' areas were used to determine the branching ratios given in Table 11-2. Not shown here are the fitted radiative Auger and $K\beta_{1,3}$ features, which also contribute to the determination of the final fit..... 302

List of Tables

Table 1-1: A glossary of terms used in the EXAFS equation. 26

Table 3-1: Experimental details of XES and XAFS measurements performed in this work. Acquisition times spanning multiple compounds refer to the time allotted to each sample. Acquisition times reported in this table only includes the time required to span the energy range shown in the corresponding figure. XAFS acquisition times are reported only for the transmission scans..... 106

Table 3-2: Selected EXAFS fitting parameters for Ni foil measured at APS and at UW as compared to literature fits, x-ray diffraction (XRD), and neutron PDF analysis. Uncertainties correspond to one standard deviation..... 114

Table 4-1: List of all bent crystal analyzers and analyzer forms used in this study. 138

Table 4-2: List of experiments performed, commercial SBCA or wafers used in the VF-BCA, and nominal Bragg angle for the absorption edge or fluorescence line from the indicated crystal reflection. 139

Table 10-1: Selected details of measured plastics. The samples contained various Cr compounds compounded in polymers: polypropylene (PP), polyethylene (PE), polyvinyl chloride (PVC), and acrylonitrile butadiene (ABS). The identity of the supplier, mass fraction and incorporated chromium compounds is also provided. For each Cr mass fraction value, the corresponding uncertainty is representative of a 95 % confidence interval. Materials, values, and uncertainty estimates are discussed in detail in the supplemental information. 271

Table 10-2: The species fractions determined by XAFS and XES are presented along with total integration times for the latter. The Cr(VI) mass fraction was calculated from the Cr(VI) species fraction and total Cr mass fraction. In the case of E5 and F6, the results of an interlaboratory

study facilitated by IEC TC 111 to determine the hexavalent chromium content via colorimetric analysis[43] are also included. Uncertainty estimates provided for the Cr(VI) mass fractions by XES are combined standard uncertainties including the uncertainty of the assigned total Cr value and the uncertainty of the found Cr(VI)/Cr ratio. All uncertainty values represent one standard deviation. 280

Table 11-1: Comparison between measured satellite energies and values predicted by the Z+1 model, referenced to the energy of the VTC diagram line. 302

Table 11-2: Comparison between experimental and predicted branching ratios (%) of the identified DI peaks and their corresponding diagram line intensity. Literature values were converted from probabilities to branching ratios following the procedure outlined in Section III. 303

Acknowledgements

There are a great many people that helped make this dissertation possible. I am deeply gratefully to my advisor Jerry Seidler for the continual life and academic lessons he has taught me. I am deeply thankful to the many collaborators who aided my research and education. This includes Timothy Fister, Joshua Kas, and Niri Govind, each of whom has taught me a great deal. I would like to acknowledge the many past and present graduate students in the Seidler group who have made my own research both possible and enjoyable. During my graduate career, I had the pleasure to share a lab with Devon Mortensen, Oliver Hoidn, Ryan Valenza, Alex Ditter, William Holden and John Ferré. I deeply appreciate the camaraderie and many scientific discussions they provided.

Finally, there are a great number of people in my life that made the past five years possible. These include my parents, Chris and Tamera, my brother, the rest of my relatives, my friends, my loved ones, and a large number of fantastic teachers. I am incredibly fortunate to have remained friends with a number of great people I met at my undergraduate institution. Thank you all for making the last five years in Seattle memorable. I would also like to acknowledge Kerry and R. Swoish, with whom I have enjoyed many exciting adventures and hope to enjoy many more.

Chapter 1. The Photoelectric Effect and its Associated Spectroscopies

1. Context and Motivation

Structure-property relationships are fundamental to modern materials research, yet the determination of atomic and electronic structure is far from trivial. Such endeavors often utilize X-ray techniques. Indeed, a wide range of experimental approaches exist for determining structural information via the interaction of X-rays with materials. As shown in Fig. 1-1, for energies below pair production the coherent, incoherent, and photoelectric absorption channels dominate. While all of these interactions have rich histories, the latter deserves special mention. The photoelectric effect was first observed by Hertz in 1887[1, 2] and explained by Einstein in 1905.[3, 4] These events represented a paradigm shift in mankind's understanding of light and are the cornerstone of technologies ranging from lasers to solar cells. Furthermore, this interaction is the foundation of several advanced X-ray spectroscopies which constitute the majority of this dissertation. For that reason, the photoelectric effect and the spectroscopies it enables will be reviewed here.

This chapter proceeds as follows. To being, in section 2 the photoelectric effect and its applications, including X-ray photoelectron spectroscopy (XPS) and X-ray absorption fine structure (XAFS), are outlined. Explanation of the latter will follow the traditional separation between the X-ray absorption near-edge structure (XANES) and the extended X-ray absorption fine structure (XAFS). A number of decay channels are accessible after the excitation of a photoelectron. These predominantly include nonradiative Auger processes or the radiative transition of an electron to fill a deeper core hole. These processes are the basis of Auger-electron spectroscopy (AES) and X-ray emission spectroscopy (XES), respectively. The latter

method will be discussed in section 3. Moreover, the naïve analysis of this process as a simple two state transitions can become complicated by other physical phenomena. Therefore, in section 4 appropriate perturbations will be outlined after introduction of the above techniques.

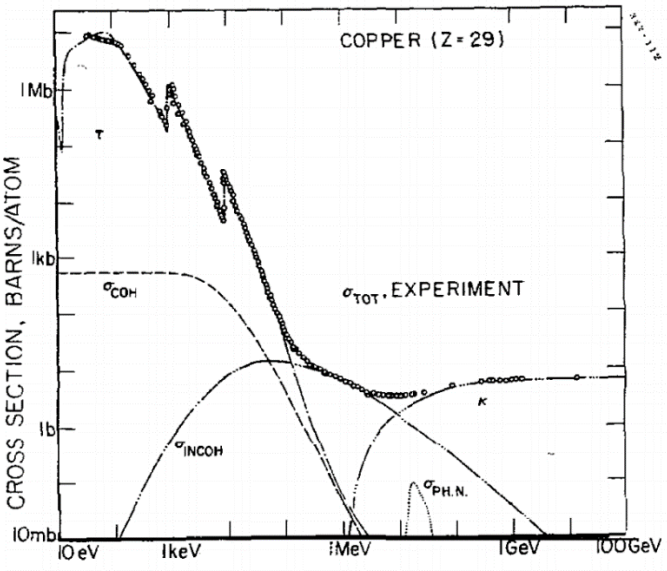

Fig. 1-1: Reproduced from Hubbell et al.5 The total cross section of Cu for photon interactions shown with its individual components: the atomic photoeffect, τ; coherent scattering, σ_{COH}; incoherent scattering, σ_{INCOH}; nuclear photoabsorption, $\sigma_{PH.N.}$; and total pair production, κ.

2. Photoelectric Processes

2A. Overview of photoelectric effects

In the framework of quantum mechanics, an electromagnetic field perturbs the ground state Hamiltonian[6] by

$$H_{EM} \propto \vec{p} \cdot \vec{A}, \tag{1-1}$$

where H_{EM} is the perturbation, $\vec{p}$ is the linear momentum operator, and $\vec{A}$ is the vector potential of the field. Fermi's golden rule then states that the transition probability, W_{fi}, is

$$W_{fi}(E) \propto |\langle \Phi_f | \vec{p} \cdot \vec{A} | \Phi_i \rangle|^2 \, \delta_{E+E_i-E_f-E_e}, \tag{1-2}$$

Where E is the energy of the photon, E_i is the energy of the initial state, E_f is the energy of the final state, and E_e is the energy of the outgoing photoelectron. The presence of the delta function serves to enforce conservation of energy throughout the absorption process. Two strategies exist which make use of the features of Eq. 1-2 for deducing chemical properties: First, the absorption coefficient, which is inversely proportional to E^3, is superimposed with sharp rises once the incident photon surpasses the binding energy of an electron, Fig. 1-2. By fixing the energy of the incident photons, the kinetic energy of the outgoing photoelectron can be measured and the binding energy deduced. Alternatively, by varying the energy of the incident photons around the immediate vicinity of a binding energy, the unoccupied density of states may be sampled subject to the interaction Hamiltonian's matrix elements in an element-specific manner. Utilizing the photoelectric effect in these ways is the basis of XPS and XAFS, respectively.

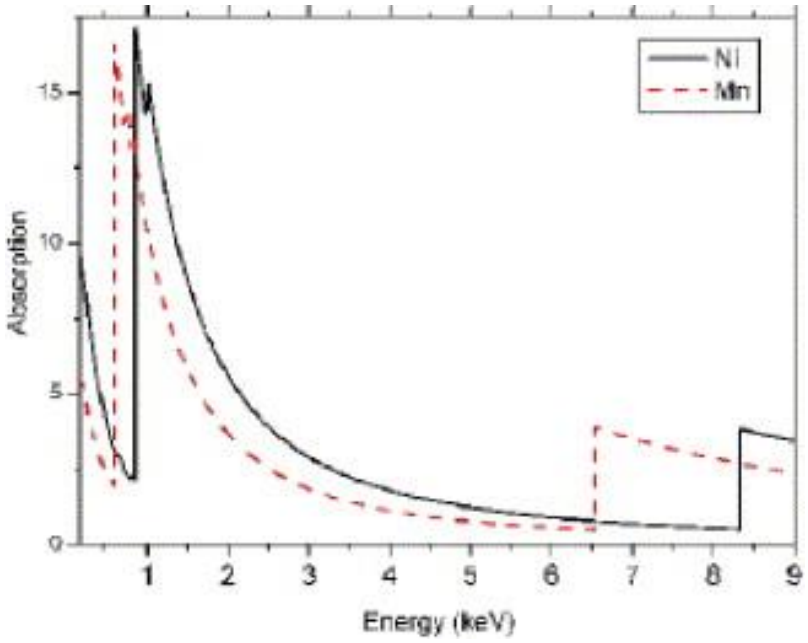

Fig. 1-2: Reproduced from de Groot et al.[7] X-ray absorption cross-sections of two transition metals. The L-edges are visible at around 1 keV and the K-edges for each element are visible between 6 and 9 keV.

2B. X-ray Photoelectron Spectroscopy (XPS)

The fundamentals and applications of XPS are now well-established,[8] and serve as a cornerstone of modern materials research[9] and industrial characterization.[10] XPS is appealing due to its ability to interrogate speciation which is predicated upon the dependence of a material's local screening and charge configuration on its chemistry as illustrated by Fig. 1-3. Here, XPS is used to assess the distribution of three different oxidation states in two V-based compounds. The different nuclear screenings present in each oxidation state yields three different chemical shifts which separate the corresponding spectral features and enables quantitative analysis. Compared to other X-ray spectroscopic methods, measuring two species of a given element often produces spectral differences that are large and easily interpretable. This frequently attributed to the fact that the transition probed by XPS only involves one atomic

level.[11] However, XPS suffers from several practical limitations. To begin, it requires a monochromatic source, which is often approximated in the laboratory by the characteristic fluorescence lines produced by an Al anode. Second, the sample must be measured under ultra-high vacuum which necessarily excludes liquids and substances with high vapor pressure. It should be noted that, in recent years, great lengths have been taken to begin to circumvent these restrictions via ambient-pressure XPS, where aggressive differential pumping allows the sample to be in a significant partial pressure, at least, while the path from the surface to the high vacuum in the electron energy analyzer is kept sufficiently short.[12-14] Finally, XPS is a surface-sensitive technique as a result of the relatively short inelastic mean free path of photoelectrons in most materials at the necessary energies,[15] see Fig. 1-4. As an additional consequence, care must be taken during sample preparation to avoid surface contamination. Nevertheless, XPS has enjoyed a rich history studying surface chemistry and, for example, the speciation of adsorbates.[16] On the other hand, the chemistry probed by XPS may not be representative of bulk behavior. Indeed, the materials measured in Fig. 1-3 were also measured by transmission-mode XANES with a large beam spot size to reveal the species distribution in the bulk.[17] The complementary sensitivities of the XANES and XPS results then verified the hypothesis that the oxygen vacancies were produced according to a gradient from the surface. Before concluding this section, it should be noted that surface-sensitivity can be substituted for deeper layer sensitivity via hard X-ray photoelectron spectroscopy (HAXPES). The information depth of HAXPES has been the subject of many studies, including that by Rubio-Zuazo *et al.*[18] Moreover, this technique has recently enabled studies on topics of substantial contemporary interest, such as the structure of the solid electrolyte interphase (SEI) in Li-ion batteries.[19] The accessibility of HAXPES may also soon increase due to breakthroughs in laboratory-based instrumentation.[20]

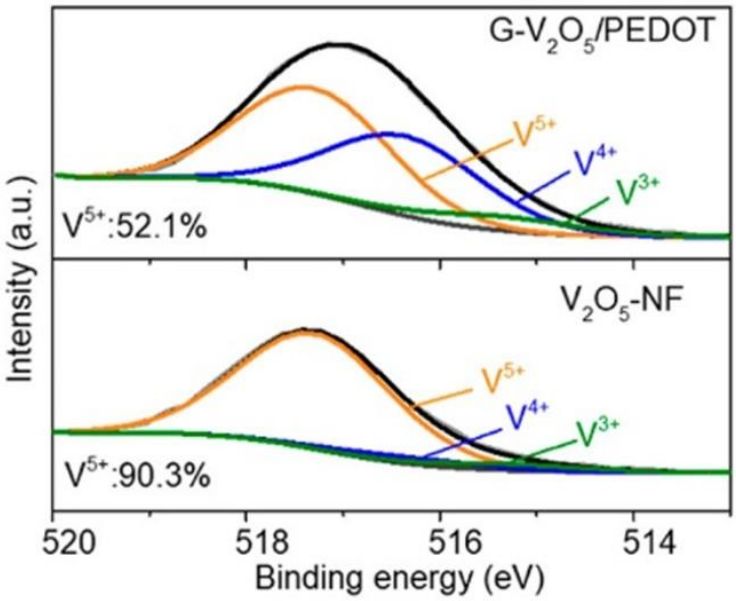

Fig. 1-3: Reproduced from Bi et al.[17] XPS of V $2p_{3/2}$ spectra of V_2O_5 nanocables with a gradient of oxygen vacancies introduced by surface polymerization with poly(3,4-ethylenedioxythiophene), G-V_2O_5/PEDOT, and V_2O_5-based nanocables, V_2O_5-NF. The V^{3+}, V^{4+}, and V^{5+} oxidations states are represented by V_2O_3, VO_2, and V_2O_5, respectively.

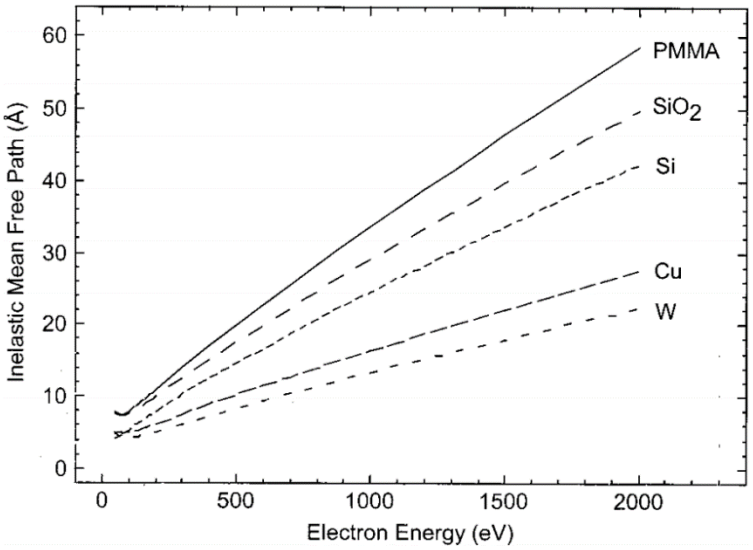

Fig. 1-4: Reproduced from Powell.[15] The calculated inelastic mean free path of an electron is shown as a function of energy for a few materials.

2C. X-ray Absorption Fine Structure (XAFS) Analysis

The sharp increase in absorption corresponding to the onset of the photoelectric effect, as seen in Fig. 1-2, is the basis for another analytical technique, X-ray Absorption Fine Structure (XAFS). The first such spectrum was observed by Herweg in 1913,[21] though credit is normally given to M. de Broglie[22] who made similar observations later that year. Both experimenters detected sharp or diffuse lines and bands next to a strong edge collected on photographic plates. However, further progress in the field was momentarily slowed as neither scientist was confident in their result. Herweg, abandoning this line of research, and M. de Broglie, claiming to have misinterpreted his first photos after substantial criticism.[23] The field of XAFS was launched in earnest by the measurements of Fricke[24] and Stenström under the supervision of Siegbahn. Around this same time, similar measurements were made by Hertz.[25] Shortly after, Lindh reported a dependence of the XAFS edge position on the chemical speciation of a range of

chlorine-based complexes.[26] The work by Lindh then helped lay the groundwork for some of the earliest theories explaining chemical shifts, such as that by Pauling in 1929.[27] This led to the 1929 observation by F. K. Richtmeyer that: while the empirical evidence available to the scientific community roughly a decade earlier suggested that, among other details, (1) the discontinuities in absorption due to the photoelectric effect were abrupt and (2) the energy at which this discontinuity occurs is independent of the chemical state of the absorber, neither of these rules were indeed correct.[28] These leaps were enabled by improvements in the energy resolution of the spectrometers of the day. Here, this manuscript will continue with a more contemporary perspective on XAFS.

The XAFS process can be thought of in the following way. When a photon interacts with a material, it has some probability of absorption by exciting an electron. The probability of absorption can be calculated after a few approximations. The vector potential of the electromagnetic wave responsible for this excitation takes the form $e^{i\vec{k}\cdot\vec{r}}$ and can be expanded as $1 + i\vec{k}\cdot\vec{r} + (higher\ terms)$, where $\vec{k}$ is the wave vector. The higher order terms are typically vanishingly small because the spatial extent of a given orbital is almost always much smaller than the wavelength of light needed for its photoelectric effect. The remaining terms give rise to the electric dipole, electric quadrupole, and magnetic dipole terms. This can be seen following the arguments of Debeer *et al.*[29] which suggests the transition amplitude in Eq. 1-2 may be rewritten in the dipole approximation as

$$I_{XAFS}(E) \sim \rho(E)|\langle\varepsilon|\hat{e}_q\cdot\vec{r}|c\rangle|^2\delta_{E+E_c-E_\varepsilon-E_{\bar{c}}}, \tag{1-3}$$

where the one electron approximation has been assumed. Note that ρ is the unoccupied density of states, ε is the free electron wave function, c is a core wave function, E is the energy of the

incident photon, E_c is the energy of the state with c occupied, E_ε is the kinetic energy of the photoelectron, $E_{\bar{c}}$ is the energy of the state with c unoccupied, and the central term corresponds to a dipole transition. Thus, the absorption probability as a function of energy corresponds to a probe of that material's unoccupied density of states as a function of energy.

The details of this measurement process will be investigated in a later section of this chapter. At present, it suffices to state that the desired result is a plot of absorption coefficient as a function of incident photon energy, Fig. 1-5. There are two distinct regions in this plot, a collection of features in the immediate vicinity of the rise in absorption due to the photoelectric effect and a series of long-range oscillations beyond the edge. The aforementioned regions are referred to as the XANES and extended X-ray absorption fine structure (EXAFS), respectively.

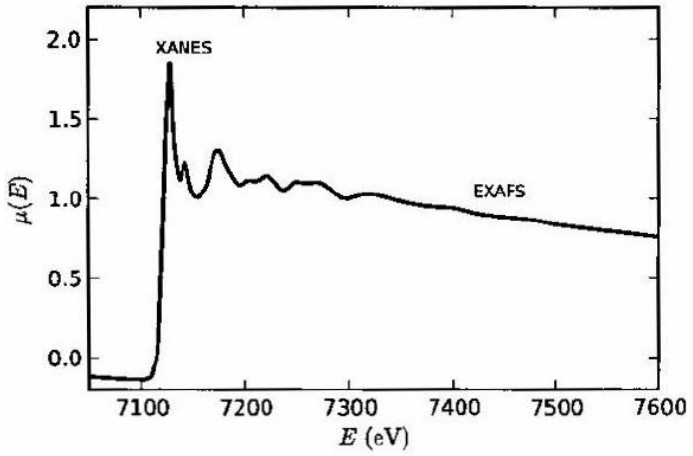

Fig. 1-5: Reproduced from Newville.[30] XAFS spectrum taken at the Fe K-edge on FeO. The XANES and EXAFS regions are shown.

2C. I. X-ray Absorption Near-Edge Structure (XANES)

The analysis of XANES spectra is traditionally performed in one of two ways: by performing density functional theory (DFT) guided simulations of the spectrum and searching for electronic

structure changes which correspond with and cause the changes in spectral features, or by using a series of features as qualitative fingerprints of certain chemical properties. A discussion of the former can be found in later chapters of this dissertation, while a guide to the latter is presented here. Specifically, in Fig. 1-6, a XANES spectrum is shown which possesses several spectral features which are often used for the purpose of qualitative finger printing. These features can be separated into a pre-edge, shoulder, edge, white line, and scattering region will be discussed in that order.

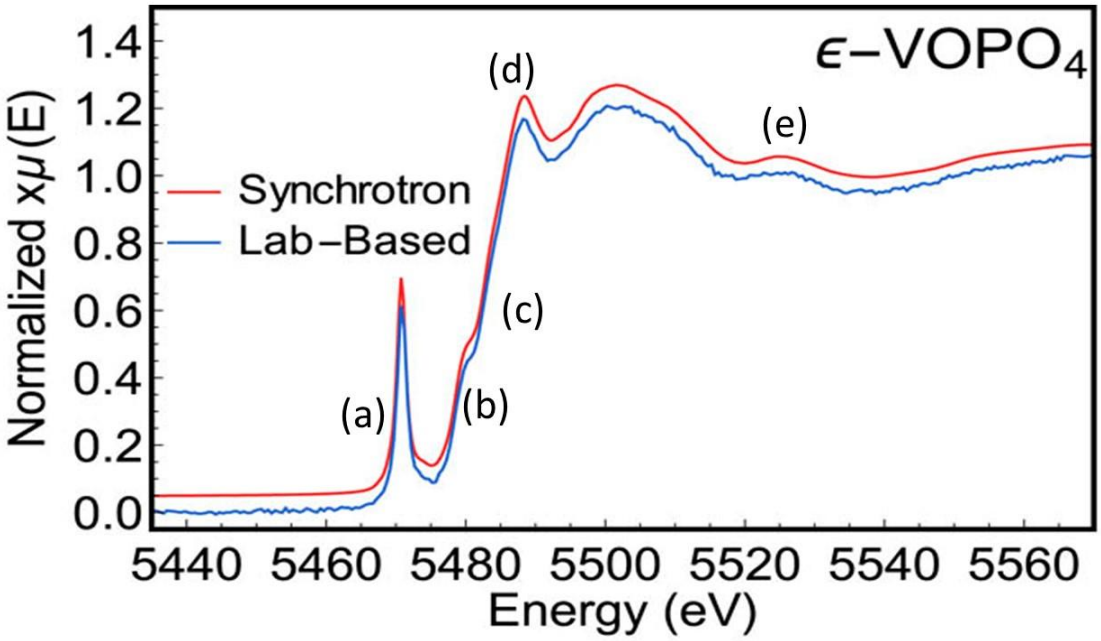

Fig. 1-6: From Jahrman et al.[31] A comparison of measurements performed at APS 9-BM (Synchrotron) and with laboratory-based instrumentation at the University of Washington (Lab-based). XANES spectra were collected at the V K-edge of an epsilon phase vanadyl phosphate lithium ion battery cathode. The following XANES features are labeled: (a) a pre-edge peak, (b) a shoulder feature, (c) the edge, (d) a white line feature, (e) a series of scattering peaks from atoms neighboring the absorbing V atom.

Pre-edge features are often used as identifiers of molecular symmetries and distortions in the system of interest. For transition metal K-edges, these correspond to transitions of a 1s core electron to an unoccupied state below the continuum, typically with non-negligible 3d character. Note that this last statement is an approximation. Indeed, as the dipole operator is odd under inversion, it can only couple states of opposite parity in system's with inversion symmetry. To better understand the preceding statements, take the case of a system with octahedral symmetry. From Eq. 1-3, we can see that the dipole operator will behave as the components of a vector. In the O_h group, this corresponds to the irreducible representation T_{1u}. As a 1s orbital corresponds to the totally symmetric representation, A_{1g}, then, from

$$T_{1u} \otimes A_{1g} = T_{1u}, \tag{1-5}$$

it can clearly be seen that the dipole transitions can only couple the 1s electron to states of the T_{1u} irreducible representation, of which d-orbitals, which are even under inversion, clearly do not belong. In the case of a molecule with T_d symmetry, the dipole operator belongs to the irreducible representation T_2, the direct product of this with the irreducible representation E, to which d_{z^2} and $d_{x^2-y^2}$ belong, does not contain the totally symmetric representation, however,

$$T_2 \otimes T_2 = A_1 + E + T_1 + T_2 \tag{1-6}$$

does. This means that orbitals belonging to the T_2 representation, such as p-orbitals, d_{xy}, d_{xz}, and d_{yz}, are not forbidden from participating in dipole transitions by group theory. However, group theory does not solely determine the possibility or magnitude of a transition. Dipole transitions may be subject to further physical restrictions, including conservation of angular momentum, which places the familiar restrictions on dipole transitions. It should be further noted that the Hamiltonian can be made block diagonal with each block corresponding to a given

irreducible representation, as a result, molecular orbitals are constructed as linear combinations of atomic orbitals of the same irreducible representation. This leads to the familiar notion that, under tetrahedral symmetry, p- and d-orbitals (specifically, those of the T_2 representation listed above) are able to mix. The component of the molecular orbital contributed by the p-orbital is then dipole-allowed and contributes significant intensity to the naively $1s \rightarrow 3d$ transition.[6, 7] As an example, refer back to Fig. 1-6.

The above arguments have the following practical consequence: molecules with distortions, or otherwise lacking inversion symmetry, tend to have amplified pre-edge features. This fact can be used for quantitative speciation distribution analyses. For Cr, nearly all hexavalent ions are of tetrahedral symmetry, while trivalent are of octahedral symmetry. Thus, a calibration curve may be constructed from these endpoints and the composition of a mixture of Cr oxidation states may be determined from the intensity of the pre-edge feature. An example from this thesis is shown in Fig. 1-7, where the pre-edge has been fit to a linear combination of three features[32-35] that are Lorentzian[36, 37] in nature. The area of the Lorentzian of intermediate energy was then used to determine the ratio of Cr(VI) to total Cr in a range of plastics.[32, 35, 38]

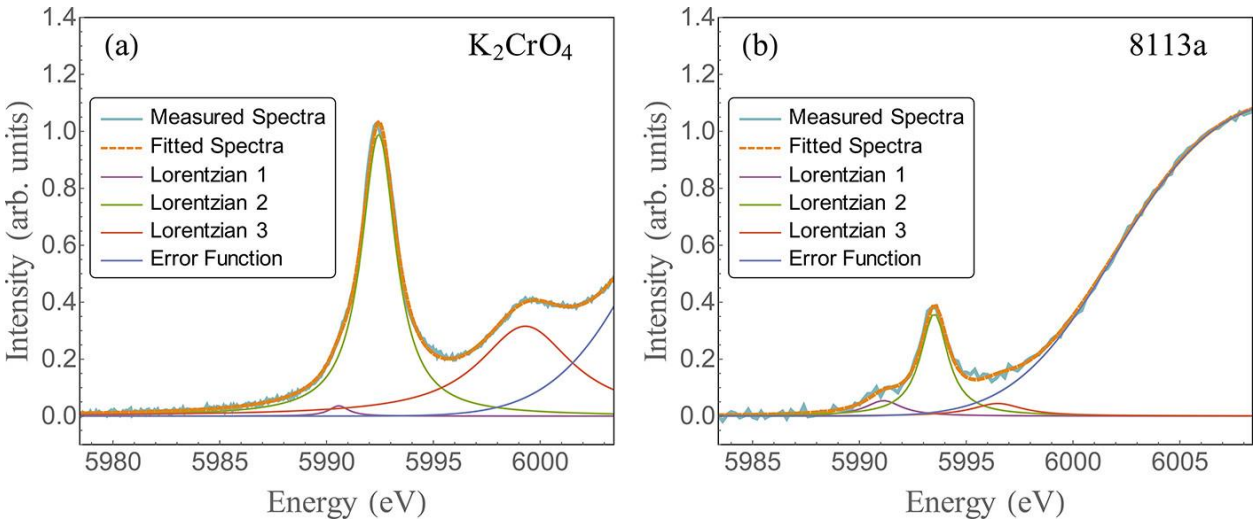

Fig. 1-7: From Jahrman et al.[39] The pre-edge peaks of the XANES spectra of (a) potassium chromate, a hexavalent reference, and (b) CRM 8113a, a standard reference material. Also shown is the fit along with its components as calculated in Athena.[40]

Additional features are often observed along the rising edge of XANES spectra, these features are referred to as shoulders and, in first row transition metals, are ascribed to 1s->4p transitions. These features are particularly sensitive to the characteristics of a material's electronic and atomic structure. This results in two consequences, the description of the underlying physical processes is liable to becoming rather involved, and the general shape can serve as a useful fingerprint. A detailed delineation of these points is beyond the scope of the present work, but can be found in reviews such as that by Gaur and Shrivastava.[41] Here, only two examples will be given to illustrate the previous statements, the shoulders of Cu and Co, as seen in Figs. 1-8 and 1-9, respectively.

In the case of Cu, Kau et al. have previously made claimed that the shoulder features are largely diagnostic of the relevant Cu complexes.[42] Here, ligand field effects separate the $4p_{xy}$ from the $4p_z$ orbitals.[43] Depending on the relevant chemistry, a variety of explanations are

traditionally given for the lower energy of the $4p_{xy}$ relative to the $4p_z$. In Cu(I), this includes the antibonding nature of the $4p_z$ orbitals entailing increased repulsion between electrons along the z axis and covalent ligand overlap along the z axis.[44] In the case of Cu(II) compounds, the 1s->$4p_{xy}$ transition is often accompanied by a shake-down transition. Beyond additional complexity, this necessitates the effect of the change in nuclear screening on the energies of the relevant orbitals be taken into account.

In the case of Co, a few representative compounds are shown in Fig. 1-9 which exhibit dramatically different shoulder features. In the highlighted study, these features were used as unique identifiers of the studied chemical species. In particular, inflection points are observed on the rising edge of the spectrum corresponding to CoP at approximately 7709.75 and 7715.75 eV. These features are different in energy and intensity from those of the nominal Co_2P phase. Here, the CoP material produced by a novel synthesis procedure was compared to an empirical standard produced by an established literature procedure.[45] The excellent agreement between the shoulder features, which served as chemical fingerprints, provides strong supporting evidence that these materials are of the same species.[46]

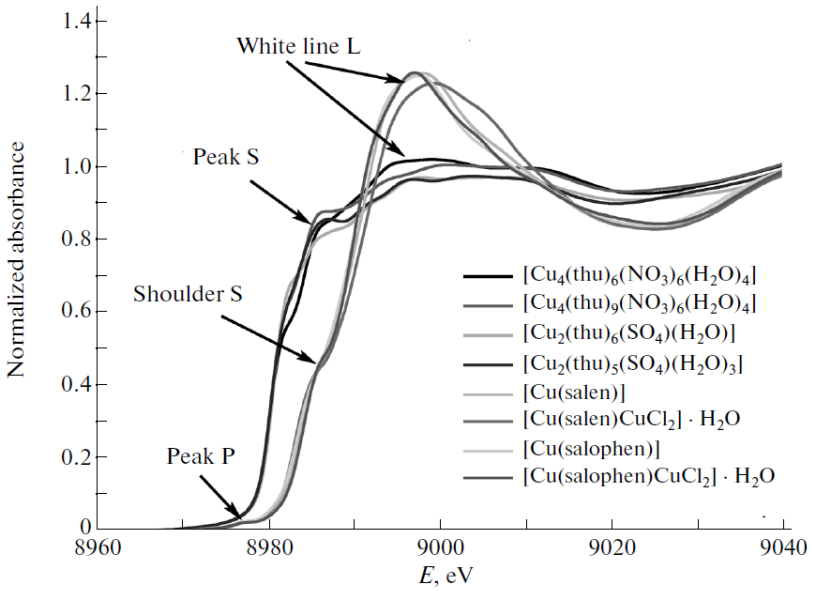

Fig. 1-8: From Gaur and Shrivastava.[46] The Cu K-edge XANES spectra of a collection of mono- and divalent Cu species. A variety of spectral features are designated, including Peak S and Shoulder S, which are collectively referred to as shoulder features in this work.

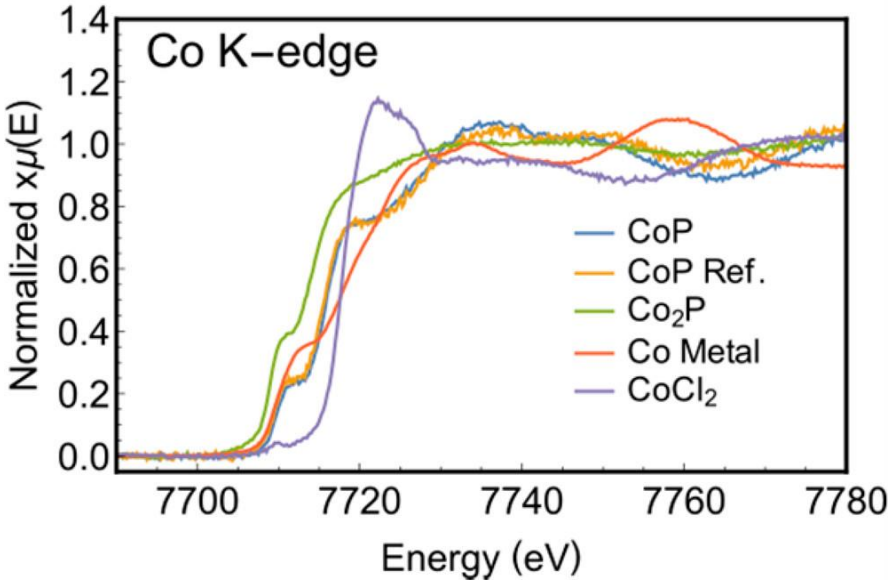

Fig. 1-9: From Mundy et al.[46] Co K-edge XANES spectra of CoP and Co_2P produced by a novel synthesis procedure, $CoCl_2$ and Co metal commercial standards, and a second CoP compound produced by an established literature procedure.[45]

Moving on, XANES analysis is frequently used in materials research to interrogate the oxidation state of a given metal within a system. This assignment is then made by identifying the energy corresponding to the rising edge of a material's XANES spectrum. This position roughly corresponds to the onset of continuum states within the material and is related to its oxidation state. As a material undergoes oxidation, the edge position observed in XANES typically moves to higher energies upon oxidation.[7, 41, 47] This idea is frequently invoked in XANES publications. Indeed, it is the most common application of XAFS in catalysis research,[48, 49] is frequently cited in energy storage research and has been proposed for monitoring the state-of-charge of cathode materials during cycling,[50] and has aided in studies of biomolecules.[51, 52]

Before moving on, a few complexities regarding this analysis deserve mention. First, it is not always convenient to identify the edge position. In some instances the position of a substitute feature may then be used.[46, 53] Second, the determination of the edge position is traditionally done in one of three ways: as the position of the first maxima of the first derivative of the spectrum, the position at which the spectrum is at one half of the edge step, or the average of the positions at which the spectrum is at 20% and 80% of the edge step.[47] All of these methods are equivalent in the absence of shoulder features. When a shoulder is present, no clear criterion is available. Rather, it is suggested that multiple methods be compared, or else an alternative feature be used, as is the case for the analysis of Fe oxidation according to its pre-edge position.[54]

The above concepts appear several times throughout the work comprising this thesis.[17, 31, 46, 55, 56] In particular, this behavior enabled the real-time analysis of the oxidation state of Ni, which is the atomic species primarily responsible for charge compensation in the cathode of Li-

ion batteries composed of Ni-rich layered oxide materials incorporating Ni, Mn, and Co.[57] In this system, Li-ions are extracted upon charge and the Ni atoms become more oxidized as a result. In Fig. 1-10, it can be seen that the Ni K-edge shifts uniformly to higher energies upon charging and to lower energies upon discharge. Furthermore, Fig. 1-11 shows that the edge position varies linearly as a function of charge stored regardless of charge rate. Thus, the edge position can serve as a valuable diagnostic tool of the state-of-charge in a Li-ion battery.

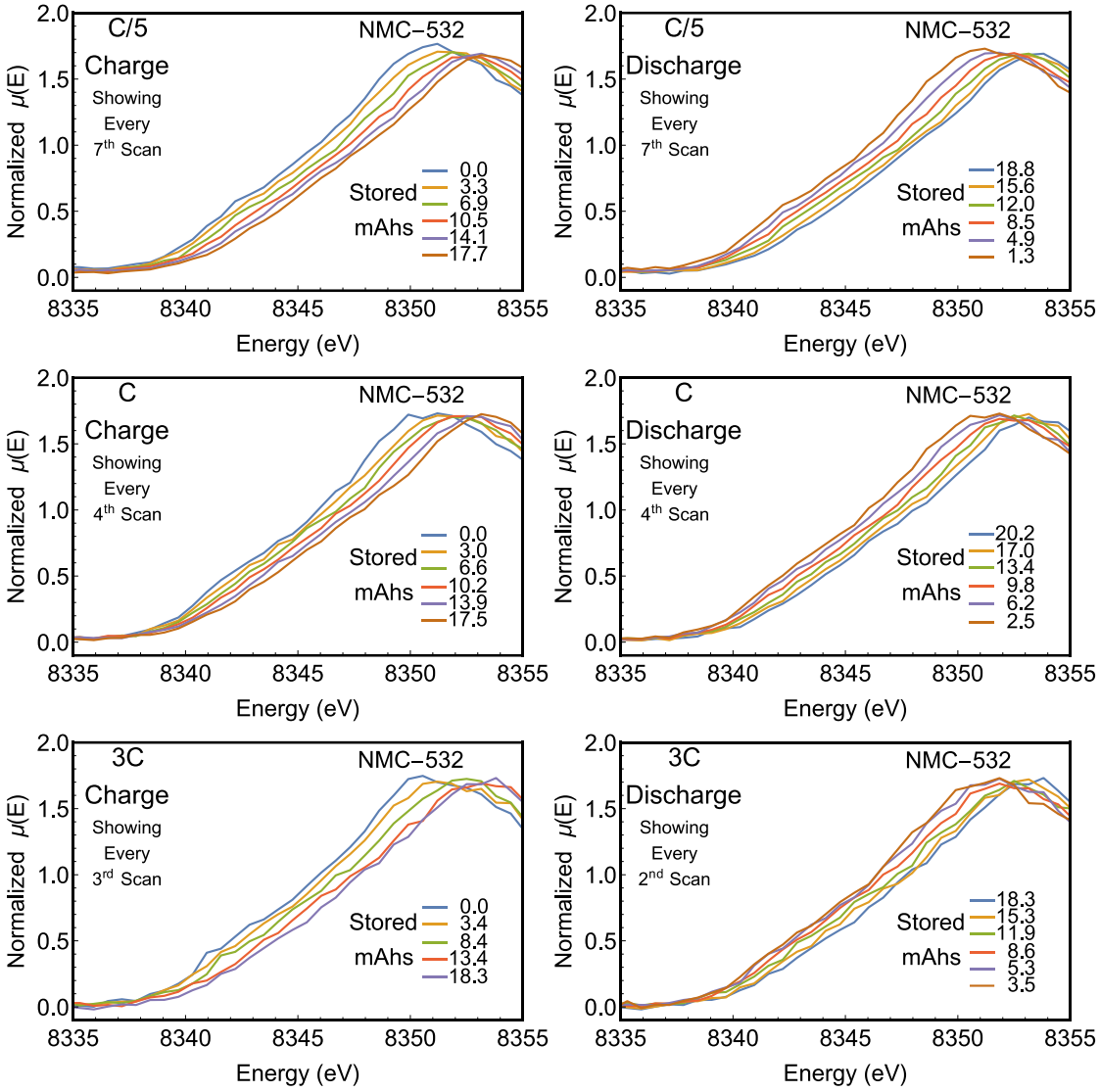

Fig. 1-10: From Jahrman et al.[56] The Ni K-edge XANES spectra of a layered oxide cathode material at different states of charge. Results were acquired *operando* at the reported charging rates.

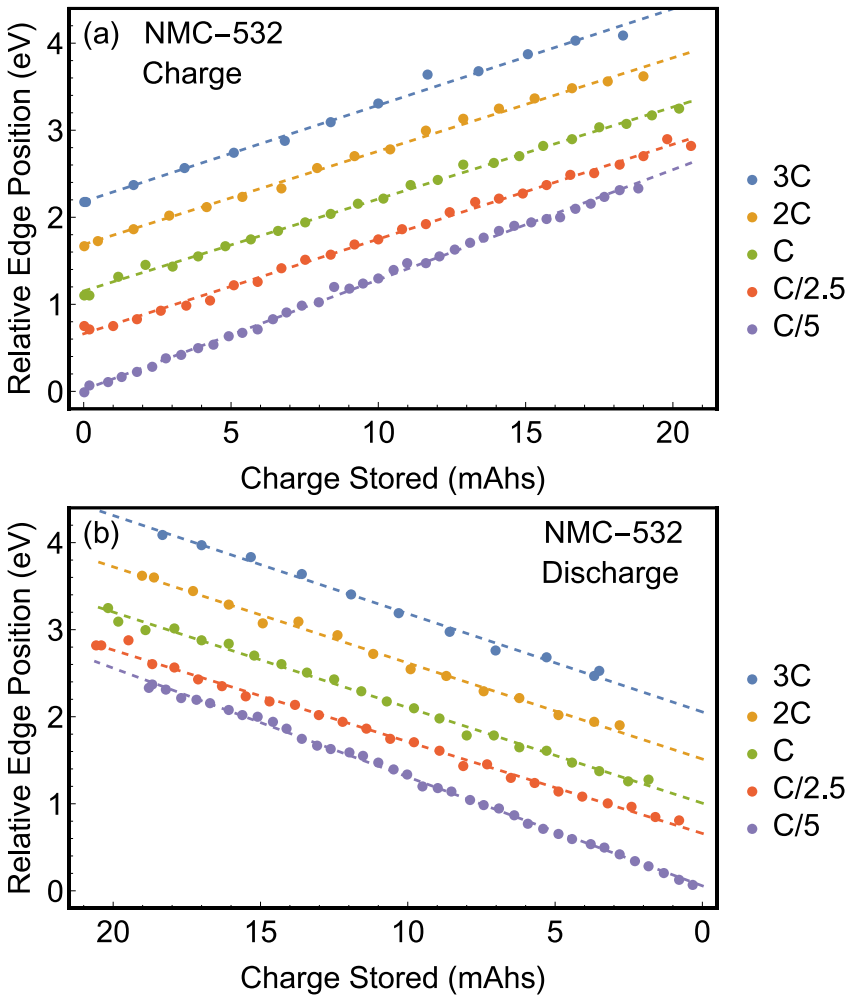

Fig. 1-11: From Jahrman et al.[56] The position of the Ni K-edge of the XANES spectrum collected at each charge state for a variety of charging and discharging rates. A few of the corresponding XANES spectra are shown in Fig. 1-10.

The white line feature is a sharp, intense absorption band at the top of the edge. Its name is derived from its historical origin as a "white line" on a photographic plate from the early years of X-ray spectroscopy.[58] Currently, the white line feature serves several useful diagnostic purposes as it measures oxidation in materials and also correlates with cluster size during nanoparticle formation.[59] In either case, this is primarily due to the origin of the white line, which is an abundance of empty states in low-lying bands of the appropriate symmetry. For

example, note that the white line intensity is often used to track charge transfer during alloying. This approach has permitted the analysis of PtGe intermetallic formation,[60] charge transfer during the synthesis of bimetallic AuPd catalysts,[61] and the production of AuAl alloys,[62] see Fig. 1-12.

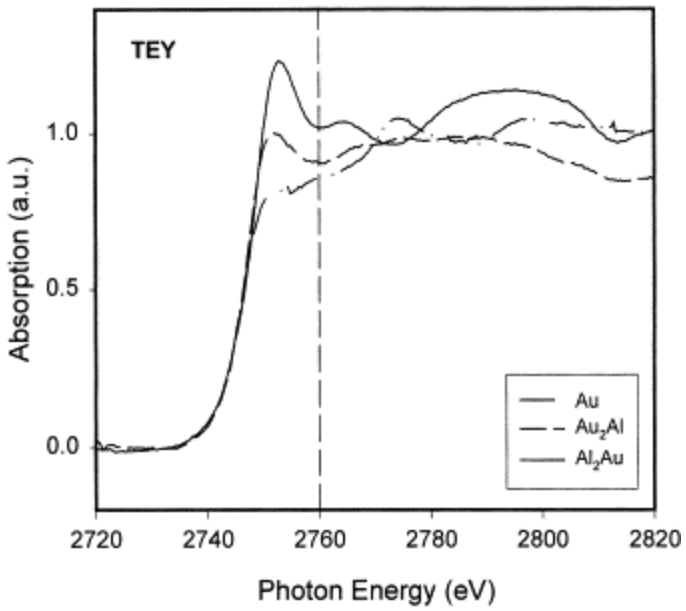

Fig. 1-12: From Piao et al.[62] The Au M_3-edge XANES spectra of Au and two Au-Al alloys collected in total electron yield (TEY).

Single and multiple scattering paths are not only important in the context of EXAFS, but also make a significant contribution in the XANES region. There are three reasons for these processes' anomalously large contribution at low photoelectron momentum. First, the EXAFS equation, which will be discussed in the next section, breaks down at low-k due to a 1/k dependence, where $\vec{k}$ is the photoelectron wave vector. Second, the inelastic mean free path of an electron dramatically increases at low-k. Third, Debye-Waller factors are considerably damped at low-k. For this reason, it is not unusual to see these processes play a role in the

interpretation of spectral features in the XANES region. Indeed, a significant portion of the white line feature of some systems can be ascribed to multiple scattering paths, including MnO[58] and some Pu complexes.[63, 64] Slightly further from the edge, wide oscillatory features can be observed which are due to scattering paths involving atoms neighboring the absorber. These peaks are the result of interference between the portion of the photoelectron's wave function traveling away from the absorbing central atom and the portion which has scattered off the potentials of the atoms adjacent to the absorber. The position of these peaks relative to the edge can be related to bond length via the familiar $1/R^2$ rule as outlined by Henderson.[47] Such analyses have been successfully applied in the study of actinides,[65, 66] small molecules,[67] and iron silicate melts.[68]

2C. II. Extended X-ray Absorption Fine Structure (EXAFS)

Over the last century, EXAFS received considerable attention and, accordingly, grew into a productive and established technique. As a result, several thorough personal and historical accounts can be found,[23, 69, 70] this section will give a more brief overview of the efforts dedicated toward developing a robust theory of EXAFS to give an appreciation for the degree of detective work the task required.

Over half a century passed between initial theoretical descriptions of EXAFS and a form consistent with the modern theoretical treatment. Early attempts to explain the fine structure beyond absorption edges did not yet appropriately incorporate continuum states. In 1920, Kossel ascribed EXAFS oscillations to transitions involving higher unoccupied orbitals belonging to the absorbing atom.[71] On the other hand, Wentzel proposed multiple electron excitations as the cause of high-energy structure.[72] Shortly thereafter, Kronig and Penney introduced a one-dimensional model describing electrons dispersing into allowed and forbidden bands by

scattering off extended linear arrays of atoms in a crystal.[73] Kronig used this model as the foundation for his first theory of EXAFS.[74] This quickly replaced the models of Kossel and Wentzel, yet suffered from several limitations. Most notably, the theory only explained the spectra of systems with long-range order. Furthermore, the strength of reflections did not always correlate with expectations, yet sufficient crystal planes often existed to explain the absorption features observed and permitted experimenters to claim agreement with theory. Thus, Kronig's theory played a significant role in physics of the 20th century. Indeed, until the 1970s, approximately 2% of papers published by *Physical Review* were devoted to X-ray absorption spectroscopy and most of these invoked Kronig's theory.[69]

The theory of EXAFS did not remain stagnant in the years following Kronig's initial publication. Motivated by the results of Hanawalt on systems with short-range order[75] Kronig developed a second theory for molecules.[76] This theory was further developed by one of Kronig's students, Petersen, and recast in the form[77, 78]:

$$\chi(E) - 1 = \sum_{l=0}^{\infty}(2l+1)\left[\frac{(-1)^{l+1}}{(k\rho)^2}\right][\sin(\delta_l)\sin(2k\rho + \delta_l)] \qquad (1\text{-}7)$$

This form, which can also be found in Lytle's summary of these events,[69] already bears striking resemblance to the modern theory. Here, $\chi(E)$ is the fine structure, $\vec{k}$ is the photoelectron wave vector, ρ is a radial distance, and δ_l is a phase constant determined by scattering theory.[79] Over the next several decades, researchers in Japan and Russia made further contributions to the development of EXAFS theory, in particular considering scattering off of neighboring potentials.[80-84] Note that many of these models were still quite computationally expensive in an era where this was a major practical limitation. A breakthrough came from Lytle, who related

the energy scale of the absorption spectra to the zeros of the half-order Bessel function, Q, allowing one to obtain the first-neighbor distance, r_s, from the slope of the relation

$$E = \left(\frac{37.6}{{r_s}^2}\right) Q. \tag{1-8}$$

This simple formula permitted determinations of structural information with minimal computational effort.[85] After developing this simple model, Lytle collaborated with Stern and his student Sayers to recast EXAFS in the form familiar to modern spectroscopists.[86] They accomplished this by proposing the following 'EXAFS equation' (Eq. 1-9) that could be Fourier transformed in a manner similar to the more established Fourier transformation of X-ray scattering data.[87]

$$\chi(k) = -kf(k)\sum_j [N_j e^{-\gamma r_j} / r_j^2] e^{-\frac{\sigma_j^2 k^2}{2}} \sin(2kr_j + 2\eta(k)) \tag{1-9}$$

Note the specific terms within the Eq. 1-9 will be discussed shortly, but are analogous to those in Table 1-1. These authors applied this theory by performing a Fourier transformation to experimental EXAFS data for crystalline and amorphous Ge, Fig. 1-13. The results confirmed their theory and demonstrated a considerable advantage, this Fourier analysis technique universally characterized systems with short-range or long-range order using a single theory. Developments were quickly made to the aspects of the technique related to experiment,[88] theory,[89] and determination of parameters[90] and, in short order, the technique saw application in amorphous semiconductors,[91] catalysts,[92] and biological materials.[93]

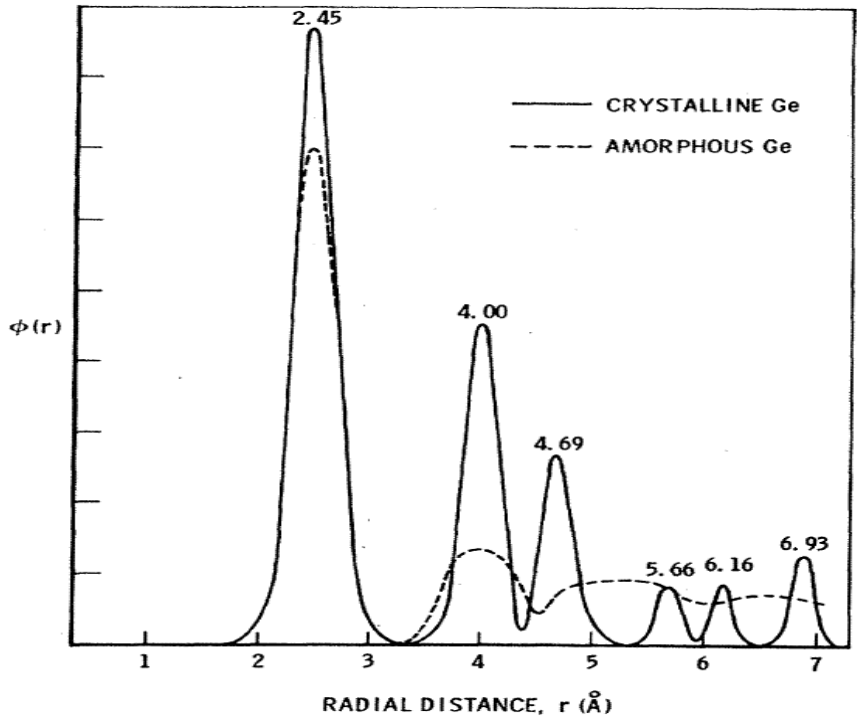

Fig. 1-13: From Sayers et al.[86] Fourier transformation of the oscillatory part of χ from crystalline and amorphous Ge, *i.e.* a radial structure function providing a measure of bond lengths in these two systems.

Above all, EXAFS is a method for determining local structural information and Eq. 1-9 provides a framework for this purpose. In practice, this involves proposing a structural model, acquiring an experimental EXAFS spectrum, fixing the parameters of Eq. 1-9 that can be calculated, and varying the remaining parameters to acquire the best possible fit of the data. Thus, the calculation and determination of physical parameters play a central role in the EXAFS technique. These parameters will now be explained, however the EXAFS equation will first be written in a more modern form to facilitate the discussion, i.e.,

$$\chi(k) = S_o^2 \sum_i [\frac{N_i F_i(k)}{kR_i^2}] e^{-2\sigma_i^2 k^2} e^{-2R_i/\lambda(k)} \sin[2kR_i + \phi_i(k)] \qquad (1\text{-}10)$$

The following two equations are also needed:

$$R_i = R_o + \Delta R \tag{1-11}$$

And

$$k^2 = 2m_e(E - E_0)/\hbar^2 \tag{1-12}$$

Equation 1-10 is a summation taken over each coordination shell, which can be generalized to include contributions from both single and multiple scattering paths, each scaled by the number of equivalent paths.where.[94] Each of the variables is defined in Table 1-1. It should also be noted that, of the above parameters, only F_i, ϕ_i, and λ may be calculated, while N_i, S_o^2, σ_i^2, E_0, and ΔR must be determined by fits to experimental data.

Naively, Eq. 1-10 looks much as a researcher with the benefit of hindsight would expect. A term resembling the leading spherical Bessel function of the first kind describes the outgoing photoelectron's wavefunction. The argument of the sine function in Eq. 1-10 corresponds to the phase rotation the electron undergoes during its path. There is also a Debye-Waller factor accounting for disorder as well as a damping term for losses due to inelastic scattering. In addition, an assortment of terms appropriately varies the amplitude of each path. Furthermore, many of these parameters have been the subject of extensive research and merit discussion.

Table 1-1: A glossary of terms used in the EXAFS equation.

Symbol	Variable Description
m_e	Electron Mass
k	Photoelectron Momentum
E	Incident Photon Energy
E_0	Edge Position
R_o	Initial Shell Size (from model)
ΔR	Change in Path Length
ϕ_i	Effective Scattering Phase Shift
N_i	Degeneracy of Paths in the Shell
F_i	Effective Scattering Amplitude
S_o^2	Passive Amplitude Reduction Factor
σ^2	Mean Square Displacement
λ	Inelastic Mean Free Path of the Electron

First, S_o^2 is, in principle, a result of the incomplete overlap between passive electrons in the ground state and the final ionic state of the system.[95] Accordingly, the absorbing atom is primarily responsible for determining S_o^2 and neighboring atoms only influence the parameter by through the final ionic state. This would suggest that it is desirable to use standard or calculated values of S_o^2, indeed, this would remove its correlation with the coordination number and allow the determination of an imaginary energy parameter to account for broadening of the EXAFS signal.[96] However, use of standard or calculated S_o^2 values is typically impractical. This is

because sample or beamline specific characteristics, particularly the energy resolution of the spectrometer, affect the value of this term determined by the fit. Thus, this parameter is only occasionally reported and values between 0.7 and 1.1 are treated as reasonable.[96]

Second, measurements of a material's EXAFS spectrum is also strongly impacted by disorder. Here, variations in atomic positions due to thermal or structural disorder causes deviations in the scattering paths which an electron may experience. The mean-square variations in position then give rise to a Gaussian Debye-Waller factor in the EXAFS equation. Thus the fit values of σ^2 reflects the degree of disorder in the system. The fit is normally constrained to one of several models with the correlated Debye model and the Einstein model the most common. These methods are discussed by Sevillano *et al.* and compared to different force-constant modes based on Monte-Carlo simulations, Fig. 1-14.[97] Note that addressing Debye-Waller factors in multiple scattering paths is slightly more involved as the motion between two atoms in a multiple scattering path can be correlated. For collinear paths, the σ^2 values are related to those of the single scattering paths as described by Hudson *et al.*[98] For triangular multiple scattering paths, approximations must be made and a discussion can be found in a text by Calvin.[99]

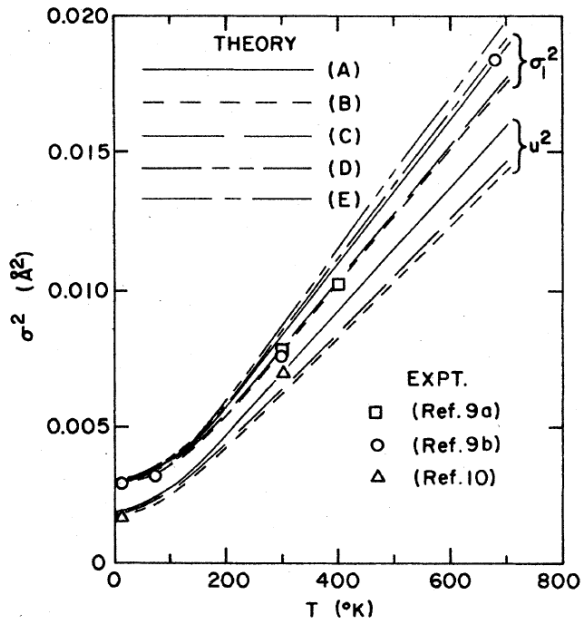

Fig. 1-14: From Sevillano *et al.*[97] First shell mean-square vibrational amplitudes for Cu as a function of temperature. A variety of force-constant models are considered and compared to experimental data in the literature. The theoretical models are (A) that of Svensson *et al.*,[100] (B) that of Nicklow *et al.*,[101] (C) that of Sevillano *et al.*,[97] (D) the Debye model, and (E) the Einstein model.

Third, another major topic in EXAFS is the calculation of scattering amplitudes. These calculations can be performed in the framework of Gurman *et al.*,[102] Filipponi *et al.*,[103] or Zabinsky *et al.*[104] In all cases, these calculations involve calculating the potential surface of a cluster of atoms in the muffin-tin model.[105, 106] This involves first placing neutral atoms[107] at the given crystal lattice sites. However, as the neutral-atom radii are relatively large, this causes significant overlap between the radii of adjacent sites. This is problematic as the electrons in overlapping regions cannot be definitively assigned to a particular atom. This is addressed through the Mattheis prescription.[108] Here, spheres are inscribed in Wigner-Seitz cells at each site and the electron density within the sphere is assigned to the central atom while the excess is

distributed through the cluster. While this model is devoid of reference to the chemical structure or bonding nature of the material, it is rather successful when more than 35 eV beyond the edge where the high kinetic energy of the photoelectron renders it relatively insensitive to details of the potential surface.[105] With this model, it is possible to proceed within one of the above computational frameworks. In FEFF for example,[109, 110] the single and multiple scattering paths can then be specified and the scattering functions calculated using default models for the atomic potentials and the Hedin-Lundqvist self-energy.[104] At this point, it is appropriate to note a shortcoming of the formalism in Eq. 1-9 and Eq. 1-10 in order to better understand the procedure employed by FEFF. Equation 1-9 was derived assuming plane-wave scattering at the location of the neighboring atoms, however, this need not be the case. An improvement was made in 1975 by Lee and Pendry[111] who considered two contributions, first, a point-scattering approximation using plane-waves, and second, a small-wavelength approximation of the Hankel-function behavior of the outgoing spherical wave as exponentials. This latter approximation was later improved upon using single-scattering, curved-wave theory with a more rigorous mathematical analysis.[112] Finally, Rehr *et al.* showed that a full theoretical treatment could be incorporated into the traditional format of the EXAFS equation by replacing the scattering amplitude from the plane-wave analysis with an effective scattering amplitude and incorporating the phase of the complex scattering function into the argument of the sine function.[94, 113]

Finally, an energy shift parameter is often introduced to align a theoretical spectrum to the experimental results. Again, this parameter is rarely emphasized in XAFS reports despite its strong correlation with the path length. It is generally desired that this number be small, however, if E_0 is improperly set, the energy shift parameter can become unreasonably large. A

discussion of these facts and further information can be found in an instructional article by Kelly and Ravel.[114]

This concludes the background information which will be given for XAS. With the above theoretical framework, an atomic configuration can be proposed for a system of interest and a measure of its physical parameters and their accuracy can be deduced by fitting this model to the corresponding EXAFS spectrum. For more information, the interested reader is recommended to peruse the following works on multiplet effects in X-ray spectroscopy,[7] wavelet transform analysis,[115] the ratio method[116] and other ways of analyzing disordered materials by EXAFS,[117] cumulants in EXAFS,[118] and further theoretical underpinnings of the technique.[119]

3. X-ray Emission Spectroscopy (XES)

3A. Overview

Photoionization, as well as K-capture, ion-bombardment, and related phenomena, are capable of creating a deep core-hole in the electronic structure of a given atom. Such a state is unstable and an electron in a higher energy orbital will transition to fill the core-hole and may emit a photon in the process. These fluorescence photons are denoted according to the atomic transition to which they correspond and traditionally follow Siegbahn or IUPAC notation, see Fig. 1-15. The following discussion will specific to 3d transition metals, which are the primary focus of this dissertation.

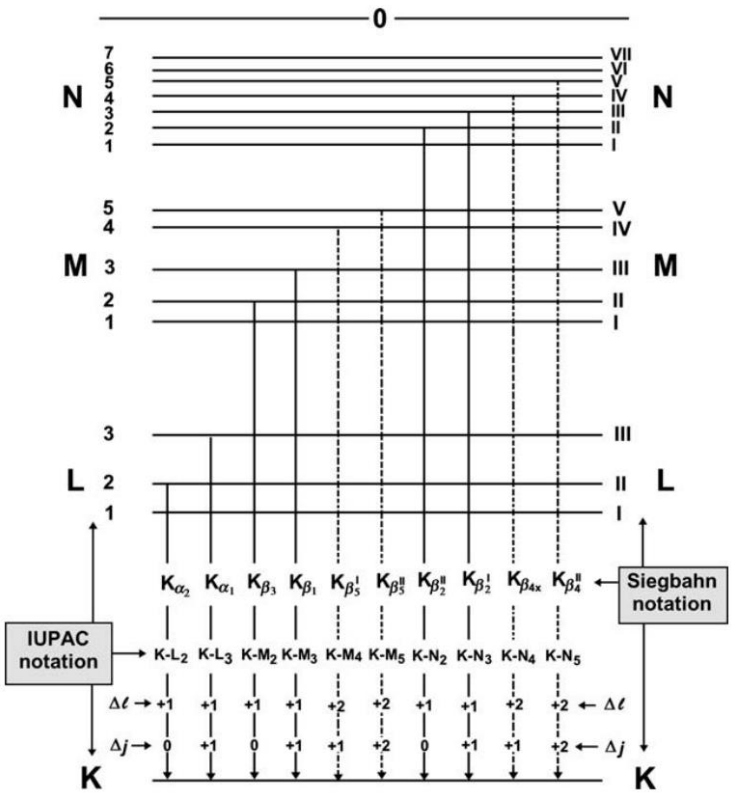

Fig. 1-15: Reproduced from Podgoršak.[120] Depiction of two popular schemes, IUPAC and Siegbahn notation, for naming X-ray transition lines involving a K-shell core hole in the initial state.

XES reflects the local electronic structure around the absorbing metal center. Specifically, this approach complements XAFS by providing a map of the occupied density of states in the system. Moreover, XES not only probes core electrons, but valence electrons directly involved in molecular bonding as well. However, while sensitivity to the behavior of the valence electrons increases in transitions involving outer shells, the intensity of such transitions declines, Fig. 1-16. It is for this reason that, while Kα and Kβ mainlines share a rich history of analysis,[7] valence-to-core emission has only recently received considerable attention due to its utility in emerging materials research, including the study of metalloenzymes for catalysis.[121, 122] Here, these transitions lines will be discussed in order of increasing photon energy.

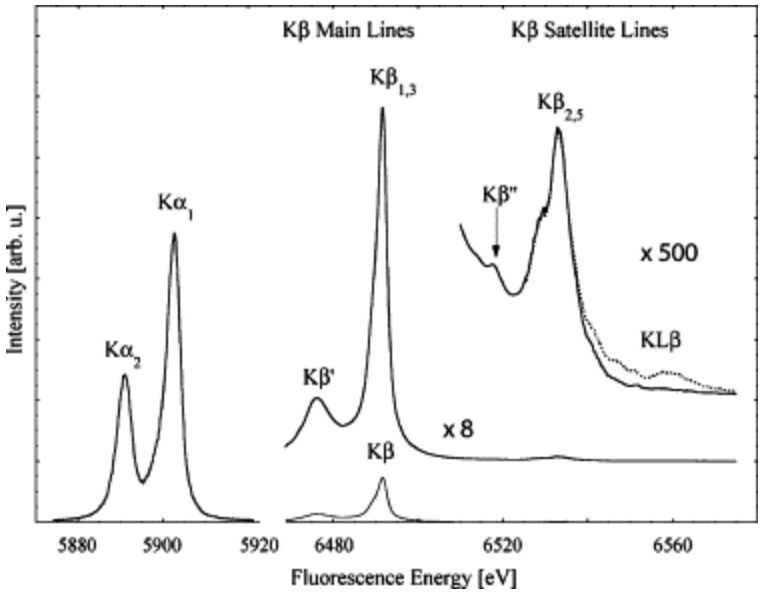

Fig. 1-16: Reproduced from Glatzel and Bergmann.[123] Mn K-shell emission lines in MnO. The Kβ main and satellite lines are shown with the specified magnifications.

3B. Kα ($KL_{II,III}$) XES

Physical effects influencing a material's Kα XES spectral shape can be naively sorted into four categories: orbital angular momentum, Coulombic interactions involving valence electrons, spin-orbit coupling, and broader multiplet or crystal-field effects. In the present discussion, orbital angular momentum can be neglected as it has been found to absent in most transition metal compounds[124] in agreement with theoretical models.[125, 126] Regarding Coulombic interactions, the small overlap of between the deep core and valence electrons renders the Kα spectrum, which arises from 2p → 1s transitions, insensitive to the fine details of the valence electron's spatial distribution. However, gross changes to the local electron density, such as changes in oxidation state, can yield a change in nuclear screening and variation in the energy of the emitted photons. This fact has seen some application in speciation assessment as in the case of oxidation state assignment of Cr-based complexes by WDXRF.[127] Spin-orbit

coupling plays a significant role in determining the relative intensities and energy positions of $K\alpha_1$ and $K\alpha_2$. To begin, the 2:1 ratio of degeneracy between the $2p_{3/2}$ and $2p_{1/2}$ states is mirrored in the relative intensities of the $K\alpha_{1,2}$ XES features with increasing deviation across the row of 3d transition metals corresponding to the onset of the intermediate coupling regime. Further, spin-orbit coupling perturbs the ground state Hamiltonian in proportion to $J^2 - L^2 - S^2$, leading to a several eV split between the lines from these two states. Finally, multiplet effects predominantly determine the remainder of the spectral shape, including the effect of (2p,3d) exchange, which leads to a linear relation between the full-width-half-maximum of the $K\alpha_1$ and the effective number of unpaired 3d electrons, Fig. 1-17.[123]

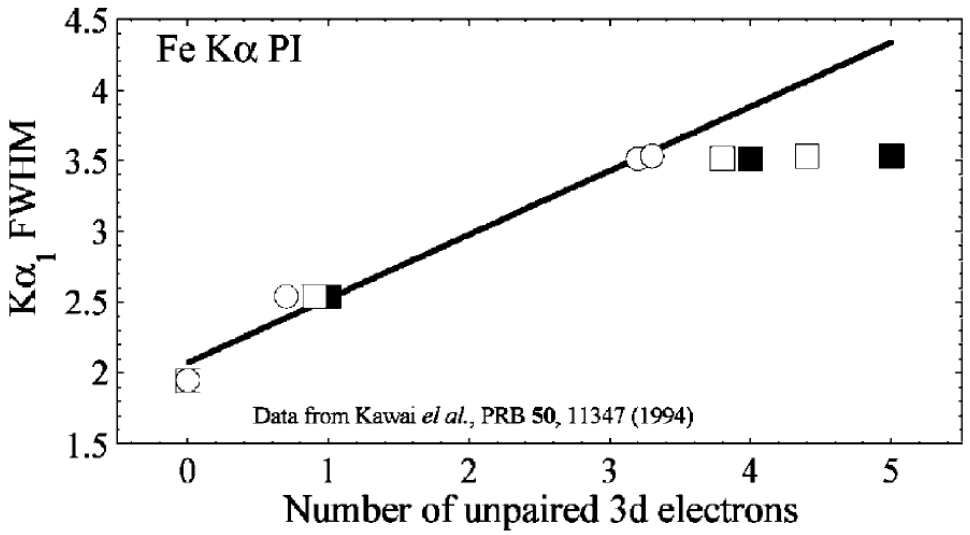

Fig. 1-17: Reproduced from Glatzel and Bergmann.[123] $K\alpha_1$ FWHM in Fe compounds measured by XES; (a) full boxes: nominal number of unpaired 3d electrons, (b) empty boxes: the effective number of unpaired 3d electrons in the ground state, (c) circles: the effective number of unpaired 3d electrons in the 1s core hole excited state. The shown linear regression is for (c).

3C. Kβ mainlines ($KM_{II,III}$) XES

Greater sensitivity to oxidation and spin-state information can often be achieved by acquiring the XES spectrum arising from the Kβ mainlines, which are due to 3p → 1s transitions. Typically, this emission region exhibits a fixed center-of-gravity for the spectra corresponding to different oxidation states of the same element.[123] This leads to a close relationship between the intensity of the Kβ' shoulder and the energy of the $K\beta_{1,3}$ peak. As the number of unpaired 3d electrons increases, so does the intensity of the Kβ' shoulder. This property has been applied to the analysis of many materials. Consider Fe along, studies include pressure-induced spin-state transitions in FeS,[128] Fe_2O_3,[129] and iron-rich silicate melts in Earth's deep mantle.[130] Roughly, these studies were conducted within the last couple decades, yet the underlying behavior has been known for quite some time and seen notable application in unveiling the electronic states of various heme proteins, Fig. 1-18. Since the center-of-gravity is fixed for the main Kβ, a rise in intensity for the Kβ' yields a shift to higher energies for the $K\beta_{1,3}$ as the Kβ' is necessarily shifted to lower energies due to (3p,3d) exchange. This can be seen in Fig. 1-19. Here the shift in energy for these emission lines is the predominant factor driving changes in integral absolute difference (IAD) plots, as it was here in the characterization of different dark states of the oxygen evolving complex (OEC).[131]

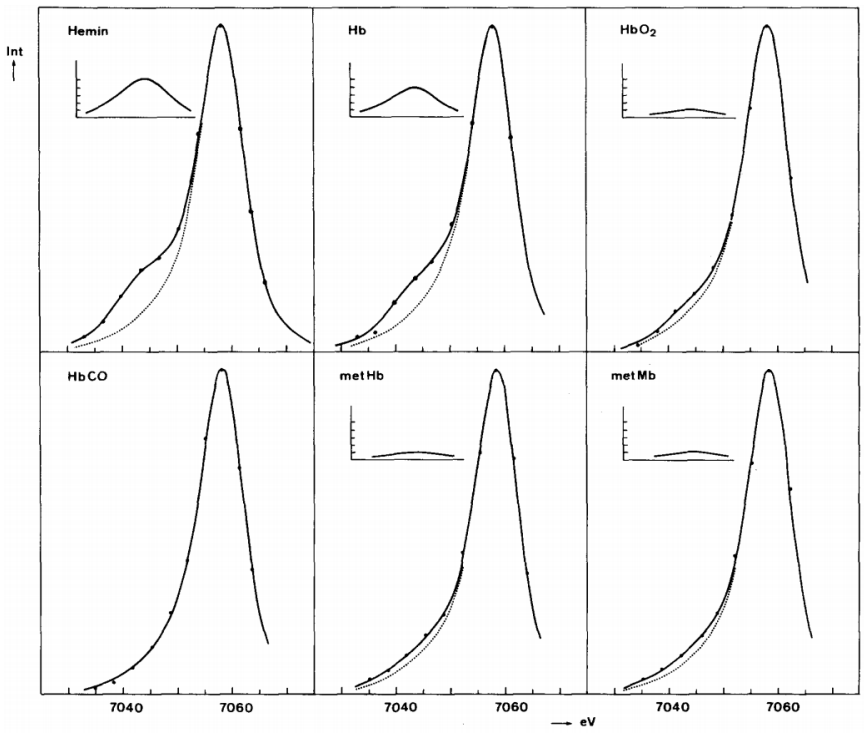

Fig. 1-18: Reproduced from Koster.[132] The Kβ emission spectra of some heme proteins: iron(III) protoporphyrin chloride (Hemin), desoxyhemoglobin (Hb), oxyhemoglobin (HbO_2), carbonmonoxidehemoglobin (HbCO), methemoglobin (metHb), and metmyoglobin (metMb). The main Kβ is subtracted from the spectrum and the bare shoulder is shown in the inset.

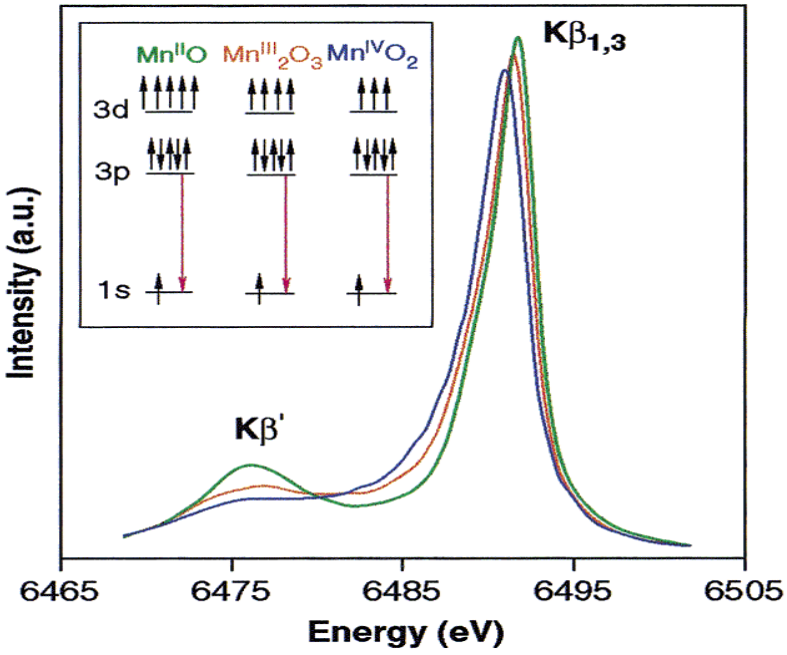

Fig. 1-19: Reproduced from Messinger et al.[131] The Kβ mainline XES measurements of several Mn oxides. A pictorial representation is given for the fluorescence transition.

3D. Kβ valence-to-core (nominally $KM_{IV,V}$) XES

Valence-to-core (VTC) XES provides a direct spectral probe into the behavior of those electrons directly involved in molecular bonding. For that reason, VTC-XES is highly sensitive to changes in molecular speciation. Two features in particular are frequently analyzed, the main feature which is the $K\beta_{2,5}$, and a crossover or ligand transfer peak referred to as the Kβ''. In the case of the former, the energy of the $K\beta_{2,5}$ is highly sensitivity to changes in nuclear screening and is known to shift considerably upon changes in covalency or oxidation. Similarly, the energy of the Kβ'' relative to the $K\beta_{2,5}$ can vary significantly depending on ligand character. Both of these details can be seen in Fig. 1-20. Finally, the intensity of the Kβ'' scales with both the absorbing atom's coordination number and the bond distance. This latter dependence is exponential in accordance with the behavior of the atomic wavefunction.

The sensitivity of VTC-XES to ligand identity deserves special mention. This feature has proven especially useful in recent studies of metalloenzymes, including the iron-molybdenum cofactor (FeMoCo), the active site of binding and reduction in nitrogenase. In a 2002 article by Einsle et al.[133], a central light atom was reported in FeMoCo the atomic identity of which was either C, N, or O. Numerous researchers applied various techniques to ascertain the identity of this ligand, however, it was not until the 2011 article by Lancaster et al.[121], which used VTC-XES measurements along with DFT simulations to show that the energy of the Kβ'' is consistent with the presence of carbon. Due to its sensitivity to molecular bonding, this technique has seen similar application in other metalloenzyme research, including oxygen ligation with the Mn_4Ca cluster in photosystem II[122] and activation of N_2 bonds by other Fe-based model catalysts.[134] However, it should be noted that, while these spectral features are highly sensitive to coordination chemistry, they are not necessarily diagnostic of the ligand atom's character. The reason for this is that the energy of the Kβ'' is not strictly unique for a given ligand, but can overlap with similar species. This fact has been thoroughly studied for the case of Cr-ligation by MacMillan et al.,[135] Fig. 1-21.

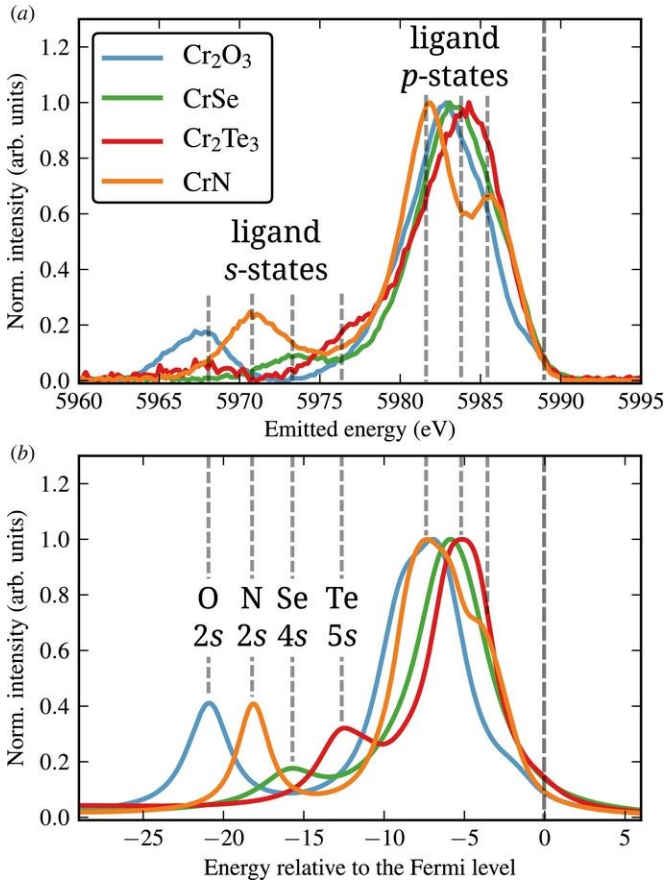

Fig. 1-20: Reproduced from Rovezzi et al.[136] Cr-based empirical references. Experimental data is shown in the top panel following removal of the tail from the lower energy Kβ main line and then peak normalization. Theoretical simulations are shown in the bottom panel. Vertical dashed lines compare the main features in simulation and experiment.

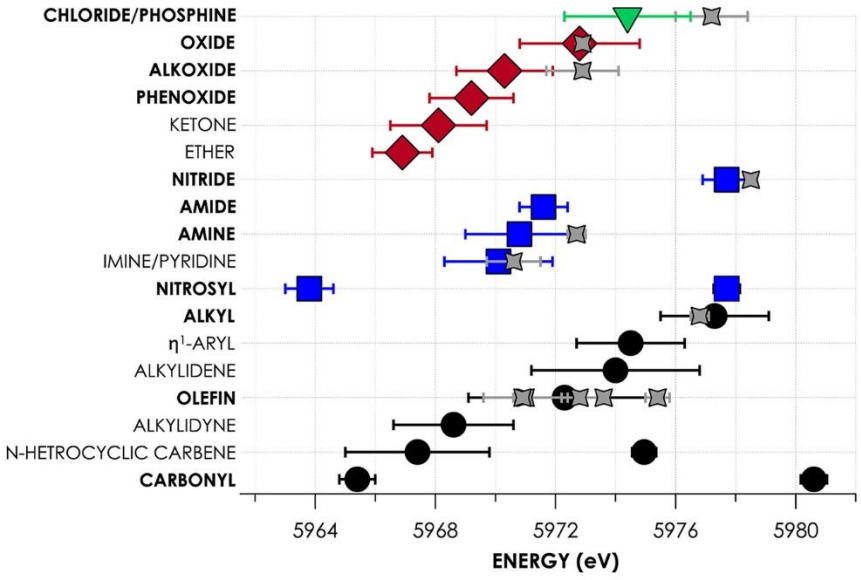

Fig. 1-21: Reproduced from MacMillan et al.[135] For the case of Cr VTC-XES, the above data points display the average, experimentally calibrated, energies of DFT-calculated Kβ'' features for ligands grouped by donor atom. Error bars represent two standard deviations. Gray bars indicate experimental values with error bars acquired from fitting analyses. Bolded ligands contribute strongly to the Kβ'' intensity, while non-bolded ligands are expected to be difficult to resolve.

4. Perturbations on two state transitions

4A. Origin of Natural Line Width

The preceding sections discussed electronic transitions within the framework of a simplified model involving one-electron transitions between an occupied and a vacant state. While useful, this fails to describe several spectral features. This section describes several physical processes that act as perturbations on this model. This discussion will bridge the gap between the model above and what is observed in an experiment. This section will proceed by explaining the origin of spectral broadening, the influence of radiative Raman and Auger effects

on emission spectra, and the multielectron excitation features which are sometimes observed in experimental results.

It is quite common to see both emission and absorption lines fit with functions of finite width due to both intrinsic and instrumental broadening. To begin, both transitions are broadened due to the intermediate core hole state. This state possesses a characteristic core hole lifetime,[137, 138] resulting in an exponential decay in the probability of occupying the state with respect to the time domain. As the experimentally observed quantity is the energy of the transition, the line is seen as the Fourier transform of this function, which is a Lorentzian. Next the spectrum is further broadened by the instrumental resolution function which, to a good approximation, involves convolving the Lorentzian with a Gaussian to form a Voigt function.[58] Finally, an additional complication is sometimes considered in the form of the super-Coster-Kronig decay process. This process introduces a LS-term dependent broadening which is particularly important for XPS and XES experiments beginning with a shallow core-level electron. Here, the Slater integrals are larger than the spin-orbit splitting of the core hole states, which leads to well defined LS states. The Auger decay process, which arises from the Coulomb interaction, then necessarily follows strict selection rules.[139] As a result, many authors introduce a term into the Lorentzian width which depends linearly on energy to represent the lifetime of the state with a core hole in the shallow core-level,[139, 140] Fig. 1-22. Inclusion of this term often leads to better agreement between experiment and theory for such transitions, see Fig. 1-23.

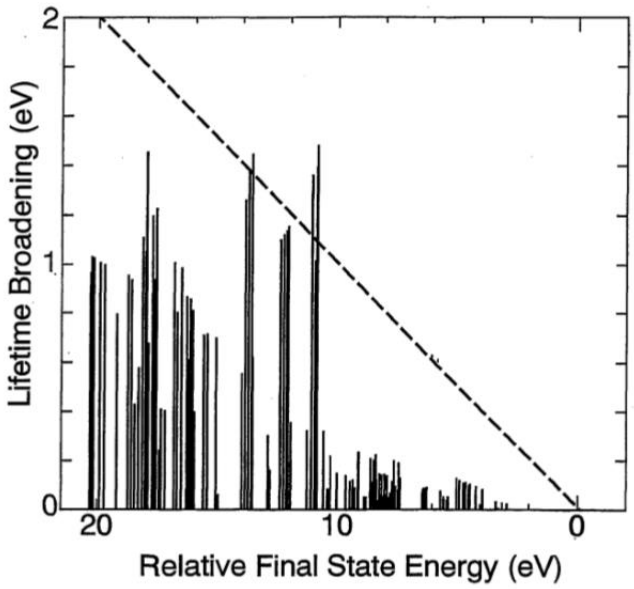

Fig. 1-22: From Taguchi et al.[140] The LS-term dependence of the lifetime of states with a 3p core hole in a free Mn^{2+} ion. The dashed line represents the linear model and the solid vertical lines represent calculated lifetimes.

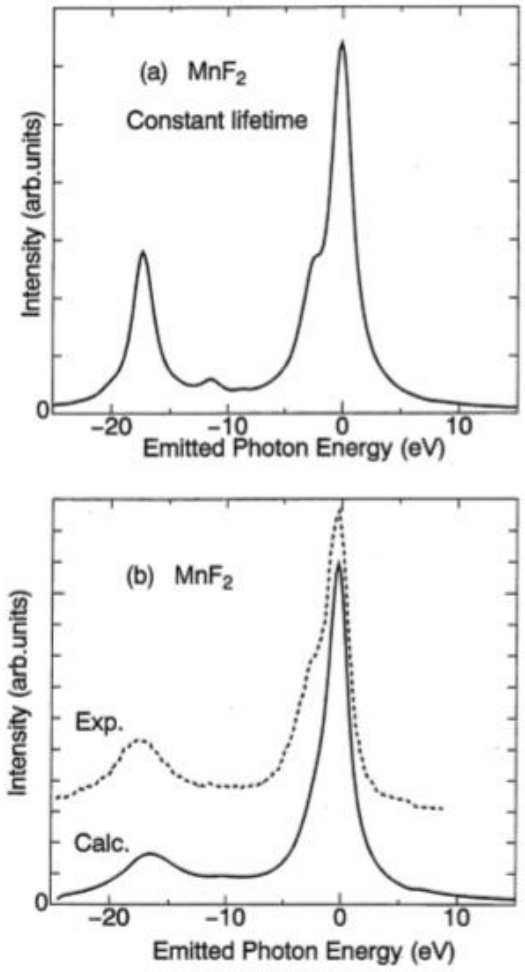

Fig. 1-23: From Taguchi et al.[140] Mn Kβ XES of MnF_2 using a constant (a) and term-dependent (b) broadening of the lifetime of the 3p core hole state.

4B. Raman and Auger Effects

When the incident photon energy is near a binding energy, the Raman effect must be considered as it can cause spectral distortions and asymmetries in XES results. Speaking generally, this is due to the interplay of the core Lorentzian with the unoccupied density of states, i.e., the resonant Raman effect.[141, 142] This process will be explained in detail here in a manner parallel to the argument of Enkisch et al.[143] Beginning with Fig. 1-24 (a), a photon of energy $\hbar\omega_1$ excites an electron in a state with energy E_{core} to a state above the Fermi-level, E_F. Here,

the dashed line represents a constant unoccupied density of states and the core Lorentzian has zero width such that the state the electron is promoted to has an energy $E_i = \hbar\omega_1 + E_{core}$. As a result, the emission spectra are made up of sharp emission lines of energy $\hbar\omega_2 = \hbar\omega_1 - (E_i - E_f)$. It is worthwhile to note explicitly that energy must be conserved during this process. This picture can be perturbed by allowing the core Lorentzian to have some finite width. In this case, a number of unoccupied states are available, each with an excitation probability equal to the value of the Lorentzian at the corresponding energy, Fig. 1-24(b). In particular, this probability distribution is truncated on one side as the unoccupied density of states terminates at the Fermi-level as is consistent with the Pauli exclusion principle. Thus, the emission profile is also a Lorentzian truncated on the higher energy side as described by equation 1-13.

$$I_{fluo}(\hbar\omega_2) \propto \int dE_i I^u(E_i) L(E_i - E_{core} - \hbar\omega_2) \times \int dE_f I^o(E_f) \delta(E_i - E_f - \hbar\omega_1 + \hbar\omega_2) \quad (1\text{-}13)$$

In Eq. 1-13, I^u and I^o represent the unoccupied and occupied densities of states, respectively, the term $\delta(E_i - E_f - \hbar\omega_1 + \hbar\omega_2)$ ensures energy conservation, and $L(E_i - E_{core} - \hbar\omega_2)$ denotes the core Lorentzian of functional form

$$L(\epsilon) = \frac{1}{\epsilon^2 + (\frac{\Gamma}{2})^2}, \quad (1\text{-}14)$$

where Γ is the inverse lifetime of the core hole. Increasingly asymmetric features are observed for excitation energies close to the Fermi-level or even below it, Fig. 1-24 (c). The assumption of a constant unoccupied density of states can be lifted to account for fine structure, Fig. 1-24 (d). In this panel, the dashed line represents the truncated Lorentzian, the dotted line represents

the unoccupied density of states, and the solid line represents the core Lorentzian after convolution. This gives rise to the depicted asymmetric energy line and is well described by the following form of Eq. 1-13, in which E_{core} is set to be zero and integration over E_f has been performed and $I_{abs}(\epsilon)$ is the product of the unoccupied density of states with the core Lorentzian.

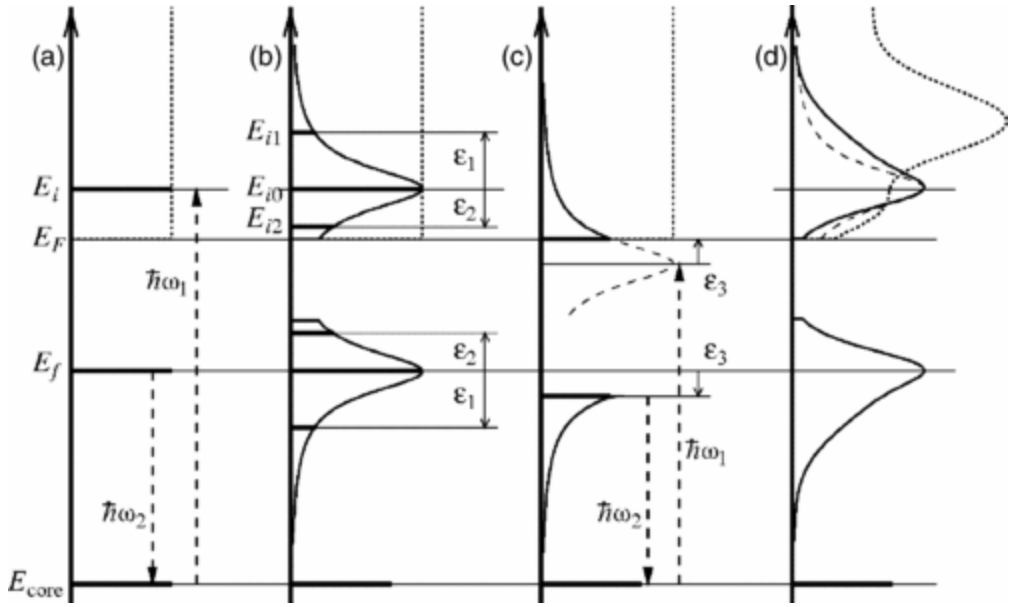

Fig. 1-24: From Enkisch et al.[143] The effect of the electronic density of states on the final emission spectrum. Schematics (a) through (d) will be discussed in the text.

Another contribution to asymmetries in the emitted spectrum is given by the radiative Auger effect. Here, the electronic system is shaken as an electron transitions to fill a lower energy hole. As a result, another electron may transition to a higher unoccupied orbital and downshift the energy of the emitted photon. If the excited electron fills an unoccupied bound state, the process is referred to as the resonant radiative Auger effect and gives rise to sharp spectral features. If the excited electron fills an unoccupied continuum state, the energy of the

photon can vary between zero and the Auger energy of the nonradiative process. The actual energy distribution of the emitted photon is then broad, extending over several hundred eVs with a steep drop toward the diagram line, as described by Eq. 1-15.[143]

$$I_{RAS}(E) = Ie^{d(E-E_0)}\left[\frac{1}{e^{\frac{E-E_0}{w}}+1}\right] \qquad (1\text{-}15)$$

In Eq. 1-15, E_0 characterizes the energy of the satellite, d the decay factor, and w the width of plateau on the high-energy side. Typically, this feature is only a few percent of the diagram line which it perturbs,[144] but can be more in some late 3d transitions metals, particularly in their valence.[145] Regarding notation, these features are designated with a letter code in which the first letter refers to the principal quantum number (or shell) of the core hole, the next to the shell of the electron transitioning to fill the hole, and the last to the shell of the electron being promoted to an unoccupied state. As an example, KLM refers to a K-shell vacancy being filled by an L-shell electron as an M-shell electron is promoted.

4C. Multielectron Excitation Satellites

Multielectron transitions in response to absorption of a single X-ray were first observed by Siegbahn and Stenstrom[146] before further study by Richtmyer[28, 147] and Druyvesteyn.[148] Over the next century, phenomena have been frequently attributed to this process, including satellites on the high-energy side of features in XES,[149-151] satellites on the low-energy side of features in XPS,[8, 152-156] and discontinuities in XAFS[156-158] measurements. Indeed, spectral contributions from multielectron transitions are frequently quite large,[159, 160] and their consideration is routinely required in analysis of transition metal XES results, especially in the valence-to-core region.[143, 150, 161-163] While this may appear as a daunting complication, analysis can often be simplified by noting that double ionizations are by far the most probable multielectron transition

in most experiments.[164] An example of such an analysis can be found by Valenza et al.,[165] Fig. 1-25, where it is useful to note that traditional nomenclature lists between brackets the orbitals from which electrons were excited. Furthermore, it is worthwhile to point out that the probability of the DI process greatly exceeds what may be expected by treating both electrons as independent,[166] but rather strongly depends on many-electron interactions.[167] Thus, multielectron transitions provide a measure of intra-atomic electron correlations. More than that, multielectron transitions serve a pragmatic role in monitoring the transition from the LS coupling scheme to intermediacy,[168, 169] probing the space-time dependence of fundamental constants,[170] and testing the Breit interaction in quantum electrodynamics.[165, 166, 171, 172]

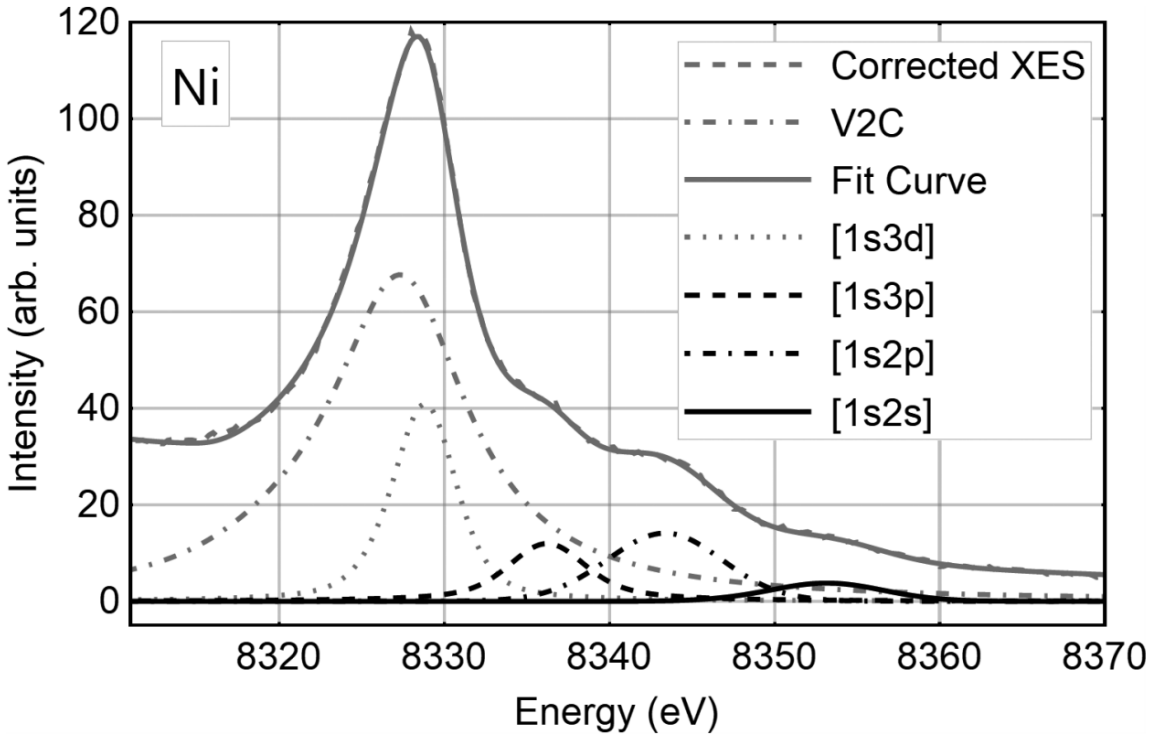

Fig. 1-25: From Valenza et al.[165] The measured XES from Ni foil in the valence-to-core region. The data is fit to a sum of pseudo-Voigt functions representing phenomenological multielectron satellites and the diagram line. Not shown are the fit components representing the Ni $K\beta_{1,3}$ and radiative Auger effect features.

With the motivations for studying multielectron excitations thoroughly established, it is now appropriate to explain the theory behind the phenomenon. The simplest model for such transitions is the shake process within the sudden approximation. Here, an incident photon first induces the ejection of a photoelectron. All other electrons then experience a sudden change in nuclear screening accompanying the creation of a core hole. The other electrons then relax and encounter an imperfect overlap between initial and final states. This results in a nonzero probability that some electrons will be excited to unoccupied bound states (shake-up) or continuum states (shake-off). The threshold for these effects,[173] as well as the size of spectral shifts relative to the original diagram line, can be readily calculated in the Z+1 approximation. This model accounts for changes in nuclear screening by treating the excitation of secondary electrons as though they occurred in the corresponding orbitals of an atom one greater in atomic number. In particular, this model predicts that the energy of satellites are given by Eq. 1-16.[165]

$$E_{\gamma'} = E_{\gamma} + BE_{Z+1} - BE_{Z} \tag{1-16}$$

In Eq. 1-16, $E_{\gamma'}$ is the satellite energy, E_{γ} is the energy of the diagram line, and BE_{Z+1} and BE_{Z} Are the binding energies of electrons ejected to form spectator holes if they instead occurred in a system with atomic number Z+1 and Z, respectively. Note that this model does not lend itself to predicting shake probabilities. Fortunaly, Midgal[174] and Feinberg[175] observed in 1941 that β decay produces an appreciable probability of ionization in all occupied orbitals of an atom, thus sparking a large number of theoretical studies in the framework of the sudden approximation.[159, 160, 164, 176, 177] Many decades later, *ab initio* relativistic Dirac-Fock multiplet calculations allow the accurate reconstruction of emission spectra,[161, 162, 178] though the best agreement is achieved in multiconfigurational frameworks.[179-181] Nevertheless, these models are liable to over-predict the intensity of some satellites, as the experimental intensity can be suppressed due to fast

Coster-Kronig transitions and other phenomena.[178, 182-185] This far, our discussion has been restricted to the sudden approximation, but, depending on the adiabaticity quantity $\frac{\Delta E \Delta t}{\hbar}$, this may not be justified. In the adiabatic regime, the perturbation by the first outgoing photoelectron must be considered, traditionally with time-dependent perturbation theory.[186, 187] This regime, as well as the transition from adiabatic to sudden (sometimes called isothermial) has been well explored experimentally.[168, 173, 184] Often, the satellite intensities are then fit by optimizing the parameters of the Thomas,[186] Roy,[188] Roy-2,[189] or Vatai[190] model. However, none of these are *ab initio*[185] and only the Vatai and Roy model identify the Coulomb interaction as the cause of excitation. As the Thomas model is the most common, it will be used as an example to explain the framework of such a calculation.

Thomas[186, 187] begins by considering the following state:

$$\phi_j(t) = \sum_i a_i(t)\phi_i^0 e^{\frac{-iE_i t}{\hbar}} \tag{1-17}$$

Then from Schiff[191]:

$$\dot{a_\imath}(t) = \sum_{n \neq i} \frac{a_n}{\Delta E_{in}} \left(e^{i\int_0^t \frac{\Delta E_{in}}{\hbar} dt'}\right) \frac{\partial H_{in}}{\partial t} \tag{1-18}$$

At this point, it is clear that $a_0(-\infty) = 1$ and $a_{n\neq 0}(-\infty) = 0$. However, a few approximations are available. First, it may be assumed that a_0 stays close to 1 and all others stay close to 0, that is, that the perturbation on the state is small. Second, it may be assumed that ΔE is independent of time, but different for neutral and ionic species. Eq. 1-18 may then be simplified to

$$\dot{a_\imath}(t) = \frac{1}{\Delta E_{i0}} \left(e^{i\int_0^t \frac{\Delta E_{i0}}{\hbar} dt'}\right) \frac{\partial H_{i0}}{\partial t}, \tag{1-19}$$

where the Hamiltonian matrix element is expressed in the unperturbed states. So far, this is just time-dependent perturbation theory with a couple of approximations. The leap comes in approximating $\frac{\partial H_{io}}{\partial t}$, which may be obtained from the time-dependent Hamiltonian[186]:

$$H = H_0 - Vf(t) \tag{1-20}$$

Where V is a perturbing potential with a time-dependent behavior described by $f(t)$. Or[187]:

$$H = H_0 + V \tag{1-21}$$

Where the time-dependence is included directly in the potential. Historically, these are the main functional forms used for the perturbed Hamiltonian, though other authors sometimes chose an exponential dependence.[192] However, Thomas notes that the actual form is not critical, only that $\frac{\partial H}{\partial t}$ is zero except near $t = 0$, where it is positive for a short time, t_0. This yields the appropriate dependence of adiabaticity on $t_0 \Delta E_{i0}$. Accordingly, Thomas chose the error function:

$$f(z) = \frac{2}{\sqrt{\pi}} \int_0^x e^{-z^2} dz \tag{1-22}$$

So that:

$$\frac{d}{dz}(erf(z)) = \frac{2}{\sqrt{\pi}} e^{-z^2} \tag{1-23}$$

Substitution then leads to:

$$\dot{a}_\iota(t) = \frac{V_{io}}{\Delta E_{i0}} \frac{1}{\sqrt{2\pi} t_0} e^{\frac{-t^2}{2{t_0}^2}} e^{\frac{i\Delta E_{i0} t}{\hbar}} \tag{1-24}$$

Of particular importance is the term $\frac{V_{io}}{\Delta E_{i0}}$, which is the usual Franck-Condon-type matrix element used to calculate the intensity of shake-up transitions in the sudden approximation. Also, notice that in the limit $\Delta t \ll \frac{\hbar}{\Delta E_{i0}}$, then:

$$\frac{dV_{i0}}{dt} = V_{io} \delta(t - t_0) \tag{1-25}$$

In either case, a functional form for $\dot{a}_i(t)$ can now be used to write the shake-up intensity μ as:

$$\begin{aligned}\mu &= |a_i|^2 \\ &= \left|\int_{-\infty}^{\infty} dt\, \frac{da_i}{dt}\right|^2 \\ &= \left|\frac{V_{i0}}{\Delta E_{i0}}\right|^2 e^{-(\frac{t_0 \Delta E_{i0}}{\hbar})^2}\end{aligned} \tag{1-26}$$

The amplitude of the exponential in Eq. 1-26 can be identified as the shake-up probability in the sudden approximation μ_∞ and, appropriately, the exponential becomes 1 for $f(t) = \delta(t - t_0)$. This covers the majority of the original theory, however it should be noted for the sake of formalism that Thomas makes an additional assumption, namely,

$$\frac{dv}{dt} = 0 \tag{1-27}$$

So that,

$${t_0}^2 = \frac{r^2}{v^2} \tag{1-28}$$

where r may be taken as a distance on the order of atomic dimensions, and

$$v^2 = \frac{2E_{ex}}{m}, \tag{1-29}$$

where E_{ex} is the excess energy above threshold. This yields the Thomas model in standard form:

$$\mu = \mu_\infty e^{-\frac{mr^2 (\Delta E)^2}{2\hbar^2 E_{ex}}} \tag{1-30}$$

5. References

1. H. Hertz, *Electric waves : being researches on the propagation of electric action with finite velocity through space*, New Dover ed. ed. (New York : Dover Publications, New York, 1962).
2. J. F. Mulligan, Physics Today **42** (3), 50-57 (1989).
3. A. B. Arons and M. B. Peppard, American Journal of Physics **33** (5), 367-374 (1965).
4. A. Einstein, Annalen der Physik **322** (6), 132-148 (1905).
5. J. H. Hubbell, H. A. Gimm and I. O/verbo, Journal of Physical and Chemical Reference Data **9** (4), 1023-1148 (1980).

6. G. Dresselhaus, A. Jorio and M. S. Dresselhaus, *Group theory : application to the physics of condensed matter*. (Berlin : Springer-Verlag, Berlin, 2008).
7. F. de Groot, Coordin Chem Rev **249** (1-2), 31-63 (2005).
8. S. Hüfner, *Photoelectron spectroscopy : principles and applications*, 3rd ed. ed. (Springer-Verlag Berlin Heidelberg, Berlin, Germany, 2003).
9. B. J. Wood, *X-ray photoelectron spectroscopy - XPS a powerful surface analysis tool for materials research and industrial problem solving*. (2011).
10. D. Briggs, Applications of Surface Science **6** (3), 188-203 (1980).
11. H. Herglotz, L. S. Birks, H. Herglotz and L. S. Birks, *X-ray spectrometry*. (New York : M. Dekker, New York, 1978).
12. H. Ali-Löytty, M. W. Louie, M. R. Singh, L. Li, H. G. Sanchez Casalongue, H. Ogasawara, E. J. Crumlin, Z. Liu, A. T. Bell, A. Nilsson and D. Friebel, The Journal of Physical Chemistry C **120** (4), 2247-2253 (2016).
13. A. Y. Klyushin, T. C. R. Rocha, M. Hävecker, A. Knop-Gericke and R. Schlögl, Physical Chemistry Chemical Physics **16** (17), 7881-7886 (2014).
14. F. Tao, Chemical Communications **48** (32), 3812-3814 (2012).
15. C. J. Powell, Journal of Vacuum Science & Technology A **21** (5), S42-S53 (2003).
16. A. Pattammattel, V. J. Leppert, H. J. Forman and P. A. O'Day, Environmental Science: Processes & Impacts **21** (3), 548-563 (2019).
17. W. Bi, Y. Wu, C. Liu, J. Wang, Y. Du, G. Gao, G. Wu and G. Cao, ACS Applied Energy Materials **2** (1), 668-677 (2019).
18. J. Rubio-Zuazo and G. R. Castro, Surf Interface Anal **40** (11), 1438-1443 (2008).
19. B. T. Young, D. R. Heskett, C. C. Nguyen, M. Nie, J. C. Woicik and B. L. Lucht, ACS Applied Materials & Interfaces **7** (36), 20004-20011 (2015).
20. A. Regoutz, M. Mascheck, T. Wiell, S. K. Eriksson, C. Liljenberg, K. Tetzner, B. A. D. Williamson, D. O. Scanlon and P. Palmgren, Review of Scientific Instruments **89** (7), 073105 (2018).
21. J. Herweg, Verhandlungen der Deutschen Physikalischen Fesellschaft **15**, 555-556 (1913).
22. M. de Broglie, Comptes Rendus de l'Academie des Sciences **157**, 924-926 (1913).
23. A. Mottana and A. Marcelli, eprint arXiv:1312.5295, arXiv:1312.5295 (2013).
24. H. Fricke, Phys Rev **16** (3), 202-215 (1920).
25. G. Hertz, Z Phys **3** (1), 19-25 (1920).
26. A. Lindh, Z Phys **6** (1), 303-310 (1921).
27. L. Pauling, Phys Rev **34** (6), 954-963 (1929).
28. F. K. Richtmyer, J Frankl Inst **208**, 325-361 (1929).
29. S. DeBeer George, T. Petrenko and F. Neese, Inorganica Chimica Acta **361** (4), 965-972 (2008).
30. M. Newville, Rev. Mineral. Geochem. **78** (1) (2014).
31. E. P. Jahrman, W. M. Holden, A. S. Ditter, D. R. Mortensen, G. T. Seidler, T. T. Fister, S. A. Kozimor, L. F. J. Piper, J. Rana, N. C. Hyatt and M. C. Stennett, Review of Scientific Instruments **90** (2), 024106 (2019).
32. S. Bajt, S. B. Clark, S. R. Sutton, M. L. Rivers and J. V. Smith, Analytical Chemistry **65** (13), 1800-1804 (1993).

33. F. W. Lytle, R. B. Greegor, G. L. Bibbins, K. Y. Blohowiak, R. E. Smith and G. D. Tuss, Corrosion Science **37** (3), 349-369 (1995).
34. S. R. Sutton, K. W. Jones, B. Gordon, M. L. Rivers, S. Bajt and J. V. Smith, Geochim Cosmochim Ac **57** (2), 461-468 (1993).
35. M. D. Szulczewski, P. A. Helmke and W. F. Bleam, Environ Sci Technol **31** (10), 2954-2959 (1997).
36. G. Calas and J. Petiau, Solid State Communications **48** (7), 625-629 (1983).
37. F. W. Lytle, R. B. Greegor and A. J. Panson, Physical Review B **37** (4), 1550-1562 (1988).
38. M. W. Kendig, A. J. Davenport and H. S. Isaacs, Corrosion Science **34** (1), 41-49 (1993).
39. E. P. Jahrman, G. T. Seidler and J. R. Sieber, Analytical Chemistry **90** (11), 6587 (2018).
40. B. Ravel and M. Newville, Journal of Synchrotron Radiation **12** (4), 537-541 (2005).
41. A. Gaur and B. D. Shrivastava, Review Journal of Chemistry **5** (4), 361-398 (2015).
42. L. S. Kau, D. J. Spira-Solomon, J. E. Penner-Hahn, K. O. Hodgson and E. I. Solomon, J Am Chem Soc **109** (21), 6433-6442 (1987).
43. A. Gaur, B. D. Shrivastava, K. Srivastava, J. Prasad and V. S. Raghuwanshi, The Journal of Chemical Physics **139** (3), 034303 (2013).
44. W. B. Kim and J. S. Lee, The Journal of Physical Chemistry B **107** (35), 9195-9202 (2003).
45. E. J. Popczun, C. G. Read, C. W. Roske, N. S. Lewis and R. E. Schaak, Angewandte Chemie **126** (21), 5531-5534 (2014).
46. M. E. Mundy, D. Ung, N. L. Lai, E. P. Jahrman, G. T. Seidler and B. M. Cossairt, Chem Mater **30** (15), 5373 (2018).
47. G. S. Henderson, F. M. F. de Groot and B. J. A. Moulton, Rev Mineral Geochem **78**, 75-+ (2014).
48. S. R. Bare, S. D. Kelly, B. Ravel, N. Greenlay, L. King and G. E. Mickelson, Physical Chemistry Chemical Physics **12** (27), 7702-7711 (2010).
49. S. R. Bare and T. Ressler, in *Advances in Catalysis* (Academic Press, 2009), Vol. 52, pp. 339-465.
50. E. Talaie, P. Bonnick, X. Q. Sun, Q. Pang, X. Liang and L. F. Nazar, Chem Mater **29** (1), 90-105 (2017).
51. C. Y. Ralston, H. Wang, S. W. Ragsdale, M. Kumar, N. J. Spangler, P. W. Ludden, W. Gu, R. M. Jones, D. S. Patil and S. P. Cramer, J Am Chem Soc **122** (43), 10553-10560 (2000).
52. J. van Elp, G. Peng, B. G. Searle, S. Mitra-Kirtley, Y. H. Huang, M. K. Johnson, Z. H. Zhou, M. W. W. Adams, M. J. Maroney and S. P. Cramer, J Am Chem Soc **116** (5), 1918-1923 (1994).
53. T. Ressler, J. Wienold, R. E. Jentoft and T. Neisius, Journal of Catalysis **210** (1), 67-83 (2002).
54. M. Wilke, F. o. Farges, P.-E. Petit, G. E. Brown, Jr. and F. o. Martin, Am Mineral **86** (5-6), 714-730 (2001).
55. W. Bi, J. Wang, E. P. Jahrman, G. T. Seidler, G. Gao, G. Wu and G. Cao, Small **15** (31), 1901747 (2019).
56. E. P. Jahrman, L. A. Pellerin, A. S. Ditter, L. R. Bradshaw, T. T. Fister, B. J. Polzin, S. E. Trask, A. R. Dunlop and G. T. Seidler, Journal of The Electrochemical Society **166** (12), A2549-A2555 (2019).
57. W. E. Gent, Y. Li, S. Ahn, J. Lim, Y. Liu, A. M. Wise, C. B. Gopal, D. N. Mueller, R. Davis, J. N. Weker, J.-H. Park, S.-K. Doo and W. C. Chueh, Advanced Materials **28** (31), 6631-6638 (2016).

58. G. Bunker, *Introduction to XAFS: A Practical Guide to X-ray Absorption Fine Structure Spectroscopy*. (Cambridge University Press, Cambridge, 2010).
59. D. Bazin, D. Sayers, J. J. Rehr and C. Mottet, J Phys Chem B **101** (27), 5332-5336 (1997).
60. S. Bare, in *EXAFS Data Collection and Analysis Course* (UOP LLC, APS, 2005).
61. A. Balerna, C. Evangelisti, E. Schiavi, G. Vitulli, L. Bertinetti, G. Martra and S. Mobilio, Journal of Physics: Conference Series **430**, 012052 (2013).
62. H. Piao, N. S. McIntyre, G. Beamson, M. L. Abel and J. F. Watts, J Electron Spec **125** (1), 35-45 (2002).
63. S. D. Conradson, K. D. Abney, B. D. Begg, E. D. Brady, D. L. Clark, C. den Auwer, M. Ding, P. K. Dorhout, F. J. Espinosa-Faller, P. L. Gordon, R. G. Haire, N. J. Hess, R. F. Hess, D. W. Keogh, G. H. Lander, A. J. Lupinetti, L. A. Morales, M. P. Neu, P. D. Palmer, P. Paviet-Hartmann, S. D. Reilly, W. H. Runde, C. D. Tait, D. K. Veirs and F. Wastin, Inorg Chem **43** (1), 116-131 (2004).
64. D. Gorman-Lewis, B. P. Aryal, T. Paunesku, S. Vogt, B. Lai, G. E. Woloschak and M. P. Jensen, Inorg Chem **50** (16), 7591-7597 (2011).
65. T. Vitova, I. Pidchenko, D. Fellhauer, T. Pruessmann, S. Bahl, K. Dardenne, T. Yokosawa, B. Schimmelpfennig, M. Altmaier, M. Denecke, J. Rothe and H. Geckeis, Chemical Communications **54** (91), 12824-12827 (2018).
66. L. Zhang, J. Zhou, J. Zhang, J. Su, S. Zhang, N. Chen, Y. Jia, J. Li, Y. Wang and J.-Q. Wang, Journal of Synchrotron Radiation **23** (3), 758-768 (2016).
67. J. Stöhr, *NEXAFS spectroscopy*. (Berlin

New York : Springer-Verlag, Berlin

New York, 1992).
68. M. Wilke, F. o. Farges, G. M. Partzsch, C. Schmidt and H. Behrens, Am Mineral **92** (1), 44-56 (2007).
69. F. W. Lytle, Journal of Synchrotron Radiation **6** (3), 123-134 (1999).
70. R. Stumm von Bordwehr, Ann. Phys. Fr. **14** (4), 377-465 (1989).
71. W. Kossel, Z Phys **1** (1), 119-134 (1920).
72. G. Wentzel, Annalen Der Physik **66** (23), 437-462 (1922).
73. R. D. Kronig and W. G. Penney, P R Soc Lond a-Conta **130** (814), 499-513 (1931).
74. R. D. Kronig, Z Phys **70** (5-6), 317-323 (1931).
75. J. D. Hanawalt, Phys Rev **37** (6), 715-726 (1931).
76. R. D. Kronig, Z Phys **75** (3-4), 191-210 (1932).
77. H. Petersen, Z Phys **76** (11-12), 768-776 (1932).
78. H. Petersen, Z Phys **80** (3-4), 258-266 (1933).
79. D. R. Hartree, R. de L. Kronig and H. Petersen, Physica **1** (7), 895-924 (1934).
80. T. Hayasi, Sci. Rep. Tohoku Univ. Ser. I **33**, 123-132 (1949).
81. I. Kostarev, Zh. Eksperim. Teor Fiz. **11**, 60-73 (1941).
82. A. Kozlenkov, Bull. Acad. Sci. USSR Phys. Ser. **25**, 968-987 (1961).
83. M. Sawada, K. Tsutsumi, T. Shiraiwa and M. Obashi, Annu. Rep. Sci. Works Osaka Univ. **7**, 1-87 (1959).
84. T. Shiraiwa, T. Ishimura and M. Sawada, J. Phys. Soc. Japan **13**, 847-859 (1958).
85. F. Lytle, Advances in X-ray Analysis **9**, 398-409 (1966).
86. D. E. Sayers, E. A. Stern and F. W. Lytle, Phys Rev Lett **27** (18), 1204-& (1971).

87. F. Zernike and J. A. Prins, *Die Beugung von Röntgenstrahlen in Flüssigkeiten als Effekt der Molekülanordnung*. (1927).
88. F. W. Lytle, D. E. Sayers and E. A. Stern, Physical Review B **11** (12), 4825-4835 (1975).
89. E. A. Stern, Physical Review B **10** (8), 3027-3037 (1974).
90. E. A. Stern, D. E. Sayers and F. W. Lytle, Physical Review B **11** (12), 4836-4846 (1975).
91. D. E. Sayers, F. W. Lytle and E. A. Stern, Journal of Non-Crystalline Solids **8-10**, 401-407 (1972).
92. F. W. Lytle, D. E. Sayers and E. B. Moore, Applied Physics Letters **24** (2), 45-47 (1974).
93. D. E. Sayers, F. W. Lytle, M. Weissbluth and P. Pianetta, J Chem Phys **62** (6), 2514-2515 (1975).
94. J. J. Rehr and R. C. Albers, Physical Review B **41** (12), 8139-8149 (1990).
95. J. J. Rehr, E. A. Stern, R. L. Martin and E. R. Davidson, Physical Review B **17** (2), 560-565 (1978).
96. S. D. Kelly, S. R. Bare, N. Greenlay, G. Azevedo, M. Balasubramanian, D. Barton, S. Chattopadhyay, S. Fakra, B. Johannessen, M. Newville, J. Pena, G. S. Pokrovski, O. Proux, K. Priolkar, B. Ravel and S. M. Webb, Journal of Physics: Conference Series **190**, 012032 (2009).
97. E. Sevillano, H. Meuth and J. J. Rehr, Physical Review B **20** (12), 4908-4911 (1979).
98. E. A. Hudson, P. G. Allen, L. J. Terminello, M. A. Denecke and T. Reich, Physical Review B **54** (1), 156-165 (1996).
99. S. Calvin, *XAFS for everyone*. (Boca Raton : CRC Press, Boca Raton, 2013).
100. E. C. Svensson, B. N. Brockhouse and J. M. Rowe, Phys Rev **155** (3), 619-632 (1967).
101. R. M. Nicklow, G. Gilat, H. G. Smith, L. J. Raubenheimer and M. K. Wilkinson, Phys Rev **164** (3), 922-928 (1967).
102. S. J. Gurman, N. Binsted and I. Ross, Journal of Physics C: Solid State Physics **19** (11), 1845-1861 (1986).
103. A. Filipponi, A. Di Cicco and C. R. Natoli, Physical Review B **52** (21), 15122-15134 (1995).
104. S. I. Zabinsky, J. J. Rehr, A. Ankudinov, R. C. Albers and M. J. Eller, Physical Review B **52** (4), 2995-3009 (1995).
105. B. Ravel, Journal of Synchrotron Radiation **22** (5), 1258-1262 (2015).
106. J. C. Slater, Phys Rev **51** (10), 846-851 (1937).
107. A. L. Ankudinov, S. I. Zabinsky and J. J. Rehr, Computer Physics Communications **98** (3), 359-364 (1996).
108. L. F. Mattheiss, Phys Rev **133** (5A), A1399-A1403 (1964).
109. J. J. Rehr, J. J. Kas, M. P. Prange, A. P. Sorini, Y. Takimoto and F. Vila, Comptes Rendus Physique **10** (6), 548-559 (2009).
110. J. J. Rehr, J. J. Kas, F. D. Vila, M. P. Prange and K. Jorissen, Physical Chemistry Chemical Physics **12** (21), 5503-5513 (2010).
111. P. A. Lee and J. B. Pendry, Physical Review B **11** (8), 2795-2811 (1975).
112. J. E. Müller and W. L. Schaich, Physical Review B **27** (10), 6489-6492 (1983).
113. J. J. Rehr, R. C. Albers, C. R. Natoli and E. A. Stern, Physical Review B **34** (6), 4350-4353 (1986).
114. S. D. Kelly and B. Ravel, AIP Conference Proceedings **882** (1), 132-134 (2007).
115. H. Funke, A. C. Scheinost and M. Chukalina, Physical Review B **71** (9), 094110 (2005).

116. G. Bunker, Nuclear Instruments and Methods in Physics Research **207** (3), 437-444 (1983).
117. B. Ravel, Journal of Synchrotron Radiation **21** (6), 1269-1274 (2014).
118. M. A. Karolewski, R. G. Cavell, R. A. Gordon, C. J. Glover, M. Cheah and M. C. Ridgway, Journal of Synchrotron Radiation **20** (4), 555-566 (2013).
119. J. J. Rehr and R. C. Albers, Reviews of Modern Physics **72** (3), 621-654 (2000).
120. E. B. Podgoršak, *Production of X Rays*. (Berlin, Heidelberg: Springer Berlin Heidelberg, Berlin, Heidelberg, 2006).
121. K. M. Lancaster, M. Roemelt, P. Ettenhuber, Y. Hu, M. W. Ribbe, F. Neese, U. Bergmann and S. DeBeer, Science **334** (6058), 974 (2011).
122. Y. Pushkar, X. Long, P. Glatzel, G. W. Brudvig, G. C. Dismukes, T. J. Collins, V. K. Yachandra, J. Yano and U. Bergmann, Angewandte Chemie International Edition **49** (4), 800-803 (2010).
123. P. Glatzel and U. Bergmann, Coordin Chem Rev **249** (1-2), 65-95 (2005).
124. N. D. Mermin and N. W. Ashcroft, *Solid state physics*. (New York : Holt, Rinehart and Winston, New York, 1976).
125. J. H. Van Vleck, *The theory of electric and magnetic susceptibilities*. (Oxford University Press, London, 1965).
126. J. S. Griffith, *The theory of transition-metal ions*. (Cambridge England University Press, Cambridge [England, 1964).
127. E. Baydaş and E. Öz, X-Ray Spectrometry **38** (5), 394-398 (2009).
128. J. P. Rueff, C. C. Kao, V. V. Struzhkin, J. Badro, J. Shu, R. J. Hemley and H. K. Mao, Phys Rev Lett **82** (16), 3284-3287 (1999).
129. J. P. Rueff, M. Krisch, Y. Q. Cai, A. Kaprolat, M. Hanfland, M. Lorenzen, C. Masciovecchio, R. Verbeni and F. Sette, Physical Review B **60** (21), 14510-14512 (1999).
130. R. Nomura, H. Tateno, S. Tateno, K. Hirose, J. Hernlund, S. Muto, H. Ishii and N. Hiraoka, *Spin crossover and iron-rich silicate melt in the Earth's deep mantle*. (2011).
131. J. Messinger, J. H. Robblee, U. Bergmann, C. Fernandez, P. Glatzel, H. Visser, R. M. Cinco, K. L. McFarlane, E. Bellacchio, S. A. Pizarro, S. P. Cramer, K. Sauer, M. P. Klein and V. K. Yachandra, J Am Chem Soc **123** (32), 7804-7820 (2001).
132. A. S. Koster, The Journal of Chemical Physics **56** (6), 3161-3164 (1972).
133. O. Einsle, F. A. Tezcan, S. L. A. Andrade, B. Schmid, M. Yoshida, J. B. Howard and D. C. Rees, Science **297** (5587), 1696 (2002).
134. C. J. Pollock, K. Grubel, P. L. Holland and S. DeBeer, J Am Chem Soc **135** (32), 11803-11808 (2013).
135. S. N. MacMillan, R. C. Walroth, D. M. Perry, T. J. Morsing and K. M. Lancaster, Inorg Chem **54** (1), 205-214 (2015).
136. M. Rovezzi and P. Glatzel, Semiconductor Science and Technology **29** (2), 023002 (2014).
137. J. C. Fuggle and S. F. Alvarado, Phys Rev A **22** (4), 1615-1624 (1980).
138. M. O. Krause and J. H. Oliver, Journal of Physical and Chemical Reference Data **8** (2), 329-338 (1979).
139. K. Okada, A. Kotani, H. Ogasawara, Y. Seino and B. T. Thole, Physical Review B **47** (11), 6203-6206 (1993).
140. M. Taguchi, T. Uozumi and A. Kotani, J Phys Soc Jpn **66** (1), 247-256 (1997).

141. P. Eisenberger, P. M. Platzman and H. Winick, Physical Review B **13** (6), 2377-2380 (1976).
142. K. Hamalainen, S. Manninen, P. Suortti, S. P. Collins, M. J. Cooper and D. Laundy, Journal of Physics: Condensed Matter **1** (34), 5955-5964 (1989).
143. H. Enkisch, C. Sternemann, M. Paulus, M. Volmer and W. Schülke, Phys Rev A **70** (2), 022508 (2004).
144. O. Keski-Rahkonen and J. Ahopelto, Journal of Physics C: Solid State Physics **13** (4), 471-482 (1980).
145. H. Enkisch, University of Dortmund, 2001.
146. M. Siegbahn and W. Stenstrom, Phys Z **17**, 48-51 (1916).
147. F. K. Richtmyer and R. D. Richtmyer, Phys Rev **34** (4), 574-581 (1929).
148. M. J. Druyvesteyn, *Het röntgenspectrum van de tweede soort*. (Rijks-Universiteit te Groningen., 1928).
149. Z. Horak, P Phys Soc Lond **77** (5), 980-986 (1961).
150. Y. Ito, T. Tochio, H. Oohashi and A. M. Vlaicu, Radiat Phys Chem **75** (11), 1534-1537 (2006).
151. M. Kavcic, M. Zitnik, D. Sokaras, T. C. Weng, R. Alonso-Mori, D. Nordlund, J. C. Dousse and J. Hoszowska, Phys Rev A **90** (2), 022513 (2014).
152. A. Bosch, H. Feil, G. A. Sawatzky and N. Martensson, Solid State Communications **41** (4), 355-357 (1982).
153. S. Hufner and G. K. Wertheim, Phys Lett A **51** (5), 299-300 (1975).
154. N. Martensson and B. Johansson, Phys Rev Lett **45** (6), 482-485 (1980).
155. D. A. Shirley, Physical Review B **5** (12), 4709-4714 (1972).
156. A. Filipponi and A. Dicicco, Phys Rev A **52** (2), 1072-1078 (1995).
157. J. Chaboy, A. Marcelli and T. A. Tyson, Physical Review B **49** (17), 11652-11661 (1994).
158. S. J. Schaphorst, A. F. Kodre, J. Ruscheinski, B. Crasemann, T. Aberg, J. Tulkki, M. H. Chen, Y. Azuma and G. S. Brown, Phys Rev A **47** (3), 1953-1966 (1993).
159. T. A. Carlson, C. W. Nestor, T. C. Tucker and F. B. Malik, Phys Rev **169** (1), 27-36 (1968).
160. T. Mukoyama and K. Taniguchi, Phys Rev A **36** (2), 693-698 (1987).
161. C. T. Chantler, J. A. Lowe and I. P. Grant, J Phys B - Ato. Mol. Opt. **46** (1), 015002 (2013).
162. M. Deutsch, G. Holzer, J. Hartwig, J. Wolf, M. Fritsch and E. Forster, Phys Rev A **51** (1), 283-296 (1995).
163. S. Galambosi, H. Sutinen, A. Mattila, K. Hamalainen, R. Sharon, C. C. Kao and M. Deutsch, Phys Rev A **67** (2), 022510 (2003).
164. A. G. Kochur and V. A. Popov, J Phys B - Ato. Mol. Opt. **39** (16), 3335-3344 (2006).
165. R. A. Valenza, E. P. Jahrman, J. J. Kas and G. T. Seidler, Phys Rev A **96** (3), 032504 (2017).
166. C. T. Chantler, M. N. Kinnane, C. H. Su and J. A. Kimpton, Phys Rev A **73** (1), 012508 (2006).
167. J. Hoszowska, J. C. Dousse, W. Cao, K. Fennane, Y. Kayser, M. Szlachetko, J. Szlachetko and M. Kavcic, Phys Rev A **82** (6), 063408 (2010).
168. R. Diamant, S. Huotari, K. Hamalainen, R. Sharon, C. C. Kao and M. Deutsch, Radiat Phys Chem **75** (11), 1434-1446 (2006).
169. J. Hoszowska, A. K. Kheifets, J. C. Dousse, M. Berset, I. Bray, W. Cao, K. Fennane, Y. Kayser, M. Kavcic, J. Szlachetko and M. Szlachetko, Phys Rev Lett **102** (7), 073006 (2009).

170. V. A. Dzuba, V. V. Flambaum, M. G. Kozlov and M. Marchenko, Phys Rev A **66** (2), 022501 (2002).
171. C. T. Chantler, J. M. Laming, J. D. Silver, D. D. Dietrich, P. H. Mokler, E. C. Finch and S. D. Rosner, Phys Rev A **80** (2), 022508 (2009).
172. J. D. Gillaspy, C. T. Chantler, D. Paterson, L. T. Hudson, F. G. Serpa and E. Takacs, J Phys B - Ato. Mol. Opt. **43** (7), 074021 (2010).
173. C. Sternemann, A. Kaprolat, M. H. Krisch and W. Schulke, Phys Rev A **61** (2), 205011-205014 (2000).
174. A. Migdal, J Phys-Ussr **4** (1-6), 449-453 (1941).
175. E. L. Feinberg, J Phys-Ussr **4** (1-6), 423-438 (1941).
176. T. Aberg, Phys Lett A **26** (10), 515-516 (1968).
177. A. G. Kochur and V. A. Popov, Radiat Phys Chem **75** (11), 1525-1528 (2006).
178. D. F. Anagnostopoulos, R. Sharon, D. Gotta and M. Deutsch, Phys Rev A **60** (3), 2018-2033 (1999).
179. C. T. Chantler, J. A. Lowe and I. P. Grant, Phys Rev A **82** (5), 052505 (2010).
180. J. A. Lowe, C. T. Chantler and I. P. Grant, Phys Lett A **374** (47), 4756-4760 (2010).
181. J. A. Lowe, C. T. Chantler and I. P. Grant, Phys Rev A **83** (6), 060501 (2011).
182. D. Coster and R. D. L. Kronig, Physica **2** (1), 13-24 (1935).
183. G. Holzer, M. Fritsch, M. Deutsch, J. Hartwig and E. Forster, Phys Rev A **56** (6), 4554-4568 (1997).
184. K. Kawatsura, T. Morikawa, K. Takahiro, M. Oura, H. Yamaoka, K. Maeda, S. Hayakawa, S. Ito, M. Terasawa and T. Mukoyama, J Phys B - Ato. Mol. Opt. **36** (20), 4065-4072 (2003).
185. T. Mukoyama, M. Uda and L. Kover, X-Ray Spectrometry **38** (5), 406-409 (2009).
186. T. D. Thomas, Phys Rev Lett **52** (6), 417-420 (1984).
187. T. D. Thomas, J Electron Spec **40** (3), 259-269 (1986).
188. M. Roy, J. D. Lindsay, S. Louch and S. J. Gurman, Journal of Synchrotron Radiation **8**, 1103-1108 (2001).
189. T. Mukoyama, M. Uda, L. Kover, Z. Berenyi, I. Cserny and W. Drube, X-Ray Spectrometry **38** (2), 138-143 (2009).
190. E. Vatai, Phys Rev A **38** (7), 3777-3780 (1988).
191. L. I. Schiff, *Quantum mechanics*, 2d ed. ed. (New York, McGraw-Hill, New York, 1955).
192. J. W. Gadzuk and M. Šunjić, Physical Review B **12** (2), 524-530 (1975).

Chapter 2. Practical Considerations for Experiments and Simulations

1. Experiment Design

a. Measurement modes

An absorption experiment is traditionally performed in one of three ways. The first is in a transmission configuration, as shown in Fig. 2-1. In this geometry the number of incident, I_0, and transmitted, I_T, photons are detected and the absorption coefficient is reported as

$$\mu(E) \cdot t = \ln \frac{I_0(E)}{I_T(E)}, \tag{2-1}$$

Which is a function of the photon energy, E, and is in accordance with the Beer-Lambert-Bouguer law.[1-3] In a second configuration, the fluorescence emitted from atoms excited by photoabsorption may be measured and taken as proportional to the number of absorbed photons. The choice of the latter method is appropriate for prohibitively thick samples or for dilute samples as the scaling of the statistical uncertainty goes as μ_x^{-1} for transmission experiments, but $\mu_x^{-1/2}$ for fluorescence, where μ_x is the absorption coefficient for the species of interest, 'x'.[4] Likewise, fluorescence experiments possess the advantage that the signal of interest may be measured with minimal background. This is contrary to transmission experiments measuring dilute compounds which would observe a small dip in transmission against the large number of transmitted photons. For the sake of completeness, it should be noted that the energy dependent attenuation of the emitted photon must be considered during sample preparation or analysis for either transmission or fluorescence mode measurements.[5]

A third option is to detect electrons ejected after the absorption event. This approach is known as electron yield detection and, due to the relatively short inelastic mean free path of electrons, is a surface-sensitive technique. Furthermore, soft X-ray research often involves total electron yield studies in which the sample is under ultra-high vacuum (UHV). Two details

warrant further comment. First, UHV is implemented to limit interactions between the emitted particles and the atmosphere. Second, the photoelectrons are measured instead of the photons because of difficulties associated with operating a photon detector in UHV. At higher energies, UHV is not strictly necessary and it is preferable to measure secondary electrons resulting from interaction of Auger electrons from the sample with gas in the ionization chamber.[6] This variation is known as conversion electron yield and requires that the sample be sufficiently conductive and can suffer from nonlinearities if the incident flux is too great.[7]

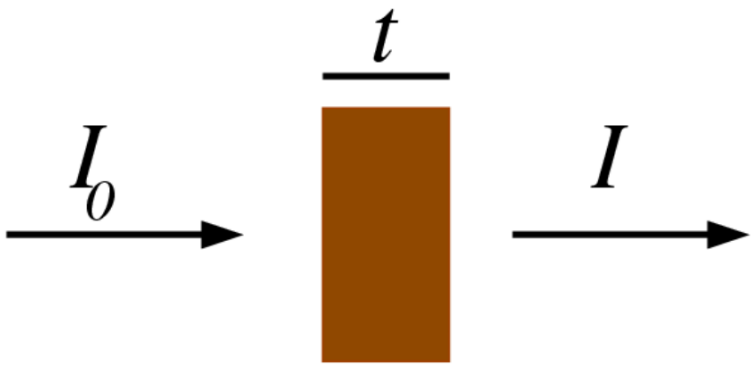

Fig. 2-1: Reproduced from Newville.[8] An incident beam of photons, I_0, passing through a material with thickness t. A final beam of photons, I, escapes the material.

b. Source Selection

Source selection necessitates a pragmatic decision. It is often desirable to describe and compare sources according to their brilliance, Fig. 2-2. There are two reasons for this, first, brilliance is an invariant quantity in ideal optical systems due to Louiville's theorem, and second, brilliant sources are more easily coupled with reasonably sized mirrors, monochromators, and focusing optics. Synchrotron light sources offer incredible technical capability, including exceptional brilliances, but are often oversubscribed. As a result, studies pushing the forefront of science are

prioritized and studies requiring routine analysis or rapid feedback are unable to make use of these resources. Fortunately, premier brilliances are not required to study bulk compounds via transmission-mode XAFS. Indeed, only 10^4 to 10^5 counts per point are necessary to resolve spectra to a degree appropriate for chemical analysis of the XANES region, while little improvement in the spectrum is achieved with 10^6 counts per point, Fig. 2-3. Thus, X-ray tube sources mounted in laboratory-based spectrometers offer are perfectly viable candidates for many materials research campaigns.[9-11] The remainder of the discussion regarding sources will focus on a few properties of X-ray tube sources, as well as important details in selecting the optimal X-ray tube source for an experiment.

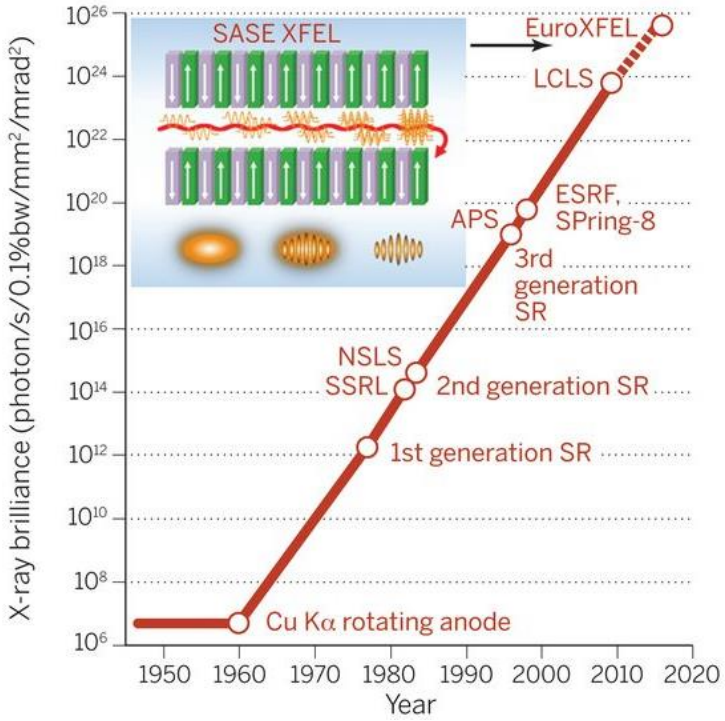

Fig. 2-2: Reproduced from Maio.[12] Historical growth of source brilliance for several institutions compared to a conventional X-ray tube source. Note that SR refers to synchrotrons, while the acronyms are Stanford synchrotron radiation lightsource (SSRL), national synchrotron light source (NSLS), advanced photon source (APS), European synchrotron radiation facility

(ESRF), the linac coherent light source (LCLS), self-amplified spontaneous emission (SASE), and X-ray free electron laser (XFEL).

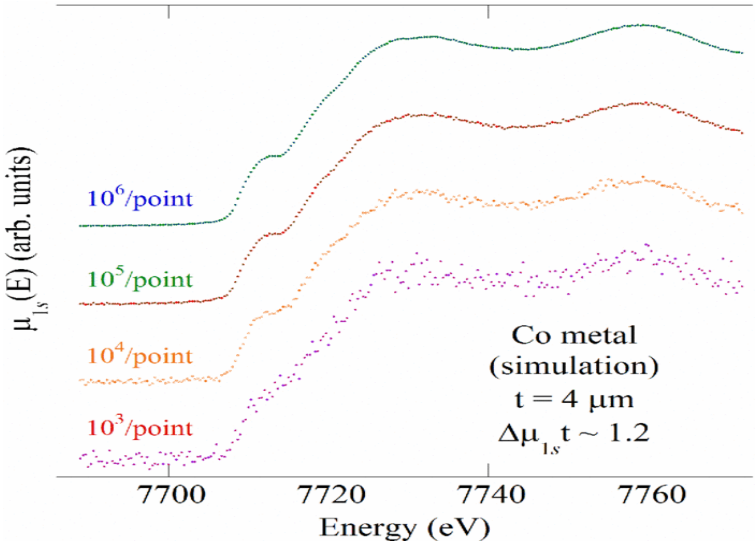

Fig. 2-3: Reproduced from Seidler.[11] Simulated Co K-edge XANES data for a Co metal foil. Poisson noise was applied to a spectrum measured at a synchrotron by assuming a given number of counts per point.

First, it should be noted that X-ray tube sources are polychromatic and must be monochromatized, often with a crystal analyzer. The output of an X-ray tube source is shown in Fig. 2-4 and is composed of a sloping bremsstrahlung profile superimposed with characteristic fluorescence lines. Note that this tube is operating at a substantially lower power than many other commercially available X-ray tube sources, yet still provides sufficient flux to meet the above Poisson requirements in each approximately 0.3 eV bin corresponding to the intrinsic energy resolution of a non-strain-relieved spherically bent crystal analyzer (SBCA).[13, 14]

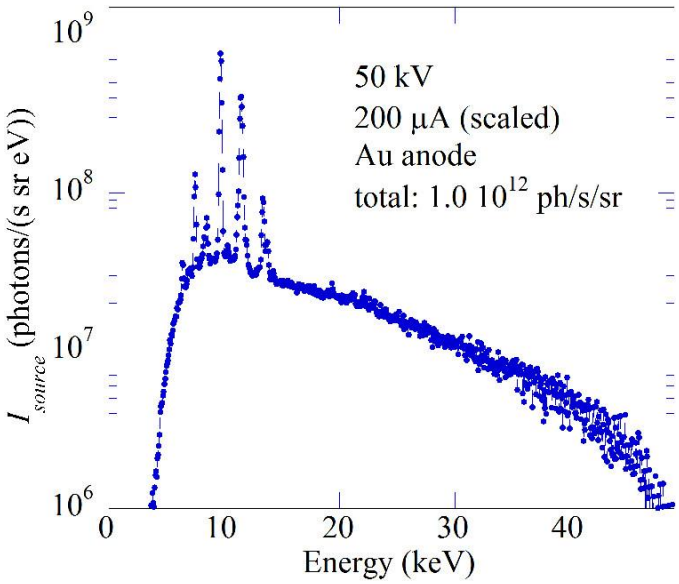

Fig. 2-4: Reproduced from Seidler.[11] The measured spectrum from a Moxtek X-ray tube source operated at 10 W tube power.

Moreover, the energy spectrum of unconventional X-ray tubes is especially efficient in non-resonant XES. In this configuration, the sample is directly illuminated by the X-ray tube and every photon with an energy sufficient to excite the core-electron of interest to an unoccupied state above the Fermi-level has the potential to stimulate fluorescence. Again, the incident photons may be characteristic fluorescence lines or originate from bremsstrahlung radiation. An appropriate anode material may be selected by considering these two factors. The intensity of bremsstrahlung radiation scales with the square of the anode material's atomic number.[15] To some degree, this gain with increased Z is offset by absorption in the anode for lower photon energies, but yields much improved count rates for higher Z anode materials. On the other hand, higher Z materials possess more electrons and, accordingly, more characteristic fluorescence lines. In XES, these lines can be advantageous if they have sufficient energy to excite the appropriate core electron. However, in XAFS, these fluorescence lines can contribute substantial flux and impose substantial deadtime on the detector. Thus, it is best to carefully

selecting the anode material to avoid elements with characteristic fluorescence lines in the energy range of interest or in the corresponding energy ranges spanned by analyzer harmonics. Note that characteristic fluorescence lines can also originate from the heat sink material inside the X-ray tube, typically Cu.

Beyond the anode's content, its geometry can also play a meaningful role in determining its potential output. X-ray tubes utilizing a 90° take-off provide ~3x greater efficiency than conventional transmission-geometry anodes due to increased absorption during photon transit through the anode material in the latter.[10] In addition, X-ray tubes with beam spot sizes of 0.5 – 1.0 mm are readily available, which is desirable as the source size in the optical plane of the monochromator is often one of the dominant geometric factors contributing to laboratory-based spectrometers.[16] Finally, it should be noted that X-ray tubes typically generate internal electrons via thermionic emission resulting from running a large current through a W filament. An unintended consequence of this is that, regardless of anode material, a small amount of W can be deposited on the anode material, giving rise to unexpected characteristic fluorescence lines.[17]

An additional detail warrants mention before concluding this topic. First, the flux of an X-ray tube source is roughly proportional to the electron beam current. Which is that the subjects of this chapter, synchrotron light sources and X-ray tube sources, are not the only sources of X-rays available. Recently, X-ray free electron lasers (XFELs),[18] high harmonic generation (HHG),[19] and electron-impact liquid-gallium-jets[20] have seen increased use and interest in recent years.

c. Monochromator Considerations

With the exception of instruments possessing a transition-edge sensor array,[21] diffraction optics are essential in hard X-ray XAFS experiments whether utilizing a synchrotron or X-ray

tube source. This is because chemical characterization typically requires an energy bandwidth of approximately 1 eV full-width half-maximum (FWHM). As has been discussed, X-ray tube sources are polychromatic. Similarly, undulators produce beams with bandwidths of order 10^2 to 10^3 eV, while wigglers produce beams with bandwidths of order 10^3 eV, and bend magnets produce very broad, essentially white beams.[7] The remainder of this discussion will be divided into a discussion of synchrotron specific considerations followed by a discussion on the types of analyzers available.

At a synchrotron, the monochromator design must account for the high brilliance of the beam. To begin, monochromators are typically stored in a vacuum container that both prevents ozone formation as a result of pink beam exposure to the air and also curtails scatter which would arise in the case of, e.g., a helium-filled monochromator. Second, the beam may deposit substantial power in the monochromator and cause a temperature gradient in the material. This can lead to a distortion in the crystal. As a result, it is crucial that an analyzer material possess a high thermal conductivity and a low thermal expansion coefficient, which can be achieved for silicon when cryogenically cooled by liquid nitrogen. Additionally, synchrotrons often employ a double crystal monochromator with the second crystal aligned by a piezoelectric tied to a fixed feedback loop to maintain beam position. Additionally, a simple technique may be used to remove harmonics. Specifically, harmonics typically have rocking curves which are much narrower than that of the fundamental. Therefore, the analyzers can be detuned, which involves introducing a slight angle between the diffracting surfaces, to substantially reject the harmonics.

In recent years, rapid advancements have been made in modeling[22, 23] and manufacturing[24-27] crystal analyzers for X-ray spectroscopies. Now, optics are frequently produced by elastic deformation, gluing, and anodic bonding. They may be diced to relieve

strain and, consequently improve energy resolution.[28] Further from back scatter, traditional Johann analyzers[29] suffer from two deficiencies which require further geometric modification. First, the surface of a Johann analyzer does not lie tangent to the Rowland circle, Fig. 2-5. Note that a description of the Rowland circle is provided by Bergmann et al. as well as a discussion of the consequences of deviations from this geometry.[16] In particular, a Johann analyzer is liable to degrade energy resolution by distorting the high energy side of spectra and has been thoroughly studied.[30] Note that this effect is exacerbated at lower Bragg angles, but can be mitigated by employing a Johansson crystal[31] which has been ground to the specified radius. In this manner, resolution, and in many cases count rates, may be recovered. Second, sagittal error is encountered away from backscatter. As a result, a point source will be refocused to a line at the detector. Although it is uncommon, this can be addressed with toroidally-bent crystal analyzers.[32-38] Finally, bent crystal analyzers with relatively small radii of curvature are gaining popularity and enabling studies of, e.g., dilute materials.[39] Despite these advances, the manufacturing processes are still rather intensive and, as a result, commercial optics often cost between $3K and $20K. As each optic spans only a finite energy range as dictated by its Miller indices, this serves as a substantial financial barrier to exploratory studies on edges or lines which an instrument has not previously studied. This is particularly true for the multi-analyzer systems which are often found at synchrotrons.[40, 41] For that reason, a component of this dissertation explored the construction of vacuum formed temporary bent crystal analyzers, Fig. 2-6, see Chapter 4.

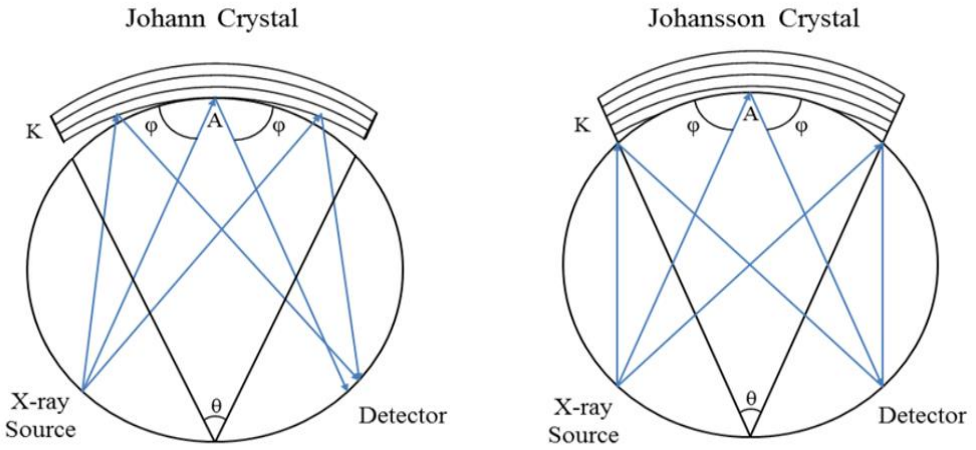

Fig. 2-5: Reproduced from Goodsell with minor modification.[42] Sketch of Johann and Johansson style crystal on the Rowland circle of a wavelength dispersive spectrometer.

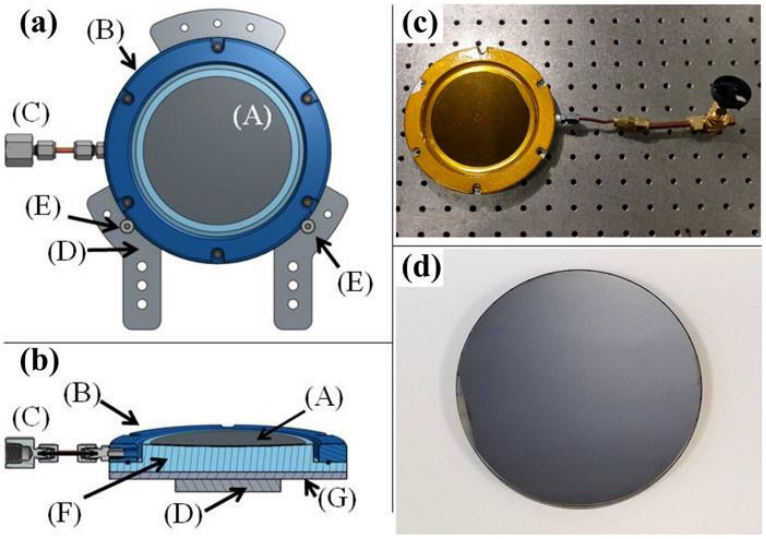

Fig. 2-6: Figure and caption reproduced from Jahrman.[43] "(a) CAD rendering front view of the vacuum formed bent crystal analyzer (VF-BCA). (A) Bent wafer; (B) front flange with polyimide film (not shown); (C) pumping line; (D) aluminum alloy vertical support plate; (E) support bolts to define the position of the outer diameter of the VF-BCA body. (b) CAD rendering section view of the VF-BCA. (F) CNC-machined vacuum form; (G) steel backing plate for magnetic mounting, where magnets (not shown) are attached alongside part (D). (c) Photograph of the VF-BCA; note the flexible orange polyimide film that allows air pressure to force the wafer into the shape of the form machined into part (F). A second, similar VF-BCA instead has a simple recess in part (F) to accept a 1-m radius of curvature concave glass lens. (d) Photograph of a commercial, anodically bonded 10-cm diameter SBCA with 1-m radius of curvature."

A final note is warranted regarding crystal materials. Typically, Si or Ge are employed. A few materials other materials are also sometimes chosen depending on application. Diamond monochromators are occasionally used at the European Synchrotron Radiation Facility (ESRF) for high heat loads.[44] Graphite optics also hold some appeal, primarily due to their mosaicity.[45]

These optics are usually formed from highly oriented pyrolytic graphite (HOPG) or, for greater energy resolution, highly annealed pyrolytic graphite (HAPG). Such analyzers have found use in laboratory-based instruments[46, 47] and, in one instance, as a RIXS polarization analyzer.[48] A component of this thesis is also dedicated to evaluating mica as a candidate material for use in XES experiments.[49] Finally, it should be noted that the above general strategies are not employed in monochromatizing soft X-rays, which are instead analyzed by grating monochromators.[50]

Before continuing it should be noted that the analyzer should be appropriately paired with the detector. If the analyzer provides significant harmonics, it is important to employ a detector with sufficient energy resolution to reject unwanted signal. This is also true if significant scattering or background noise is present in the experiment. Also, the detector should be chosen and its shaping time set such that dead time is kept minimal to enable accurate correction.

d. Sample Considerations

Before an XAS experiment may be performed, appropriate samples must be selected and prepared. Often times, it is necessary to choose an assortment of reference compounds whose bonding networks span the range of possibilities hypothesized for the materials of interest. Samples should be validated by various characterization techniques. Once the material identities are confirmed, appropriate samples can be prepared, however, it is important that their properties not be altered during the preparation process and should therefore be monitored by appropriate analyses. The criteria for sample optimization varies between transmission and fluorescence mode experiments. Therefore, these experiments will be discussed in turn.

Transmission mode experiments require that a sample be homogenous and of a favorable thickness. Several XAFS resources recommend a sample thickness which leads to an edge jump

of unity, $\Delta\mu t \sim 1$, at the edge of interest.[7, 51] Furthermore, too great of a thickness will lead to distortions in the measured spectrum. This is due to the Parratt effect which arises due to the tails of the monochromator response function.[52] As a result, the total sample thickness of $\mu_T x = 2.6$, which is ideal according to statistical considerations,[53] is liable to produce distortions at edge steps greater than $\Delta\mu_0 x > 1.5$.[54] Similarly, inhomogeneities, particularly in the form of particle aggregation, can lead to pinhole effects that tends to distort XAFS oscillations toward the atomic background.[55] Accordingly, it is prudent to grind, sieve, and, if necessary, employ a sedimentation procedure to acquire particle sizes several times smaller than the X-ray attenuation length of the material.[7] As these characteristics have a pronounced effect on the resulting spectrum, researchers have outlined model based correction procedures[56-58] which occasionally make use of the temperature dependence of EXAFS oscillations.[59] Furthermore, it should be noted that it is unwise to employ especially thick samples, even with small edge steps. Not only is this statistically disadvantageous, but thick samples disproportionately transmit high energy harmonics which can cause deleterious artifacts in the resulting spectrum, particularly if acquired using gas ionization detectors. As a final note, it is not only important that the sample be homogenous along its thickness, but spatially within the extent of the beam. Moreover, it is beneficial that the beam be spatially uniform,[60] which can be problematic at many insertion devices.

In fluorescence mode studies, spatial uniformity is not critical, however, small particle size is crucial to avoid self-absorption effects. This effect, as well as its corrections, is well documented in the literature.[5, 61, 62] It occurs when the penetration depth in a sample being measured is dominated by the element of interest. This can cause considerable enhance of sharp pre-edge features and damping of both XANES features past the edge and EXAFS oscillations, Fig. 2-7.

Corrections to the spectrum can be applied and are readily available in two limits; for thin, concentrated samples and conversely for thick, dilute samples.[63] However, it is generally advisable that samples be prepared sufficiently thin and, if possible, dilute so that such corrections are not necessary.

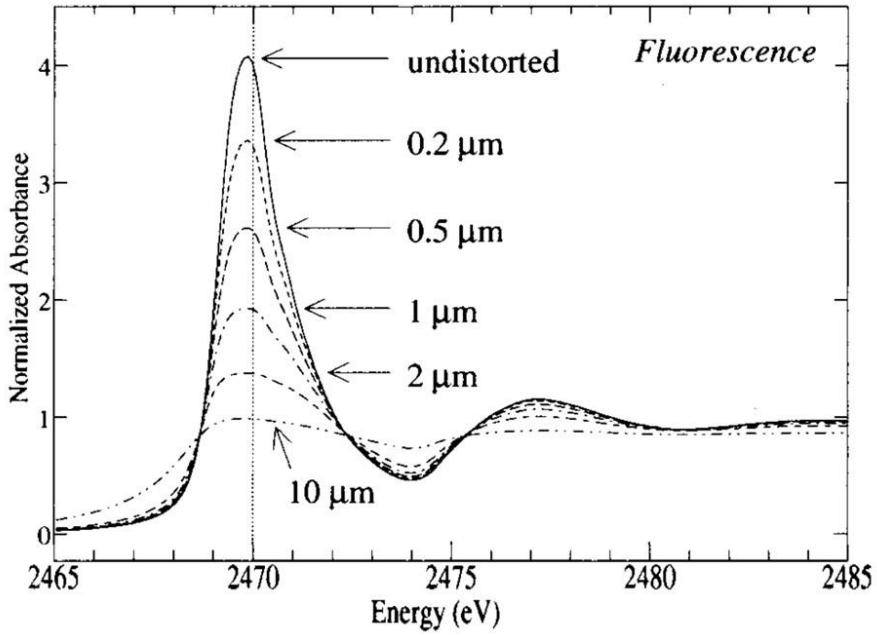

Fig. 2-7: Reproduced from Pickering with minor modification.[64] S K-edge XANES measurements of S_8 particles prepared at various particle sizes.

e. Data Collection and Analysis

There are several important considerations when setting up an experiment. This include mitigating radiation damage, removal of unwanted signal via chemical and spatial filters, and general alignment procedures. To begin, the intensity of X-rays incident on a sample is often quite large in X-ray spectroscopy experiments. At one end of the spectrum, XFELs are liable to produce sufficient irradiation to strip a system of a substantial portion of its electron density. The resulting positively charged cluster is then unstable and breaks apart in a so-called Coulomb

explosion.[65-67] In these instances, it is often desirable to try to operate in a single-shot or pump-probe motif so that spectra are collected before the atomic structure is perturbed. At substantially lower intensities, other mechanisms for radiation damage dominant,[68-71] however, such processes vary from sample to sample and are generally complex with multiple pathways and, consequently, not well understood. One pathway which is frequently discussed is the change of chemical structure following radical formation, this is particularly relevant in studies of biological molecules and studies in aqueous media where photolysis is liable to occur.[72] Some strategies for dealing with this damage distribute the radiation over a large sample volume. Alternatively, the sample can be mounted on a rotating wheel to distribute the dose around a ring.[73] It is also possible to frequently replenish the sample. For liquid samples, this can be achieved with a liquid jet or pump.[74, 75] For solid samples, it is possible, but not preferable, to replace the sample multiple times and join the spectra after proper normalization. Two other common practices exist for studying samples prone to radiation damage. The easier of the two options is to use a dispersive spectrometer design or quick scans to measure the sample before substantial damage is incurred. The more difficult approach is to measure the sample under cryogenic conditions which limits the diffusion of ozone through the material. Finally, it is worthwhile to note that radiation damage concerns are frequently absent in XANES experiments using laboratory-based instruments equipped with conventional X-ray tube sources. This is because the 10^4-10^6 incident photons per second are typically insufficient to produce substantial changes in chemical structure and, furthermore, the X-ray spot sizes are several mm^2 in such experiments.

When performing fluorescence mode studies, the sample composition of the material should also be considered to ameliorate the impact of other fluorescing elements in the

compound beside the one of interest. In this case, it is often appropriate reject the fluorescence lines with an energy-dispersive detector. If the fluorescence line is quite close the edge of interest, it may be necessary to use a "Z-1" filter. It should be noted that it is rare that chemical filters are used to reject fluorescence lines, and are more commonly used to reject elastic scatter. Nonetheless, the general concept is outlined in Fig. 2-8, assuming interference from a fluorescence line. In order to preferentially attenuate the interference, a chemical filter is inserted between the sample and detector. The filter is usually made of a material an atomic number lower than the element of interest. This can sometimes cause the problem that fluorescence from the filter then contaminates the signal. In these instances, it is possible to use a spatial filter which focuses on the sample of interest.[76] A modern example of one such filter is shown in Fig. 2-9.

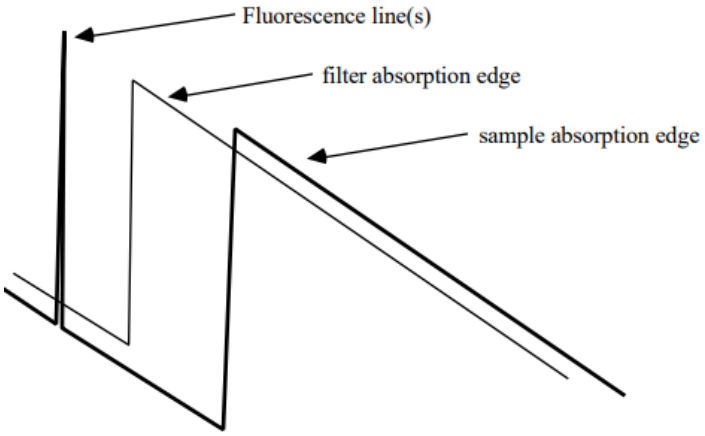

Fig. 2-8: Reproduced from Bunker.[77] The concept of a chemical filter is outlined.

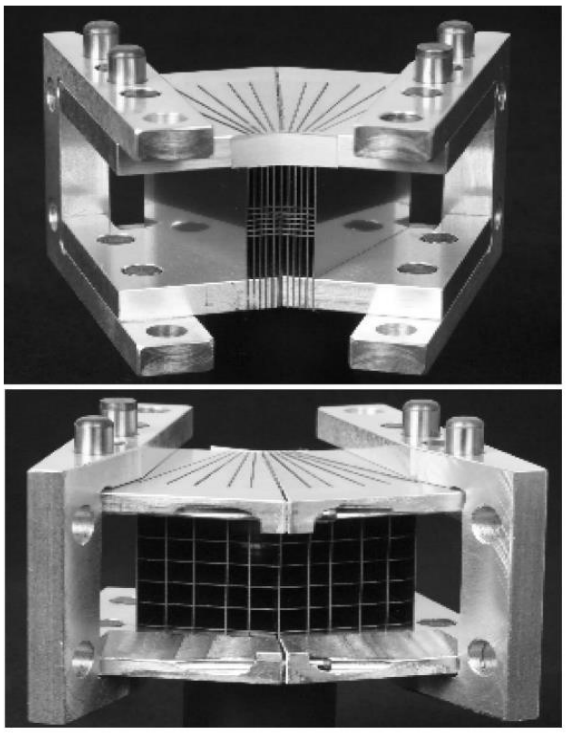

Fig. 2-9: Reproduced from Behne.[78] A compact, focusing spatial filter made from interleaved W sheets. The entrance is shown in the top and exit on bottom.

2. Theoretical Calculations

A variety of theoretical methods have been applied to X-ray absorption and X-ray emission phenomena. These methods include self-consistent field (SCF) calculations,[79-81] perturbative wave function analysis,[82] Green's function approaches,[83, 84] solving Bethe-Salpeter equations,[85-87] density functional theory (DFT),[88, 89] DFT with the transition-potential (TP) method,[90] time-dependent density functional theory (TDDFT),[91-93] and equation of motion coupled cluster theory at the singly- and doubly-excited level of theory.[94] Some of the above works deserve special mention for drawing comparisons between their results and predictions by other theories.[89, 93, 94] This furthers the field's understanding of the strengths and shortcomings of the respective approaches. This text will begin with an overview of the foundations of DFT. From there a

commentary on TDDFT will be provided. This section will conclude with an overview of some pragmatic concerns related to performing theoretical calculations.

DFT is highly efficient because it recasts the interacting many-electron system into a set of single-particle equations. This stems from the work of Hohenberg, Kohn, and Sham in the 1960's.[95-97] Here, it is conventional to write the Kohn-Sham equations as[98]

$$\left(-\frac{1}{2}\nabla^2 + v^C(\boldsymbol{r})\right)\psi_i(\boldsymbol{r}) + \int v^{XC}(\boldsymbol{r},\boldsymbol{r}')\psi_i(\boldsymbol{r}')d\boldsymbol{r}' = \epsilon_i\psi_i(\boldsymbol{r}). \qquad (2\text{-}2)$$

The Coulomb potential includes classical contributions from the nuclei and from electron density:

$$v^C(\boldsymbol{r}) = -\sum_\alpha \frac{Z_\alpha}{|\boldsymbol{R}_\alpha - \boldsymbol{r}|} + \int \frac{\rho(\boldsymbol{r},\boldsymbol{r})}{|\boldsymbol{r}-\boldsymbol{r}'|}d\boldsymbol{r}' \qquad (2\text{-}3)$$

Z_α and $\boldsymbol{R}_\alpha$ represent the position and charges of nuclei in the system, while the electron density consists of the diagonal elements of the electron density matrix:

$$\rho(\boldsymbol{r},\boldsymbol{r}') = \sum_\alpha \psi_\alpha^*(\boldsymbol{r})\psi_\alpha(\boldsymbol{r}') \qquad (2\text{-}4)$$

The many-electron interactions are captured by the exchange-correlation potential v^{XC}. However, a closed form expression for v^{XC} is not available outside of diagrammatic expansions.[99, 100] The above is a traditional introduction to DFT which uses formalism consistent with that of Valiev et al.[98] Similar descriptions are provided in many other reviews of DFT.[101]

In lieu of a closed form expression, several approximations for the exchange-correlation potential exist. This includes the local density approximation (LDA), which writes the exchange-correlation potential as a functional of the electron density.[102, 103] For this approximation to be successful in modeling real systems, either the errors in local exchange and local correlation must cancel, or, if correlation effects are small, local exchange must satisfactorily describe the interactions in the system.[104] This frequently occurs to at least some extent. LDA tends to underestimate exchange in the system while overestimating correlation.[101]

For greater generality, spin-polarization can also be included within the local spin density approximation (LSDA).[105] For still greater accuracy, the gradient of the electron density may be included as in the generalized gradient approximation (GGA).[106] GGA functionals are frequently parameterized according to experimental data. However, it is possible to derive a GGA functional with all parameters, other than those in the LSDA, specified by fundamental constants. One notable example is the functional derived by Perdew, Burke and Ernzerhof (PBE)[107] which works for a wide range of systems including bulk metals. For that reason, it is often the preferred functional for solid-state calculations.[101] A final note on functionals is that greater accuracy is sometimes desired in treating exchange. In these cases, hybrid functionals can be implemented. These functionals mix in some part of exact exchange as calculated with Hartree-Fock exchange integrals evaluated with Kohn-Sham orbitals. Here, it is desirable to only mix a small fraction of exact exchange to maintain the favorable cancellation errors discussed above. This fraction is typically 20% to 25%.[101]

The above approximations and functionals represent a choice of theoretical framework; but in order to perform a calculation, it is necessary to select a set of basis functions. For finite systems, it is common to select a basis of orbitals expressed using exponential or Gaussian functions. For example, Slater-type orbitals may be written in spherical polar coordinates as[108]

$$\chi_{nlm} = Nr^{n-1}e^{-\zeta r}Y_{lm}(\theta,\phi) \tag{2-5}$$

where l and m are angular momentum quantum number, ζ is the exponential decay parameter, and N is the normalization constant for the orbital. Compared to other basis set options, these orbitals demonstrate superior short- and long-range behavior. Still, it can be problematic to tune these orbitals to achieve the proper cusp at the nucleus or the proper decay rate for the exponential tail.[108] Similarly, Cartesian Slater orbitals can be written by replacing the radial

power law and spherical harmonic with independent power laws along each Cartesian axis. Linear combinations of Cartesian Slater can be constructed to form spherical polynomials of well-defined angular momentum. As an alternative to Slater-type orbitals, Cartesian Gaussian orbitals may be written[108]

$$\chi_{kmn} = N x^k y^m z^n e^{-\zeta r^2}. \quad (2\text{-}6)$$

No finite linear combination of these orbitals can properly describe the cusp at the nucleus or the desired exponential decay. Nonetheless, these orbitals greatly reduce computational costs as a consequence of the general Gaussian product theorem which yields an algebraic expression for any general multicenter Gaussian-type orbital product.[109] As a result, atom-centered contracted Cartesian Gaussian orbitals are the most popular choice in quantum chemistry.[101] In treating the behavior of valence electrons, it is often useful to replace some set of core electrons in the system with an effective potential. This greatly reduces computational costs both because a large number of Gaussians is typically required to describe the core basis functions, and also because most quantum chemical calculations scale in a deleterious manner with the number of explicitly treated electrons.[110, 111]

In order to model infinite systems, a plane wave basis set must be used or a finite system must be constructed to represent the infinite system. Plane wave basis sets are the subject of numerous careful analyses and are frequently employed in DFT calculations.[112-116] Several advantages are associated with plane wave basis sets; plane wave basis sets are amenable to fast Fourier transform procedures, provide equal treatment to all regions of the system, and are not liable to over-completeness or superposition errors. However, plane waves inefficiently describe the rapid oscillations near atomic nuclei and intractably large numbers are thus required to accurately represent such behavior. In addition, plane wave DFT codes typically do not support

hybrid forms of exchange-correlation potentials, albeit with some notable exceptions.[98] Rather than use a plane wave DFT code, a periodic substance can be approximated as a finite cluster. In these cases, it is often desirable to passivate the surface with pseudo-hydrogens superimposed with point charges. In this way, the electronic structure of the cluster can be made to imitate that of the periodic system.[117-119] Indeed, this method is used in Chapter 9 of this dissertation and has been used and described in other works.[120, 121]

Formally, ground-state DFT calculations can only predict ground-state properties, not electronic excitations.[101] Of course, there are approximations which address this limitation, including configuration interaction with single substitutions (CIS) and the random-phase approximation (RPA) which are based on Hartree-Fock methods. However, TDDFT has emerged as a favorable alternative to these methods.[122] In particular, TDDFT is particularly well-suited to the treatment of time-varying external potentials, as are produced by propagating electromagnetic waves. For that reason, TDDFT has achieved considerable success in simulating X-ray absorption and X-ray emission processes.[91, 92, 94] Furthermore, TDDFT is superior to ground-state DFT calculations in that it is able to simulate excitation and de-excitation processes involving multiple orbital pairs. In some instances, this can lead to TDDFT correctly predicting features that do not appear in DFT calculations. For example, feature P3 is missing from the DFT calculation in Fig. 2-10(a), but is present as feature D in the TDDFT calculation of Fig. 2-10(b).

The general process for performing a TDDFT simulation of an XES spectrum is described by Wadey and Besley.[94] To begin, the electronic structure of a neutral molecule is calculated in its ground state. The molecular orbitals generated by this calculation are used as the input for a DFT or SCF calculation with a full core hole (FCH) in the appropriate orbital[79, 81,

[123] subject to a maximum overlap condition.[80, 124] This allows relaxation of the excited electronic state and improved agreement with experimental spectra, see Fig. 2-11. Finally, the molecular orbitals calculated for the excited state are used as input for the TDDFT calculation. Here, the de-excitations arise naturally as the poles of the response function with corresponding oscillator strengths that can be calculated as described by Elliott *et al.*[101] Moreover, the computational cost of the TDDFT calculation is often reduced by employing the Tamm-Dancoff approximation which neglects the so-called B-matrix.[92, 122, 125, 126] Finally, the transition probabilities can be calculated via their relation to the oscillator strengths of the transition.[127]

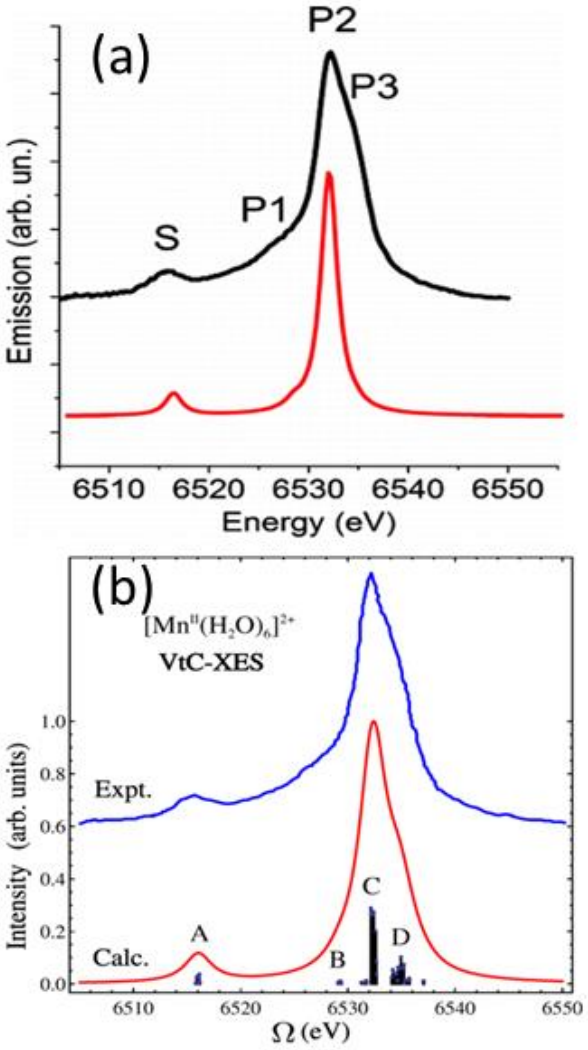

Fig. 2-10: (a) Reproduced from Smolentsev.[128] Mn VTC-XES spectra of hydrated Mn^{2+} ions measured experimentally (top, black) and calculated by DFT according to a cluster of six water molecules coordinated to a Mn^{2+} ion (bottom, red). (b) Reproduced from Zhang.[93] Mn VTC-XES spectra of hydrated Mn2+ ions measured experimentally (top, blue) and calculated by TDDFT (bottom, red).

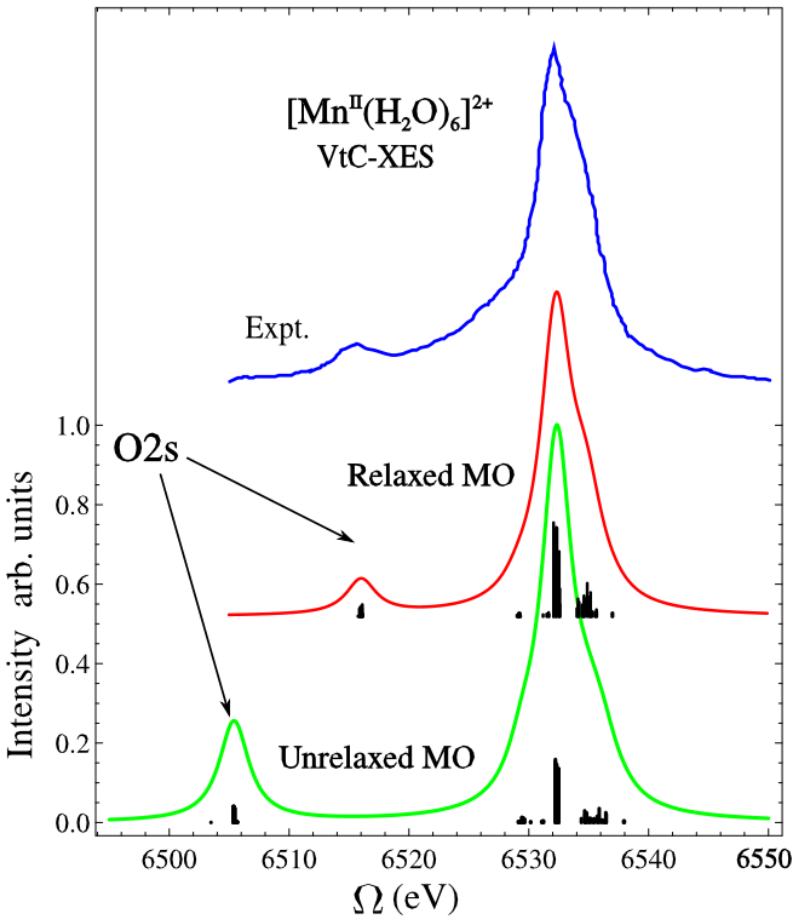

Fig. 2-11: Reproduced from the supporting information provided by Zhang.[93] Mn VTC-XES spectra of hydrated Mn2+ ions measured experimentally (top, blue), TDDFT result in the FCH procedure (middle, red), TDDFT result without relaxation of the excited state (bottom, green).

3. References

1. A. Beer, Annalen der Physik **162** (5), 78-88 (1852).
2. P. Bouguer, *Essai d'optique sur la gradation de la lumiere*. (Chez Claude Jombert ... A Paris, 1729).
3. J. H. Lambert, *I.H. Lambert Academiae Scientiarum Electoralis Boicae ... Photometria, siue, De mensura et gradibus luminis, colorum et umbrae*. (Sumptibus Viduae Eberhardi Klett, typis Christophori Petri Detleffsen, Augustae Vindelicorum, 1760).
4. J. Jaklevic, J. A. Kirby, M. P. Klein, A. S. Robertson, G. S. Brown and P. Eisenberger, Solid State Communications **23** (9), 679-682 (1977).
5. C. H. Booth and F. Bridges, Phys Scripta, 202 (2005).

6. S. L. M. Schroeder, G. D. Moggridge, R. M. Ormerod, R. M. Lambert and T. Rayment, Physica B: Condensed Matter **208-209**, 215-216 (1995).
7. G. Bunker, *Introduction to XAFS: A Practical Guide to X-ray Absorption Fine Structure Spectroscopy*. (Cambridge University Press, Cambridge, 2010).
8. M. Newville, edited by U. o. Chicago (Consortium for Advanced Radiation Sources, 2004).
9. A. S. Ditter, L. R. Bradshaw, E. P. Jahrman, X. Xia and G. T. Seidler, In Preparation (2019).
10. E. P. Jahrman, W. M. Holden, A. S. Ditter, D. R. Mortensen, G. T. Seidler, T. T. Fister, S. A. Kozimor, L. F. J. Piper, J. Rana, N. C. Hyatt and M. C. Stennett, Review of Scientific Instruments **90** (2), 024106 (2019).
11. G. T. Seidler, D. R. Mortensen, A. J. Remesnik, J. I. Pacold, N. A. Ball, N. Barry, M. Styczinski and O. R. Hoidn, Review of Scientific Instruments **85** (11), 113906 (2014).
12. J. Miao, T. Ishikawa, I. K. Robinson and M. M. Murnane, Science **348** (6234), 530 (2015).
13. K. Hämäläinen, C. C. Kao, J. B. Hastings, D. P. Siddons, L. E. Berman, V. Stojanoff and S. P. Cramer, Physical Review B **46** (21), 14274-14277 (1992).
14. K. Hämäläinen, D. P. Siddons, J. B. Hastings and L. E. Berman, Phys Rev Lett **67** (20), 2850-2853 (1991).
15. R. Evans, *The Atomic Nucleus*. (McGraw-Hill Book Company, Inc., New York, 1955).
16. U. Bergmann and S. P. Cramer, presented at the SPIE's International Symposium on Optical Science, Engineering, and Instrumentation, 1998 (unpublished).
17. W. Thulke, R. Haensel and P. Rabe, Review of Scientific Instruments **54** (2), 277-283 (1983).
18. A. Doerr, Nature Methods **15**, 33 (2018).
19. A. S. Johnson, D. Wood, D. R. Austin, C. Brahms, A. Gregory, K. B. Holzner, S. Jarosch, E. W. Larsen, S. Parker, C. Strüber, P. Ye, J. W. G. Tisch and J. P. Marangos, Review of Scientific Instruments **89** (8), 083110 (2018).
20. M. Otendal, T. Tuohimaa, U. Vogt and H. M. Hertz, Review of Scientific Instruments **79** (1), 016102 (2008).
21. K. M. Morgan, Physics Today **71** (8), 28-34 (2018).
22. A.-P. Honkanen, C. Ferrero, J.-P. Guigay and V. Mocella, Journal of Applied Crystallography **51** (2), 514-525 (2018).
23. A.-P. Honkanen, G. Monaco and S. Huotari, Journal of Applied Crystallography **49** (4), 1284-1289 (2016).
24. E. Collart, A. Shukla, F. Gelebart, M. Morand, C. Malgrange, N. Bardou, A. Madouri and J.-L. Pelouard, Journal of Synchrotron Radiation **12** (4), 473-478 (2005).
25. H. Okuda, K. Nakajima, K. Fujiwara, K. Morishita and S. Ochiai, Journal of Applied Crystallography **41** (4), 798-799 (2008).
26. A. H. Said, H. Sinn and R. Divan, Journal of Synchrotron Radiation **18** (2), 492-496 (2011).
27. R. Verbeni, M. Kocsis, S. Huotari, M. Krisch, G. Monaco, F. Sette and G. Vanko, Journal of Physics and Chemistry of Solids **66** (12), 2299-2305 (2005).
28. S. Huotari, F. Albergamo, G. Vankó, R. Verbeni and G. Monaco, Review of Scientific Instruments **77** (5), 053102 (2006).
29. H. H. Johann, Z Phys **69** (2-4), 185-206 (1931).
30. K. Q. Lu and E. A. Stern, (1980), Vol. 64, pp. 104-108.

31. T. Johansson, Z Phys **82** (7-8), 507-528 (1933).
32. G. Askari Germi, S. J. Pestehe and A. Rastkar Ebrahimzadeh, Journal of Applied Crystallography **50** (4), 1104-1116 (2017).
33. A. Hauer, J. D. Kilkenny and O. L. Landen, Review of Scientific Instruments **56** (5), 803-805 (1985).
34. D. B. Wittry and W. Z. Chang, J Appl Phys **72** (8), 3440-3446 (1992).
35. D. B. Wittry and S. Sun, J Appl Phys **68** (2), 387-391 (1990).
36. D. B. Wittry and S. Sun, J Appl Phys **67** (4), 1633-1638 (1990).
37. D. B. Wittry and S. Sun, J Appl Phys **69** (7), 3886-3892 (1991).
38. D. B. Wittry and S. Sun, J Appl Phys **71** (2), 564-568 (1992).
39. M. Rovezzi, C. Lapras, A. Manceau, P. Glatzel and R. Verbeni, Review of Scientific Instruments **88** (1), 013108 (2017).
40. T. T. Fister, G. T. Seidler, L. Wharton, A. R. Battle, T. B. Ellis, J. O. Cross, A. T. Macrander, W. T. Elam, T. A. Tyson and Q. Qian, Review of Scientific Instruments **77** (6), 063901 (2006).
41. P. Glatzel and U. Bergmann, Coordin Chem Rev **249** (1-2), 65-95 (2005).
42. A. V. Goodsell, Texas A&M University, 2012.
43. E. P. Jahrman, W. M. Holden, A. S. Ditter, S. A. Kozimor, S. L. Kihara and G. T. Seidler, Review of Scientific Instruments **90** (1), 013106 (2019).
44. P. Van Vaerenbergh, C. Detlefs, J. Härtwig, T. A. Lafford, F. Masiello, T. Roth, W. Schmid, P. Wattecamps and L. Zhang, *High Heat Load Diamond Monochromator Project at ESRF*. (2010).
45. I. Grigorieva, A. Antonov and G. Gudi, Condensed Matter **4** (1) (2019).
46. W. Malzer, D. Grötzsch, R. Gnewkow, C. Schlesiger, F. Kowalewski, B. Van Kuiken, S. DeBeer and B. Kanngießer, Review of Scientific Instruments **89** (11), 113111 (2018).
47. C. Schlesiger, L. Anklamm, H. Stiel, W. Malzer and B. Kanngießer, Journal of Analytical Atomic Spectrometry **30** (5), 1080-1085 (2015).
48. X. Gao, C. Burns, D. Casa, M. Upton, T. Gog, J. Kim and C. Li, Review of Scientific Instruments **82** (11), 113108 (2011).
49. E. Joseph, E. P. Jahrman and G. T. Seidler, In Prep (2019).
50. H. Petersen, C. Jung, C. Hellwig, W. Peatman and W. Gudat, in *Rev. Sci. Instrum.* (1995), Vol. 66, pp. 1-14.
51. D. C. Koningsberger and R. Prins, *X-ray absorption: principles, applications, techniques of EXAFS, SEXAFS, and XANES*. (John Wiley and Sons,New York, NY, United States, 1988).
52. L. G. Parratt, C. F. Hempstead and E. L. Jossem, Phys Rev **105** (4), 1228-1232 (1957).
53. M. E. Rose and M. M. Shapiro, Phys Rev **74** (12), 1853-1864 (1948).
54. E. A. Stern and K. Kim, Physical Review B **23** (8), 3781-3787 (1981).
55. K.-q. Lu and E. A. Stern, Nuclear Instruments and Methods in Physics Research **212** (1), 475-478 (1983).
56. Y. A. Babanov, A. V. Ryazhkin and T. Miyanaga, Nuclear Instruments and Methods in Physics Research Section A: Accelerators, Spectrometers, Detectors and Associated Equipment **470** (1), 278-282 (2001).
57. N. V. Bausk, S. B. Erenburg and L. N. Mazalov, Journal of Synchrotron Radiation **6** (2), 268-270 (1999).
58. A. Ryazhkin, Y. Babanov and T. Miyanaga, Journal of Synchrotron Radiation **8** (2), 291-293 (2001).

59. E. Voronina, D. Guy and T. Miyanaga, Nuclear Instruments and Methods in Physics Research Section B: Beam Interactions with Materials and Atoms **215** (2), 525-530 (2004).
60. E. Curis, J. Osan, G. Falkenberg, S. Bénazeth and S. Török, *Simulating systematic errors in X-ray absorption spectroscopy experiments: Sample and beam effects*. (2005).
61. J. Goulon, C. Goulon-Ginet, R. Cortes and J. M. Dubois, J. Phys. France **43** (2), 539-548 (1982).
62. R. M. Trevorah, C. T. Chantler and M. J. Schalken, IUCrJ **6** (4), 586-602 (2019).
63. M. Newville, Rev. Mineral. Geochem. **78** (1) (2014).
64. I. J. Pickering, G. N. George, E. Y. Yu, D. C. Brune, C. Tuschak, J. Overmann, J. T. Beatty and R. C. Prince, Biochemistry **40** (27), 8138-8145 (2001).
65. R. Alonso-Mori, J. Kern, R. J. Gildea, D. Sokaras, T.-C. Weng, B. Lassalle-Kaiser, R. Tran, J. Hattne, H. Laksmono, J. Hellmich, C. Glöckner, N. Echols, R. G. Sierra, D. W. Schafer, J. Sellberg, C. Kenney, R. Herbst, J. Pines, P. Hart, S. Herrmann, R. W. Grosse-Kunstleve, M. J. Latimer, A. R. Fry, M. M. Messerschmidt, A. Miahnahri, M. M. Seibert, P. H. Zwart, W. E. White, P. D. Adams, M. J. Bogan, S. Boutet, G. J. Williams, A. Zouni, J. Messinger, P. Glatzel, N. K. Sauter, V. K. Yachandra, J. Yano and U. Bergmann, Proceedings of the National Academy of Sciences **109** (47), 19103 (2012).
66. A. Fratalocchi and G. Ruocco, Phys Rev Lett **106** (10), 105504 (2011).
67. B. F. Murphy, T. Osipov, Z. Jurek, L. Fang, S. K. Son, M. Mucke, J. H. D. Eland, V. Zhaunerchyk, R. Feifel, L. Avaldi, P. Bolognesi, C. Bostedt, J. D. Bozek, J. Grilj, M. Guehr, L. J. Frasinski, J. Glownia, D. T. Ha, K. Hoffmann, E. Kukk, B. K. McFarland, C. Miron, E. Sistrunk, R. J. Squibb, K. Ueda, R. Santra and N. Berrah, Nature Communications **5**, 4281 (2014).
68. J. Christensen, P. N. Horton, C. S. Bury, J. L. Dickerson, H. Taberman, E. F. Garman and S. J. Coles, IUCrJ **6** (4), 703-713 (2019).
69. T. Coffey, S. G. Urquhart and H. Ade, J Electron Spec **122** (1), 65-78 (2002).
70. H. B. Stanley, D. Banerjee, L. van Breemen, J. Ciston, C. H. Liebscher, V. Martis, D. H. Merino, A. Longo, P. Pattison, G. W. M. Peters, G. Portale, S. Sen and W. Bras, CrystEngComm **16** (29), 9331-9339 (2014).
71. S. A. Vaselabadi, D. Shakarisaz, P. Ruchhoeft, J. Strzalka and G. E. Stein, Journal of Polymer Science Part B: Polymer Physics **54** (11), 1074-1086 (2016).
72. G. N. George, I. J. Pickering, M. J. Pushie, K. Nienaber, M. J. Hackett, I. Ascone, B. Hedman, K. O. Hodgson, J. B. Aitken, A. Levina, C. Glover and P. A. Lay, Journal of Synchrotron Radiation **19** (6), 875-886 (2012).
73. E. P. Jahrman, G. T. Seidler and J. R. Sieber, Analytical Chemistry **90** (11), 6587 (2018).
74. S. Y. Chang, T. A. Kathyola, E. A. Willneff, C. J. Willis, P. Wilson, P. J. Dowding, G. Cibin, A. B. Kroner, E. J. Shotton and S. L. M. Schroeder, Reaction Chemistry & Engineering **4** (4), 679-687 (2019).
75. U. Weierstall, Philosophical Transactions of the Royal Society B: Biological Sciences **369** (1647), 20130337 (2014).
76. E. A. Stern and S. M. Heald, Review of Scientific Instruments **50** (12), 1579-1582 (1979).
77. G. Bunker, in *Optimizing X-ray Filters*, edited by B. C. A. Team (1994).
78. E. A. Behne, Y. Feng and G. T. Seidler, Review of Scientific Instruments **72** (10), 3908-3913 (2001).

79. H. Ågren, V. Carravetta, O. Vahtras and L. G. M. Pettersson, Theoretical Chemistry Accounts **97** (1), 14-40 (1997).
80. N. A. Besley, A. T. B. Gilbert and P. M. W. Gill, The Journal of Chemical Physics **130** (12), 124308 (2009).
81. W. J. Hunt and W. A. Goddard, Chem Phys Lett **3** (6), 414-418 (1969).
82. K. Kunnus, W. Zhang, M. G. Delcey, R. V. Pinjari, P. S. Miedema, S. Schreck, W. Quevedo, H. Schröder, A. Föhlisch, K. J. Gaffney, M. Lundberg, M. Odelius and P. Wernet, The Journal of Physical Chemistry B **120** (29), 7182-7194 (2016).
83. J. Kas, J. Rehr, M. Tromp, R. J. Thomas and P. Glatzel, Journal of Physics: Conference Series **430**, 012003 (2013).
84. J. Zaanen, G. A. Sawatzky, J. Fink, W. Speier and J. C. Fuggle, Physical Review B **32** (8), 4905-4913 (1985).
85. R. Laskowski and P. Blaha, Physical Review B **82** (20), 205104 (2010).
86. E. L. Shirley, Phys Rev Lett **80** (4), 794-797 (1998).
87. E. L. Shirley, J Electron Spec **136** (1), 77-83 (2004).
88. M. W. D. Hanson-Heine, M. W. George and N. A. Besley, The Journal of Chemical Physics **146** (9), 094106 (2017).
89. N. Lee, T. Petrenko, U. Bergmann, F. Neese and S. DeBeer, J Am Chem Soc **132** (28), 9715-9727 (2010).
90. L. Triguero, L. G. M. Pettersson and H. Ågren, Physical Review B **58** (12), 8097-8110 (1998).
91. O. Bunău and Y. Joly, Physical Review B **85** (15), 155121 (2012).
92. S. DeBeer George, T. Petrenko and F. Neese, Inorganica Chimica Acta **361** (4), 965-972 (2008).
93. Y. Zhang, S. Mukamel, M. Khalil and N. Govind, Journal of Chemical Theory and Computation **11** (12), 5804-5809 (2015).
94. J. D. Wadey and N. A. Besley, Journal of Chemical Theory and Computation **10** (10), 4557-4564 (2014).
95. P. Hohenberg and W. Kohn, Phys Rev **136** (2B), B864-B871 (1964).
96. W. Kohn and L. J. Sham, Phys Rev **140** (4A), A1133-A1138 (1965).
97. L. J. Sham and W. Kohn, Phys Rev **145** (2), 561-567 (1966).
98. M. Valiev, E. J. Bylaska, N. Govind, K. Kowalski, T. P. Straatsma, H. J. J. Van Dam, D. Wang, J. Nieplocha, E. Apra, T. L. Windus and W. A. de Jong, Computer Physics Communications **181** (9), 1477-1489 (2010).
99. L. J. Sham, Physical review. **32** (6), 3876-3882 (1985).
100. M. Valiev and G. W. Fernando, Phys Lett A **227** (2), 265-270 (1997).
101. P. Elliott, F. Furche and K. Burke, Reviews in Computational Chemistry, 91-165 (2008).
102. M. T. Entwistle, M. J. P. Hodgson, J. Wetherell, B. Longstaff, J. D. Ramsden and R. W. Godby, Physical Review B **94** (20), 205134 (2016).
103. K. Jackson and M. R. Pederson, Physical Review B **42** (6), 3276-3281 (1990).
104. V. Sahni, K. P. Bohnen and M. K. Harbola, Phys Rev A **37** (6), 1895-1907 (1988).
105. J. P. Perdew and A. Zunger, Physical Review B **23** (10), 5048-5079 (1981).
106. P. Ziesche, S. Kurth and J. P. Perdew, Computational Materials Science **11** (2), 122-127 (1998).

107. J. P. Perdew, K. Burke and M. Ernzerhof, Phys Rev Lett **77** (18), 3865-3868 (1996).
108. E. R. Davidson and D. Feller, Chemical Reviews **86** (4), 681-696 (1986).
109. E. Besalú and R. Carbó-Dorca, Journal of Mathematical Chemistry **49** (8), 1769-1784 (2011).
110. T. V. Russo, R. L. Martin and P. J. Hay, The Journal of Physical Chemistry **99** (47), 17085-17087 (1995).
111. W. R. Wadt and P. J. Hay, The Journal of Chemical Physics **82** (1), 284-298 (1985).
112. G. Kresse and J. Furthmüller, Computational Materials Science **6** (1), 15-50 (1996).
113. G. Kresse and J. Furthmüller, Physical Review B **54** (16), 11169-11186 (1996).
114. M. Marsman, A. Grüneis, J. Paier and G. Kresse, The Journal of Chemical Physics **130** (18), 184103 (2009).
115. J. Paier, R. Hirschl, M. Marsman and G. Kresse, The Journal of Chemical Physics **122** (23), 234102 (2005).
116. M. D. Segall, R. Shah, C. J. Pickard and M. C. Payne, Physical Review B **54** (23), 16317-16320 (1996).
117. M. Casarin, C. Maccato and A. Vittadini, The Journal of Physical Chemistry B **102** (52), 10745-10752 (1998).
118. M. L. Sushko, A. Y. Gal and A. L. Shluger, The Journal of Physical Chemistry B **110** (10), 4853-4862 (2006).
119. L.-W. Wang and J. Li, Physical Review B **69** (15), 153302 (2004).
120. N. Govind, K. Lopata, R. Rousseau, A. Andersen and K. Kowalski, The Journal of Physical Chemistry Letters **2** (21), 2696-2701 (2011).
121. D. R. Mortensen, G. T. Seidler, J. J. Kas, N. Govind, C. P. Schwartz, S. Pemmaraju and D. G. Prendergast, Physical Review B **96** (12), 125136 (2017).
122. S. Hirata and M. Head-Gordon, Chem Phys Lett **314** (2), 291-299 (1999).
123. H. Ågren, V. Carravetta, O. Vahtras and L. G. M. Pettersson, Chem Phys Lett **222** (1), 75-81 (1994).
124. A. T. B. Gilbert, N. A. Besley and P. M. W. Gill, The Journal of Physical Chemistry A **112** (50), 13164-13171 (2008).
125. A. Dreuw and M. Head-Gordon, Chemical Reviews **105** (11), 4009-4037 (2005).
126. I. P. E. Roper and N. A. Besley, The Journal of Chemical Physics **144** (11), 114104 (2016).
127. T. Mukoyama, Spectrochimica Acta Part B: Atomic Spectroscopy **59** (8), 1107-1115 (2004).
128. G. Smolentsev, A. V. Soldatov, J. Messinger, K. Merz, T. Weyhermüller, U. Bergmann, Y. Pushkar, J. Yano, V. K. Yachandra and P. Glatzel, J Am Chem Soc **131** (26), 13161-13167 (2009).

Chapter 3. An Improved Laboratory-Based X-ray Absorption Fine Structure and X-ray Emission Spectrometer for Analytical Applications in Materials Chemistry Research

Originally published as: E. P. Jahrman, W. M. Holden, A. S. Ditter, D. R. Mortensen, G. T. Seidler, T. T. Fister, S. A. Kozimor, L. F. J. Piper, J. Rana, N. C. Hyatt, and M. C. Stennett. Review of Scientific Instruments **90**, 013106 (2019). E. P. Jahrman led the design, construction, commission, and operation of this instrument.

X-ray absorption fine structure (XAFS) and x-ray emission spectroscopy (XES) are advanced x-ray spectroscopies that impact a wide range of disciplines. However, unlike the majority of other spectroscopic methods, XAFS and XES are accompanied by an unusual access model, wherein; the dominant use of the technique is for premier research studies at world-class facilities, i.e., synchrotron x-ray light sources. In this paper we report the design and performance of an improved XAFS and XES spectrometer based on the general conceptual design of Seidler, et al., Rev. Sci. Instrum. 2014. New developments include reduced mechanical degrees of freedom, much-increased flux, and a wider Bragg angle range to enable extended x-ray absorption fine structure (EXAFS) for the first time with this type of modern laboratory XAFS configuration. This instrument enables a new class of routine applications that are incompatible with the mission and access model of the synchrotron light sources. To illustrate this, we provide numerous examples of x-ray absorption near edge structure (XANES), EXAFS, and XES results for a variety of problems and energy ranges. Highlights include XAFS and XES measurements of battery electrode materials, EXAFS of Ni with full modeling of results to validate monochromator performance, valence-to-core XES for 3d transition metal compounds, and uranium XANES and

XES for different oxidation states. Taken en masse, these results further support the growing perspective that modern laboratory-based XAFS and XES have the potential to develop a new branch of analytical chemistry.

LA-UR-18-26355

1. Introduction

X-ray absorption fine structure (XAFS) analysis is an especially capable and impactful tool for interrogating a material's local electronic and atomic structure. This element-specific technique encompasses both the x-ray absorption near edge structure (XANES), an acutely sensitive probe of a compound's oxidation state and molecular geometry, and the extended x-ray absorption fine structure (EXAFS), which is routinely used to extract multi-shell coordination numbers and bond lengths. These techniques enable premier scientific research campaigns in catalysis,[1-2] energy storage,[3-4] actinide chemistry,[5-7] heavy metal speciation in the environment,[8-10] etc. Likewise, the partner process, x-ray emission spectroscopy (XES), has been used to assess spin and ligand character, notably in critical discoveries of magnetic phase transitions under geophysical conditions.[11-12] At present, XES continues to emerge as an important measure of valence-level (occupied) electronic state properties through improved theoretical treatment of the valence-to-core (VTC) and core-to-core (CTC) XES. However, as has been pointed out several times in the modern history of XAFS and XES, and most recently by Seidler,[13] these x-ray spectroscopies suffer from an anomalous access model. In general, XAFS and XES studies require access to synchrotron facilities with entry requirements that limit more introductory, routine, or high-throughput analytical studies that, by contrast, are common for NMR, XPS, or optical spectroscopies where high-access benchtop equipment is easily available.

Over the last several decades, the capabilities of lab-based XAFS and XES instruments have rapidly grown. Researchers now report spectrometers operating as low as the C K-edge (284 eV)[14] using a laser-produced plasma source. Other spectrometers probe the S and P K emission lines (~ 2-2.5 keV) using double crystal monochromators,[15-17] a dispersive Rowland circle geometry,[18-21] and an instrument in the von Hamos geometry.[22] A variety of von Hamos instruments exist which are intended to operate in the ~3-12 keV range needed for studies of first row transition metals and lanthanides.[23-26] Many spectrometers operating in this range can be directly integrated into synchrotron beamlines.[27] For similar energies, a large number of XAFS spectrometers employing a Rowland circle geometry exist.[28-33] Lastly, higher energies, including the Au Kβ (78 keV), are accessible via Laue-type spectrometers.[34] We focus here on the case of Rowland circle geometries with a spherically bent crystal analyzer (SBCA), which has been extensively developed by some of the present authors.[13, 35-40]

The purpose of the present manuscript is to describe the design and performance of what is our latest-generation of improvements upon the first prototype instrument using an SBCA.[13] These are embodied in two nearly identical spectrometers, one at the University of Washington (UW) in Seattle and one at Los Alamos National Laboratory (LANL). Each of these sites is more than 1000 km away from the nearest synchrotron x-ray light source. The spectrometer improvements include several simplifications to the monochromator mechanical system that decrease its operation from five to only two motorized degrees of freedom and the selection of a ten-fold higher power x-ray tube that retains the small size and necessary anode characteristics to meet the needs of laboratory XAFS and XES.

The manuscript continues as follows: First, in section II, we describe the new monochromator. Important highlights include decreased mechanical complexity of the new

design and modification of the drive configuration to increase its Bragg angle range while minimizing its air-absorption path and overall footprint. Second, in Section III we present and discuss results for XANES and EXAFS of several materials reflecting contemporary interest in materials chemistry and other specialties. Examples include reference metal foils, battery electrode laminates of several different compositions, a family of reference Ce compounds, and uranium-rich materials. In all cases we find good agreement with prior synchrotron studies. For the recorded EXAFS spectrum of the metal foil, we further present a full Fourier-transform analysis using standard methods, and again find high quality results. Next, in Section VI we present and discuss results for XES from a wide variety of elements, chemical systems, and emission lines. This includes both deep-shell emission lines and the VTC XES that provides direct insight into chemical bonding. In sections III and IV, care is taken to provide measurement times, thus serving as useful benchmarks for assessing the feasibility of future studies using SBCA-based laboratory monochromators.

2. Experimental

a. Monochromator Design

Throughout the period between first publication[13] and this work, several advances in the spectrometer design have been made. Specifically, we have integrated a higher powered x-ray source, rotated and greatly elongated the source and detector stages, implemented passive tracking of the SBCA position (removing a motorized degree of freedom), and enacted the tiltless optic alignment introduced by Mortensen *et al.*[39] (removing two additional motorized degrees of freedom). These changes were motivated by a focus on greater count rates, instrument stability, ease-of-use, and achieving a wider useful energy range with each analyzer crystal orientation.

An overview of the new spectrometer design is given in Fig. 3-1. The approach uses linear translation stages to generate fine rotations (Bragg angle steps) and 'steering bars' to maintain alignment between the source, detector, and SBCA. This design was based directly on our prototype system.[13] We now summarize similarities and differences of the two new instruments with respect to the prototype instrument.

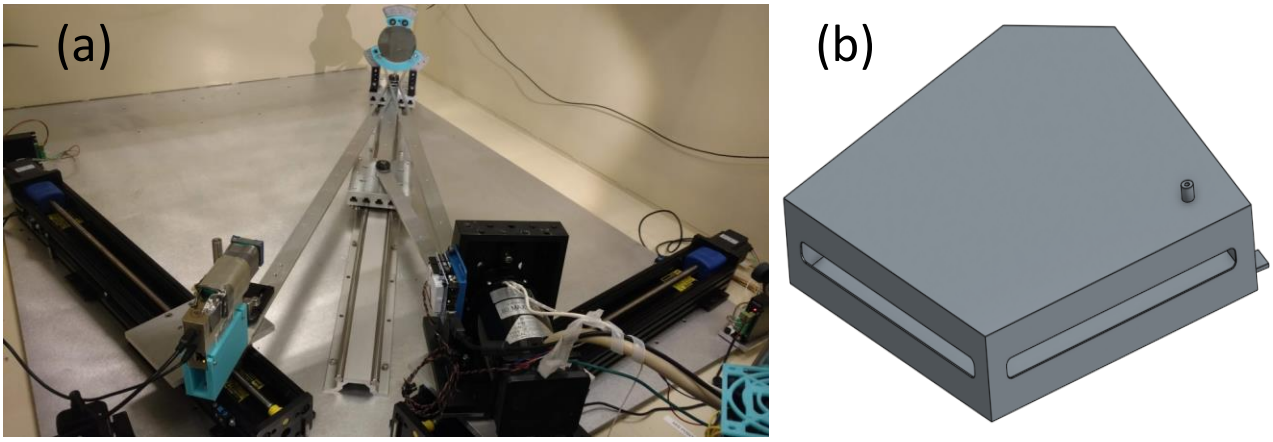

Fig. 3-1: (a) Corner perspective of spectrometer in XANES configuration. The SBCA and source are mechanically coupled to the center carriage. The two-axis tilt is no longer utilized. Source and detector are at $\alpha = 40°$ (see Fig. 3-2). (b) CAD rendering of the helium box (removed from frame (a)) enclosing the x-ray beampath. The slots on the left and right faces are oriented at the height of source and detector, while a rectangular cutout on the far face permits transit of x-rays to the SBCA. Each slot is typically covered by a polyimide film attached to the frame of the helium box.

First, the prototype system used a motorized translation stage underneath the SBCA to maintain its position on the 1-m Rowland circle while the source and detector positions (and hence Bragg angles) were scanned. In the present instrumentation, a passive linear translation stage with two carriages is used; one carriage for the SBCA and another carriage for a pin located at the moving center of the Rowland circle. Coupling bars with lengths equal to the

radius of the Rowland circle constrain the Rowland-center pin to be the correct distance (0.5 m) from pins underneath both the SBCA and the source location. This direct mechanical coupling provides exceptional scan-to-scan reproducibility and decreases instrument complexity by removing one motorized degree of freedom.

Second, the source and detector stages have been rotated and made much longer than in the earlier system. The longer travel range allows access to Bragg angles between 55 and 85 degrees, a considerable improvement over the prototype that allows a much wider energy range for each crystal orientation of SBCA. This change decreases the total number of SBCA optics required of XAFS and XES analysis. Moreover, it extends the utility of the spectrometer beyond XANES, enabling EXAFS studies for several elements. The stage rotation requires some careful comment. The resulting stage geometry is shown in Fig. 3-1 and the rotation parameter α is defined in Fig. 3-2a. The issue that motivates the rotation of the stages is the desire to minimize the linear travel of the SBCA needed to maintain its position on the (traveling) 1-m Rowland circle. Long SBCA travel is not mechanically onerous, but clearance is required with respect to the helium box (Fig. 3-1b) enclosing the beampath to reduce air absorption. When the SBCA has a long travel, the helium box must be made shorter which results in higher air absorption for most operations. To address this problem, a suitable value of α can be deduced from geometric considerations. As the source and detector are swept outward to smaller Bragg angles, the SBCA is necessarily displaced to ensure the source and detector remain on the Rowland circle. This displacement $d(\theta_B)$ is given by

$$d(\theta_B) = -R * sec[\alpha] * (cos[\theta_o - \alpha] + cos[\alpha + 2\theta_B]), \quad (1)$$

where R is the radius of the Rowland circle, θ_B is the Bragg angle, and the displacement is measured relative to the position of the SBCA when $\theta_B = 85°$, this value is denoted above as θ_o.

In Figure 3-2b, Eq. 1 is plotted as a function of θ_B for various values of α. It is apparent that translation of the SBCA, and consequently attenuation due to air outside of a fixed helium enclosure, can be minimized by an appropriate choice of α. This translation is minimized when the SBCA's travel is symmetric across the angle range, which can be enforced by choosing α to be equal to 180° minus twice the midpoint of the angle range. For a θ_B range of 85° to 55° the SBCA's displacement is minimized when α = 40°, as is utilized in Figure 3-1. Moreover, an additional benefit of the stage rotations is a smaller instrument footprint.

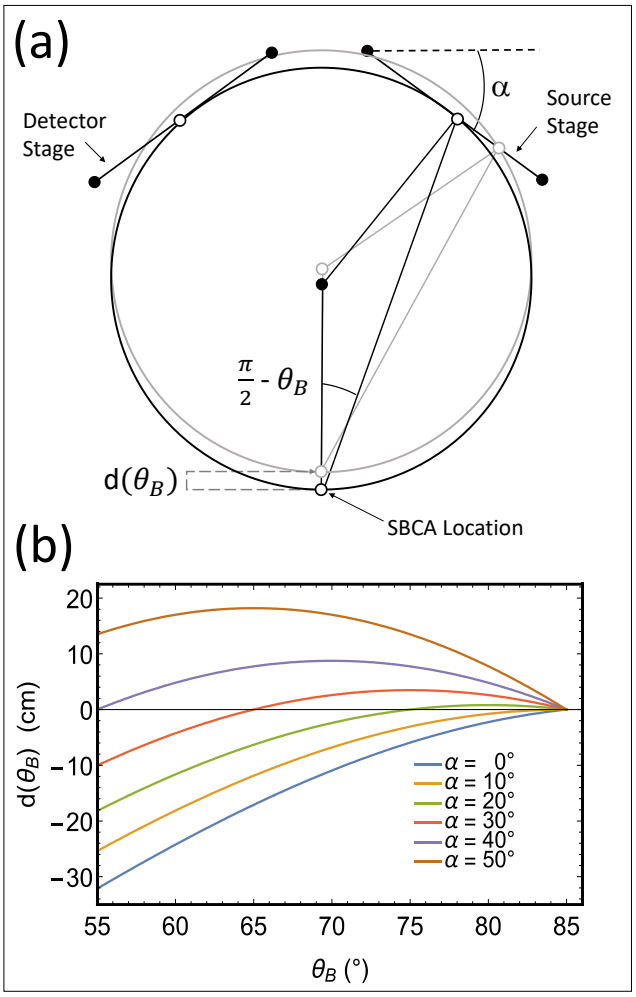

Fig. 3-2: (a) Illustration depicting the parameter α and θ_B. The SBCA resides at the bottom of the Rowland circle while the carriage coupling the SBCA location and the source as represented by the hollow dot is at the center of the Rowland circle. The diagonal line represents the travel range of the source with dots at its end points. (b) The magnitude of the SBCA's displacement from its location, d(θ_B), at $\theta_B = 85°$ is plotted as a function of θ_B for various values of α.

Third, the present design discontinues the traditional two-axis tilt alignment of the SBCA in favor of orienting the crystal miscut into the plane of the source and detector and enforcing a constant angular offset of the detector, as described by Mortensen and Seidler.[39] This removes two motorized degrees of freedom and also enables easy, reproducible exchange of different

SBCAs for different energy ranges. Here, SBCAs are aligned by performing repeated detector scans at different rotations of the optic about its natural cylindrical axis. This fast process gives a permanent alignment orientation. See Fig. 3-3 for representative calibration scans. Note that the highest count rates are generally observed when the crystal miscut is oriented into the Rowland plane, as the SBCA is rotated in either direction away from this orientation, the centroid of the corresponding scans move in the same direction away from the peak at optimal orientation.

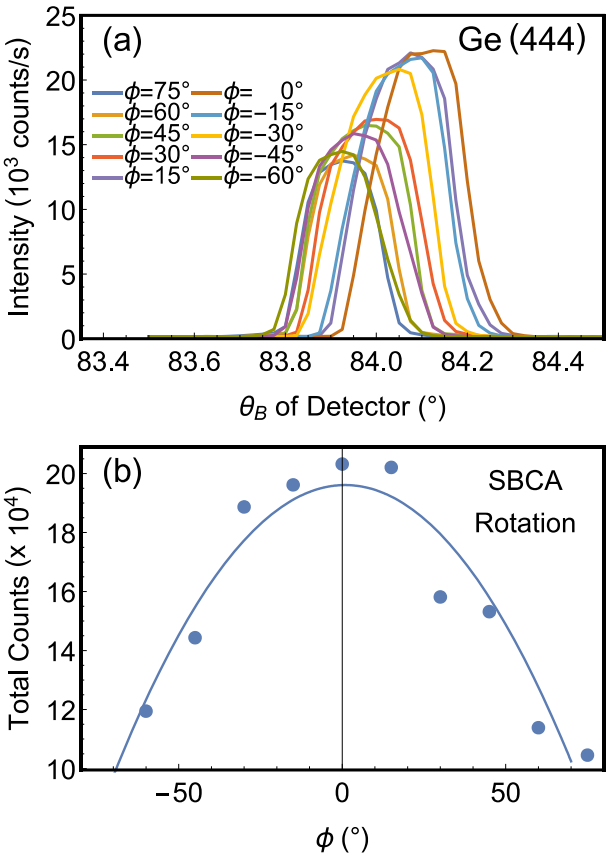

Fig. 3-3: (a) While holding the source fixed at $\theta_B = 84°$, the detector was scanned from 83.5 to 84.5°. Scans were taken at various rotations of the SBCA about its center with the optimum position designated as 0°. Data was taken off the 444 harmonic of a Ge SBCA using a x-ray tube source with a Pd anode operated at 52.5 W tube power. The duration of each scan was approximately 45 seconds. (b) The total number of counts, as integrated over the range from 83.5 to 84.5° for each scan, is shown as a function of the analyzer's angular rotation. The solid line is a quadratic fit.

Fourth, from a practical standpoint, the primary benefit of a high-flux source is shorter acquisition times and thus higher potential instrument throughput. Moreover, greater flux can broaden an instrument's limit-of-detection, thus enabling studies of particularly dilute samples or weak transition lines. Nonetheless, there exist several points of concern when utilizing a high-

powered tube source. Namely, high-powered sources typically increase demands on cooling, require progressively more expensive components and high voltage supplies, and their size typically scales in a nontrivial way with increasing tube power, thus posing a challenge toward integration into the synchronous scanning motif. To balance these considerations, the Varex VF50 and VF80 x-ray tube sources are used in the present instruments. These tube sources operate at 50 and 100 W, respectively, and we use either W or Pd anodes as needed to optimize signal levels or avoid tube-source fluorescence lines. These x-ray tubes have small spot sizes (0.5 – 1 mm) and use a 90-degree take-off geometry giving especially efficient generation of x-ray flux per unit electron beam power. By comparison, the x-ray tubes used in the prototype spectrometer[13] were 5-12 W total power and used transmission-geometry anodes with ~3x lower efficiency per unit electron beam power due to absorption during transit through the anode material itself.

Fifth, the high voltage supplies (Spellman uX at LANL and both uX and uXHP at UW) are factory customized to not exceed 35 kV accelerating potential. Since the tube can still be operated at maximum power at these accelerating potentials, this has little effect on the final flux generated at useful energies but has the considerable advantage that the radiation enclosure can then be made from 3.175 mm steel. The new radiation enclosure is a welded steel box with two gas-spring loaded top-facing doors for access to the spectrometer. Two labyrinths provide pass-throughs for cables and gas flow lines.

Finally, at UW the same silicon drift detector (Amptek X-123 SDD) is used as in the prototype spectrometer, while a PIN diode is used in the spectrometer at LANL (Amptek X-123 Si-PIN). Here, however, the ~4-mm active height of each detector does prove somewhat limiting. As θ_B deviates strongly from backscatter (decreasing θ_B) the height of the refocused

beam on the detector quickly becomes taller than the active height of the detector, resulting in significant inefficiency. As discussed below, and in more detail in an upcoming manuscript,[41] this can be ameliorated by incorporation of a taller SDD or by use of a toroidal curved crystal analyzer that is tailored to the Bragg angle range of interest.

b. Sample Preparation Details

In the results and discussion below, we present numerous studies of both XAFS and XES for a wide range of materials. In this subsection we briefly summarize the preparation or provenance of each system.

CeO_2 was prepared by thermal decomposition of cerium (IV) oxalate, $Ce(C_2O_4)_2 \cdot xH_2O$ at 800 °C, for 1h, in air, as described by Stennett *et al.*[42] $CePO_4$ (with the monazite structure) was prepared by solid state reaction of stoichiometric quantities of CeO_2 and $NH_4H_2PO_4$: an intimate mixture of these reagents, prepared by hand grinding with a mortar and pestle, was heated at 1100 °C, for 8h, in air. Analysis of the products by powder X-ray diffraction confirmed the synthesis of single phase materials. Specimens were prepared for XAS analysis by sieving to less than 63 μm before mixing with polyethylene glycol and pressing into 13-mm diameter pellets having suitable μx for transmission-mode study.

ε-$VOPO_4$ investigated in the present study was prepared by hydrothermal synthesis.[43] Thin laminates for XAS investigation were prepared by mixing ε-$VOPO_4$ powder with graphene and polyvinylidene fluorine (PVDF) as binder in a weight ratio 75:15:10 using 1-methyl-2-pyrrolidinine (NMP) as the solvent. The resultant slurry was tape cast onto an aluminum foil and dried in air at 60 °C. Circular discs of about 13mm diameter were punched out of the coated aluminum foil and sealed between the adhesive-coated Kapton tapes.

Commercial nickel- manganese- cobalt- (NMC) oxide battery cathode laminates were manufactured in a 6:2:2 stoichiometric ratio between the transition metals. The cathode laminate was cast with a 5 wt % PVDF binder and carbon on a 10 µm thick aluminum current collector. Laminates were prepared in two states of charge, a pristine uncharged laminate and a charged laminate harvested from a coin cell. The latter was sealed in an aluminum-coated polyimide envelope during measurement to reduce interaction with air.

Uranium(IV) hexachloride, $(PPh_4)_2UCl_6$, was prepared as previously described.[44] Uranyl tetrachloride was prepared in a modified version of previous syntheses.[45-46] This involved addition of two equivalents of tetramethyl ammonium chloride (NMe_4Cl) to UO_2^{2+} in concentrated hydrochloric acid (HCl, 12 M). Within 1 week crystals formed and the compounds identity was then confirmed by single crystal X-ray diffraction.

Caution! *^{238}U is a low specific-activity (half-life 4.4 billion years) a-emitter, which is hazardous to human health. This type of research should only be performed in a facility equipped with appropriate controls for the safe handling of radioactive materials.*

Samples were prepared by grinding the $(PPh_4)_2UCl_6$ (20 mg) with boron nitride (BN, 40 mg) for two minutes. An aluminum spacer with interior dimensions 1 mm x 5 mm x 20 mm was filled with the resulting powder and sealed in two layers of polyimide tape.

Finally, metal foils were acquired from EXAFS Materials. These include a 6 µm Ni foil, a 5 µm V foil, a -400 mesh Mn foil, and a 25 µm Y foil. Also, the V_2O_3, VO_2, V_2O_5, $NaAsO_2$, and $Na_2HAsO_4{\cdot}7H_2O$ powders measured in XES were purchased from commercial vendors.

c. Synchrotron XAS Measurement Details

XAS measurements of ε-VOPO4 were carried out at the beamline 9-BM of Advanced Photon Source (APS) in USA. Data were collected in the transmission mode at the V K-edge

using the Si (111) double-crystal monochromator, which was slightly detuned to suppress higher harmonics. Absolute energy calibration of the monochromator was carried out by measuring the reference foil of pure V simultaneously with the sample. Intensities of the incident beam and the beams transmitted through the sample and the reference foil were recorded using the gas-filled ionization chambers. All spectra were energy-calibrated with respect to the first peak in the derivative spectrum of pure V. Data processing operations were carried out using ATHENA.[47]

Ce L_3 edge XAS data of CeO_2 and $CePO_4$ (with the monazite structure) were acquired on beamline X23A2 of the National Synchrotron Light Source (NSLS), Brookhaven National Laboratory (BNL), USA. The experimental configuration and details described in Hyatt et al.[48] were repeated for the present study. Here, the data were acquired in transmission mode using finely ground specimens dispersed in polyethylene glycol (PEG) to achieve a thickness of one absorption length. 0.5 eV steps were used over the absorption edge with a dwell time of 5 seconds per point.

The U L_3 XANES spectra were measured at the Stanford Synchrotron Radiation Lightsource (SSRL) on end station 11-2 according to the methods of Pattenaude et al.[49] This includes the use of a double-crystal Si (220) monochromator, along with collimating and focusing mirrors, on a 26-pole, 2.0 tesla wiggler.

3. XAFS and EXAFS Results and Discussion

a. Basic Instrument Performance

The present instrumentation was evaluated according to several performance criteria, including typical count rates. In Figure 3-4, the intensity of the incident beam in an absorption configuration was measured across the full angular range of the instrument. Near backscatter (θ_B = 90 °), count rates near 50,000/s are observed at 100 W x-ray tube power with the Pd anode

(this and all subsequent measurements were performed at 35 kV accelerating potential), yet the count rate quickly drops to around 15 % of this value at especially low Bragg angles. The reason for this decline is the limited size of the detector. In the present design, x-rays are refocused to a line at the detector due to sagittal error. The height of this line increases as the source and detector travel to lower Bragg angles and only a portion of this line is measured as permitted by the finite size of the detector. The decline in count rates observed in Figure 3-4 is consistent with ray tracing simulations reported elsewhere.[41] If a larger detector or toroidal optic is integrated into the design, consistent count rates could be observed across the instrument's angular range.[41]

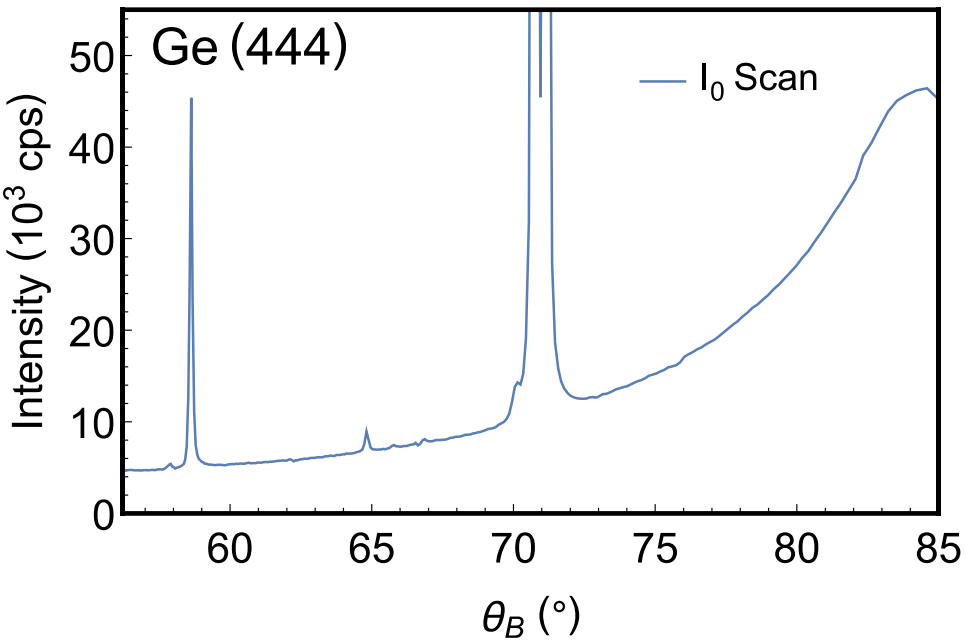

Fig. 3-4: An I_0 scan spanning the entire range of the instrument. Data was collected using the 444 harmonic of a Ge SBCA. An x-ray tube source with a Pd anode was operated at 100 W power. Fluorescence lines can be seen from Cu Kα and Kβ lines as well as a small W line around 8400 eV. This last line is likely due to some small number of W atoms from the filament being deposited onto the surface of the target anode as has been discussed elsewhere.[31]

The spectrometer's reliability was assessed according to its scan-to-scan reproducibility. Figure 3-5 shows a series of consecutive scans collected in a transmission mode XANES configuration across the Mn K-edge of the Mn foil. Also shown is the residual of each scan with respect to the first and an envelope of two standard deviations as calculated from the incident flux by Poisson statistics. The residuals are well captured by Poisson statistics.

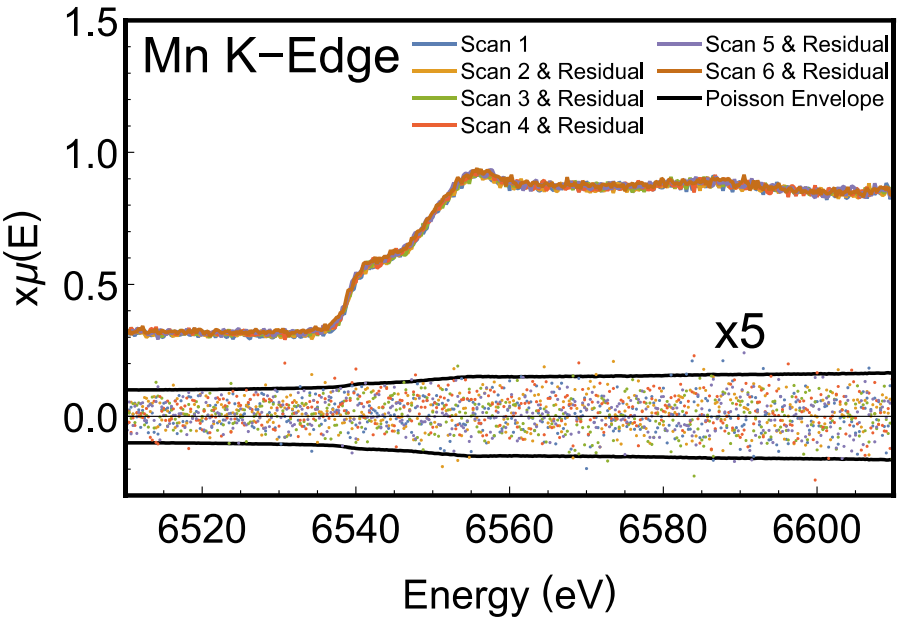

Fig. 3-5: Six consecutive scans are shown of a transmission mode measurement across the K-edge of the Mn foil. Measurements were collected using a Si (440) SBCA. An x-ray tube source with a W anode was operated at 25 W with a 10 μm thick Zn foil acting as an absorber to suppress the W fluorescence line observed on the Si (660) harmonic in accordance with methods previously reported, although done here without a slit system.[50] The residuals between subsequent scans are shown at the bottom of the figure (magnified five times) with a Poisson envelope enclosing two standard deviations.

The monochromator performs well in a final, critical performance metric, its energy resolution. This parameter was assessed by measuring the XANES spectrum of a V metal foil. From Figure 3-6a, the laboratory-based instrumentation produces spectra nearly identical to those acquired at the synchrotron, however, minor changes in resolution can be observed by magnifying the especially sharp pre-edge feature found in this system. Convolving the synchrotron spectrum with a 0.4 eV FWHM Gaussian yields excellent agreement with the first set of laboratory-based measurements. One contribution to the broadening is that although the V

K-edge is located at a Bragg angle of 79.2 ° for the Ge (422) optic, the spectrum will still exhibit some broadening due to Johann error. To investigate this effect, the outer portion of the SBCA was blocked with a Pb mask to produce a spectrum that is now broadened by only 0.2 eV relative to the spectrum reported by NSLS X23A2. Although the critical metric for extracting scientific inference is the ability to resolve spectral features and not any quoted energy resolution, the question of absolute energy resolution, both for XAFS and for XES, deserves special mention.

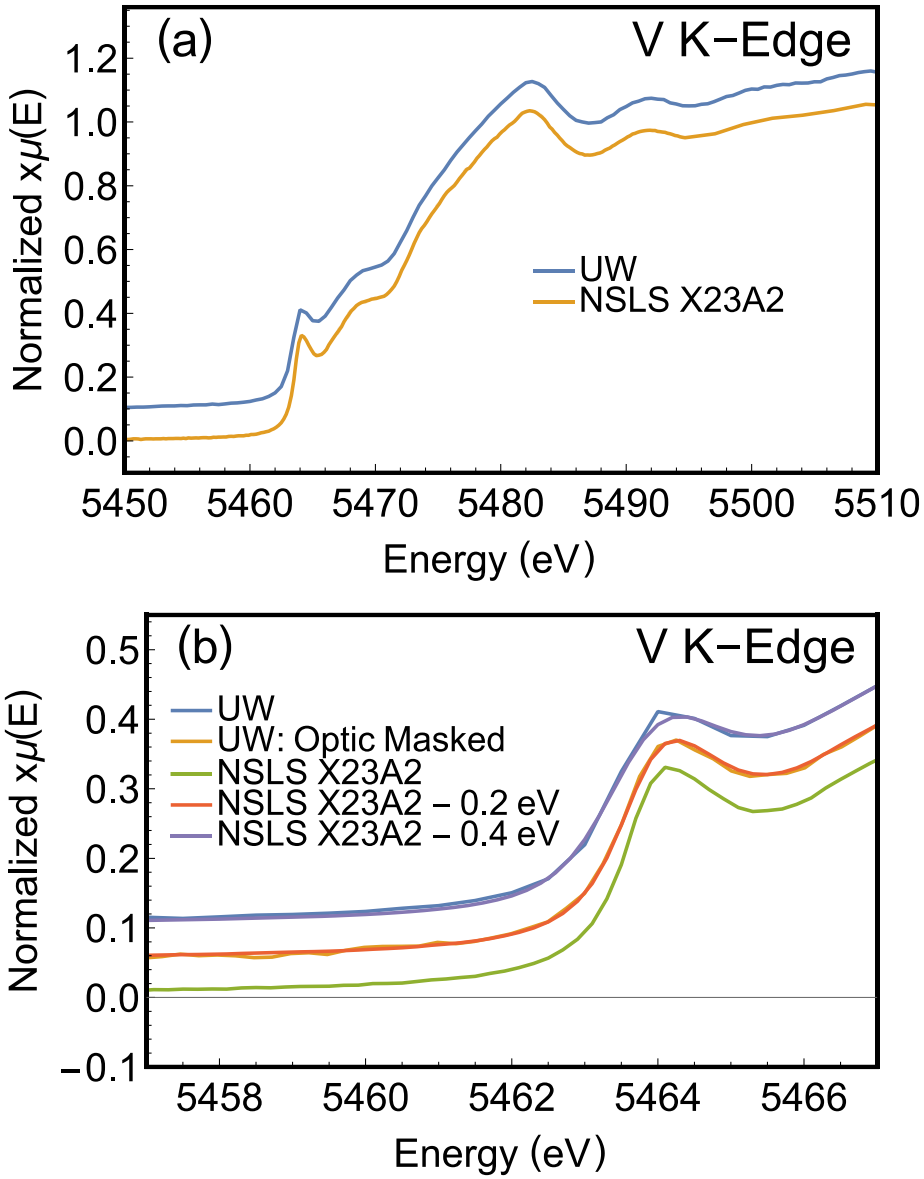

Fig. 3-6: (a) XANES spectra of the V foil collected using an x-ray tube source with a W anode and operated at 50 W power. Comparison was made to synchrotron results and offset for clarity, see the text for discussion. (b) An enlarged view of the pre-edge feature at ~5464 eV including comparison with synchrotron results with the indicated Gaussian broadening. Laboratory-based measurements used either a masked or unmasked Ge (422) SBCA. Spectra are offset for clarity.

Three primary factors dictate the present instrument's energy resolution. First, the intrinsic energy resolution of the non-strain-relieved SBCA at the energy of interest is

approximately 0.3 eV based on the results of Hämäläinen et al.,[51-52] which are consistent with those of Rovezzi et al. in the 6 - 11 keV energy range.[53] Second, the use of a Johann analyzer yields an energy broadening of at most 0.25 eV in the present case,[54-56] however, the severity of this error will increase at lower Bragg angles. Third, the source size in the Rowland plane gives a purely geometric energy broadening which can be calculated from the differential form of Bragg's law.[53, 56] While this is usually set for the XAFS configuration by the 1-mm x-ray source spot size (upper bound), we note that our implementation of an entrance slit on the source side provides a means to tune this aberration.[38] Yet in the present scenario, this geometric factor contributes a maximum broadening of 1 eV. From the work of Bergmann and Cramer,[56] we can see that other geometric sources of broadening are negligible here and report a conservatively estimated nominal absolute energy resolution of 1.1 eV.

b. XAFS Demonstration Studies

Here, we present the results of several XAFS studies using the lab spectrometer. These include XANES of battery materials, lanthanide and actinide compounds and also EXAFS of reference metal foils. The times for scan acquisitions of all demonstration studies are summarized in Table 3-1. Taken *en masse*, the results strongly support the usefulness of the lab spectrometer for a very wide range of concentrated systems where transmission-mode studies are possible. We begin with XANES.

Table 3-1: Experimental details of XES and XAFS measurements performed in this work. Acquisition times spanning multiple compounds refer to the time allotted to each sample. Acquisition times reported in this table only includes the time required to span the energy range shown in the corresponding figure. XAFS acquisition times are reported only for the transmission scans.

Figure #	Anode	Power (W)	SBCA	Compound	Measurement	Acquisition Time (h)
7a	W	50	Ge (422)	ε-$VOPO_4$	XANES	3.0
7b	Pd	50	Si (444)	NMC	XANES	0.22
7c	W	50	Si (444)	NMC	XES K$\beta_{1,3}$	0.06
8a	W	50	Si (422)	CeO_2	XANES	1.0
				$CePO_4$		
8b	Pd	50	Si (12,6,6)	$(PPh_4)_2UCl_6$	XANES	44
9	Pd	100	Si (551)	Ni	EXAFS	6.9
10a	W	50	Ge (422)	ε-$VOPO_4$	XES Kβ	12.4
				V		
				V_2O_3		
				VO_2		
				V_2O_5		
10b	W	50	Ge (422)	V_2O_3	XES K$\beta_{1,3}$	4.5
				VO_2		
				V_2O_5		
11	Pd	100	Ge (555)	Zn	XES K$\beta_{2,5}$	9.6
				ZnO		8.0
				$ZnCl_2$		11.5
12a	W	50	Si (555)	$NaAsO_2$	XES Kα	1.4
				$Na_2HASO_4{\cdot}7H_2O$		0.8
12b	Pd	50	Si (12,6,6)	$(PPh_4)_2UCl_6$	XES Lβ	30
				$TBA_2UO_2Cl_4$		24

First, electrical energy storage is a particularly promising application for laboratory-based x-ray spectroscopies.[57-60] Here, XANES is already established as a useful tool for the study of electronic properties at various levels of detail. For example, a routine approach utilizes XANES to assess the redox reversibility of battery materials during cycling.[61] Similarly, many examples

exist of x-ray spectroscopies addressing more complex speciation inquiries, including lithiation dynamics in nickel cobalt aluminum oxide cathode materials,[62] discernment of the soluble Mn ion in a Li-Mn spinel electrode,[4] and evaluation of sulfide precipitation and under-utilization of active material as competing hypotheses for sub-optimal capacities in lithium sulfur batteries.[3]

Several other factors suggest lithium ion battery (LIB) cathode materials as an ideal system for laboratory-based x-ray instrumentation. Most importantly, the typical thickness of the metal oxide layer found on a cathode frequently gives edge steps $\Delta\mu \cdot x \sim 1-2$, as is desirable for XAS studies.[63] Also, the electrochemically active elements in modern LIB cathodes are often 3*d* transition metals, for which the K-edges are at energies high enough so that some air attenuation can be tolerated but low enough that the SBCA and other Bragg-based analyzers still have good efficiency.

The XANES spectra of two archetypal Li-ion battery materials, ε-$VOPO_4$ and NMC oxide laminates, are presented in Fig. 3-7a and Fig. 3-7b. The agreement between lab-based and synchrotron spectra in Fig. 3-7a is excellent, including the details of the pre-edge feature which is important for elucidating the molecular symmetry at the metal center.[64] Figure 3-7b presents NMC electrodes at two different states of charge. The charged and uncharged laminates exhibit multiple differences, including a pronounced shift in the edge position of the two systems. Such an edge shift is traditionally attributed to a change in oxidation state[65] and, in the present case, confirms the instrument's capability for element-specific tracking of redox behavior in cathode materials.

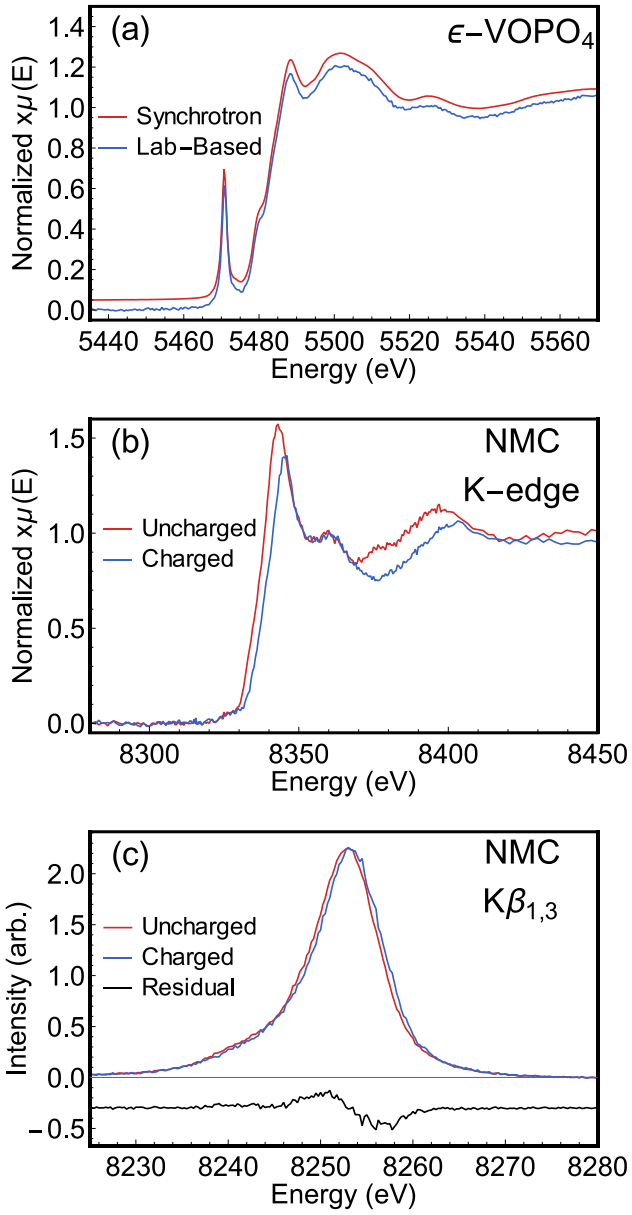

Fig. 3-7: (a) The V K-edge XANES spectra of a vanadyl phosphate-based battery laminate. Spectra were acquired with the present instrumentation (Lab-Based) and at APS 9-BM (Synchrotron). The spectra are offset for clarity of presentation. The full range of scans was chosen to extend from 5390 eV out to 10 $\mathbf{Å^{-1}}$ to ensure proper normalization and background removal for comparison to the synchrotron. (b) XANES spectra of uncharged and charged battery laminates of NMC composition. Data was again acquired out to 10 $\mathbf{Å^{-1}}$ and data was collected at lower energies to aid background removal. (c) XES spectra of a charged and

uncharged NMC laminate. The residual of the two spectra is displaced below the main results. Peak count rates were around 12,000 counts per second for the uncharged laminate and 6,000 for the charged laminate.

Moving away from the 3d transition metals, it is useful to next discuss lanthanide compounds. The L3-edges of the lanthanides are in a very similar energy range as the 3d transition metals, strongly suggesting good performance for our system, and there exists a large body of research using the dependence of XAFS spectral features on the speciation of lanthanide compounds.[66-68] Sample applications include high temperature, *in situ* analysis of: ceria-based oxide materials used in the activation and storage of oxygen,[69] the effect of annealing temperature on the valence state of cerium oxide nanoparticles manufactured to catalyze the oxidation of organic compounds or reduction of heavy metals in industrial waste streams,[70] and the mechanism by which cerium-containing films inhibit the corrosion of aluminum.[71]

XANES spectra of $CePO_4$ and CeO_2 taken in the lab are presented in Fig. 3-8a. The lab-based spectra are energy corrected by alignment with the reference cerium dioxide spectrum found in Hephaestus.[47] In particular, note that Poisson errors observed in Fig. 3-8a are far from eclipsing the shape of spectral features and that scan acquisition times, just as with the above transition metal study, are reasonable for many applications involving routine analytical characterization. This is true throughout the energy range from 6 keV to as high as the actinide L_3 edges at and above 17 keV, as we now show. The difference in height of the CeO_2 near-edge peak may be due to different preparation of the samples, as oxygen deficiency can commonly influence that feature.

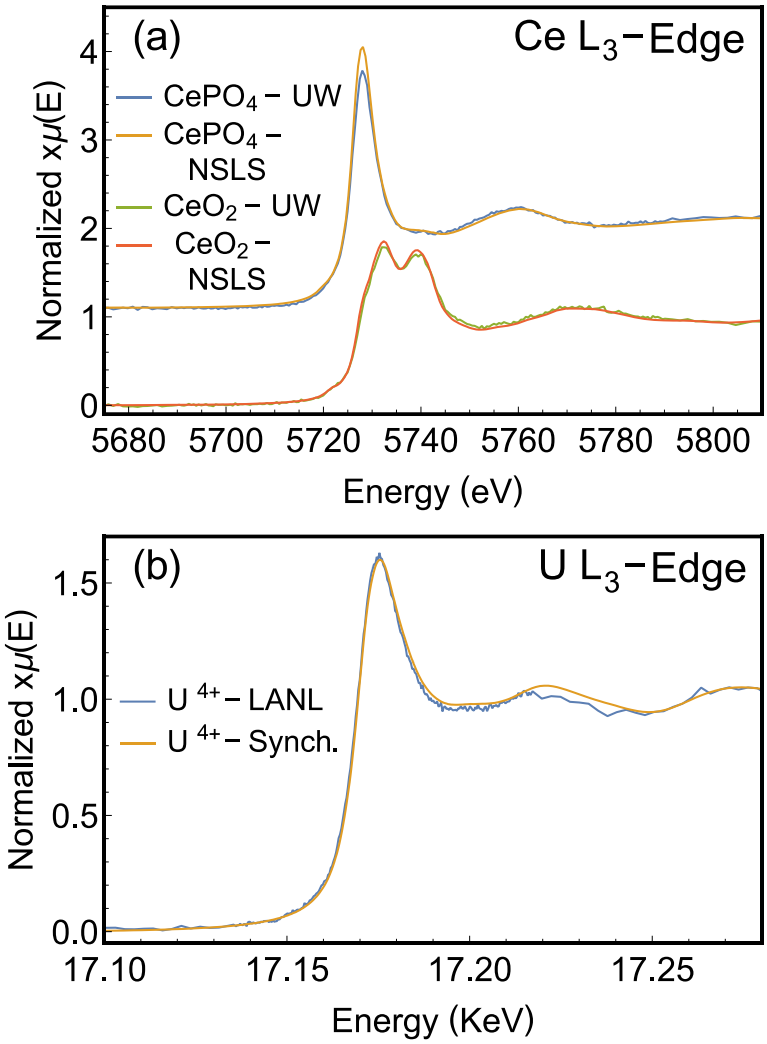

Fig. 3-8: (a) XANES spectra of $CePO_4$ and CeO_2, representative Ce^{3+} and Ce^{4+} compounds, respectively. Reference spectra were acquired on beamline X23-A2 of the National Synchrotron Light Source (NSLS). (b) Comparison of synchrotron (endstation 11-2 at SSRL) and lab-based U L_3-edge XANES for $(PPh_4)_2UCl_6$, a U^{4+} reference compound. Data was calibrated to the maximum of the first derivative of the K-edge spectrum of a yttrium foil at 17038.4 eV.

Next, we address the high-energy range for applications of the laboratory spectrometer. While the present instrument design is not optimal for operation at 17 keV and beyond, it has proven quite effective. U L_3-edge XANES spectra for $(PPh_4)_2UCl_6$ is presented in Fig. 3-8b and directly compared to a synchrotron-based measurement. These measurements used the older, 50

W x-ray tube in the spectrometer at LANL. Clearly, U L_3 XANES can be measured in useful study times with our spectrometer; comparable results with a spectrometer of similar design have recently been reported by Bès, *et al.*[72]

The decreased performance of the lab spectrometers at high photon energy is due to limitations in the source, Bragg optic, and detector. The bremsstrahlung spectrum from the tube has the usual $\sim 1/E$ roll-off at high energy. This is complicated here, however, by our choice to hardware-limit the high-voltage supply to 35 kV, resulting in somewhat less proportional generation of ~17 keV photons than would be the case with a higher accelerating potential and the same total electron beam power. Combined with the narrower Darwin width of the SBCA for higher order reflections, the integral reflectivity is greatly decreased at higher photon energy.[73] There are some studies of higher-energy XAFS using laboratory-based instruments having Laue-style analyzers where the optic has much higher integral reflectivity from lower-order reflections, but where the effective solid angle is typically much reduced.[34, 74] The present detector also limits the efficiency for two reasons: it has only ~50 % quantum efficiency at these energies, and the active region of the detector used in the actinide study was only ~5-mm tall, so that ~2x flux was lost because of the vertical extent of the beam. Hence, the corresponding obvious upgrades to a 100-W x-ray tube and a taller detector with higher quantum efficiency will yield ~8x improved count rates on the same monochromator. The question of optimum lab-spectrometer design for high-energy XANES is very much an open question that could have high impact in heavy element chemistry (via L-edges) and 4*d*-chemistry (via K-edges).

The above studies demonstrate the broad versatility of the lab-based system for XANES studies. The extended oscillations pose a more stringent challenge, due to both the limitations

imposed by Poisson statistics and the requirement of correct monochromator function over a wider energy range.

Face-centered cubic, metallic nickel was chosen as a model system to assess the present instrument's EXAFS capabilities relative to a synchrotron. The forward Fourier transform of Ni's EXAFS spectrum was performed for photoelectron momentum up to $k = 12$ **Å^{-1}**. An isotropic expansion model was used for both systems and distinct Debye-Waller (DW) factors were assigned to the single scattering path associated with each neighboring atom. DW factors for collinear paths were calculated in the manner of Hudson *et al.*[75] while triangular paths were approximated from the single scattering path's DW factors. Fits were performed in Artemis[47] from R=1 to R=5.5 Å and included all scattering paths in that range. Resulting R-factors reveal the spectra to be well described by the fitted model. Similarly, the passive reduction factor, which is subject to inconsistencies according to individual beamline characteristics,[76] is within the range of values typically reported for robust fits. In Figure 3-9, excellent agreement is found between the lab and synchrotron-based measurements, as well as between experimental results and fitted models. Likewise, the physical quantities produced by the EXAFS fits are presented in Table 3-2, revealing excellent agreement between data acquired at different instruments and with previously reported values.

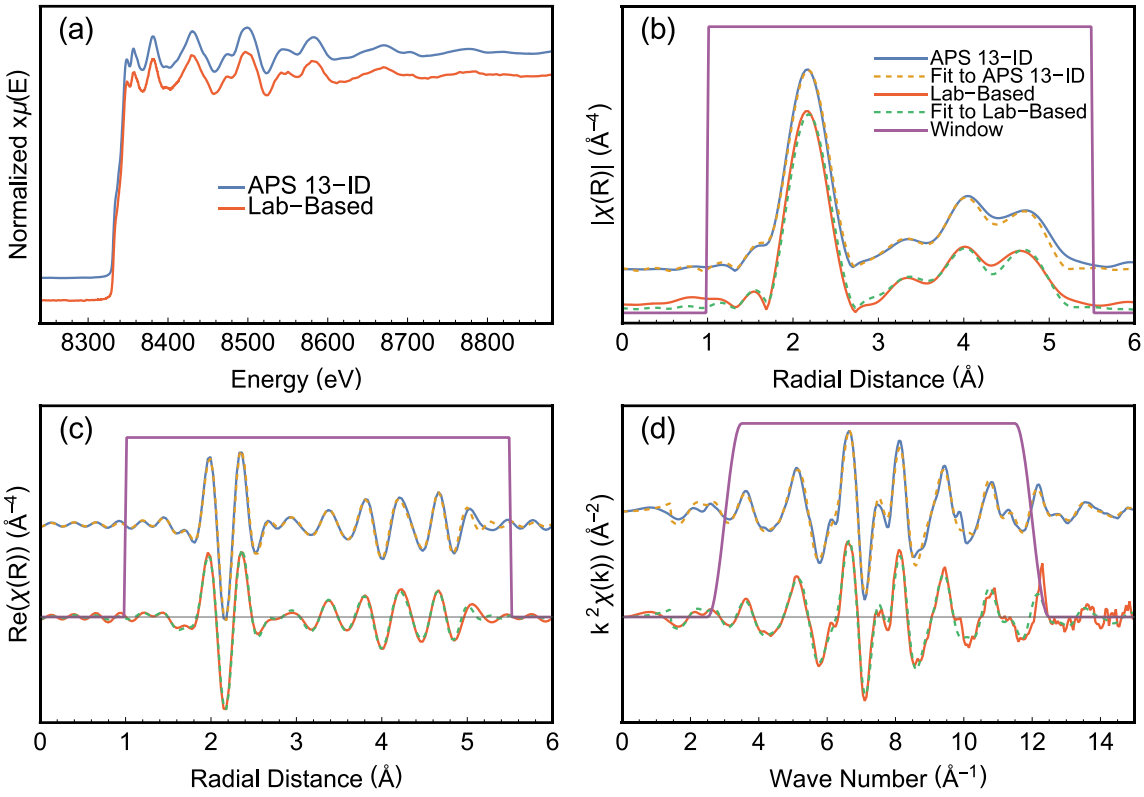

Fig. 3-9: EXAFS of Ni Foil collected at UW (Lab-based) compared to synchrotron results (APS 13-ID). Results are shown in energy space (a), along with the magnitude of the EXAFS in radial space (b), the real part of the EXAFS in radial space (c), and the EXAFS with quadratic weighting in k-space (d), respectively. Also shown are the fitted models acquired from Artemis.[47] Data was collected using 100 W power for a Pd anode x-ray tube and using a Si (551) SBCA. Measurement times were 1.7 and 6.9 h for I_0 and I_T, respectively.

Table 3-2: Selected EXAFS fitting parameters for Ni foil measured at APS and at UW as compared to literature fits, x-ray diffraction (XRD), and neutron PDF analysis. Uncertainties correspond to one standard deviation.

			Shell1		Shell2		Shell3		Shell4	
	S_o^2	R-factor	Ni-Ni (Å)	σ^2 (10^{-4} Å^2)	Ni-Ni (Å)	σ^2 (10^{-4} Å^2)	Ni-Ni (Å)	σ^2 (10^{-4} Å^2)	Ni-Ni (Å)	σ^2 (10^{-4} Å^2)
XRD[77]			2.4863		3.5161		4.3063		4.9725	
Neutron PDF[78]			2.487 (1)	64 ± 1						
XAFS Lit.[79]			2.493 (2)	65 ± 2						
XAFS Lit.[78]	0.84 (2)		2.485 (2)	64 ± 2						
APS 13-ID[47]	0.90 (6)	0.015	2.493 (4)	67 ± 6	3.525 (5)	96 ± 19	4.317 (6)	91 ± 10	4.985 (7)	79 ± 8
UW	0.81 (6)	0.016	2.490 (4)	61 ± 6	3.522 (5)	76 ± 16	4.314 (7)	92 ± 11	4.981 (8)	79 ± 9

c. XES Demonstration Studies

X-ray emission spectroscopy (XES) is seeing rapid growth as both a complement to XANES and as an emergent technique in its own right. Its sensitivity to the occupied local electronic density of states can often aid in assessing the oxidation state, spin state, covalency, state of protonation, or ligand environment of a given metal atom.[80-82]

From an experimental perspective, XES benefits from several pragmatic advantages in the laboratory environment. While the simpler sample preparation for XES than for transmission-mode XAFS is often relevant, the dominant issue is the efficient use of the incident x-ray flux. Conventional x-ray tubes are inherently broadband, showing a few strong fluorescence lines on top of a bremsstrahlung background. Monochromatizing the raw tube spectrum with a crystal analyzer selects only a modest solid angle of the total tube emission and

also a tiny slice of the entire tube energy spectrum, decreasing broadband, wide-angle fluxes of ~10^{13} /s or more to only $10^4 - 10^5$/s. However, direct illumination of the sample, as in non-resonant XES, utilizes a large solid angle and makes every incident photon above the relevant binding energy capable of stimulating the creation of a core-hole. Accordingly, a recent publication by the authors demonstrated lab-based XES measurements as a viable route to quantitatively assess metal speciation even in very dilute systems,[40] even with the very low powered x-ray tube of the earlier prototype spectrometer.[13]

Here, we present the results of several XES studies using the lab spectrometer. Thematically, the XES results are presented from lowest to highest energy emission lines. This begins with an overview of the Kβ lines for a collection of vanadium compounds including metallic vanadium, a suite of vanadium oxides, and vanadyl phosphate, a candidate material for energy storage applications. Similarly, routine valence-to-core (VTC) XES measurements of assorted zinc compounds sampling a variety of ligand environments are discussed. Next, arsenic Kα XES results suggest the potential of the present instrumentation for speciation studies of dilute environmental samples. Finally, less standard measurements of actinide L emission lines are presented. Note that, again, the acquisition times for all studies are summarized in Table 3-1 and repeated in the figure captions.

First, a range of chemical information is accessible in the V Kβ spectra in Fig. 3-10a. For example, note that the wide-energy range accessible by a single scan permits careful branching ratio studies of vanadium oxide $K\beta_{1,3}$ and $K\beta_{2,5}$ features which, as can be seen in Fig. 3-10a, are exceedingly well resolved. An additional advantage of this range is the feasibility of robustly subtracting the tail of the main Kβ emission from the VTC region to aid the analysis of the latter. Furthermore, Fig. 3-10b shows the $K\beta_{1,3}$ of a variety of vanadium oxide moieties, with a clear

evolution in the spectrum as oxidation state changes. Likewise, the Kβ', which is split from the $K\beta_{1,3}$ by (3p,3d) exchange, can be seen to vary in intensity across the oxides. For transition metals, the intensity of this feature often correlates with the number of unpaired 3*d* electrons and thus provides a measure of the spin state of the probed atom. For some systems, the dependence of the $K\beta_{1,3}$ emission's energy on oxidation state can be muted, as is the case for Ni oxides.[83-84] However, it can be seen in Fig. 3-7c that there is a small but measurable shift between the $K\beta_{1,3}$ XES of two NMC laminates at different states of charge. These spectra are also intense, allowing acquisition times on the order of minutes.

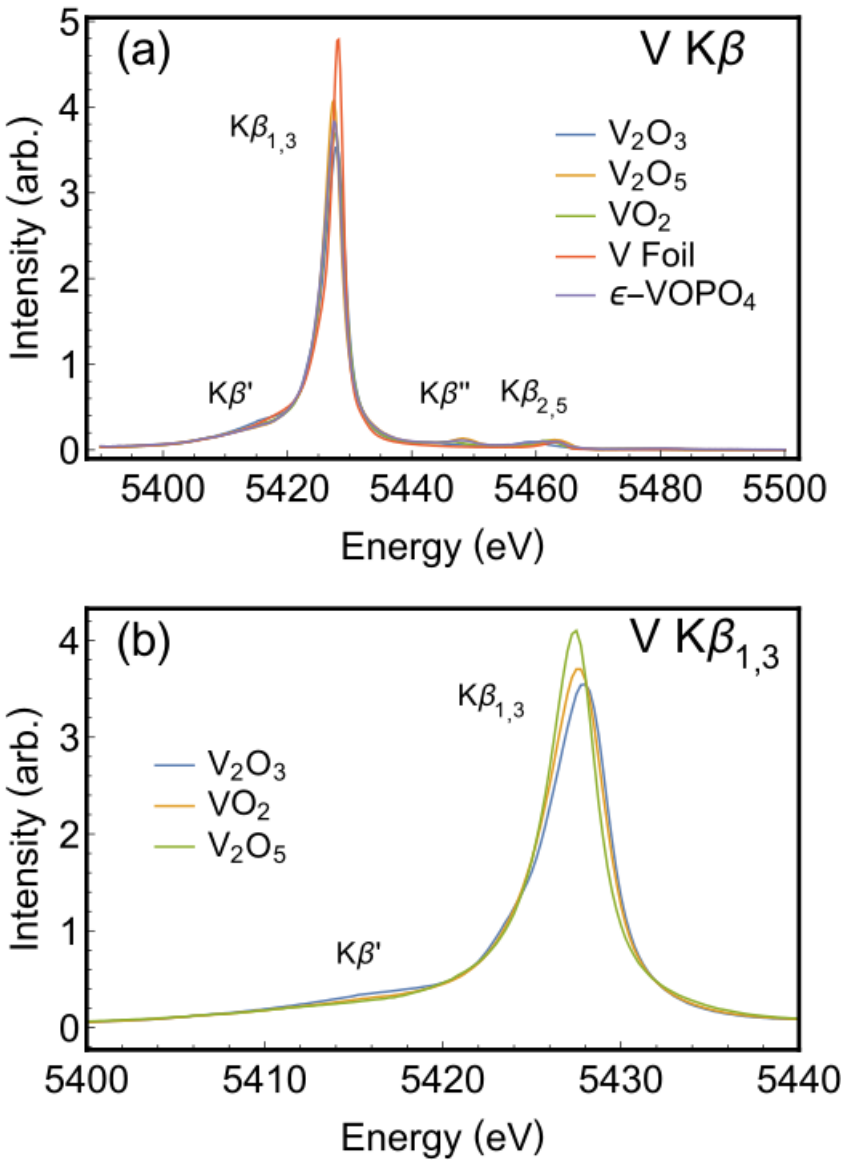

Fig. 3-10: (a) The full range of V Kβ XES from a collection of V compounds measured in the lab spectrometer. Measurement times were 12.4 h for all samples. Note that the vanadyl phosphate data represents three scan ranges, with the main scans spanning 5395 eV to 5485 eV, this range was joined with supplemental data sets to span the entire range shown and permit equivalent background subtractions for all systems. (b) V $K\beta_{1,3}$ XES from a suite of oxides measured in the lab spectrometer.

The VTC region for some Zn compounds is presented in Fig. 3-11. The significance of this region warrants some discussion. In recent years, VTC-XES has emerged as a highly useful tool for the interrogation of a system's local electronic structure. This method permits a direct probe of the orbitals involved in chemical bonding, and, as a result, is highly-sensitive to changes in oxidation state, covalency, state of protonation, and coordination environment. As a unique case in point, VTC-XES is sometimes able to discern which of several light elements is ligated to a central metal atom, with considerable impact. In 2002, Einsle *et al.* reported the presence of carbon, oxygen, or nitrogen as a central atom in iron-molybdenum cofactor (FeMoco), a cluster which acts as the active site of substrate binding and reduction in nitrogenase.[85] Despite intense study, the identity of this atom could not be unambiguously established until the Fe VTC-XES study of Lancaster and co-workers.[86] Likewise, the utility of this method has, on numerous occasions, been evidenced in recent catalysis research. For example, Pushkar *et al.* demonstrated the feasibility of VTC-XES for detecting and probing the oxo bridges found in the Mn_4Ca cluster of photosystem II, establishing a powerful tool for studying the O-O bond formation preceding O_2 evolution.[87] Due to its increasing popularity, much research has been conducted to develop the theoretical underpinnings of VTC-XES and to identify spectral features that can serve as measures of various chemical parameters. For example, a recent article by Pollock, *et al.*,[88] identifies a feature in the VTC-XES spectra of several Fe-N_2 complexes that can be attributed to a transition from the 2s2s σ^* antibonding-orbital to the 1s core-hole. The energy of this feature is then related to the N-N bond length and serves as a measure of the degree of activation of small molecules during catalytic reduction.[88] Finally, several review articles can be found that discuss VTC-XES in various levels of detail.[80-81, 89]

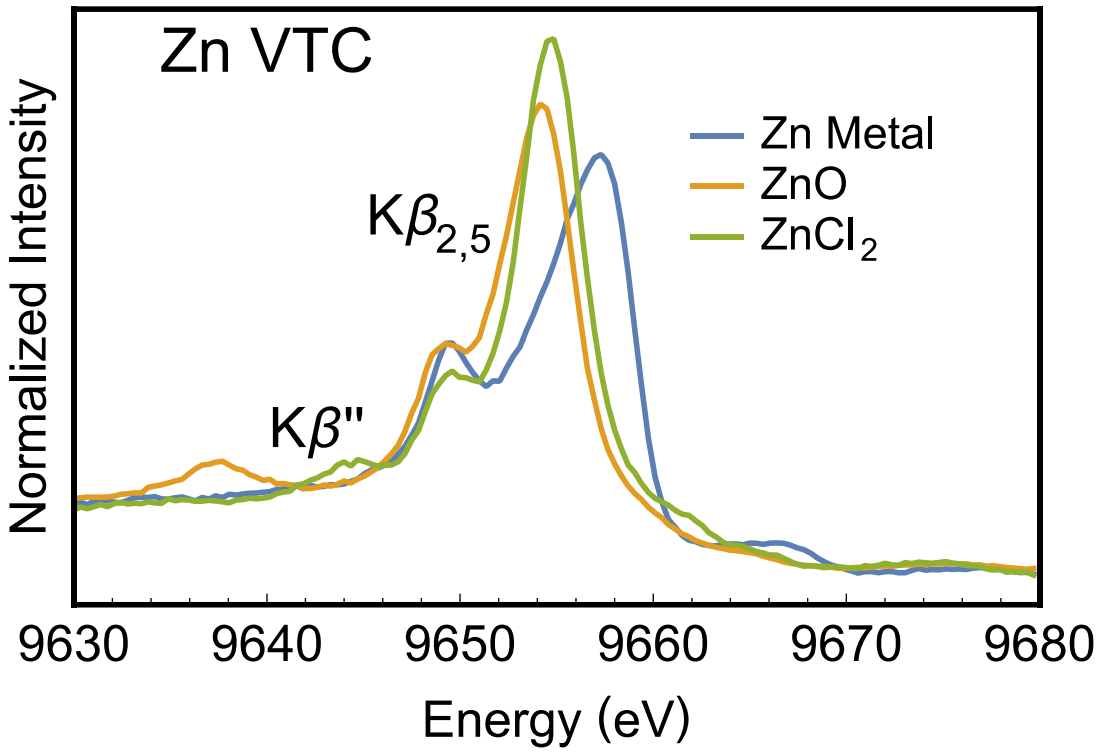

Fig. 3-11: VTC-XES spectra of Zn metal, ZnO, and $ZnCl_2$ after background subtraction and integral normalization across the full VTC energy range.

Here, a system of Zn compounds comprised of Zn metal, ZnO, and $ZnCl_2$ was chosen to reflect the feasibility of VTC-XES measurements with the present instrumentation along with its sensitivity to a variety of ligand environments. A similar study using an earlier, lower powered instrument investigated similar compounds and made a critical comparison across several theoretical treatments of VTC-XES.[37] Despite the present instrument's increase in flux, background removal only required the subtraction of a constant as determined by the measured intensity at the highest energies sampled and typically five percent or less of the peak intensity in the VTC region. As can be seen in Fig. 3-11, the present instrumental resolution also clearly resolves the double-peak structure of the $K\beta_{2,5}$ lines. In addition, the Kβ'' transitions indicative of the ligand environment are clearly discernible for the oxide and chloride systems, with the former ~17 eV below the main peak, in rough agreement with values reported elsewhere for the

relative Kβ'' position.[90] Finally, the non-resonant excitation process utilized with a broadband source again gives rise to multielectron features that can be observed toward high energies in the spectrum of metallic zinc. We note that similar XES features have been reported for other sample matrices elsewhere.[35, 91-92] However, it is interesting to note that while multielectron features were largely suppressed in the ligated Zn-compounds due to charge-transfer effects, this is expected not to be the case for early row transition metals whose properties are better described by the motif of Mott-insulators than charge-transfer semiconductors.[93]

Beyond investigations of the electronic details discussed so far, there exists a wealth of applications that would benefit from routine oxidation state analysis using laboratory-based XES. This has recently been demonstrated for hexavalent Cr identification using Cr Kα spectroscopy with the UW instrument,[40] and has also been used for identification of sulfur oxidation state in biochars[94] and phosphorus oxidation state in InP quantum dots[95-96] using a different very high-resolution lab-based XES system at UW. Indeed, this theme of routine access enabling XAFS and XES studies has been borne out in several fields. Of particular note, laboratory-based instrumentation has been applied to the coordination analysis of the Ni^{2+}-EDTA-CN^{-} ternary system,[97] oxidation state analysis of a reactive dinuclear Ni(IV) oxido complex,[98] chemical state analysis of a mesoporous perovskite proposed for energy-related applications,[72, 99] and the spin-state analysis of model Fe compounds.[100] Indeed, similar arguments which advocate for laboratory-based instrumentation as high-access tools to accelerate research have been made by Bès et al. regarding studies which address nuclear fuel development and nuclear waste disposal.[72]

Here, we consider whether benchtop XES can address the oxidation state of environmental arsenic. A pioneering work by Penrose found that of the two most common

oxidation states, the trivalent species of arsenic is generally more toxic than the pentavalent.[101] XAFS techniques have emerged as essential alternatives for quantitative species fraction determinations of arsenic in solid matrices, such as in soils where the methodology can be paired with sequential extraction procedures[102] or HPLC-ICP-MS[8] to provide insights into the behavior of arsenic in ecological systems. Here, representative As(III) and As(V) compounds are presented as a demonstration study relevant for potential environmental speciation studies in a laboratory setting. For this study, samples were obtained in powder form and directly transferred to a polyimide pouch easily positioned in front of the source. As can be seen in Fig. 3-12a, the As Kα XES measurements reveal several noticeable spectral differences, including an energy shift that can be used as an indicator of oxidation state. Figure 3-12a also highlights the high intensity of these features, suggesting the potential of this technique in studies of dilute environmental samples. This approach to As speciation requires further investigation, as would other As fluorescence lines. We note that while the As Kα does have a clear energy shift, true environmental samples with As contamination also commonly have nontrivial Pb content, and that the Pb $L_{III}M_V$ emission line at 10551.6 eV can interfere with the As Kα XES.

Finally, we address XES of actinide materials. The L emission lines in U lie between 10 and 21 keV, with most toward the latter. Similar detector, source, and analyzer inefficiencies discussed above in the context of actinide XANES are problematic in U XES studies as well. In addition, the L-shell fluorescence lines more likely to be sensitive to chemical bonding are those involving shells closer to the valence and are consequently weaker transitions, again requiring instrumentation with minimal backgrounds. Nonetheless, U XES measurements of $(PPh_4)_2UCl_6$ and $(NMe_4)_2UO_2Cl_4$ are presented in Fig. 3-12b. The most prominent feature is the $L\beta_1$ ($L_{II}M_{IV}$) found around 17220 eV.[103] Other than a shift of the $(PPh_4)_2UCl_6$ emission spectrum to about 0.5

eV higher energy than that of $(NMe_4)_2UO_2Cl_4$, little sensitivity to speciation was observed. While other L emission lines are observed in this energy region their inadequate separation from the tails of these features complicates their use as fingerprints for the relevant U species.

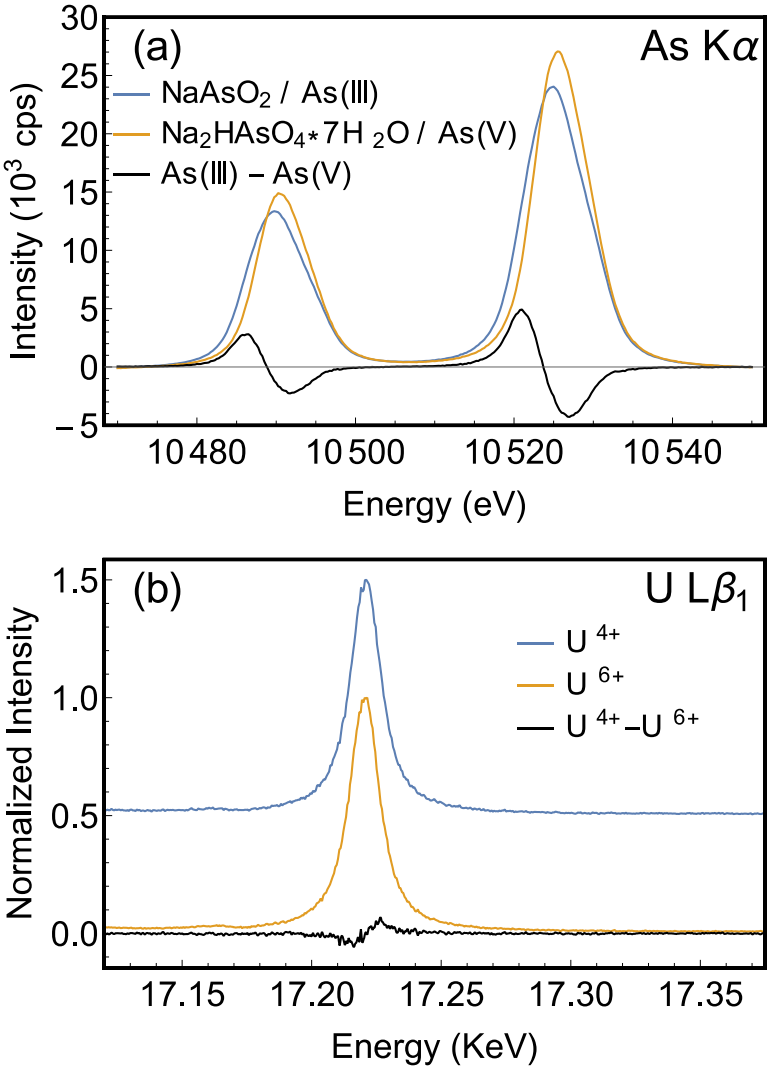

Fig. 3-12: (a) The As Kα XES spectra of trivalent and pentavalent arsenic oxide species (a). The intensity scale is for the $NaAsO_2$ sample; the intensity of the Na_2HAsO_4*7H20 has been scaled upward by ~30% to give it the same integral intensity for ease of comparison for the energy shift as a function of As oxidation state. The study used a Si (555) toroidally bent crystal analyzer following an in-house design.[41] (b) Collected $L\beta_1$ XES spectra of $(PPh_4)_2UCl6$ and $(NMe_4)_2UO_2Cl_4$, which are in the U^{4+} and U^{6+} state, respectively. The most intense spectral

feature is the $L\beta_1$, though less intense features can be found toward lower energies. The spectra are peak normalized here for comparison. A residual is provided and spectra are offset for clarity. No change in spectrum was observed across any of the scans, indicating no radiation damage. The data was calibrated to the maximum of the $K\alpha$ of a Mo foil at 17480 eV.

4. Summary and Conclusions

We present the instrumentation details and a wide variety of test study results for an improved laboratory spectrometer for XAFS and XES. This includes measurements that demonstrate important extremes for lab-based capability: EXAFS, VTC XES, and higher-energy performance. The assembled body of work using this new spectrometer, building on top of numerous studies by our research group[13, 35-41, 94-95, 104-105] and also ongoing research of several other research groups[23, 25-26, 34, 72, 106] strongly supports the position that laboratory XAFS and XES should not be judged in competition with synchrotron capability but should instead be appreciated for the new analytical capabilities that are enabled. These new capabilities hold high promise for routine materials analysis that can accelerate progress in electrical energy storage, coordination chemistry,[107] actinide chemistry,[72] and environmental and regulatory testing,[40] to name only a few prominent examples.

5. Acknowledgements

E. P. Jahrman and T. T. Fister were supported in part by the Joint Center for Energy Storage Research (JCESR), an Energy Innovation Hub funded by the U.S. Department of Energy, Office of Science, and Basic Energy Sciences, and by the U.S. Department of Energy through the Chemical Science and Engineering Division of Argonne National Laboratory. This material is based in part upon work supported by the State of Washington through the University

of Washington Clean Energy Institute. The work of J. Rana and L. F. J. Piper was supported as part of the NorthEast Center for Chemical Energy Storage (NECCES), and Energy Frontier Research Center funded by the U.S. Department of Energy, Office of Science, Basic Energy Sciences under Award# DE-SC0012583. The work of N. C. Hyatt and M. C. Stennett was supported, in part by, the Nuclear Decommissioning Authority and EPSRC under grant numbers EP/N017617/1 and EP/R511754/1; and utilized the MIDAS facility at The University of Sheffield established with financial support from the Department for Business, Energy & Industrial Strategy. The authors would like to acknowledge the efforts of Carrie Siu and Dr. M. Stanley Whittingham in synthesizing the phase pure epsilon-VOPO4 and the efforts of Mateusz Zuba in collecting the synchrotron XAS data of that sample. R&D associated with the Los Alamos National Laboratory (LANL) spectrometer was funded under the Heavy Element Chemistry Program by the Division of Chemical Sciences, Geosciences, and Biosciences, Office of Basic Energy Sciences, U.S. Department of Energy and the U.S. Department of Energy. LANL is operated by Los Alamos National Security, LLC, for the National Nuclear Security Administration of U.S. Department of Energy (contract DE-AC52-06NA25396). Use of the Stanford Synchrotron Radiation Lightsource, SLAC National Accelerator Laboratory, was supported by the U.S. Department of Energy, Office of Science, Office of Basic Energy Sciences under Contract No. DE-AC02-76SF00515. This research used resources of the Advanced Photon Source, a U.S. Department of Energy (DOE) Office of Science User Facility operated for the DOE Office of Science by Argonne National Laboratory under Contract No. DE-AC02-06CH11357. Finally, we note that three of the authors (W. Holden, D. Mortensen, and G. Seidler) have a significant financial interest in easyXAFS LLC, which is commercializing

laboratory XAFS and XES technology. No funding from easyXAFS was used in the present work.

6. References

1. Clausen, B. S.; Topsøe, H., In Situ high pressure, high temperature XAFS studies of Cu-based catalysts during methanol synthesis. *Catalysis Today* **1991,** *9* (1), 189-196.
2. Chen, Y.; Fulton, J. L.; Linehan, J. C.; Autrey, T., In Situ XAFS and NMR Study of Rhodium-Catalyzed Dehydrogenation of Dimethylamine Borane. *J Am Chem Soc* **2005,** *127* (10), 3254-3255.
3. Cuisinier, M.; Cabelguen, P. E.; Evers, S.; He, G.; Kolbeck, M.; Garsuch, A.; Bolin, T.; Balasubramanian, M.; Nazar, L. F., Sulfur Speciation in Li-S Batteries Determined by Operando X-ray Absorption Spectroscopy. *J Phys Chem Lett* **2013,** *4* (19), 3227-3232.
4. Banerjee, A.; Shilina, Y.; Ziv, B.; Ziegelbauer, J. M.; Luski, S.; Aurbach, D.; Halalay, I. C., On the Oxidation State of Manganese Ions in Li-Ion Battery Electrolyte Solutions. *J Am Chem Soc* **2017,** *139* (5), 1738-1741.
5. Schelter, E. J.; Wu, R.; Veauthier, J. M.; Bauer, E. D.; Booth, C. H.; Thomson, R. K.; Graves, C. R.; John, K. D.; Scott, B. L.; Thompson, J. D.; Morris, D. E.; Kiplinger, J. L., Comparative Study of f-Element Electronic Structure across a Series of Multimetallic Actinide and Lanthanoid-Actinide Complexes Possessing Redox-Active Bridging Ligands. *Inorg Chem* **2010,** *49* (4), 1995-2007.
6. Lind, O. C.; Salbu, B.; Janssens, K.; Proost, K.; García-León, M.; García-Tenorio, R., Characterization of U/Pu particles originating from the nuclear weapon accidents at Palomares, Spain, 1966 and Thule, Greenland, 1968. *Science of The Total Environment* **2007,** *376* (1), 294-305.
7. Le Naour, C.; Trubert, D.; Di Giandomenico, M. V.; Fillaux, C.; Den Auwer, C.; Moisy, P.; Hennig, C., First Structural Characterization of a Protactinium(V) Single Oxo Bond in Aqueous Media. *Inorg Chem* **2005,** *44* (25), 9542-9546.
8. Takahashi, Y.; Ohtaku, N.; Mitsunobu, S.; Yuita, K.; Nomura, M., Determination of the As(III)/As(V) Ratio in Soil by X-ray Absorption Near-edge Structure (XANES) and Its Application to the Arsenic Distribution between Soil and Water. *Analytical Sciences* **2003,** *19* (6), 891-896.
9. Szulczewski, M. D.; Helmke, P. A.; Bleam, W. F., Comparison of XANES analyses and extractions to determine chromium speciation in contaminated soils. *Environ Sci Technol* **1997,** *31* (10), 2954-2959.
10. Fandeur, D.; Juillot, F.; Morin, G.; Olivi, L.; Cognigni, A.; Webb, S. M.; Ambrosi, J. P.; Fritsch, E.; Guyot, F.; Brown, G. E., XANES Evidence for Oxidation of Cr(III)) to Cr(VI) by Mn-Oxides in a Lateritic Regolith Developed on Serpentinized Ultramafic Rocks of New Caledonia. *Environ Sci Technol* **2009,** *43* (19), 7384-7390.
11. Rueff, J. P.; Krisch, M.; Cai, Y. Q.; Kaprolat, A.; Hanfland, M.; Lorenzen, M.; Masciovecchio, C.; Verbeni, R.; Sette, F., Magnetic and structural alpha-epsilon phase transition in Fe monitored by x-ray emission spectroscopy. *Physical Review B* **1999,** *60* (21), 14510-14512.

12. Nomura, R.; Tateno, H.; Tateno, S.; Hirose, K.; Hernlund, J.; Muto, S.; Ishii, H.; Hiraoka, N., *Spin crossover and iron-rich silicate melt in the Earth's deep mantle*. 2011; Vol. 473, p 199-202.
13. Seidler, G. T.; Mortensen, D. R.; Remesnik, A. J.; Pacold, J. I.; Ball, N. A.; Barry, N.; Styczinski, M.; Hoidn, O. R., A laboratory-based hard x-ray monochromator for high-resolution x-ray emission spectroscopy and x-ray absorption near edge structure measurements. *Review of Scientific Instruments* **2014,** *85* (11), 113906.
14. Mantouvalou, I.; Witte, K.; Grötzsch, D.; Neitzel, M.; Günther, S.; Baumann, J.; Jung, R.; Stiel, H.; Kanngießer, B.; Sandner, W., High average power, highly brilliant laser-produced plasma source for soft X-ray spectroscopy. *Review of Scientific Instruments* **2015,** *86* (3), 035116.
15. Sugiura, C.; Gohshi, Y.; Suzuki, I., Sulfur $K\ensuremath{\beta}$ x-ray emission spectra and electronic structures of some metal sulfides. *Physical Review B* **1974,** *10* (2), 338-343.
16. Gohshi, Y.; Hukao, Y.; Hori, K., A wide-range, single-axis, vacuum two-crystal spectrometer for fluorescent X-ray analysis. *Spectrochimica Acta Part B: Atomic Spectroscopy* **1972,** *27* (3), 135-142.
17. Chikara, S.; Yohichi, G.; Isao, S., Kβ Emission and K Absorption Spectra of Sulfur in MnS. *Jpn J Appl Phys* **1972,** *11* (6), 911.
18. Yu, M. Y.; Trofimova, V. A.; Dolgih, V. E.; Korotin, M. A.; Kurmaev, E. Z.; Aguiar, J. A.; Ferreira, J. M.; Pavao, A. C., X-ray emission spectra and valence state of sulphur atoms of YBa 2 ((CuO) 1-x (NiS) x) 3 O 4- delta. *Journal of Physics: Condensed Matter* **1995,** *7* (1), 213.
19. Yarmoshenko, Y. M.; Trofimova, V. A.; Kurmaev, E. Z.; Slater, P. R.; Greaves, C., X-ray emission spectra of YSr2Cu3O7−δ containing sulphate and phosphate groups. *Physica C: Superconductivity* **1994,** *224* (3), 317-320.
20. Yarmoshenko, Y. M.; Trofimova, V. A.; Elokhina, L. V.; Kurmaev, E. Z.; Butorin, S.; Cloots, R.; Ausloos, M.; Aguiar, J. A.; Lobatchevskaya, N. I., Possibility of sulphur-oxygen substitution in YBa2Cu3O6+xSy analyzed by means of X-ray emission spectroscopy. *Journal of Physics and Chemistry of Solids* **1993,** *54* (10), 1211-1214.
21. Dolgih, V. E.; Cherkashenko, V. M.; Kurmaev, E. Z.; Goganov, D. A.; Ovchinnikov, E. K.; Yarmoshienko, Y. M., X-ray fluorescent spectrometer with linear position sensitive detector. *Nuclear Instruments and Methods in Physics Research* **1984,** *224* (1), 117-119.
22. Kavčič, M.; Dousse, J. C.; Szlachetko, J.; Cao, W., Chemical effects in the Kβ X-ray emission spectra of sulfur. *Nuclear Instruments and Methods in Physics Research Section B: Beam Interactions with Materials and Atoms* **2007,** *260* (2), 642-646.
23. Németh, Z.; Szlachetko, J.; Bajnóczi, É. G.; Vankó, G., Laboratory von Hámos X-ray spectroscopy for routine sample characterization. *Review of Scientific Instruments* **2016,** *87* (10), 103105.
24. Kayser, Y.; Błachucki, W.; Dousse, J. C.; Hoszowska, J.; Neff, M.; Romano, V., Laboratory-based micro-X-ray fluorescence setup using a von Hamos crystal spectrometer and a focused beam X-ray tube. *Review of Scientific Instruments* **2014,** *85* (4), 043101.
25. Hoszowska, J.; Dousse, J. C.; Kern, J.; Rhême, C., High-resolution von Hamos crystal X-ray spectrometer. *Nuclear Instruments and Methods in Physics Research Section A: Accelerators, Spectrometers, Detectors and Associated Equipment* **1996,** *376* (1), 129-138.

26. Anklamm, L.; Schlesiger, C.; Malzer, W.; Grötzsch, D.; Neitzel, M.; Kanngießer, B., A novel von Hamos spectrometer for efficient X-ray emission spectroscopy in the laboratory. *Review of Scientific Instruments* **2014,** *85* (5), 053110.
27. Tirao, G.; Stutz, G.; Cusatis, C., An inelastic X-ray scattering spectrometer at LNLS. *Journal of Synchrotron Radiation* **2004,** *11* (4), 335-342.
28. Yuryev, Y. N.; Lee, H.-J.; Park, H.-M.; Cho, Y.-K.; Lee, M.-K.; Pogrebitsky, K. J., Variable Rowland radius laboratory vacuum surface-sensitive x-ray absorption fine structure spectrometer. *Review of Scientific Instruments* **2007,** *78* (2), 025108.
29. Williams, A., Laboratory x-ray spectrometer for EXAFS and XANES measurements. *Review of Scientific Instruments* **1983,** *54* (2), 193-197.
30. Tohji, K.; Udagawa, Y.; Kawasaki, T.; Masuda, K., Laboratory EXAFS spectrometer with a bent crystal, a solid-state detector, and a fast detection system. *Review of Scientific Instruments* **1983,** *54* (11), 1482-1487.
31. Thulke, W.; Haensel, R.; Rabe, P., Versatile curved crystal spectrometer for laboratory extended x-ray absorption fine structure measurements. *Review of Scientific Instruments* **1983,** *54* (3), 277-283.
32. Knapp, G. S.; Chen, H.; Klippert, T. E., Development of a laboratory EXAFS facility. *Review of Scientific Instruments* **1978,** *49* (12), 1658-1666.
33. Cohen, G. G.; Fischer, D. A.; Colbert, J.; Shevchik, N. J., Tunable laboratory extended x-ray absorption fine structure system. *Review of Scientific Instruments* **1980,** *51* (3), 273-277.
34. Szlachetko, M.; Berset, M.; Dousse, J. C.; Hoszowska, J.; Szlachetko, J., High-resolution Laue-type DuMond curved crystal spectrometer. *Review of Scientific Instruments* **2013,** *84* (9), 093104.
35. Valenza, R. A.; Jahrman, E. P.; Kas, J. J.; Seidler, G. T., Double-ionization satellites in the x-ray emission spectrum of Ni metal. *Phys Rev A* **2017,** *96* (3), 032504.
36. Seidler, G. T.; Mortensen, D. R.; Ditter, A. S.; Ball, N. A.; Remesnik, A. J., A Modern Laboratory XAFS Cookbook. *Journal of Physics: Conference Series* **2016,** *712* (1), 012015.
37. Mortensen, D. R.; Seidler, G. T.; Kas, J. J.; Govind, N.; Schwartz, C. P.; Pemmaraju, S.; Prendergast, D. G., Benchmark results and theoretical treatments for valence-to-core x-ray emission spectroscopy in transition metal compounds. *Physical Review B* **2017,** *96* (12), 125136.
38. Mortensen, D. R.; Seidler, G. T.; Ditter, A. S.; Glatzel, P., Benchtop Nonresonant X-ray Emission Spectroscopy: Coming Soon to Laboratories and XAS Beamlines Near You? *Journal of Physics: Conference Series* **2016,** *712* (1), 012036.
39. Mortensen, D. R.; Seidler, G. T., Robust optic alignment in a tilt-free implementation of the Rowland circle spectrometer. *J Electron Spec* **2017,** *215*, 8-15.
40. Jahrman, E. P.; Seidler, G. T.; Sieber, J. R., Determination of Hexavalent Chromium Fractions in Plastics Using Laboratory-Based, High-Resolution X-ray Emission Spectroscopy. *Analytical Chemistry* **2018,** *90* (11), 6587.
41. Jahrman, E. P.; Holden, W. M.; Ditter, A. S.; Kihara, S. L.; Seidler, G. T., Vacuum Formed Temporary Spherical and Toroidal Bent Crystal Analyzers for High Resolution X-ray Spectroscopy. *In Prep* **2018**.
42. Stennett, M. C.; Corkhill, C. L.; Marshall, L. A.; Hyatt, N. C., Preparation, characterisation and dissolution of a CeO2 analogue for UO2 nuclear fuel. *Journal of Nuclear Materials* **2013,** *432* (1), 182-188.

43. Siu, C.; Seymour, I. D.; Britto, S.; Zhang, H.; Rana, J.; Feng, J.; Omenya, F. O.; Zhou, H.; Chernova, N. A.; Zhou, G.; Grey, C. P.; Piper, L. F. J.; Whittingham, M. S., Enabling multi-electron reaction of ε-VOPO4 to reach theoretical capacity for lithium-ion batteries. *Chemical Communications* **2018,** *54* (56), 7802-7805.
44. Minasian, S. G.; Boland, K. S.; Feller, R. K.; Gaunt, A. J.; Kozimor, S. A.; May, I.; Reilly, S. D.; Scott, B. L.; Shuh, D. K., Synthesis and Structure of (Ph4P)2MCl6 (M = Ti, Zr, Hf, Th, U, Np, Pu). *Inorg Chem* **2012,** *51* (10), 5728-5736.
45. Watkin, D. J.; Denning, R. G.; Prout, K., Structure of Dicesium Tetrachlorodioxouranium(Vi). *Acta Crystallogr C* **1991,** *47*, 2517-2519.
46. Spencer, L. P.; Yang, P.; Minasian, S. G.; Jilek, R. E.; Batista, E. R.; Boland, K. S.; Boncella, J. M.; Conradson, S. D.; Clark, D. L.; Hayton, T. W.; Kozimor, S. A.; Martin, R. L.; MacInnes, M. M.; Olson, A. C.; Scott, B. L.; Shuh, D. K.; Wilkerson, M. P., Tetrahalide Complexes of the [U(NR)2]2+ Ion: Synthesis, Theory, and Chlorine K-Edge X-ray Absorption Spectroscopy. *J Am Chem Soc* **2013,** *135* (6), 2279-2290.
47. Ravel, B.; Newville, M., ATHENA, ARTEMIS, HEPHAESTUS: data analysis for X-ray absorption spectroscopy using IFEFFIT. *Journal of Synchrotron Radiation* **2005,** *12* (4), 537-541.
48. Hyatt, N. C.; Schwarz, R. R.; Bingham, P. A.; Stennett, M. C.; Corkhill, C. L.; Heath, P. G.; Hand, R. J.; James, M.; Pearson, A.; Morgan, S., Thermal treatment of simulant plutonium contaminated materials from the Sellafield site by vitrification in a blast-furnace slag. *Journal of Nuclear Materials* **2014,** *444* (1), 186-199.
49. Pattenaude, S. A.; Mullane, K. C.; Schelter, E. J.; Ferrier, M. G.; Stein, B. W.; Bone, S. E.; Lezama Pacheco, J. S.; Kozimor, S. A.; Fanwick, P. E.; Zeller, M.; Bart, S. C., Redox-Active vs Redox-Innocent: A Comparison of Uranium Complexes Containing Diamine Ligands. *Inorg Chem* **2018,** *57* (11), 6530-6539.
50. Stern, E. A.; Heald, S. M., X-ray filter assembly for fluorescence measurements of x-ray absorption fine structure. *Review of Scientific Instruments* **1979,** *50* (12), 1579-1582.
51. Hämäläinen, K.; Siddons, D. P.; Hastings, J. B.; Berman, L. E., Elimination of the Inner-Shell Lifetime Broadening in X-Ray-Absorption Spectroscopy. *Phys Rev Lett* **1991,** *67* (20), 2850-2853.
52. Hämäläinen, K.; Kao, C. C.; Hastings, J. B.; Siddons, D. P.; Berman, L. E.; Stojanoff, V.; Cramer, S. P., Spin-dependent x-ray absorption of MnO and ${\mathrm{MnF}}_{2}$. *Physical Review B* **1992,** *46* (21), 14274-14277.
53. Rovezzi, M.; Lapras, C.; Manceau, A.; Glatzel, P.; Verbeni, R., High energy-resolution x-ray spectroscopy at ultra-high dilution with spherically bent crystal analyzers of 0.5 m radius. *Review of Scientific Instruments* **2017,** *88* (1), 013108.
54. Suortti, P.; Buslaps, T.; Fajardo, P.; Honkimaki, V.; Kretzschmer, M.; Lienert, U.; McCarthy, J. E.; Renier, M.; Shukla, A.; Tschentscher, T.; Meinander, T., Scanning X-ray spectrometer for high-resolution Compton profile measurements at ESRF. *Journal of Synchrotron Radiation* **1999,** *6* (2), 69-80.
55. Lu, K. Q.; Stern, E. A., Johann and Johansson focussing arrangements

Analytical analysis. 1980; Vol. 64, pp 104-108.

56. Bergmann, U.; Cramer, S. P. In *High-resolution large-acceptance analyzer for x-ray fluorescence and Raman spectroscopy*, SPIE's International Symposium on Optical Science, Engineering, and Instrumentation, SPIE: 1998; p 12.
57. Tabuchi, M.; Nakashima, A.; Shigemura, H.; Ado, K.; Kobayashi, H.; Sakaebe, H.; Kageyama, H.; Nakamura, T.; Kohzaki, M.; Hirano, A.; Kanno, R., Synthesis, Cation Distribution, and Electrochemical Properties of Fe-Substituted Li2MnO3 as a Novel 4 V Positive Electrode Material. *Journal of The Electrochemical Society* **2002,** *149* (5), A509-A524.
58. Shigemura, H.; Sakaebe, H.; Kageyama, H.; Kobayashi, H.; West, A. R.; Kanno, R.; Morimoto, S.; Nasu, S.; Tabuchi, M., Structure and Electrochemical Properties of LiFe x Mn2 − x O 4 (0 ⩽ x ⩽ 0.5) Spinel as 5 V Electrode Material for Lithium Batteries. *Journal of The Electrochemical Society* **2001,** *148* (7), A730-A736.
59. McLaren, V. L.; West, A. R.; Tabuchi, M.; Nakashima, A.; Takahara, H.; Kobayashi, H.; Sakaebe, H.; Kageyama, H.; Hirano, A.; Takeda, Y., Study of the Capacity Fading Mechanism for Fe-Substituted LiCoO2 Positive Electrode. *Journal of The Electrochemical Society* **2004,** *151* (5), A672-A681.
60. Kageyama, H.; Shigemura, H.; Tabuchi, M.; Ado, K.; Kobayashi, H., XAFS study of LiCo1-xFexO2 cathode for rechargeable lithium battery by laboratory XAFS spectrometer. *Journal of Synchrotron Radiation* **2001,** *8* (2), 863-865.
61. Talaie, E.; Bonnick, P.; Sun, X. Q.; Pang, Q.; Liang, X.; Nazar, L. F., Methods and Protocols for Electrochemical Energy Storage Materials Research. *Chem Mater* **2017,** *29* (1), 90-105.
62. Nowack, L.; Grolimund, D.; Samson, V.; Marone, F.; Wood, V., Rapid Mapping of Lithiation Dynamics in Transition Metal Oxide Particles with Operando X-ray Absorption Spectroscopy. *Scientific Reports* **2016,** *6*.
63. Jaklevic, J.; Kirby, J. A.; Klein, M. P.; Robertson, A. S.; Brown, G. S.; Eisenberger, P., Fluorescence detection of exafs: Sensitivity enhancement for dilute species and thin films. *Solid State Communications* **1977,** *23* (9), 679-682.
64. Gaur, A.; Shrivastava, B. D., Speciation using X-ray absorption fine structure (XAFS). *Review Journal of Chemistry* **2015,** *5* (4), 361-398.
65. Agarwal, B. K. V., V. P., A rule for chemical shifts of x-ray absorption edges. *Journal of Physics C: Solid State Physics* **1970,** *3* (3), 535-537.
66. Allen, P. G.; Bucher, J. J.; Shuh, D. K.; Edelstein, N. M.; Craig, I., Coordination Chemistry of Trivalent Lanthanide and Actinide Ions in Dilute and Concentrated Chloride Solutions. *Inorg Chem* **2000,** *39* (3), 595-601.
67. Asakura, H.; Shishido, T.; Teramura, K.; Tanaka, T., Local Structure and L1- and L3-Edge X-ray Absorption Near Edge Structure of Late Lanthanide Elements (Ho, Er, Yb) in Their Complex Oxides. *The Journal of Physical Chemistry C* **2015,** *119* (15), 8070-8077.
68. Upadhyaya, G. K.; Shah, G.; Gupta, S. N., XANES studies of rare earth metals and compounds. *Physica B: Condensed Matter* **1995,** *208-209*, 297-299.
69. Rothensteiner, M.; Sala, S.; Bonk, A.; Vogt, U.; Emerich, H.; Van Bokhoven, J. A., Ce K edge XAS of ceria-based redox materials under realistic conditions for the two-step solar thermochemical dissociation of water and/or CO 2. *Phys. Chem. Chem. Phys.* **2015,** *17* (40), 26988-26996.
70. Zhang, J.; Wu, Z.; Liu, T.; Hu, T.; Wu, Z.; Ju, X., XANES study on the valence transitions in cerium oxide nanoparticles. *J. Synchrot. Radiat.* **2001,** *8*, 531-532.

71. Davenport, A. J.; Isaacs, H. S.; Kendig, M. W., XANES investigation of the role of cerium compounds as corrosion inhibitors for aluminum. *Corrosion Science* **1991,** *32* (5), 653-663.
72. Bès, R.; Ahopelto, T.; Honkanen, A. P.; Huotari, S.; Leinders, G.; Pakarinen, J.; Kvashnina, K., Laboratory-scale X-ray absorption spectroscopy approach for actinide research: Experiment at the uranium L3-edge. *Journal of Nuclear Materials* **2018,** *507*, 50-53.
73. Gog, T.; Casa, D. M.; Said, A. H.; Upton, M. H.; Kim, J.; Kuzmenko, I.; Huang, X.; Khachatryan, R., Spherical analyzers and monochromators for resonant inelastic hard X-ray scattering: a compilation of crystals and reflections. *Journal of Synchrotron Radiation* **2013,** *20* (1), 74-79.
74. Lecante, P.; Jaud, J.; Mosset, A.; Galy, J.; Burian, A., A laboratory EXAFS spectrometer in transmission dispersive mode. *Review of Scientific Instruments* **1994,** *65* (4), 845-849.
75. Hudson, E. A.; G. Allen, P.; Terminello, L.; Denecke, M.; Reich, T., *Polarized x-ray-absorption spectroscopy of the uranyl ion: Comparison of experiment and theory*. 1996; Vol. 54, p 156-165.
76. Kelly, S. D.; Bare, S. R.; Greenlay, N.; Azevedo, G.; Balasubramanian, M.; Barton, D.; Chattopadhyay, S.; Fakra, S.; Johannessen, B.; Newville, M.; Pena, J.; Pokrovski, G. S.; Proux, O.; Priolkar, K.; Ravel, B.; Webb, S. M., Comparison of EXAFS foil spectra from around the world. *Journal of Physics: Conference Series* **2009,** *190* (1), 012032.
77. Li, G.; Bridges, F.; H. Booth, C., *X-ray-absorption fine-structure standards: A comparison of experiment and theory*. 1995; Vol. 52, p 6332-6348.
78. Krayzman, V.; Levin, I.; Woicik, J. C.; Proffen, T.; Vanderah, T. A.; Tucker, M. G., A combined fit of total scattering and extended X-ray absorption fine structure data for local-structure determination in crystalline materials. *Journal of Applied Crystallography* **2009,** *42* (5), 867-877.
79. Karolewski, M. A.; Cavell, R. G.; Gordon, R. A.; Glover, C. J.; Cheah, M.; Ridgway, M. C., Predicting XAFS scattering path cumulants and XAFS spectra for metals (Cu, Ni, Fe, Ti, Au) using molecular dynamics simulations. *Journal of Synchrotron Radiation* **2013,** *20* (4), 555-566.
80. Glatzel, P.; Bergmann, U., High resolution 1s core hole X-ray spectroscopy in 3d transition metal complexes - electronic and structural information. *Coordin Chem Rev* **2005,** *249* (1-2), 65-95.
81. Gallo, E.; Glatzel, P., Valence to Core X-ray Emission Spectroscopy. *Advanced Materials* **2014,** *26* (46), 7730-7746.
82. Pollock, C. J.; DeBeer, S., Valence-to-Core X-ray Emission Spectroscopy: A Sensitive Probe of the Nature of a Bound Ligand. *J Am Chem Soc* **2011,** *133* (14), 5594-5601.
83. Kawai, J.; Ohta, M.; Konishi, T., Chemical Effects in High-Resolution Nickel K_α X-Ray Fluorescence Spectra. *Analytical Sciences* **2005,** *21* (7), 865-868.
84. Gul, S.; Ng, J. W. D.; Alonso-Mori, R.; Kern, J.; Sokaras, D.; Anzenberg, E.; Lassalle-Kaiser, B.; Gorlin, Y.; Weng, T.-C.; Zwart, P. H.; Zhang, J. Z.; Bergmann, U.; Yachandra, V. K.; Jaramillo, T. F.; Yano, J., Simultaneous detection of electronic structure changes from two elements of a bifunctional catalyst using wavelength-dispersive X-ray emission spectroscopy and in situ electrochemistry. *Physical Chemistry Chemical Physics* **2015,** *17* (14), 8901-8912.

85. Einsle, O.; Tezcan, F. A.; Andrade, S. L. A.; Schmid, B.; Yoshida, M.; Howard, J. B.; Rees, D. C., Nitrogenase MoFe-Protein at 1.16 Å Resolution: A Central Ligand in the FeMo-Cofactor. *Science* **2002,** *297* (5587), 1696.
86. Lancaster, K. M.; Roemelt, M.; Ettenhuber, P.; Hu, Y.; Ribbe, M. W.; Neese, F.; Bergmann, U.; DeBeer, S., X-ray Emission Spectroscopy Evidences a Central Carbon in the Nitrogenase Iron-Molybdenum Cofactor. *Science* **2011,** *334* (6058), 974.
87. Pushkar, Y.; Long, X.; Glatzel, P.; Brudvig, G. W.; Dismukes, G. C.; Collins, T. J.; Yachandra, V. K.; Yano, J.; Bergmann, U., Direct Detection of Oxygen Ligation to the Mn4Ca Cluster of Photosystem II by X-ray Emission Spectroscopy. *Angewandte Chemie International Edition* **2010,** *49* (4), 800-803.
88. Pollock, C. J.; Grubel, K.; Holland, P. L.; DeBeer, S., Experimentally Quantifying Small-Molecule Bond Activation Using Valence-to-Core X-ray Emission Spectroscopy. *J Am Chem Soc* **2013,** *135* (32), 11803-11808.
89. Rovezzi, M.; Glatzel, P., *Hard x-ray emission spectroscopy: A powerful tool for the characterization of magnetic semiconductors*. 2013; Vol. 29.
90. Bergmann, U.; Horne, C. R.; Collins, T. J.; Workman, J. M.; Cramer, S. P., Chemical dependence of interatomic X-ray transition energies and intensities – a study of Mn Kβ" and Kβ2,5 spectra. *Chem Phys Lett* **1999,** *302* (1), 119-124.
91. Enkisch, H.; Sternemann, C.; Paulus, M.; Volmer, M.; Schulke, W., 3d spectator hole satellites of the CuK beta(1,3) and K beta(2,5) emission spectrum. *Phys Rev A* **2004,** *70* (2), 022508.
92. Sternemann, C.; Kaprolat, A.; Krisch, M. H.; Schulke, W., Evolution of the germanium K beta ''' X-ray satellites from threshold to saturation. *Phys Rev A* **2000,** *61* (2), 205011-205014.
93. Kawai, J.; Takami, M.; Satoko, C., Multiplet Structure in Ni K-Beta X-Ray-Fluorescence Spectra of Nickel Compounds. *Phys Rev Lett* **1990,** *65* (17), 2193-2196.
94. Holden, W. M.; Seidler, G. T.; Cheah, S., Sulfur Speciation in Biochars by Very High Resolution Benchtop Kα X-ray Emission Spectroscopy. *The Journal of Physical Chemistry A* **2018**.
95. Stein, J. L.; Holden, W. M.; Venkatesh, A.; Mundy, M. E.; Rossini, A. J.; T., S. G.; Cossairt, B. M., *Chem Mater* **2018,** *Submitted*.
96. Stein, J. L.; Holden, W. M.; Cossairt, B. M.; Seidler, G. T., Something something InP. *In Prep* **2018**.
97. Bajnóczi, É. G.; Németh, Z.; Vankó, G., Simultaneous Speciation, Structure, and Equilibrium Constant Determination in the Ni2+–EDTA–CN– Ternary System via High-Resolution Laboratory X-ray Absorption Fine Structure Spectroscopy and Theoretical Calculations. *Inorg Chem* **2017,** *56* (22), 14220-14226.
98. Padamati, S. K.; Angelone, D.; Draksharapu, A.; Primi, G.; Martin, D. J.; Tromp, M.; Swart, M.; Browne, W. R., Transient Formation and Reactivity of a High-Valent Nickel(IV) Oxido Complex. *J Am Chem Soc* **2017,** *139* (25), 8718-8724.
99. Kuai, L.; Kan, E.; Cao, W.; Huttula, M.; Ollikkala, S.; Ahopelto, T.; Honkanen, A.-P.; Huotari, S.; Wang, W.; Geng, B., Mesoporous LaMnO3+δ perovskite from spray–pyrolysis with superior performance for oxygen reduction reaction and Zn–air battery. *Nano Energy* **2018,** *43*, 81-90.
100. Joe, Y. I.; O'Neil, G. C.; Miaja-Avila, L.; Fowler, J. W.; Jimenez, R.; Silverman, K. L.; Swetz, D. S.; Ullom, J. N., Observation of iron spin-states using tabletop x-ray emission spectroscopy

and microcalorimeter sensors. *Journal of Physics B: Atomic, Molecular and Optical Physics* **2016,** *49* (2), 024003.
101. Penrose, W. R.; Woolson, E. A., Arsenic in the marine and aquatic environments: Analysis, occurrence, and significance. *C R C Critical Reviews in Environmental Control* **1974,** *4* (1-4), 465-482.
102. Niazi, N. K.; Singh, B.; Shah, P., Arsenic Speciation and Phytoavailability in Contaminated Soils Using a Sequential Extraction Procedure and XANES Spectroscopy. *Environ Sci Technol* **2011,** *45* (17), 7135-7142.
103. Bearden, J. A., X-ray wavelengths. *Reviews of Modern Physics* **1967,** *39* (1), 78-124.
104. Mundy, M. E.; Ung, D.; Lai, N. L.; Jahrman, E. P.; Seidler, G. T.; Cossairt, B. M., Aminophosphines as Versatile Precursors for the Synthesis of Metal Phosphide Nanocrystals. *Chem Mater* **2018,** *30* (15), 5373.
105. Holden, W. M.; Hoidn, O. R.; Ditter, A. S.; Seidler, G. T.; Kas, J.; Stein, J. L.; Cossairt, B. M.; Kozimor, S. A.; Guo, J.; Ye, Y.; Marcus, M. A.; Fakra, S., A compact dispersive refocusing Rowland circle X-ray emission spectrometer for laboratory, synchrotron, and XFEL applications. *Review of Scientific Instruments* **2017,** *88* (7), 073904.
106. Schlesiger, C.; Anklamm, L.; Stiel, H.; Malzer, W.; Kanngießer, B., XAFS spectroscopy by an X-ray tube based spectrometer using a novel type of HOPG mosaic crystal and optimized image processing. *Journal of Analytical Atomic Spectrometry* **2015,** *30* (5), 1080-1085.
107. Haldrup, K.; Gawelda, W.; Abela, R.; Alonso-Mori, R.; Bergmann, U.; Bordage, A.; Cammarata, M.; Canton, S. E.; Dohn, A. O.; van Driel, T. B.; Fritz, D. M.; Galler, A.; Glatzel, P.; Harlang, T.; Kjaer, K. S.; Lemke, H. T.; Moller, K. B.; Nemeth, Z.; Papai, M.; Sas, N.; Uhlig, J.; Zhu, D. L.; Vanko, G.; Sundstrom, V.; Nielsen, M. M.; Bressler, C., Observing Solvation Dynamics with Simultaneous Femtosecond X-ray Emission Spectroscopy and X-ray Scattering. *J Phys Chem B* **2016,** *120* (6), 1158-1168.

Chapter 4. Vacuum Formed Temporary Spherical and Toroidal Bent Crystal Analyzers for X-ray Absorption and Emission Spectroscopy

Originally published as: E. P. Jahrman, W. M. Holden, A. S. Ditter, S. A. Kozimor, S. L. Kihara, and G. T. Seidler. Review of Scientific Instruments **90**, 013106 (2019). E. P. Jahrman contributed to the design of the spectrometer and led the effort to characterize the optic with various spectroscopies. E. P. Jahrman and W. M. Holden collected the X-ray camera measurements. E. P. Jahrman and W. M. Holden contributed equally to this work.

We demonstrate that vacuum forming of 10-cm diameter silicon wafers of various crystallographic orientations under an x-ray permeable, flexible window can easily generate spherically bent crystal analyzers (SBCA) and toroidally bent crystal analyzers (TBCA) with ~1-eV energy resolution and a 1-m major radius of curvature. In applications at synchrotron light sources, x-ray free electron lasers, and laboratory spectrometers these characteristics are generally sufficient for many x-ray absorption fine structure (XAFS), x-ray emission spectroscopy (XES), and resonant inelastic x-ray scattering (RIXS) applications in the chemical sciences. Unlike existing optics manufacturing methods using epoxy or anodic bonding, vacuum forming without adhesive is temporary in the sense that the bent wafer can be removed when vacuum is released and exchanged for a different orientation wafer. Therefore, the combination of an x-ray compatible vacuum-forming chamber, a library of thin wafers, and a small number of forms having different secondary curvatures can give extreme flexibility in spectrometer energy range. As proof of this method we determine the energy resolution and reflectivity for several such vacuum-formed bent crystal analyzers (VF-BCA) in laboratory based XAFS and XES studies using a conventional

x-ray tube. For completeness we also show x-ray images collected on the detector plane to characterize the resulting focal spots and optical aberrations.

1. Introduction

Doubly-curved Bragg optics see extensive use in advanced x-ray spectroscopies at x-ray free electron lasers, synchrotron x-ray light sources, laser plasma facilities, and laboratories performing in-house x-ray absorption fine structure and x-ray emission spectroscopy. This has been made possible by a large body of work aimed at characterizing and evaluating the properties of doubly-curved optics.[1-7] These optics are available commercially; the traditional production methods use glue or anodic bonding to affix crystal wafers after pressing into precision glass or metallic substrates.[8-11] Other production techniques such as vacuum-bent analyzers[12, 13] and hot plastic deformation techniques[14] have also been explored. Another approach is to use a spherical bending apparatus that allows the curvature to be characterized before fixing to a permanent shape.[15]

Even with a variety of available production techniques, acquiring a large number of such optics for multi-analyzer systems can be challenging. Synchrotron endstations for x-ray emission spectroscopy (XES), high energy resolution fluorescence detection (HERFD) of x-ray absorption fine structure (XAFS), or nonresonant inelastic x-ray scattering (NRIXS) now often use from five to as many as ~100 such optics.[16-23] In addition to cost issues, for XES there is a pragmatic issue: different synchrotron users may come with experiments requiring acquisition of an entirely new set of optics for some energy range that has not previously been explored at that facility. The same issue arises with the increasing use of laboratory-based spectrometers,[24-32] where again the elements and energy ranges that are capable of being studied depend on the availability of analyzers having a variety of crystal cuts to achieve the necessary Bragg angles and energy

resolutions. As an additional issue, when used in a Rowland circle spectrometer the most common doubly-curved optics, spherically bent crystal analyzers (SBCA) in the Johann configuration[33], sagittal bending error results in large spot sizes out of the Rowland plane when far from backscatter. Toroidally bent crystal analyzers (TBCA) are needed for a truer point-to-point focus, but are far less common and their secondary curvature must be tuned to match a chosen Bragg angle.

The purpose of this paper is to address the above concerns, at least for applications requiring only the 'modest' energy resolution of ~1-eV, such as is frequently sufficient in the chemical sciences.[34] Specifically, we demonstrate a simple method to make temporary SBCA's and TBCA's with good performance and very high ease of use. Unlike methods using epoxy or anodic bonding, vacuum forming without adhesive is temporary in the sense that the bent wafer can be removed when vacuum is released and exchanged for a different orientation wafer. While vacuum formed bent crystal analyzers have been utilized before in other applications, this work demonstrates the efficacy of these analyzers in x-ray absorption and emission spectroscopy. The combination of an x-ray compatible vacuum-forming chamber, a suitable library of thin single-crystal wafers, and a small number of forms having different secondary curvatures can give extreme flexibility in spectrometer or monochromator energy range at low cost and with great flexibility for addition of new energy ranges, as needed.

2. Methods

The overall concept and resulting design of the vacuum-formed bent crystal analyzer (VF-BCA) is presented in Fig. 4-1. Front-view and section-view computer aided design (CAD) renderings are shown in Fig. 4-1(a) and (b), respectively. The key point is that an x-ray transparent, flexible polyimide window serves to seal the volume containing the wafer and the machined

aluminum alloy or glass lens form from the outside atmosphere. When pumping on the VF-BCA, outside air pressure forces the polyimide window to collapse inward, pressing the wafer firmly onto the underlying form. A photograph of a VF-BCA is shown in Fig. 4-1(c), and for comparison, a commercial, anodically-bonded analyzer (XRS TECH LLC) is shown in Fig. 4-1(d).

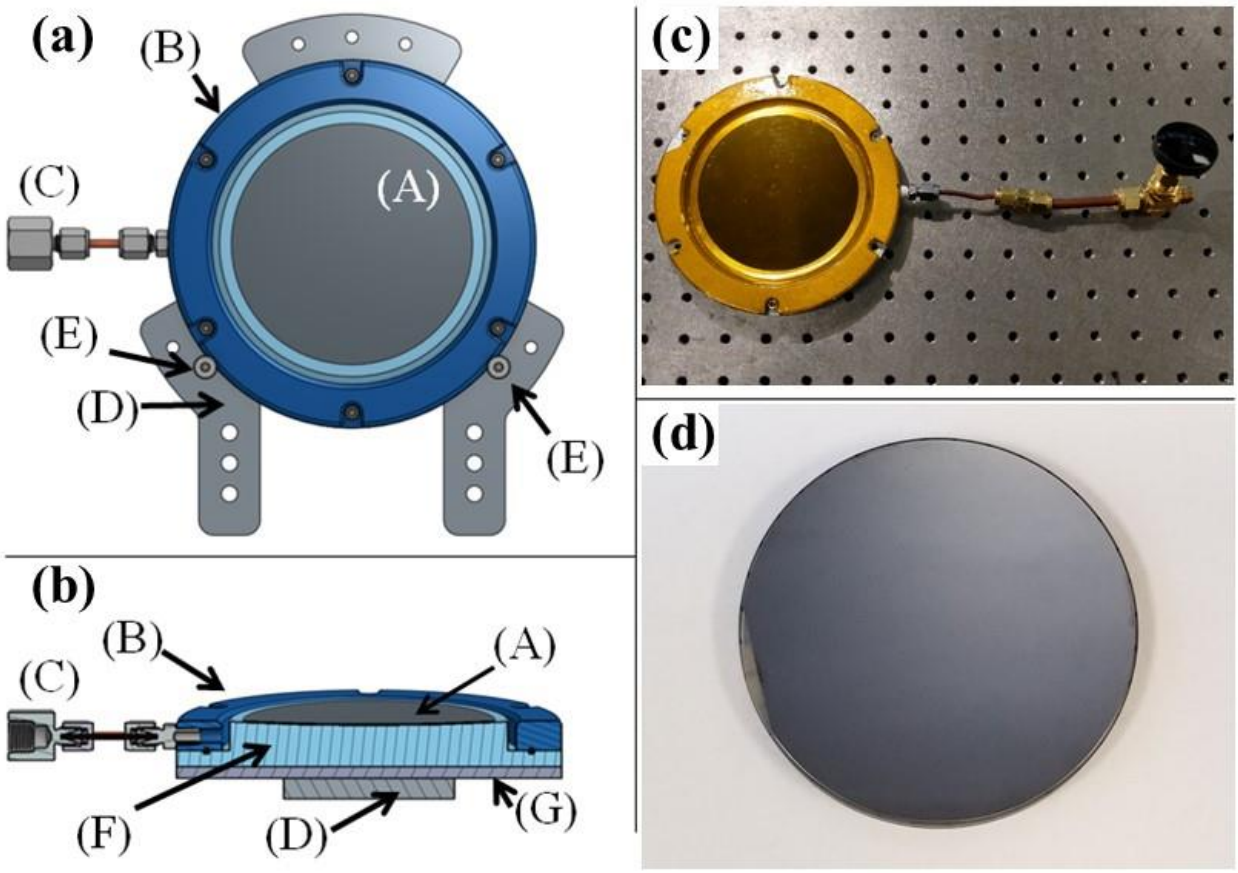

Fig. 4-1: (a) CAD rendering front view of the vacuum formed bent crystal analyzer (VF-BCA). (A) bent wafer; (B) front flange with polyimide film (not shown); (C) pumping line; (D) aluminum alloy vertical support plate; (E) support bolts to define the position of the outer diameter of the VF-BCA body. (b) CAD rendering section view of the VF-BCA. (F) CNC-machined vacuum form; (G) steel backing plate for magnetic mounting, where magnets (not shown) are attached alongside part (D). (c) Photograph of the VF-BCA, note the flexible orange polyimide film that allows air pressure to force the wafer into the shape of the form machined into part (F). A second, similar VF-BCA instead has a simple recess in part (F) to accept a 1-m radius of curvature concave glass lens. (d) Photograph of a commercial, anodically-bonded 10-cm diameter SBCA with 1-m radius of curvature.

Several different supporting forms were used, all with the 1-m major radius of curvature required by the laboratory spectrometer[28] that served as an extremely convenient testbed for this project. Table 4-1 defines the character of the different forms. The lens form was a plano-concave spherical lens made of BK7 glass from Esco Optics with 125 mm diameter, 1-meter ± 1% radius of curvature, and thickness 10 mm. When the forming contact surface was machined from aluminum 6061 alloy, a Mitsubishi M-V5Cn-L vertical machining center was used. The necessary cutting paths were generated under the target scallop deviation of 5 μm with a ball end mill having a ball-end radius of ~7.14 mm. The resulting surfaces were cleaned with solvents but otherwise not modified by, e.g., polishing or lapping.

Table 4-1: List of all bent crystal analyzers and analyzer forms used in this study.

Optic name	Major radius (cm)	Perpendicular radius (cm)	Vacuum form surface
SBCA	100.0	100.0	Wafer anodically bonded to
VF-BCA-1	100.0	100.0	Glass lens
VF-BCA-2	100.0	100.0	Al6061 spherical recess
VF-BCA-3	100.0	88.3	Al6061 torus, $\theta^* = 70$ °

The wafers used in the VF-BCA were standard 10-cm diameter double side polished Si wafers of various orientations, all nominally 400-μm thick. Different crystal orientations yield different energy ranges over the useful Bragg angle range. A list of absorption edges or fluorescence lines studied and the corresponding commercial SBCA or wafer used in a VF-BCA is given in Table 4-2.

Table 4-2: List of experiments performed, commercial SBCA or wafers used in the VF-BCA, and nominal Bragg angle for the absorption edge or fluorescence line from the indicated crystal reflection.

Study	Commercial SBCA	Wafer for VF-BCA	Bragg angle (deg)
Ni XAFS	Si (551)	Si (711)	78.0
Ni XAFS	Si (444)	Si (444)	71.6
Cu Kα XES	Si (444)	Si (444)	79.3

The laboratory spectrometer used here[28] is a 1-m diameter Rowland circle spectrometer based on the approach of Seidler, et al.,[24] as modified by tilt-free alignment[35] and by the use of a higher-powered x-ray tube and longer translation stages to give a wider range in Bragg angle (θ_B). Across several instrument generations this overall approach using a conventional x-ray tube and a 'scissors' monochromator has been used in several studies with ~1-eV energy resolution for either transmission-mode XAFS or XES[25, 27, 30, 35-37] and the present instrument and its performance have been described in detail in Jahrman, et al.[28]

Measurements were performed with a Varex VF-80 x-ray tube with Pd-anode operating at 35 kV accelerating potential and 100 W total electron beam power. A silicon drift diode (Amptek X-123 SDD) with ~4.6-mm diameter active region was the final detector for all XAFS and XES scans. In Fig. 2 we show a schematic of the Rowland circle implementation for this spectrometer, a photograph of the spectrometer in an XAFS configuration, and a photograph of the VF-BCA installed at the optic location.

Under the protocol for tilt-free alignment,[35] spherical analyzers are rotated about their circular symmetry axis until the wafer's miscut is in the Rowland plane. For a toroidal VF-BCA,

the wafer orientation must be determined in a spherical VF-BCA prior to installation into the toroidal vacuum form holder with the miscut oriented in the Rowland plane, i.e., in the plane of the 1-m major radius of curvature. The use of magnets inside a plastic 3D-printed part (Fig. 4-2(c)) allows the VF-BCA to be magnetically mounted rather than mechanically affixed, making it particularly convenient to rotate about the necessary axis in the Rowland plane.

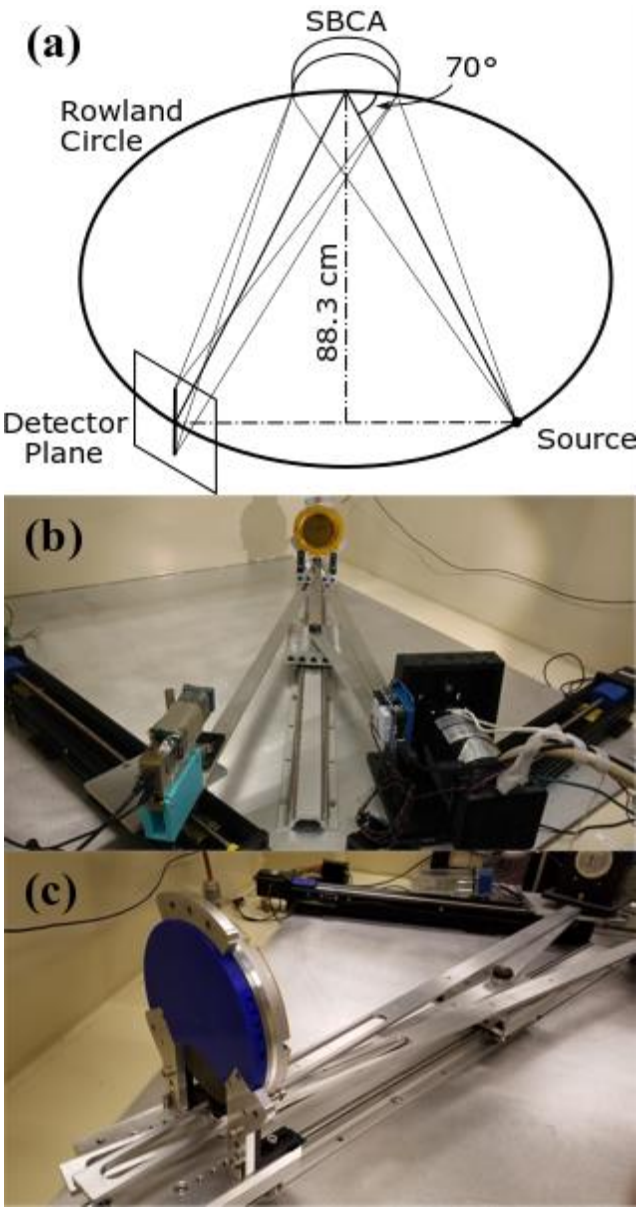

Fig. 4-2: (a) The Rowland circle implementation for the laboratory spectrometer, shown for a 70 ° Bragg angle. Note the definition of the detector plane. Also note that perfect point-to-point focusing by the optic would require that its radius of curvature out of the Rowland plane be equal to the normal distance from the source-detector arc to the optic, i.e., the sagitta of the reflexive arc from the source point on the Rowland circle to the detector point, indicated as 88.3cm on the diagram above. This motivates the use of toroidally curved forms, as discussed in the text. (b) Photograph of the laboratory spectrometer. (c) Photograph from the reverse side of a vacuum-formed bent crystal analyzer installed into the spectrometer. Note the presence of small magnets inside visible channels of the plastic 3D-printed part coupled to the steel mounting plate (part (G) in Fig. 1) to hold the analyzer in location but allow easy rotation about the azimuthal angle.

Imaging of the x-ray intensity on the detector plane was performed using a small home-built CMOS x-ray camera. This is an updated version[38] of an earlier camera[39] that has seen good use in a lower-energy XES instrument.[40-43] The camera has a 3.2 × 5.6 mm^2 field of view. It was mounted on a micrometer-driven vertical translation stage and manually repositioned to achieve mosaic coverage of the x-ray intensity's spatial distribution. Furthermore, the camera's ability to identify both the location and energy of individual x-ray photons allowed the rejection of stray fluorescence by energy-windowing.

Ray tracing software written in Mathematica was used to assess Johann error and beam spreading perpendicular to the Rowland plane due to sagittal error, i.e., the use of optics whose second radius of curvature is not equal to the perpendicular distance from the optic center to the line connecting the source and detector points on the Rowland circle (the sagitta). Unlike recent work aiming to give an advanced treatment of the interplay between strain effects and, e.g., dynamical diffraction in SBCAs,[44, 45] here we only seek purely geometric optics effects on slightly sub-mm length scales. Consequently, the Monte-Carlo ray tracing code generated x-rays from a 1-mm diameter source spot, reflected them from the bent optic using simple, specular Bragg reflection assuming zero wafer miscut, and then recorded the position of the intersection of those rays with the detector plane.

Transmission-mode XAFS measurements were performed on a 6-μm thick Ni foil from EXAFS Materials. XES measurements were performed on a 75-μm thick sheet of commercial Cu foil. All measurements were performed with the sample in air under ambient conditions, and a helium space was used to reduce air-absorption. In some cases, small corrections for slow leaks in the helium space have been made to ensure that all comparisons are on a common efficiency basis. All XAFS spectra were dead time corrected and subsequently processed in

Athena where standard background removal and normalization procedures were followed.[46] For XES, all spectra are dead time corrected and approximately aligned to a common energy scale.

3. Results

Optic performance encompasses both its focal properties, as this is crucial for coupling to the final detector, and also its energy resolution. We begin with focal properties. In Fig. 4-3 we present the x-ray intensity in the detector plane for the commercial, anodically bonded Si (551) SBCA and for a Si (711) wafer in VF-BCA-1, VF-BCA-2, and VF-BCA-3 (see Table 4-1 for the definitions of these terms). Note that these two crystal orientations have the same *d*-spacing, and consequently are identical for present purposes, giving the same energy range over the same span of Bragg angles. The qualitative agreement is very good. All optics show strong in-Rowland-plane focusing and also the expected degree of out-of-Rowland-plane focusing subject to sagittal distortion. VF-BCA-2 and VF-BCA-3, which are based on machined, unpolished metal forms, have slightly inferior focal properties. As discussed below, precision polishing of machined surfaces is an obvious future direction for improvement.

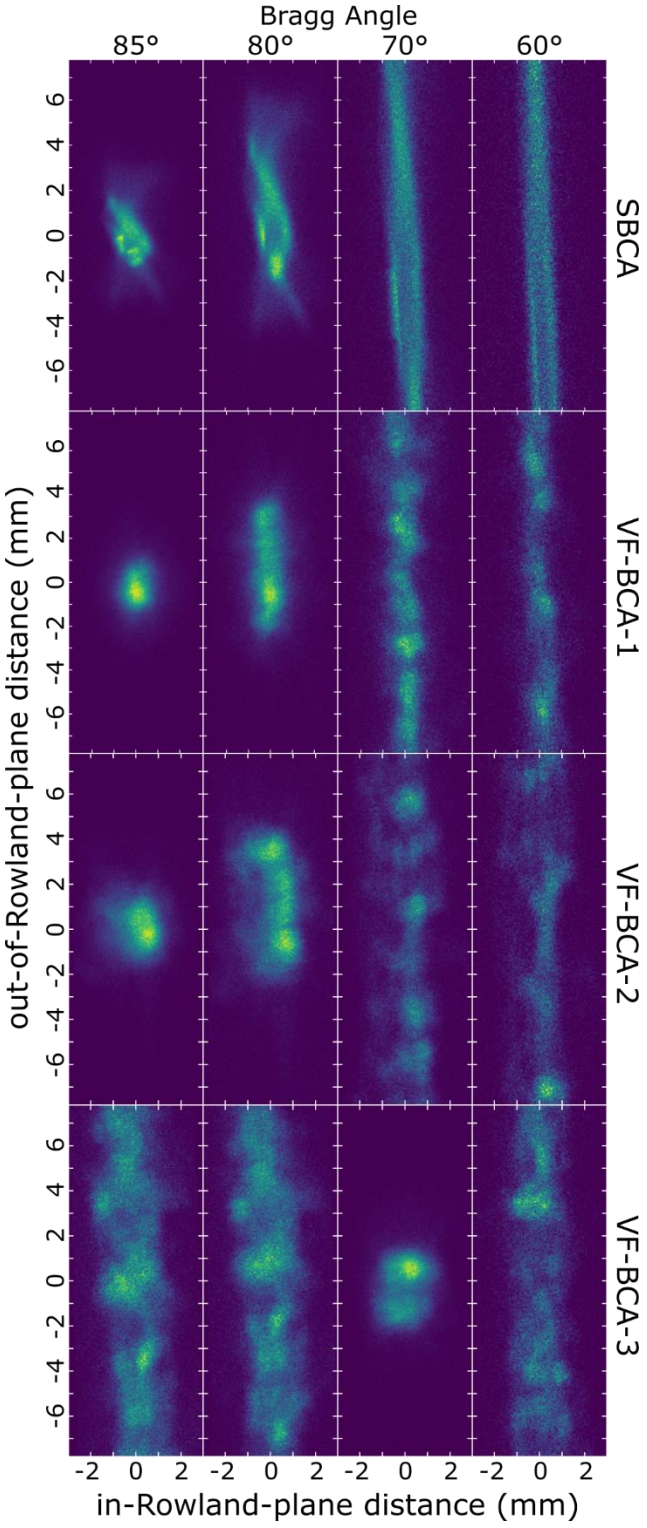

Fig. 4-3: Characterization of the spatial distribution of x-ray intensity on the detector plane from (top) a commercial Si (551) analyzer (SBCA); (second from top) VF-BCA-1 with a Si (711) wafer and (second from bottom) VF-BCA-2 with a Si (711) wafer; (bottom) VF-BCA-3 with a Si (711) wafer, a torus optimized for $\theta_B = 70$ °. The orientations are defined relative to the plane of the Rowland focusing circle. The colorscale of each frame is independently normalized; for a comparison of intensities, see Fig. 4-4.

In Fig. 4-4(a), we show the in-Rowland-plane intensity spread across the detector plane at different Bragg angles for each of the above optics and a Si (711) or equivalent wafer. Although the in-plane focal qualities of SBCA and VF-BCA-1 are similar, the profile of VF-BCA-2 is found to be broader and skewed. The out-of-Rowland-plane intensity spread is shown in Fig. 4-4(b). Near backscatter, the out-of-plane focal quality of both VF-BCA-1 and VF-BCA-2 is found to be comparable to the SBCA. At lower values of θ_B, VF-BCA-1 and VF-BCA-2 demonstrate clear inhomogeneities, although the total refocused intensity remains comparable.

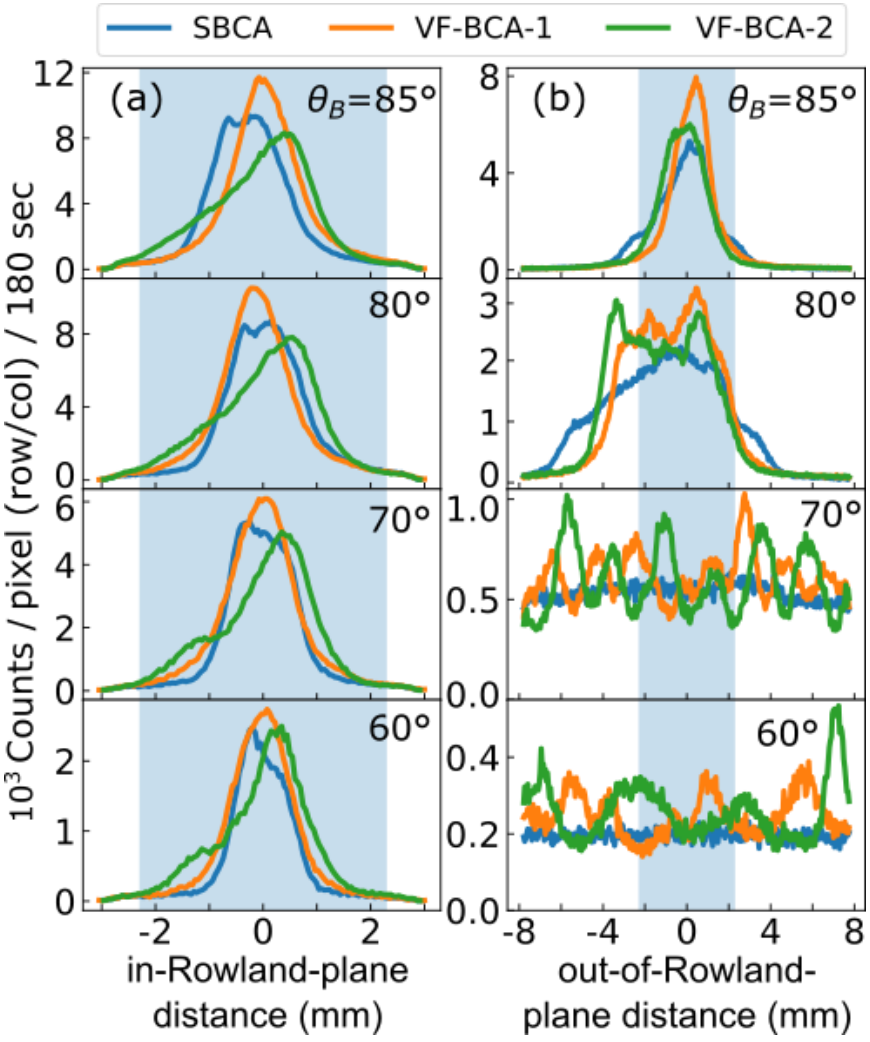

Fig. 4-4: (a) Comparison of beam profiles in the Rowland plane for different optics. (b) Comparison of beam profiles in the direction perpendicular to the Rowland plane different optics. The extent of the silicon SDD's active region is represented by the shaded regions.

For the out-of-plane focal quality, it is clear that the use of a SBCA sufficiently far away from backscatter ($\theta_B = 90$ deg) results in rapid spreading of the beam in the out-of-plane direction as expected from sagittal error. In this configuration, the out-of-Rowland-plane spread of the beam exceeds the height of the detector's active area, as shown in Fig. 4-4(b). This raises the question of using toroidal optics where the primary radius of curvature is dictated by the Rowland circle diameter but where the secondary radius of curvature is chosen for ideal point-to-point focusing for a selected 'design' Bragg angle θ^*. For the Johann geometry, with a Rowland circle of radius D, the secondary radius of curvature R^* is given by $R^* = D \sin^2 \theta_B$. Ray-tracing calculations for the out-of-plane beam height as a function of θ_B are shown in Fig. 4-5(a) for TBCA's having design θ^* varying from 55 to 90°, the lattermost being simply an SBCA. These simulations strongly suggest that TBCA should give a more efficient coupling to the finite-sized detector when the secondary radius of the TBCA is chosen to eliminate sagittal error for θ^* in the middle of the angular range dictated by the energies of interest. Consequently, in the bottom panel of Fig. 4-3 we show the intensity distributions on the detector plane for VF-BCA-3 with a Si (711) wafer. The out-of-plane focal properties of the TBCA are clearly much superior to the SBCA when θ_B is in the vicinity of the designed θ^*.

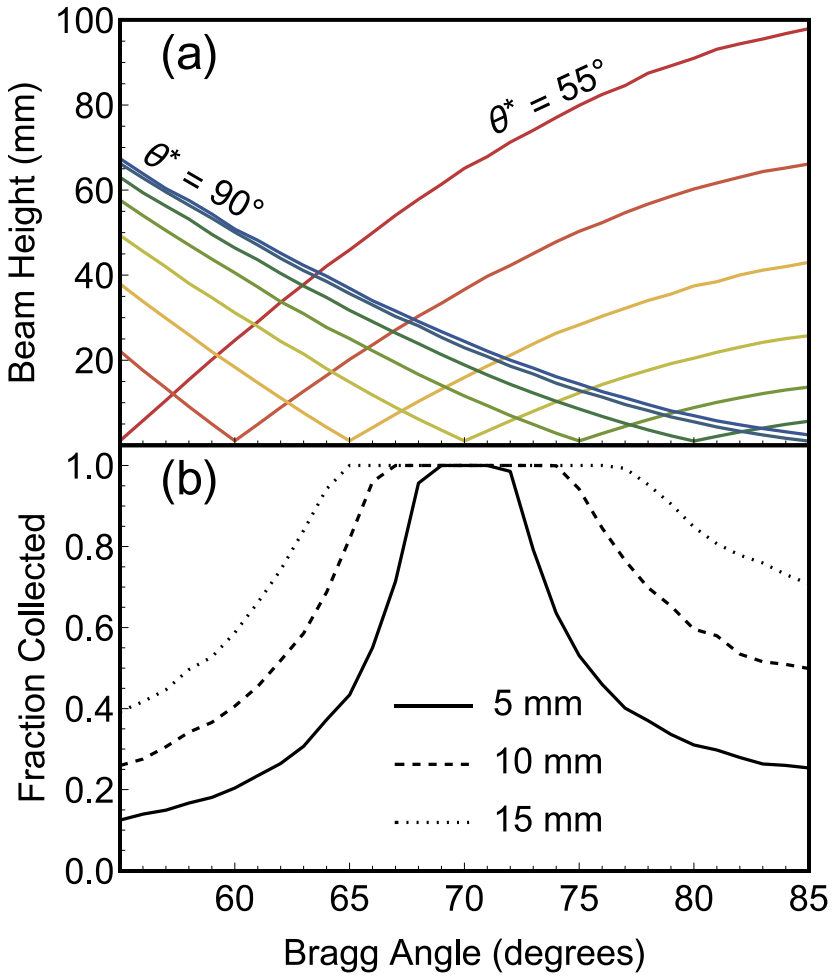

Fig. 4-5: (a) The modeled beam height as a function of θ_B for doubly-curved optics with a 1-m principal radius of curvature but with secondary curvatures designed for point-to-point focus as design Bragg angles θ^* varying in 5° steps from 55° to 90°, the latter being for a fully spherical analyzer. (b) For a θ^* = 70° toroidal optic, the modeled fraction of x-rays hitting three different circular detectors with diameters of 5 mm, 10 mm, and 15 mm.

The improved spectrometer performance when using a TBCA at θ_B near the designed θ^* is demonstrated in Fig. 4-6. Here, the intensity of x-rays refocused at the SDD by each optic is shown across the full angular range of the instrument. The very short detectors used in the test studies (~4.6-mm active height) gives an especially high sensitivity to out-of-Rowland-plane

beam spread, resulting in the narrow experimental Bragg angle range for optimum performance of the TBCA. Ray tracing calculations for TBCA simulating different detector heights are given in Fig. 4-5(b). In each case, there is an optimal, flat-top region of Bragg angles where all of the reflected x-rays are collected by the detector when the height of the reflected beam is smaller than the detector diameter. This agrees well with the experimental data of Fig. 6, which shows the same flat top near the θ^*, and a decrease in count rate far from θ^*. Further, the ray tracing demonstrates the utility of a larger detector which increases both the width of the flat-top region as well as the count rate when θ_B is far from θ^*.

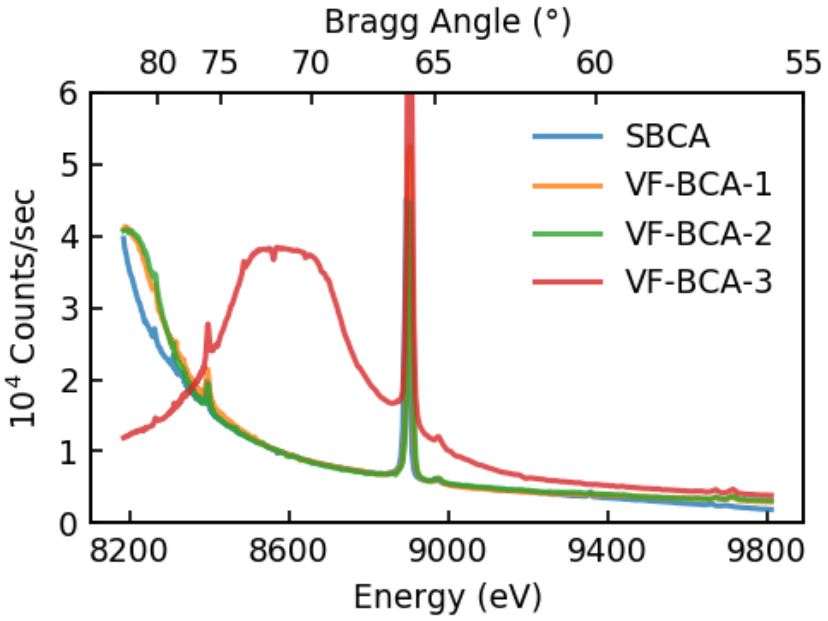

Fig. 4-6: Monochromator count rate as a function of photon energy using a Si (551) or equivalent wafer. The sharp features at, e.g., ~8900 eV, are Cu Kβ fluorescence lines from the heatsink of the x-ray tube anode. The rapid roll-off for the spherical optics is due the steadily increasing out-of-plane spread upon decreasing Bragg angle, causing the beam to become taller than the 4-mm active height of the SDD. The toroidal optic shows much improved performance in the designed Bragg angle range.

The preceding discussion has only addressed focal properties. Now we report on the energy resolution using the vacuum clamped optics. The measured Ni K-edge XANES for all optics using a Si (551) or equivalent wafer are shown in Fig. 4-7(a). It can be seen that all optics produced nearly identical spectra, suggesting a negligible loss in energy resolution from the commercial to vacuum clamped optics. The high quality of the XANES spectra is typical of modern laboratory based XAFS systems.[24, 25, 28, 47, 48] Indeed, Fig. 4-8 compares the energy resolution of the current measurements to literature results acquired at a synchrotron and confirms the present energy resolution provided by the commercial and temporary optics to be satisfactory for chemical analysis. Similarly, Fig. 4-7(b) presents again Ni K-edge XANES where the spectra are instead measured with the Si (444) reflection by several different optics. Again, spectra are nearly identical, with only minor differences observable in the extent of the shoulder at ~8334 eV and in the magnitude of the oscillation at ~8352 eV

In Fig. 4-7(c), Cu Kα XES results are presented for all optics using the Si (444) reflection. Here again, spectra were found to be nearly identical, however some small differences in peak ratios can be observed in accordance with small differences in energy resolution and also small differences in the angular response functions between optics. Recall again that the analyzed radiation is being imperfectly focused in the out-of-Rowland-plane dimension, with a spread larger than the detector height. Consequently, small changes in spectrometer alignment can lead to few-percent differences in net monochromator efficiency as a function of energy.

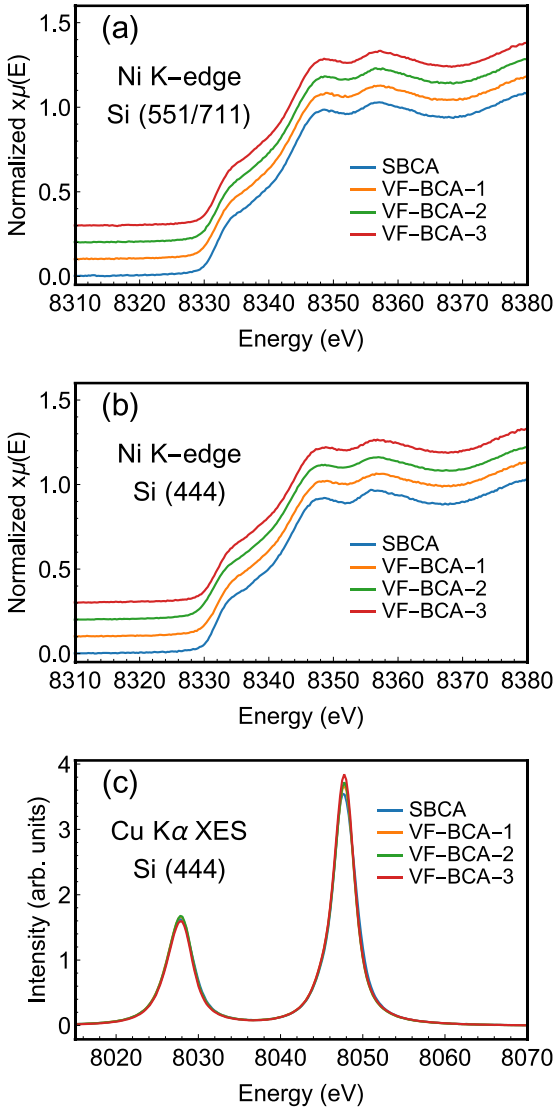

Fig. 4-7: Representative spectra demonstrating the capability of the vacuum-clamped optics to perform high-resolution measurements. (a) Comparison of Ni XANES measured with each optic using Si (551) or equivalent wafers. (b) Comparison of Ni XANES measured with each optic using Si (444) wafers. (c) Comparison of Cu Kα XES with each optic using Si (444) wafers.

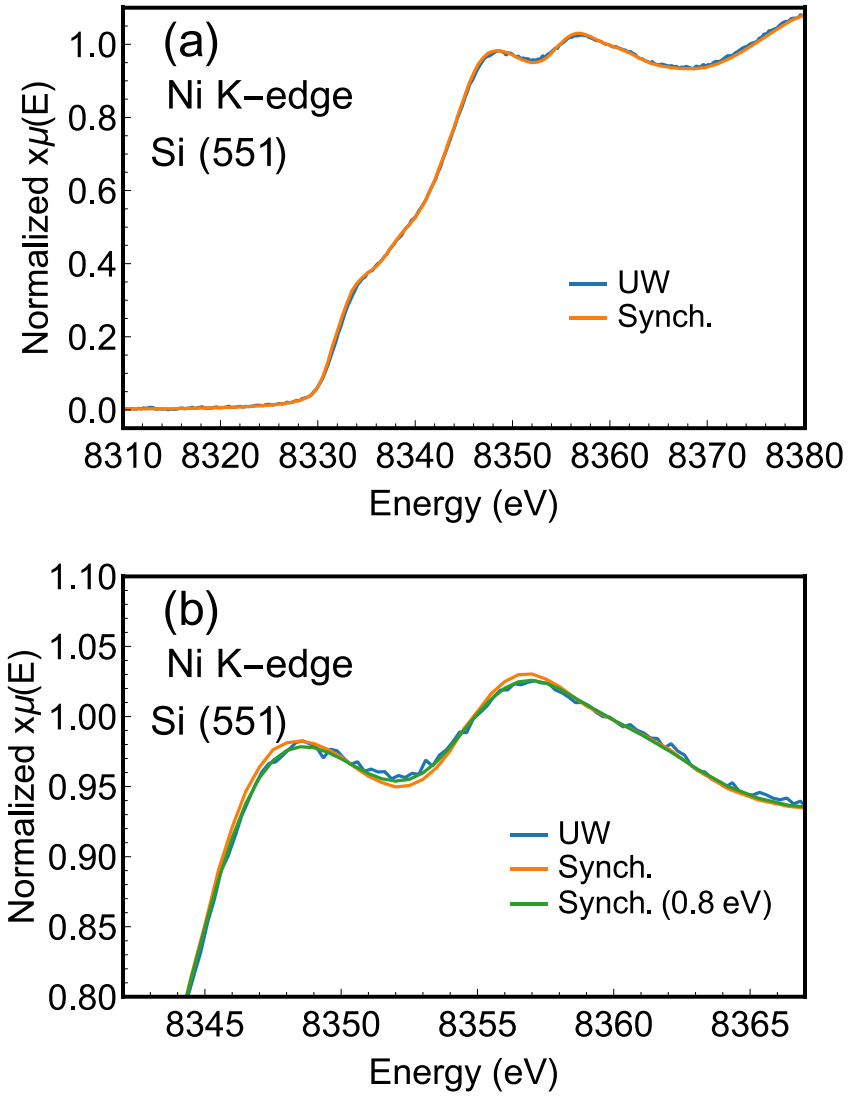

Fig. 4-8: Spectra demonstrating the energy resolution achievable in the instrument given a commercial optic. (a) Ni XANES measured with the Si (551) SBCA (UW) and at the synchrotron (Synch.) as referenced in Hephaestus.[46] (b) Comparison of a small region of the Ni XANES shown in (a) along with a spectrum representing the literature results after convolution with a 0.8 eV Gaussian in Athena.[46]

Given the success and limitations shown in this effort to make temporary doubly-bent crystal analyzers, there are several future directions that merit comment. First, the focal quality

of optics should be improved by lapping and polishing the surfaces of the machined forms, or by acquiring precision surface-ground glass forms for the toroidal case, in analogy to the high-quality lens used for the spherical case. While this is not particularly relevant for the ~1-eV resolution needed for many measurements in a point-to-point Rowland circle configuration, the same would not be true for higher-energy resolution applications or the important case of dispersive spectrometers based on spherical analyzers, as is commonly used at synchrotron light sources.[49-51] Second, the efficiency of each optic across wider angular ranges of the instrument could be improved by implementing a taller detector. Third, it would be interesting to explore forms with smaller primary radii of curvature or using wafers composed of crystalline materials besides silicon, each with the goal of obtaining higher signal levels. Fourth, although we have only used this method for intact round wafers, one should expect that the same apparatus can be used for segmented wafers, such as is used in the recent development of 0.5-m radius of curvature SBCAs,[9] or for pieces of multiple wafers integrated to obtain a larger BCA solid angle than could be obtained with any single wafer. This lattermost opportunity is likely relevant for materials where the *de facto* standard 10-cm diameter wafers are not available.

4. Conclusions

We report the development and performance of spherically and toroidally bent crystal analyzers for use in x-ray absorption and emission spectroscopies. Unlike the present practice of gluing or bonding the necessary crystalline wafers to a high-precision glass lens, we instead use only air pressure to hold the wafer against the shaping form that provides the necessary profile. The specifications for the shaping form are found to be rather modest, in that modern machined metal forms suffice and high-precision, high-cost surface ground lenses are not needed. The resulting optics demonstrate resolutions and efficiencies comparable to their commercially

available counterparts as determined by XANES and XES measurements using a laboratory spectrometer. These results establish a considerable convenience, simplicity, and flexibility that may prove useful for Rowland circle spectrometers in the lab for XAFS and XES studies, as well as at synchrotron and x-ray free electron laser x-ray facilities for XES, high-energy resolution fluorescence detection (HERFD), and resonant inelastic x-ray scattering (RIXS).

5. Acknowledgements

E. Jahrman was supported in part by the Joint Center for Energy Storage Research (JCESR), an Energy Innovation Hub funded by the U.S. Department of Energy, Office of Science, and Basic Energy Sciences, and by the U.S. Department of Energy through the Chemical Science and Engineering Division of Argonne National Laboratory. W. Holden and G. Seidler were supported by the Joint Plasma Physics Program of the National Science Foundation and the Department of Energy under Grant No. DE-SC0016251. R&D associated with the Los Alamos National Laboratory (LANL) spectrometer was funded under the Heavy Element Chemistry Program by the Division of Chemical Sciences, Geosciences, and Biosciences, Office of Basic Energy Sciences, U.S. Department of Energy and the U.S. Department of Energy. LANL is operated by Los Alamos National Security, LLC, for the National Nuclear Security Administration of U.S. Department of Energy (contract DE-AC52-06NA25396).

6. References

1. D. B. Wittry and S. Sun, J Appl Phys **71** (2), 564-568 (1992).
2. D. B. Wittry and S. Sun, J Appl Phys **69** (7), 3886-3892 (1991).
3. D. B. Wittry and S. Sun, J Appl Phys **67** (4), 1633-1638 (1990).
4. D. B. Wittry and S. Sun, J Appl Phys **68** (2), 387-391 (1990).
5. D. B. Wittry and W. Z. Chang, J Appl Phys **72** (8), 3440-3446 (1992).
6. A. Hauer, J. D. Kilkenny and O. L. Landen, Review of Scientific Instruments **56** (5), 803-805 (1985).
7. G. Askari Germi, S. J. Pestehe and A. Rastkar Ebrahimzadeh, Journal of Applied Crystallography **50** (4), 1104-1116 (2017).

8. R. Verbeni, M. Kocsis, S. Huotari, M. Krisch, G. Monaco, F. Sette and G. Vanko, Journal of Physics and Chemistry of Solids **66** (12), 2299-2305 (2005).
9. M. Rovezzi, C. Lapras, A. Manceau, P. Glatzel and R. Verbeni, Review of Scientific Instruments **88** (1), 013108 (2017).
10. M. Krämer, K. Kuzushita, S. Maeo, T. Utaka and K. Taniguchi, Spectrochimica Acta Part B: Atomic Spectroscopy **63** (12), 1408-1414 (2008).
11. E. Collart, A. Shukla, F. Gelebart, M. Morand, C. Malgrange, N. Bardou, A. Madouri and J.-L. Pelouard, Journal of Synchrotron Radiation **12** (4), 473-478 (2005).
12. P. Suortti, T. Buslaps, V. Honkimäki, N. Hiraoka and U. Lienert, Zeitschrift für Physikalische Chemie **220** (7), 831-847 (2006).
13. J. A. Maj and C. Harmata, United States Patent No. 20120256332 (2012).
14. H. Okuda, K. Nakajima, K. Fujiwara, K. Morishita and S. Ochiai, Journal of Applied Crystallography **41** (4), 798-799 (2008).
15. A. H. Said, H. Sinn and R. Divan, Journal of Synchrotron Radiation **18** (3), 492-496 (2011).
16. S. Huotari, C. J. Sahle, C. Henriquet, A. Al-Zein, K. Martel, L. Simonelli, R. Verbeni, H. Gonzalez, M. C. Lagier, C. Ponchut, M. M. Sala, M. Krisch and G. Monaco, J. Synchrot. Radiat. **24**, 521-530 (2017).
17. R. Verbeni, T. Pylkkanen, S. Huotari, L. Simonelli, G. Vanko, K. Martel, C. Henriquet and G. Monaco, J. Synchrot. Radiat. **16**, 469-476 (2009).
18. T. T. Fister, G. T. Seidler, L. Wharton, A. R. Battle, T. B. Ellis, J. O. Cross, A. T. Macrander, W. T. Elam, T. A. Tyson and Q. Qian, Rev. Sci. Instrum. **77** (6), 063901 (2006).
19. D. Sokaras, D. Nordlund, T. C. Weng, R. A. Mori, P. Velikov, D. Wenger, A. Garachtchenko, M. George, V. Borzenets, B. Johnson, Q. Qian, T. Rabedeau and U. Bergmann, Rev. Sci. Instrum. **83** (4), 043112 (2012).
20. D. Sokaras, T. C. Weng, D. Nordlund, R. Alonso-Mori, P. Velikov, D. Wenger, A. Garachtchenko, M. George, V. Borzenets, B. Johnson, T. Rabedeau and U. Bergmann, Rev. Sci. Instrum. **84** (5), 053102 (2013).
21. I. Llorens, E. Lahera, W. Delnet, O. Proux, A. Braillard, J. L. Hazemann, A. Prat, D. Testemale, Q. Dermigny, F. Gelebart, M. Morand, A. Shukla, N. Bardou, O. Ulrich, S. Arnaud, J. F. Berar, N. Boudet, B. Caillot, P. Chaurand, J. Rose, E. Doelsch, P. Martin and P. L. Solari, Rev. Sci. Instrum. **83** (6), 063104 (2012).
22. M. M. Sala, K. Martel, C. Henriquet, A. Al Zein, L. Simonelli, C. J. Sahle, H. Gonzalez, M. C. Lagier, C. Ponchut, S. Huotari, R. Verbeni, M. Krisch and G. Monaco, J. Synchrot. Radiat. **25**, 580-591 (2018).
23. E. Kleymenov, J. A. van Bokhoven, C. David, P. Glatzel, M. Janousch, R. Alonso-Mori, M. Studer, M. Willimann, A. Bergamaschi, B. Henrich and M. Nachtegaal, Rev. Sci. Instrum. **82** (6), 065107 (2011).
24. G. T. Seidler, D. R. Mortensen, A. J. Remesnik, J. I. Pacold, N. A. Ball, N. Barry, M. Styczinski and O. R. Hoidn, Review of Scientific Instruments **85** (11), 113906 (2014).
25. G. T. Seidler, D. R. Mortensen, A. S. Ditter, N. A. Ball and A. J. Remesnik, Journal of Physics: Conference Series **712** (1), 012015 (2016).
26. D. R. Mortensen, G. T. Seidler, J. J. Kas, N. Govind, C. P. Schwartz, S. Pemmaraju and D. G. Prendergast, Physical Review B **96** (12), 125136 (2017).

27. D. R. Mortensen, G. T. Seidler, A. S. Ditter and P. Glatzel, Journal of Physics: Conference Series **712** (1), 012036 (2016).
28. E. P. Jahrman, W. M. Holden, A. S. Ditter, D. R. Mortensen, G. T. Seidler, T. T. Fister, S. A. Kozimor, L. F. J. Piper, J. Rana, N. C. Hyatt and M. C. Stennett, Review of Scientific Instruments **Submitted** (2018).
29. W. M. Holden, O. R. Hoidn, A. S. Ditter, G. T. Seidler, J. Kas, J. L. Stein, B. M. Cossairt, S. A. Kozimor, J. Guo, Y. Ye, M. A. Marcus and S. Fakra, Review of Scientific Instruments **88** (7), 073904 (2017).
30. R. A. Valenza, E. P. Jahrman, J. J. Kas and G. T. Seidler, Phys Rev A **96** (3), 032504 (2017).
31. M. E. Mundy, D. Ung, N. L. Lai, E. P. Jahrman, G. T. Seidler and B. M. Cossairt, Chem Mater **30** (15), 5373-5379 (2018).
32. W. M. Holden, G. T. Seidler and S. Cheah, The Journal of Physical Chemistry A **122** (23), 5153-5161 (2018).
33. H. H. Johann, Zeitschrift Fur Physik **69** (3-4), 185-206 (1931).
34. P. Glatzel and U. Bergmann, Coordin Chem Rev **249** (1-2), 65-95 (2005).
35. D. R. Mortensen and G. T. Seidler, J Electron Spec **215**, 8-15 (2017).
36. M. E. Mundy, D. Ung, N. L. Lai, E. P. Jahrman, G. T. Seidler and B. M. Cossairt, Chem Mater (2018).
37. E. P. Jahrman, G. T. Seidler and J. R. Sieber, Analytical Chemistry **90** (11), 6587-6593 (2018).
38. W. M. Holden, O. R. Hoidn, G. T. Seidler and A. D. DiChiara, Rev. Sci. Instrum. **accepted** (2018).
39. O. R. Hoidn and G. T. Seidler, Review of Scientific Instruments **86** (8), 086107 (2015).
40. W. M. Holden, O. R. Hoidn, A. A. Ditter, G. T. Seidler, J. Kas, J. Stein, C. B.M., S. A. Kozimor, J. Guo, Y. Ye, M. A. Marcus and S. Fakra, Rev. Sci. Instrum. **88** (7), 073904 (2017).
41. W. M. Holden, G. T. Seidler and S. Cheah, Journal of Physical Chemistry A **122** (23), 5153-5161 (2018).
42. J. L. Stein, W. M. Holden, A. Venkatesh, M. E. Mundy, A. J. Rossini, G. T. Seidler and B. M. Cossairt, Chem Mater (2018).
43. B. M. Cossairt, J. L. Stein, W. M. Holden and G. T. Seidler, SID Symposium Digest of Technical Papers **49** (1), 21-24 (2018).
44. A.-P. Honkanen, C. Ferrero, J.-P. Guigay and V. Mocella, Journal of Applied Crystallography **51** (2), 514-525 (2018).
45. A.-P. Honkanen, G. Monaco and S. Huotari, Journal of Applied Crystallography **49** (4), 1284-1289 (2016).
46. B. Ravel and M. Newville, Journal of Synchrotron Radiation **12** (4), 537-541 (2005).
47. R. Bès, T. Ahopelto, A. P. Honkanen, S. Huotari, G. Leinders, J. Pakarinen and K. Kvashnina, Journal of Nuclear Materials **507**, 50-53 (2018).
48. Z. Németh, J. Szlachetko, É. G. Bajnóczi and G. Vankó, Review of Scientific Instruments **87** (10), 103105 (2016).
49. S. Huotari, T. Pylkkänen, R. Verbeni, G. Monaco and K. Hämäläinen, Nature Materials **10**, 489 (2011).
50. S. Huotari, F. Albergamo, G. Vankó, R. Verbeni and G. Monaco, Review of Scientific Instruments **77** (5), 053102 (2006).

51. S. Huotari, G. Vankó, F. Albergamo, C. Ponchut, H. Graafsma, C. Henriquet, R. Verbeni and G. Monaco, Journal of Synchrotron Radiation **12** (4), 467-472 (2005).

Chapter 5. Spherically Bent Mica Analyzers as Universal Dispersing Elements for X-ray Emission Spectroscopy

In preparation for publication: E. S. Joseph, E. P. Jahrman, and G. T. Seidler. Journal of Synchrotron Radiation (2019). E. P. Jahrman assisted in the initial characterization of the mica materials, and led the eventual X-ray absorption fine structure component of the study. This chapter represents a significant portion of this dissertation and, as such, significant efforts were devoted to its completion.

Spherically-bent crystal analyzers (SBCAs) are the most common optics used in high-resolution hard x-ray spectroscopy, whether at the synchrotron or in the laboratory. While Si and Ge are the most frequently used diffractive components of SBCAs, we consider here the somewhat classical choice of muscovite mica as the dispersing element. We find that the various harmonics of a highest-quality mica-based SBCA show ~5% to ~40% of the integral reflectivity of a typical Si or Ge SBCA in the hard x-ray range, and that the mica SBCA have comparable energy resolution to the traditional SBCA. Interestingly, the choice of mica comes with a practical benefit: the primary (0,0,2) reflection has sufficiently strong harmonics that are fairly tightly spaced in energy so that they span the complete energy range from ~4 keV to ~11 keV when used at convenient Bragg angles. Hence, a single mica SBCA can be used for every K-shell emission line of 3d transition metals and every L-shell emission line of the lanthanide elements simply by selecting the correct mica (0,0,2) harmonic with a final energy-dispersive solid state detector. Hence, the loss in efficiency is counteracted by an operational efficiency, the 'universal' application of a single analyzer over a very large range of elements. This performance suggests

future application of mica SBCAs in both laboratory-based XES and synchrotron-based photon-in, photon-out spectroscopies in the hard x-ray range.

1. Introduction

High-resolution x-ray spectroscopies based on photon emission (x-ray fluorescence) in the few keV to ~20 keV range have a strong scientific profile in research on catalysis,[1-3] correlated electron physics,[4-7] and heavy element chemistry,[8-11] to name three prominent examples. At synchrotron light sources, this includes high-energy resolution fluorescence detection to decrease core-hole lifetime broadening, resonant inelastic x-ray scattering, and both resonant and nonresonant x-ray emission spectroscopy.[12-17] There is also a renewed and growing trend to perform nonresonant x-ray emission spectroscopy in the laboratory.[18-24]

Typically, these measurements at ~1-eV or finer energy resolution use Bragg analyzers to provide the necessary wavelength discrimination. While some other configurations are also employed,[25-28] the dominant analyzer for high-resolution studies of x-ray fluorescence, usually called x-ray emission spectroscopy (XES) in the synchrotron community, is spherically bent crystal analyzers (SBCAs) on the Rowland circle.[20, 23, 29, 30] Semiconductor-industry grade Si and Ge are the most commonly used diffracting elements in SBCAs, although quartz, GaAs, and other very high quality single crystal materials are occasionally used. When using perfect single crystals, the principle of operation of the Rowland circle is illustrated in Fig. 5-1a. The performance of these optics is outstanding, but from a pragmatic standpoint there is the problem: each such optic typically covers only a modest energy range at useful Bragg angles, and consequently both synchrotron endstations and laboratory-based facilities must purchase or fabricate a suite of such analyzers to cover the various fluorescence lines of any significant number of elements. Thes3e considerations are compounded at synchrotron endstations that seek to measure the most dilute systems and hence multiplex several SBCA to increase solid angle.

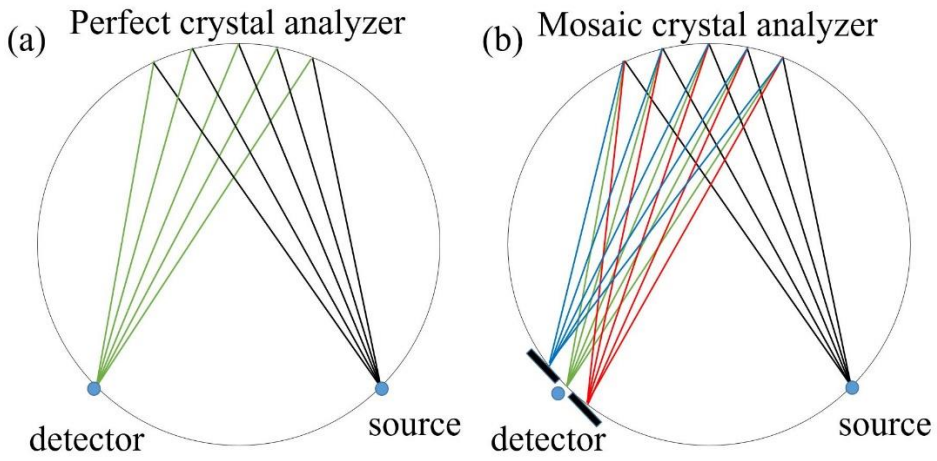

Fig. 5-1: Discussion of the relationship between analyzer mosaicity and energy resolution. (a) The usual Rowland configuration with a perfect crystal analyzer, where a polychromatic source results in a single monochromatic refocused spot. (b) For a mosaic crystal analyzer, some small range of Bragg angles is accessed resulting in a band of spectrally-unique refocal spots on the detector side of the Rowland circle, moving from lower energy (red) closer to backscatter to higher energy (blue) farther from backscatter.

This problem motivates us to study muscovite mica (henceforth 'mica') as a candidate diffractive material in SBCAs for XES. Specifically, we choose to study mica because of its many strong, closely-spaced high-order (0,0,2*n*) Bragg reflections in the hard x-ray range.[31] This situation suggests that a single SBCA using a mica diffracting element could be used for XES studies over a very wide energy range, using the energy resolution of the final solid-state detector to select an appropriate Bragg harmonic for the fluorescence line of interest. Mica has a long history in x-ray analysis,[32-44] most commonly for lower-energy x-rays because of its large *d*-spacing, but also benefitting from its high flexibility, easily enabling curved Bragg optics, and its often high crystallinity in natural form. These benefits, however, are countered by the nontrivial mosaic spread in natural mica. In a Rowland circle spectrometer, mosaic spread has two main

effects. First, as shown in Fig. 5-1b, a point source results in dispersion on the detector arc, requiring either a position sensitive detector (not shown) or a simple detector slit to recover the optic's finest energy resolution. This dispersion is, of course, still subject to source broadening and other degradations in actual operation. Second, a mosaic spread can increase the practical total reflectivity in Bragg analyzers,[45, 46] a subtlety that can be expected to partially offset the lower atomic form factors and imperfect constructive interference in the large mica unit cell, when compared to, e.g., Si or Ge.

With this motivation given, three issues arise. First, we need to investigate the energy resolution of mica SBCAs. Second, the efficiency of mica SBCAs across multiple harmonics needs to be compared, head-to-head, against that of traditional Si or Ge SBCAs. Finally, the impact of the particular mica sample in the SBCA, i.e., its mosaic spread, needs to be correlated with the above two performance factors. Our investigation of these issues demonstrates that the harmonics of a simple vacuum-formed mica-based SBCA using high-quality mica have ~5% to ~40% the efficiency of traditional Si or Ge SBCA in the 4 keV to 11 keV energy range and typically comparable energy resolution, all while providing operation over that energy range with a single optic, i.e., a 'universal' analyzer for this energy range. We propose that the lost analyzer efficiency will in many cases be irrelevant (i.e., when studying concentrated samples with strong fluorescence) and in other cases is offset by matters of convenience or cost (i.e., when the needed Si or Ge analyzer is not immediately available or is cost-prohibitive). As such, we see considerable potential for future use of mica in SBCA in both synchrotron facilities and laboratory-based spectrometers.

2. Methods

Mica was acquired in many different grades from several vendors. Sample 'mica 1' is a 'highest-grade' mica from Changchun Taiyuan Fluorophlogopite Co., having dimensions of approximately 4.89 cm x 4.94 cm and thickness of 0.2 mm. Sample 'mica 2' is grade 'V1' from Ted Pella Co., having dimensions of approximately 4.98 cm x 7.53 cm and thickness of 0.275 mm. These were compared to two lower-grade micas. Sample 'mica 3' was 'stove mica' from Asheville Mica Co., and 'mica 4' was 'muscovite block mica', also from Asheville. Sample mica 3 was cut to have an area of ~78 cm^2, while mica 4 was cut to have area of ~60 cm^2.

The mica SBCA use the vacuum form methods recently described in Jahrman, et al.[47] Briefly, the mica samples are placed on top of a high-quality concave glass lens having a 1.00-m radius of curvature, and then these components are placed together into a small vacuum chamber that is sealed with a flexible polyimide window over the face of the mica. When vacuum is established, air pressure then forces the mica to take the shape of the glass lens. The resulting assembly is then placed into the analyzer location in the spectrometer and otherwise operates with the same protocols as a commercial analyzer having the same radius of curvature. The same process when applied to Si wafers gave SBCAs with performance quite similar to those of glued or bonded commercial SBCA.

The mica SBCA performance was tested for both x-ray absorption fine structure (XAFS) and also XES using a laboratory-based monochromator based on a 1-m Rowland circle. This instrument uses a 100-W conventional x-ray tube (Varex VF-80) and a small silicon drift diode (SDD, from Amptek) as source and detector, respectively. The instrument has been described in detail elsewhere,[20] wherein numerous applications are presented that show approximately synchrotron-level energy resolution. For example, this instrument has recently been used in

several combined x-ray photoelectron spectroscopy and x-ray absorption fine structure to determine the relative surface and bulk oxidation state of transition metals in nanophases.[48-50] In the present paper, all data was collected with a Pd anode operated at 35 kV accelerating potential and 2.855 mA electron beam current.

For means of comparison, efficiency measurements were also taken on traditionally bonded or glued Si (5,5,1), Si (1,1,0), and Ge (6,2,0) spherically bent crystal analyzers (XRS Tech LLC.). These optics are 10-cm diameter and again have a 1-m radius of curvature. When comparisons are made across the family of mica analyzers or between mica and traditional SBCAs, we use units normalized to the surface area of the relevant Bragg element. As a measure of energy resolution, we perform XAFS of the Ni K-edge for a standard Ni foil (Exafs Materials), Fig. 5-2. These spectra were collected using the (0,0,26) harmonic of mica as selected by the energy dispersive SDD. For this harmonic, the Ni K-edge position is at a Bragg angle of ~76°. For each mica grade, spectra were collected in two configurations. In the first, the active region of the detector was fully exposed in the direction of the SBCA. In the second, a Pb mask with a central slit was used to limit the extent of x-rays reaching the detector to 1 mm in the Rowland plane, while the direction out of the Rowland plane was left unobstructed. Spectra were collected from a photon energy ~80 eV below the K-edge to a photoelectron momentum of 14 $Å^{-1}$ above the edge. Data were normalized in Athena and compared to a reference Ni foil spectrum from Hephaestus.[51]

As a demonstration sample to highlight the wide energy range of the mica analyzers for XES, a 'mixed pellet' sample was made consisting of roughly equal masses of MnO, Fe_2O_3, Co_3O_4, CuO, ZnO, CeO_2, and Eu_2O_3 mixed with hexagonal BN and pressed into a 13-mm diameter pellet. All source chemicals were 99% or greater purity.

3. Results and Discussion

To begin, we characterize the energy resolution of the mica analyzers. As a convenient test case, we choose XAFS at the Ni K-edge. Note that a previous publication compared this reference spectrum to one acquired in the present spectrometer with a conventional SBCA or with a Si wafer in the temporary vacuum-formed optic, and that in that case the energy resolution in each configuration was found to be roughly comparable.[47] Results for the present study are shown in Figure 5-2. The spectra collected with exposed detectors demonstrated somewhat degraded energy resolution in all cases. However, the higher-quality mica 1 and mica 2 SBCAs recovered spectra roughly identical to the reference spectrum upon use of a 1-mm detector slit.

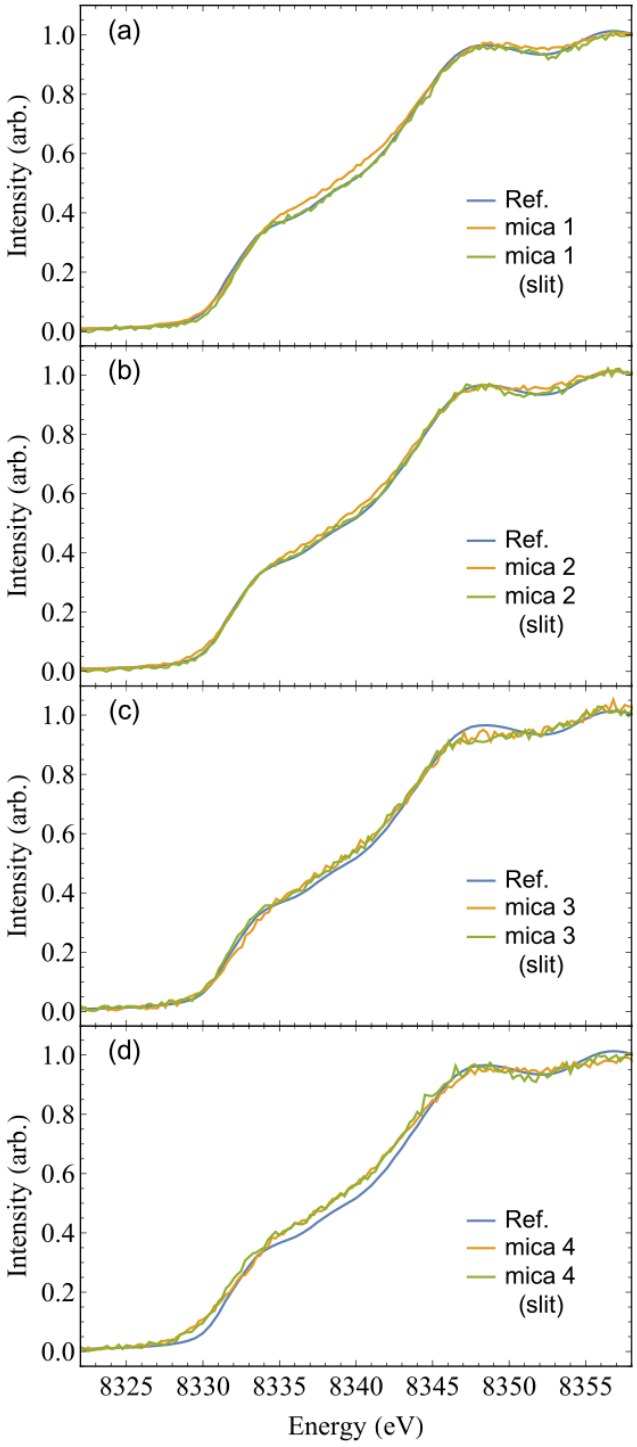

Fig. 5-2: The Ni K-edge XANES spectrum of a Ni foil. Each mica grade is separated into a separate subpanel and was tested with and without a 1-mm wide Pb detector slit ('slit' in the figure panels), so as to investigate the degradation due to the mosaic spread of the various mica samples. In each subpanel, the collected XANES spectra were compared to a spectrum collected at APS 13ID and reported in the Hephaestus package.[51]

Next, we study the reflection efficiency of the mica SBCAs compared across mica quality and also compared to standard Si and Ge SBCAs. In Fig. 5-3a we show energy dispersive x-ray spectra for the four mica SBCAs, these detector exposures were acquired in the spectrometer with the source and detector at Bragg angles of 85°. The many peaks are the result of Bragg scattering from the broad bremsstrahlung spectrum of the x-ray tube from the indicated (0,0,*l*) harmonics with *l* even. The widths of the observed energy peaks are due to the limited energy resolution of the SDD. The observed count rates have been normalized by the area of the respective mica samples. The two higher-quality micas show superior reflectivity, with mica 1 (Changchun Co.) noticeably outperforming all other mica SBCAs. Note that we have not attempted to correct for air absorption, which strongly attenuates lower energies, or for the shape of the bremsstrahlung energy spectrum from the x-ray tube. In Fig. 5-3b we compare the 'mica 1' SBCA to three commercial SBCAs. Intensities have again been normalized by the areas of the respective SBCA. While inferior to the Si and Ge efficiency, the mica 1 SBCA is clearly still useful, and in many cases reaches ~40% the efficiency of a nearby Si or Ge reflection.

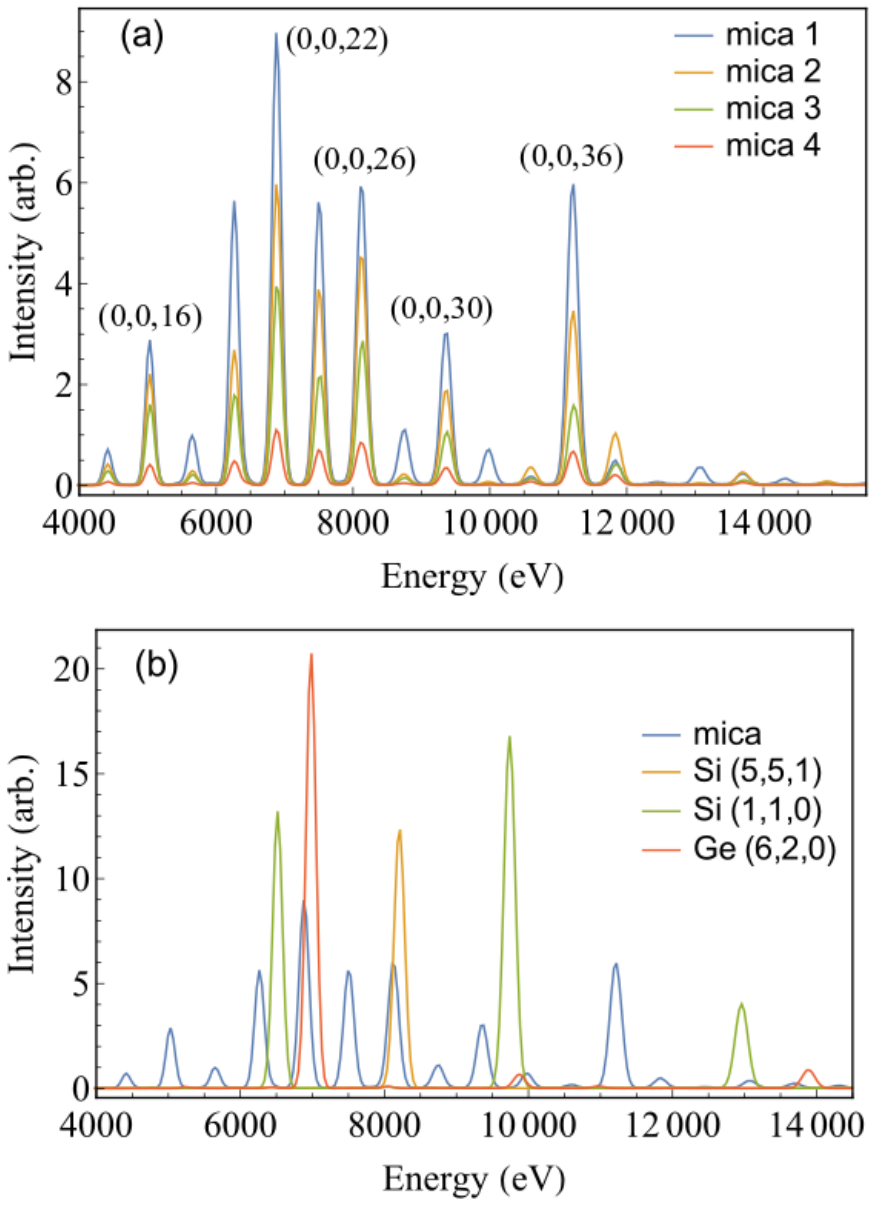

Fig. 5-3: Energy dispersive x-ray spectra taken at 85 degrees Bragg angle. All intensities are in units of counts per second per unit analyzer crystal area. (a) Comparison of efficiencies for the four mica spherically bent analyzers. Several of the (0,0,*l*) reflections of mica are labeled. (b) Comparison of the mica 1 analyzer to the three indicated commercial analyzers.

Given the demonstrated energy resolution and efficiency, we now move to the proposed application of mica SBCA: x-ray emission spectroscopy. Using the 'mixed pellet' sample of

seven metal oxides (see methods), we show in Fig. 5-4 the result of an XES scan from ~55.8° to 82.5° Bragg angle at 30 seconds integration per point. The angle steps were chosen to provide constant 0.25 eV energy steps for radiation analyzed on the mica (0,0,22) reflection. Every strong fluorescence line from the seven metal elements in the 'mixed pellet' is observed in a single scan across the angular range specified above. In some cases, fluorescence lines are observed in more than one harmonic channel, such as the appearance of the Cu Kβ in each of the (0,0,24), (0,0,26), and (0,0,28) harmonics at appropriately different Bragg angles. The multipliers shown under the harmonic labels in the figure show the necessary scaling to bring the observed peaks to the same height for ease of presentation. The quite large multiplier for the (0,0,14) is substantially due to strong air absorption (which also contributes to the low net harmonic intensity in Figures 5-3 and 5-4) and also because of stronger sample-internal absorption of the low-energy fluorescence. The lowest-energy peaks in the weak (0,0,14) reflection are SDD escape peaks from the very high intensity fluorescence lines in the (0,0,20) reflection.

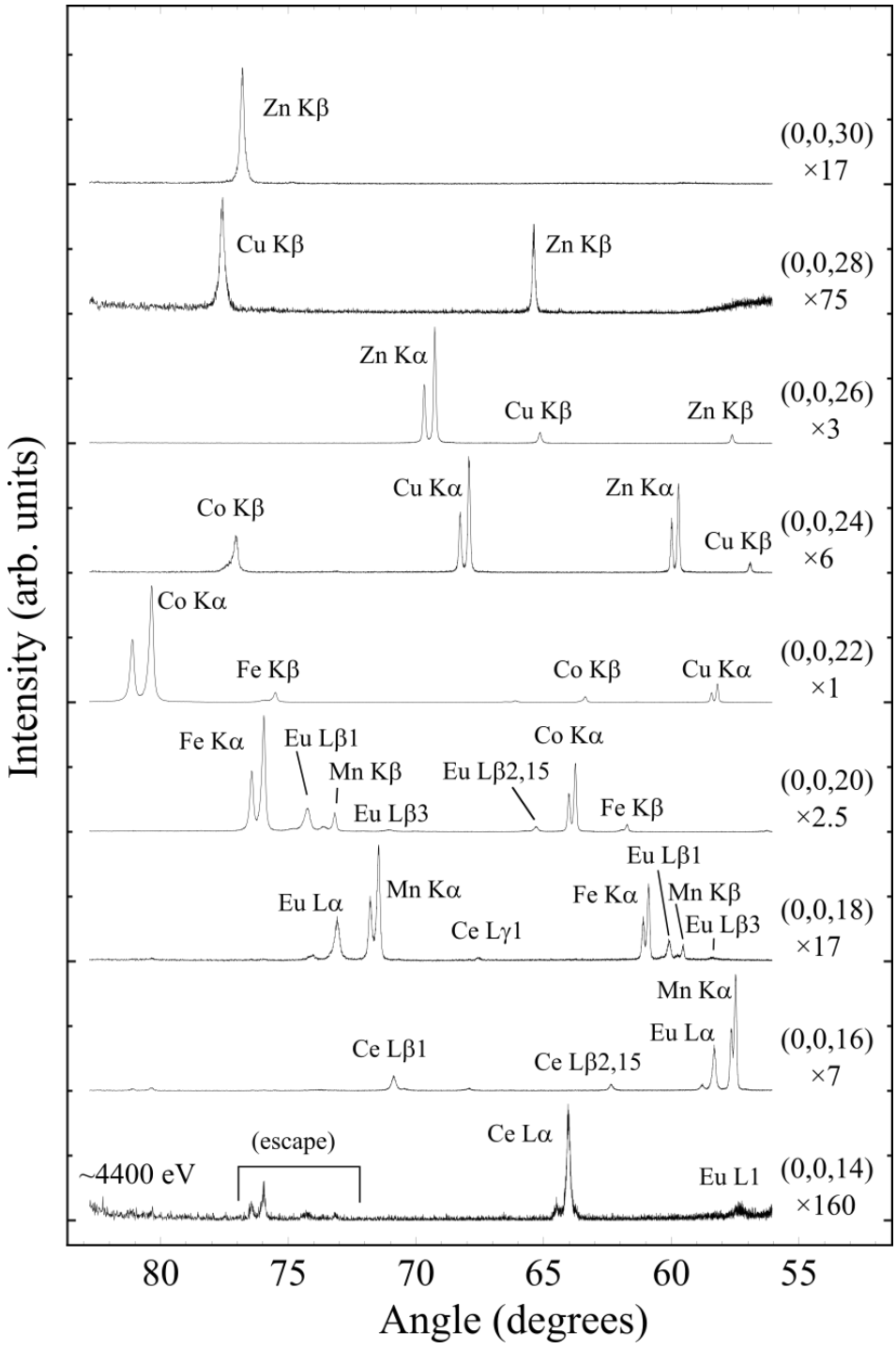

Fig. 5-4: X-ray emission spectra for each harmonic of the mica 1 SBCA as a function of Bragg angle, using the energy resolution of the SDD to select independent regions of interest for each of the nonvanishing harmonics from (0,0,14) to (0,0,30). The multipliers under the (0,0,*l*) label indicated the data scaling needed to bring the signal to common levels for purposes of display. The cluster of weak peaks marked 'escape' at ~75 degrees on the (0,0,14) reflection are from detector escape peaks from the high intensities on the (0,0,20) reflection.

It is useful to perform an additional head-to-head comparison between the mica 1 analyzer and conventional SBCAs. This is shown in Fig. 5-5, where the Cu Kα doublet has been studied with SBCAs made from mica 1, Ge (6,2,0), and Si (4,4,4). The different apparent energy resolutions are partly due to different analyzer quality but are significantly influenced by source-size broadening. Note that the Bragg angles are 79.3°, 67.9°, and 59.5°, for the Si (444), mica, and Ge (620) analyzers, respectively. In any event, the energy resolution of the mica analyzer is again at least roughly comparable to traditional SBCAs, and certainly sufficient for the great majority of nonresonant XES studies.

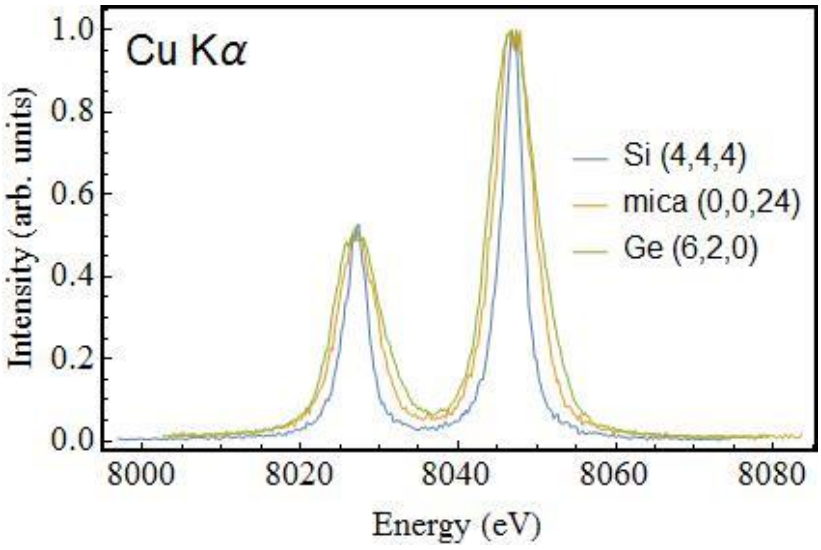

Fig. 5-5: Comparison of the mica 1 SBCA with standard analyzers commercial analyzers, all applied to the Cu Kα fluorescence line. The differing apparent energy resolutions are partly due to analyzer quality and partly due to different source broadening at the three different Bragg angles used in the study.

Looking to the future, the main issue in the present context will be to either obtain larger pieces of the highest quality mica plates, or else to tile several smaller plates onto a single SBCA. Recall that the results above for count rates have been normalized to the area of the

respective samples. An added future direction of considerable interest would be to fabricate mica doubly curved analyzers having much smaller radii of curvature in either spherical or toroidal geometries. Such analyzers would allow miniaturization of the overall spectrometer design and thus make it simpler to engineer a system that can perform at lower photon energies, likely using a 'color' x-ray camera to sort harmonics, similar to what has been achieved recently with a Si cylindrical analyzer.[18, 52]

4. Conclusions

We characterize the energy resolution and reflection efficiencies of several mica samples when curved to a 1-m radius of curvature and used as a Bragg analyzer in a high-resolution x-ray spectrometer. For a high-grade mica, the analyzer energy resolution is comparable to conventional Si or Ge analyzers but its efficiency ranges from ~5% to ~40% depending on the particular (0,0,*l*) mica harmonic. The presence of a large number of harmonics that are relatively closely spaced in energy allows a 'universal analyzer' performance, where selection of different harmonics in the final energy-dispersive detector allows a single mica analyzer to study all x-ray fluorescence lines from ~5 keV to at least ~10 keV. The generally good performance of the mica analyzer coupled with this great convenience suggest good future utility.

5. Acknowledgements

EPJ was supported in part by the Joint Center for Energy Storage Research (JCESR), an Energy Innovation Hub funded by the U.S. Department of Energy, Office of Science, and Basic Energy Sciences. EPJ was also supported by a subcontract from the National Institute of Standards and Technology. Opinions, recommendations, findings, and conclusions presented in this manuscript and associated materials does not necessarily reflect the views or policies of NIST or the United States Government. Part of this work was conducted at the Molecular Analysis Facility, a

National Nanotechnology Coordinated Infrastructure site at the University of Washington which is supported in part by the National Science Foundation (grant NNCI- 1542101), the University of Washington, the Molecular Engineering & Sciences Institute, and the Clean Energy Institute.

6. References

1. K. M. Lancaster, M. Roemelt, P. Ettenhuber, Y. Hu, M. W. Ribbe, F. Neese, U. Bergmann and S. DeBeer, Science **334** (6058), 974 (2011).
2. B. Lassalle-Kaiser, T. T. Boron, 3rd, V. Krewald, J. Kern, M. A. Beckwith, M. U. Delgado-Jaime, H. Schroeder, R. Alonso-Mori, D. Nordlund, T.-C. Weng, D. Sokaras, F. Neese, U. Bergmann, V. K. Yachandra, S. DeBeer, V. L. Pecoraro and J. Yano, Inorg Chem **52** (22), 12915-12922 (2013).
3. Y. Pushkar, X. Long, P. Glatzel, G. W. Brudvig, G. C. Dismukes, T. J. Collins, V. K. Yachandra, J. Yano and U. Bergmann, Angewandte Chemie International Edition **49** (4), 800-803 (2010).
4. J. Badro, G. Fiquet, V. V. Struzhkin, M. Somayazulu, H.-k. Mao, G. Shen and T. Le Bihan, Phys Rev Lett **89** (20), 205504 (2002).
5. C. H. Booth, S. A. Medling, Y. Jiang, E. D. Bauer, P. H. Tobash, J. N. Mitchell, D. K. Veirs, M. A. Wall, P. G. Allen, J. J. Kas, D. Sokaras, D. Nordlund and T. C. Weng, J Electron Spec **194**, 57-65 (2014).
6. J. P. Rueff, C. C. Kao, V. V. Struzhkin, J. Badro, J. Shu, R. J. Hemley and H. K. Mao, Phys Rev Lett **82** (16), 3284-3287 (1999).
7. J. P. Rueff, M. Krisch, Y. Q. Cai, A. Kaprolat, M. Hanfland, M. Lorenzen, C. Masciovecchio, R. Verbeni and F. Sette, Physical Review B **60** (21), 14510-14512 (1999).
8. C. H. Booth, Y. Jiang, D. L. Wang, J. N. Mitchell, P. H. Tobash, E. D. Bauer, M. A. Wall, P. G. Allen, D. Sokaras, D. Nordlund, T. C. Weng, M. A. Torrez and J. L. Sarrao, Proceedings of the National Academy of Sciences **109** (26), 10205 (2012).
9. S. Heathman, J. P. Rueff, L. Simonelli, M. A. Denecke, J. C. Griveau, R. Caciuffo and G. H. Lander, Physical Review B **82** (20), 201103 (2010).
10. J. P. Rueff, S. Raymond, A. Yaresko, D. Braithwaite, P. Leininger, G. Vankó, A. Huxley, J. Rebizant and N. Sato, Physical Review B **76** (8), 085113 (2007).
11. J. G. Tobin, S. W. Yu, C. H. Booth, T. Tyliszczak, D. K. Shuh, G. van der Laan, D. Sokaras, D. Nordlund, T. C. Weng and P. S. Bagus, Physical Review B **92** (3), 035111 (2015).
12. G. Henderson, F. De Groot and B. Moulton, Reviews in Mineralogy and Geochemistry **78** (1), 75-138 (2014).
13. P. Glatzel and U. Bergmann, Coordin Chem Rev **249** (1-2), 65-95 (2005).
14. E. Gallo and P. Glatzel, Advanced Materials **26** (46), 7730-7746 (2014).
15. F. de Groot, Chemical Reviews **101** (6), 1779-1808 (2001).
16. U. Bergmann and P. Glatzel, Photosynth Res **102** (2-3), 255-266 (2009).
17. C. J. Pollock and S. DeBeer, J Am Chem Soc **133** (14), 5594-5601 (2011).

18. W. M. Holden, O. R. Hoidn, A. S. Ditter, G. T. Seidler, J. Kas, J. L. Stein, B. M. Cossairt, S. A. Kozimor, J. Guo, Y. Ye, M. A. Marcus and S. Fakra, Review of Scientific Instruments **88** (7), 073904 (2017).
19. W. M. Holden, G. T. Seidler and S. Cheah, The Journal of Physical Chemistry A (2018).
20. E. P. Jahrman, W. M. Holden, A. S. Ditter, D. R. Mortensen, G. T. Seidler, T. T. Fister, S. A. Kozimor, L. F. J. Piper, J. Rana, N. C. Hyatt and M. C. Stennett, Review of Scientific Instruments **90** (2), 024106 (2019).
21. E. P. Jahrman, G. T. Seidler and J. R. Sieber, Analytical Chemistry **90** (11), 6587 (2018).
22. D. R. Mortensen, G. T. Seidler, J. J. Kas, N. Govind, C. P. Schwartz, S. Pemmaraju and D. G. Prendergast, Physical Review B **96** (12), 125136 (2017).
23. G. T. Seidler, D. R. Mortensen, A. J. Remesnik, J. I. Pacold, N. A. Ball, N. Barry, M. Styczinski and O. R. Hoidn, Review of Scientific Instruments **85** (11), 113906 (2014).
24. J. L. Stein, W. M. Holden, A. Venkatesh, M. E. Mundy, A. J. Rossini, G. T. Seidler and B. M. Cossairt, Chem Mater **30** (18), 6377-6388 (2018).
25. L. Anklamm, C. Schlesiger, W. Malzer, D. Grötzsch, M. Neitzel and B. Kanngießer, Review of Scientific Instruments **85** (5), 053110 (2014).
26. J. Hoszowska, J. C. Dousse, J. Kern and C. Rhême, Nuclear Instruments and Methods in Physics Research Section A: Accelerators, Spectrometers, Detectors and Associated Equipment **376** (1), 129-138 (1996).
27. Y. Kayser, W. Błachucki, J. C. Dousse, J. Hoszowska, M. Neff and V. Romano, Review of Scientific Instruments **85** (4), 043101 (2014).
28. Z. Németh, J. Szlachetko, É. G. Bajnóczi and G. Vankó, Review of Scientific Instruments **87** (10), 103105 (2016).
29. M. Rovezzi, C. Lapras, A. Manceau, P. Glatzel and R. Verbeni, Review of Scientific Instruments **88** (1), 013108 (2017).
30. D. Sokaras, T. C. Weng, D. Nordlund, R. Alonso-Mori, P. Velikov, D. Wenger, A. Garachtchenko, M. George, V. Borzenets, B. Johnson, T. Rabedeau and U. Bergmann, Review of Scientific Instruments **84** (5), 053102 (2013).
31. S. G. Lee, J. G. Bak, Y. S. Jung, M. Bitter, K. W. Hill, G. Hölzer, O. Wehrhan and E. Förster, Review of Scientific Instruments **74** (12), 5046-5052 (2003).
32. Y. Aglitskiy, F. G. Serpa, E. S. Meyer, J. D. Gillaspy, C. M. Brown, A. Y. Faenov and T. A. Pikuz, Physica Scripta **58** (2), 178-181 (1998).
33. Z. W. Chen and D. B. Wittry, Applied Physics Letters **71** (13), 1884-1886 (1997).
34. Z. W. Chen and D. B. Wittry, Journal of Applied Physics **84** (2), 1064-1073 (1998).
35. A. Y. Faenov, T. A. Pikuz, A. A. Firsov, L. A. Panchenko, Y. I. Koval, M. Fraenkel and A. Zigler, Physica Scripta **55** (2), 167-169 (1997).
36. M. Haugh and R. Stewart, Review of Scientific Instruments **81** (10) (2010).
37. J. Lu, S. L. Xiao, Q. G. Yang, X. B. Huang and H. C. Cai, Optik **124** (16), 2414-2416 (2013).
38. M. I. Mazuritsky, A. V. Soldatov, V. L. Lyashenko, E. M. Latush, A. T. Kozakov, S. I. Shevtsova and A. Marcelli, Technical Physics Letters **27** (1), 11-13 (2001).
39. S. A. Pikuz, V. M. Romanova, T. A. Shelkovenko, T. A. Pikuz, A. Y. Faenov, E. Forster, J. Wolf and O. Wehrhan, Kvantovaya Elektronika **22** (1), 21-24 (1995).
40. D. L. Robbins, H. Chen, P. Beiersdorfer, A. Y. Faenov, T. A. Pikuz, M. J. May, J. Dunn and A. J. Smith, Review of Scientific Instruments **75** (10), 3717-3719 (2004).

41. J. Shi, S. L. Xiao, H. J. Wang, X. B. Huang, L. B. Yang and S. Y. Liu, Chinese Optics Letters **6** (8), 622-624 (2008).
42. E. Wainstein, Comptes Rendus De L Academie Des Sciences De L Urss **35**, 233-235 (1942).
43. J. Workman, T. Tierney, S. Evans, G. Kyrala and J. Benage, Review of Scientific Instruments **70** (1), 613-616 (1999).
44. G. Zhu, X. C. Xiong, X. X. Zhong and Y. Yang, Science and Technology of Nuclear Installations (2012).
45. A. Pak, G. Gregori, J. Knight, K. Campbell, D. Price, B. Hammel, O. L. Landen and S. H. Glenzer, Review of Scientific Instruments **75** (10), 3747-3749 (2004).
46. C. Schlesiger, L. Anklamm, H. Stiel, W. Malzer and B. Kanngießer, Journal of Analytical Atomic Spectrometry **30** (5), 1080-1085 (2015).
47. E. P. Jahrman, W. M. Holden, A. S. Ditter, S. A. Kozimor, S. L. Kihara and G. T. Seidler, Review of Scientific Instruments **90** (1), 013106 (2019).
48. W. Bi, J. Huang, M. Wang, E. P. Jahrman, G. T. Seidler, J. Wang, Y. Wu, G. Gao, G. Wu and G. Cao, Journal of Materials Chemistry A **7** (30), 17966-17973 (2019).
49. W. Bi, E. Jahrman, G. Seidler, J. Wang, G. Gao, G. Wu, M. Atif, M. AlSalhi and G. Cao, ACS Applied Materials & Interfaces **11** (18), 16647-16655 (2019).
50. W. Bi, J. Wang, E. P. Jahrman, G. T. Seidler, G. Gao, G. Wu and G. Cao, Small **0** (0), 1901747 (2019).
51. B. Ravel and M. Newville, Journal of Synchrotron Radiation **12** (4), 537-541 (2005).
52. W. M. Holden, O. R. Hoidn, G. T. Seidler and A. D. DiChiara, Review of Scientific Instruments **89** (9), 093111 (2018).

Chapter 6. Overview of Energy Storage Research and the Contributions of X-ray Spectroscopy

1. Historical Context and Societal Impact

This chapter outlines the social and scientific context for contemporary research in energy storage. This chapter begins with a brief discussion of the recent, rapid growth of clean technologies. This serves as a critical foundation for discussing energy storage, as batteries are key enabling technologies for expanding renewable energy production in the grid and deploying electric vehicles. Therefore, the impact of energy storage research is closely tied to the longevity and intensity of social, economic, and scientific interest in clean energy technologies. Next, a deeper discussion of the role of energy storage research is given, augmented with some future projections. This is followed by a summary of available battery chemistries with a special focus on lithium-ion batteries (LIBs), which comprise the bulk of energy storage research in Chapters 3, 8, and 9. An overview of research strategies to achieve performance improvements is provided. This includes a discussion on conversion and intercalation chemistries, microstructure design, electrode composition, and other cell components. Finally, a review of recent X-ray spectroscopic studies into novel battery chemistries is presented.

A recent article argued clean technologies have attained irreversible momentum due to four reasons, namely: (1) the decoupling of emissions from economic growth; (2) private sector emission reductions and emphasis on energy efficiency; (3) market forces in the power sector; (4) and the global support for clean energy innovation.[1] Briefly, the first point is evidenced by the following fact: between the years 2008 and 2015, the US economy grew by 10% while CO_2 emissions by the energy sector dropped by 9.5% and the amount of CO_2 per unit of energy

consumed dropped by 8%.[2] An excellent indicator of our nation's progress toward the second point is that the number of Americans, 2.2 million, employed in the production of energy-efficiency goods outstrips the number employed in the production of fossil fuels by a factor of two.[3] Concerning the third point, market forces, the cost of renewable electricity fell precipitously between the years 2008 and 2015. With a 41% decrease for wind, 54% for rooftop photovoltaics, and 64% for utility-scale photovoltaics,[4] renewables are now less expensive than new coal production in parts of the United States.[2] Moreover, the devices used for renewable energy production are continually improving. For example, new photovoltaic efficiency records are frequently set, Fig. 6-1. Finally, with more than 110 countries committing to the Paris Climate Agreement, the consensus at the follow-up meeting in Marrakesh was that climate action could not be derailed.[5] Despite the clear societal momentum toward implementing clean energy solutions, these technologies still face many technical barriers.

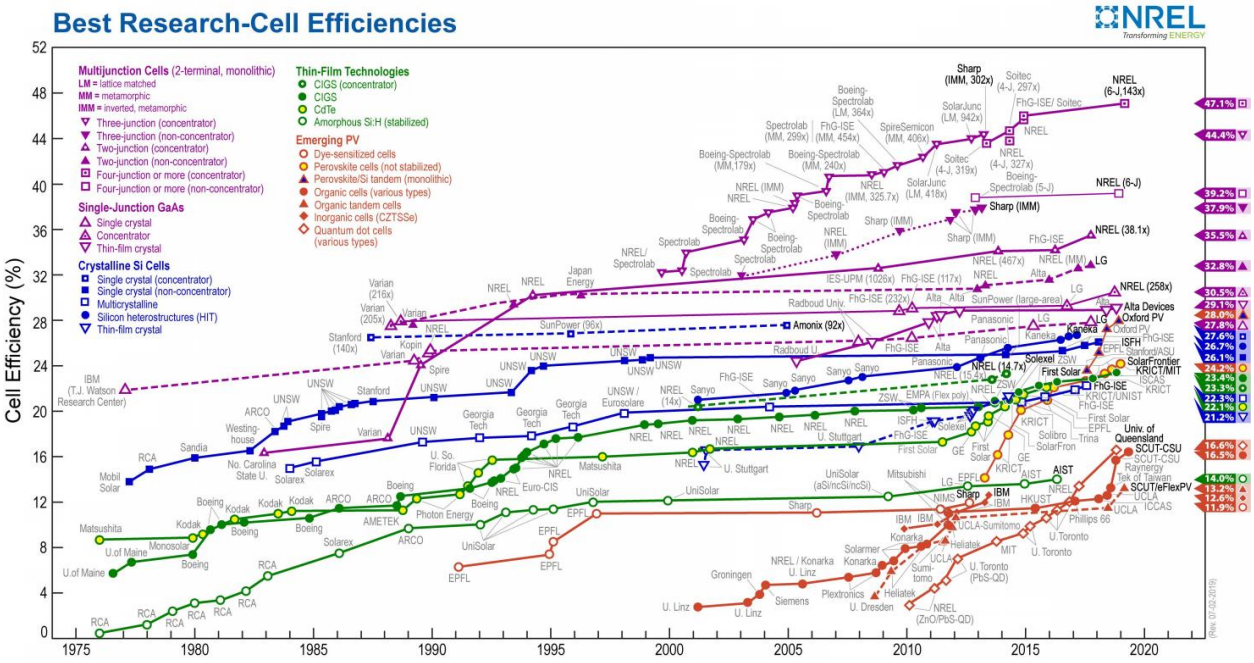

Fig. 6-1: The National Renewable Energy Laboratory's traditional representation of photovoltaic efficiency records as tabulated by Green *et al.*[6]

Energy production by renewable resources is often intrinsically intermittent, resulting in several logistical problems preventing grid integration. As an example, consider the so-called 'Duck Curve' in Fig. 6-2. Here, it can be seen that net load is highly variable throughout the day. This can be understood as follows. At any point in time, the amount of electricity consumed by the grid must be equal to the amount of electricity provided to the grid. This poses a challenge. Not only does demand fluctuate throughout the day, but the amount of electricity provided by renewable energies also varies throughout the day. This leads to two primary concerns, oversupply during peak hours for renewable generation and an inability to implement automated response to grid frequency fluctuations. Oversupply can be addressed by market manipulation; driving the price of electricity negative and paying utilities to consume electricity. However, automated frequency response requires an additional technological solution. This is

because renewable energy resources typically run at maximum capacity, i.e., wind turbines cannot control incident wind speeds and photovoltaics cannot vary the flux of sunlight on a solar panel. Both of the above barriers can be remedied by deploying energy storage capabilities. As the conventional tool for chemically storing energy is the battery, it is necessary to discuss battery technologies available at present and how those technologies can be adapted to meet increasing market demands.

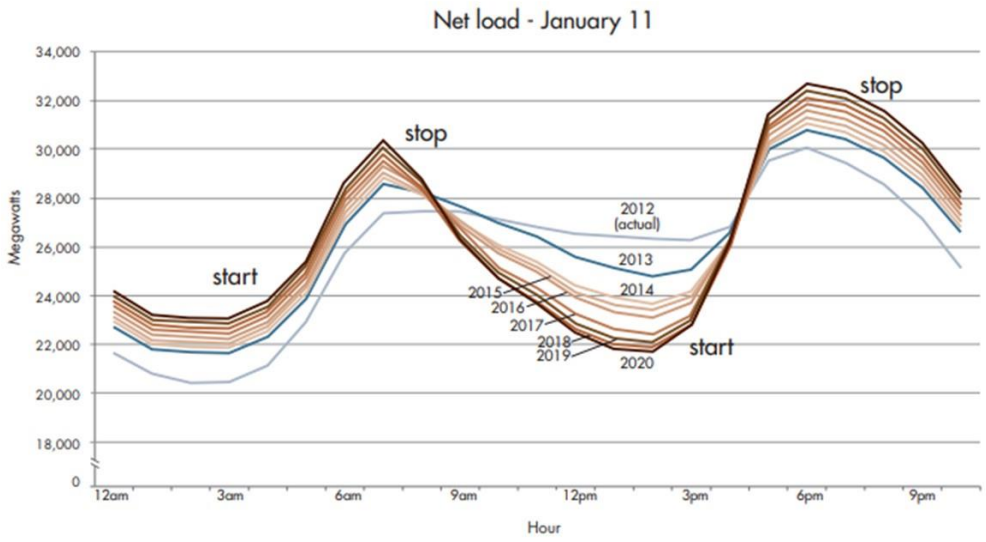

Fig. 6-2: Reproduced from the California Independent System Operator Corporation.[7] Net load is shown as a function of time-of-day. Net load is the difference between forecasted load and expected electricity production from variable generation resources. Measurements were collected on January 11, 2012. Other years represent projected values. Four regions are visible: (1) ~ 4:00 a.m. people start to wake up and make use of electrical appliances. (2) ~ 7:00 a.m. the sun rises and solar generation resources become active. (3) ~ 4:00 p.m. the sun begins to set and people return home from their daily routines and begin using at-home electronic devices. (4) ~ 7:00 p.m. demand on the system begins to decrease as individuals retire for the evening.

The selection of a battery material is subject to the requirements of the application. Typically, a wide variety of candidate systems are available, and must be assessed via benchmarks for capacity, capacity retention, power density, safety, reliability, and economic feasibility. As a perspective, consider Fig. 6-3. Here, it can be seen that the choice of battery chemistry may be optimized to meet energy requirements within a desirable volume or weight. This is particularly important in mobile applications which require batteries be easily transportable. Other considerations dominate for stationary applications. Indeed, large-scale energy storage, such as for grid applications, has increasingly favored redox-flow systems due to their scalability, intrinsic safety, cost, and long lifetimes.[8] Of these, vanadium and iron-chromate chemistries are particularly popular,[9] however organic chemistries have also garnered considerable recent interest.[10] On occasion, LIBs are also promoted for grid storage.[11] However, LIBs are predominantly seen in portable consumer electronics[12] and electric vehicles.[13] Production of LIBs for transportation applications is expected to increase rapidly over the coming decades, Fig. 6-4. For that reason, the components of a LIB, as well as proposed strategies for improvements, merits discussion.

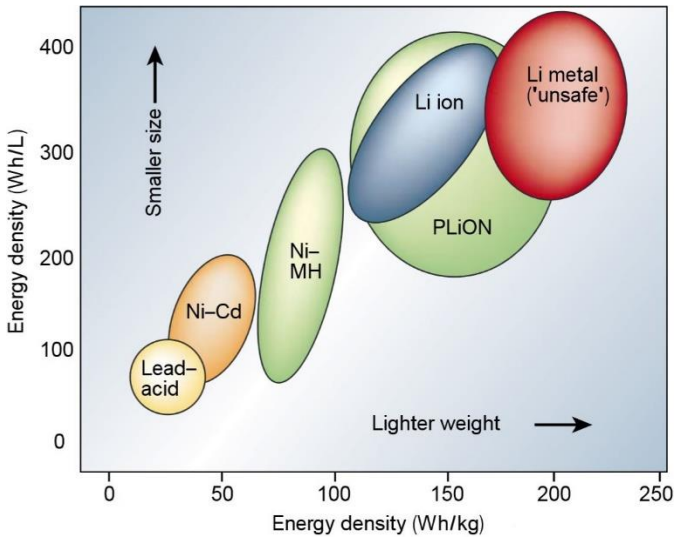

Fig. 6-3: Reproduced from Tarascon.[14] Energy densities and specific energies of various rechargeable battery chemistries.

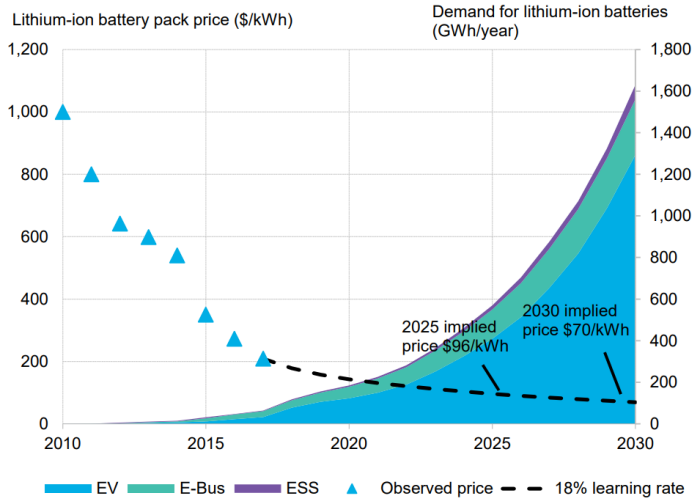

Fig. 6-4: Reproduced from Bloomberg New Energy Finance.[15] Historical LIB pack prices are denoted by triangles with projected priced represented by a dashed line. The shaded regions show projected demand for LIBs. Note that ESS encompasses stationary energy storage applications, while E-Bus refers to electric buses.

2. Research strategies to achieve improvements

For the sake of organization, the discussion of recent research efforts will be framed such that each component of an LIB is discussed in turn. Therefore, it is convenient to begin with an outline of a typical LIB's composition, Fig. 6-5. Modern LIBs consist of two electrodes which are coated onto current collectors. The anode is typically comprised of a graphitic material and is routinely mixed with some amount of conductive additive, such as carbon black, and polyvinylidene fluoride dissolved in N-Methyl-2-Pyrrolidone. The anode is traditionally coated onto a Cu current collector. Similarly, the cathode is often a layered oxide or spinel structure that can be mixed with a conductive additive and coated onto a current collector, traditionally made from Al. The actual choice of electrode material is acutely sensitive to several factors which effect critical performance metrics. These factors include electrochemical considerations, such as the standard electrode potential of the material, Fig. 6-6. The electrodes are divided by a separator,[16] which is traditionally polyolefin.[17, 18] Note that the separator's thickness and porosity plays a significant role in its performance.[19] Finally, the components are wetted by an electrolyte, commonly $LiPF_6$ in ethylene carbonate. It is also common to add diethyl carbonate or dimethyl carbonate to reduce viscosity and improve ion transfer,[20] and also promote specific properties through the use of additives[21] such as fluoroethylene carbonate or vinylene carbonate.[22] This can be repeated for many layers and packaged into a pouch, coin, prismatic, or cylindrical cell. Note that the comparative performance of these forms has been investigated in the context of automobile applications.[23] This summarizes the general structure of LIBs, however, other variations exist, including the implementation of polymer electrolytes[24] and all-solid-state LIBs.[25] The rest of this section summarizes improvements through microstructural

design of electrodes, alterations to the mechanism governing Li storage, and the implementation of novel chemical compositions.

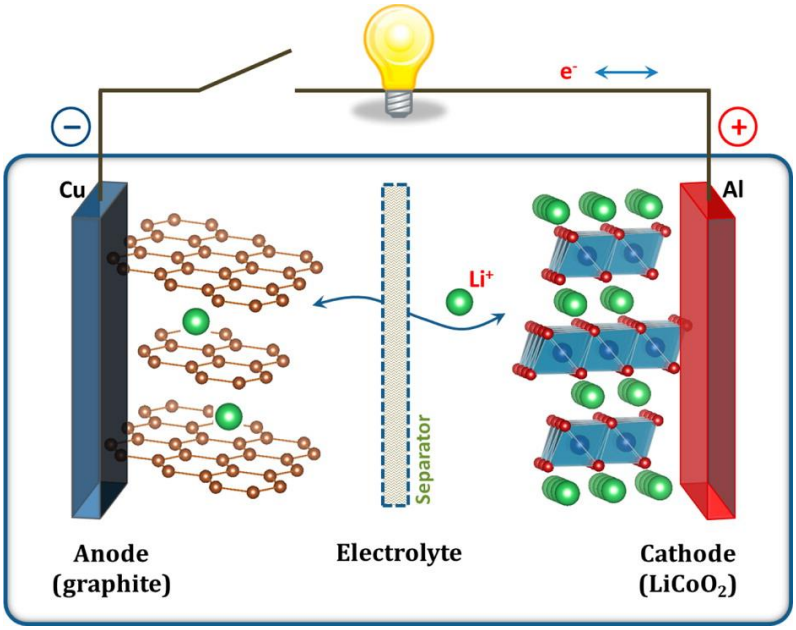

Fig. 6-5: Reproduced from Goodenough.[26] Schematic of a conventional LIB showing the flow of transport of Li ions and electrons.

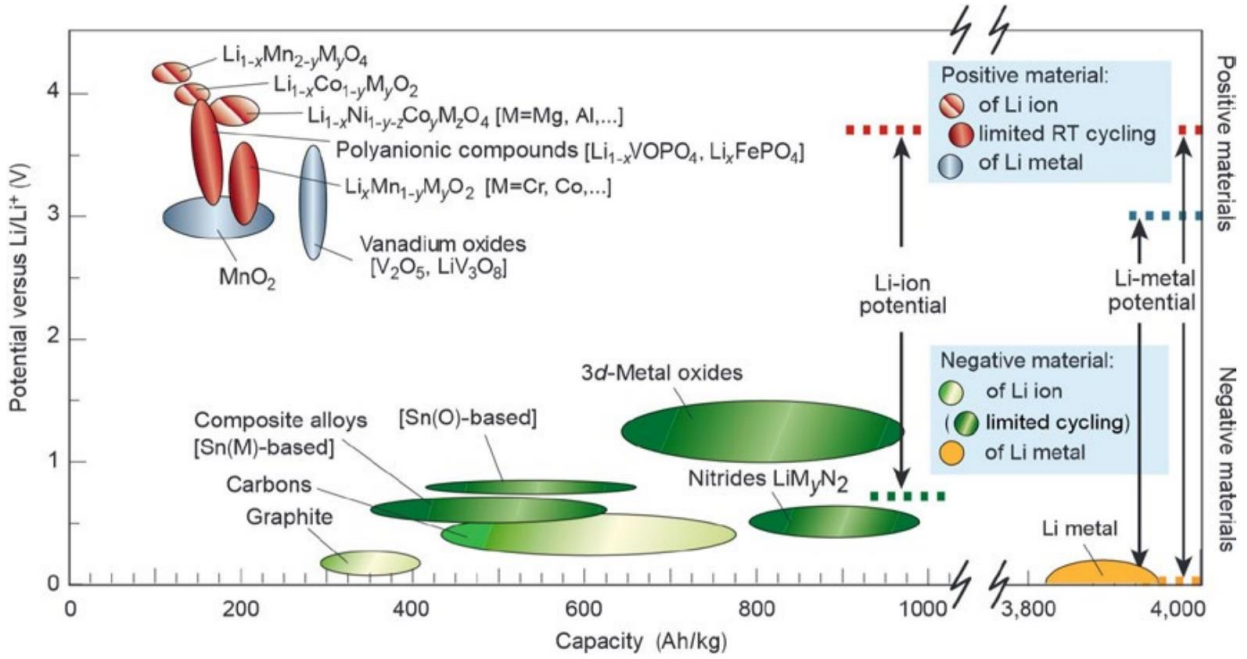

Fig. 6-6: Reproduced from Deng.[20] The electrode potentials and achievable capacities spanned by a variety of candidate electrode materials.

Geometric factors play a key role in determining energy storage device performance. Consequently, microstructural design represents a viable route for improving the performance metrics of a device. In practice, optimal design varies according to electrode classification. Traditionally, electrodes are classified according to the mechanism of Li storage, Fig. 6-7, and in the case of insertion devices, Li transport, Fig. 6-8. The articles from which these figures were reproduced provide further information regarding these classifications, here, the discussion will be limited to a few select examples to be discussed in the following paragraphs. At present, it will suffice to describe a few instances in which microstructural design enabled key technological breakthroughs. For example, a recent study demonstrated that 3D patterned Si wafers, as prepared by established techniques in the semiconductor manufacturing industry, could be electrochemically activated to yield large, stable charge capacities while retaining high

Coulombic efficiency despite the large volume expansion of the Si-based electrode during lithiation.[27] Note that other attempts to address the large volumetric expansion have been reported, including the production of nanowires, hollow nanostructures, and clamped hollow nanostructures.[28] Similarly, microstructural design can be utilized to achieve desirable mechanical properties, including the integration of carbon fibre-based electrodes to better carry mechanical load[29] and the selection of core shell nanoparticles for the cathode of a Ni-rich layered transition metal oxide system to mitigate strain and improve cycle life at elevated cycle rates.[30] Clearly insights into an electrode's microstructure are critical in understanding device performance and developing improved devices. Accordingly, a collection of real-time techniques have been developed for assessing microstructural dynamics.[31, 32] An alternative approach to optimizing geometric factors inside an energy storage device is to employ thick electrodes to achieve high energy density LIBs. Nevertheless, this approach is subject to several limiting factors,[33, 34] including increased cell polarization and underutilization of active material as influenced by Li diffusion in the electrode and Li depletion in the medium of the electrolyte.

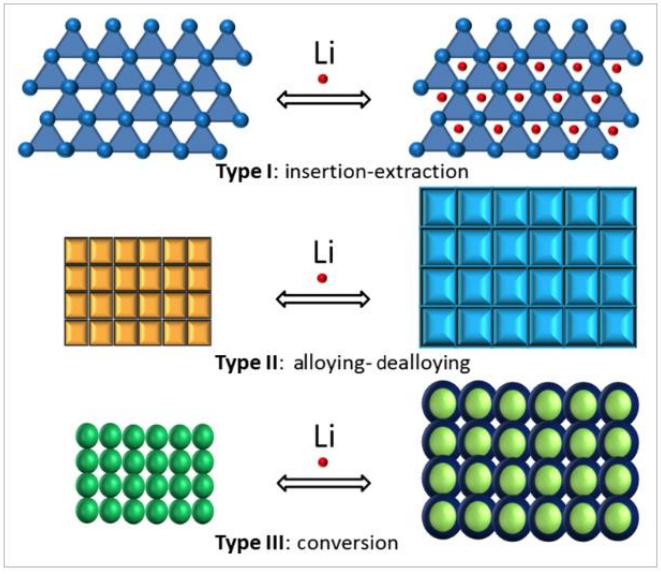

Fig. 6-7: Reproduced from Deng.[20] Three mechanisms for Li storage in LIBs.

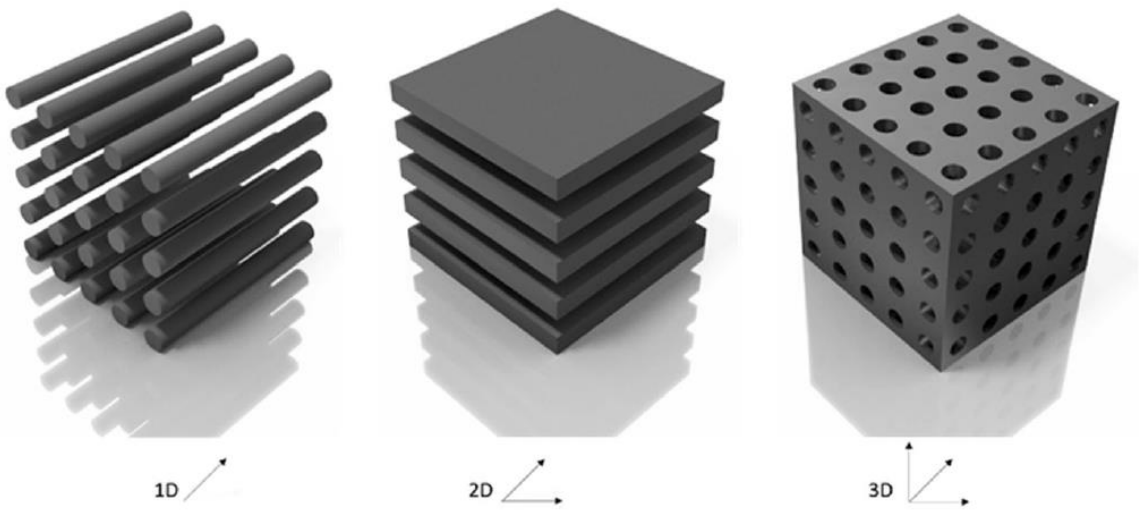

Fig. 6-8: Reproduced from Kasnatscheew.[21] Three motifs for Li transport within the active material of an electrode. These motifs include 1D transport along channels (as in olivine structure types), 2D transport along defined sheets (as with layered structure types), or 3D diffusion (as in spinel structure types).

There are several other prominent Li storage devices, including Li-S and Li-air batteries.[35] This text will focus on Li-S, which is a archetypal conversion device and exhibits several of the advantages and disadvantages characteristic of such technologies. To begin, Li-S batteries have garnered substantial attention as candidate next-generation battery materials due the their high theoretical specific energy density of 2500 Wh/kg and theoretical specific capacity of 1675 mAh/g.[36] However, they suffer from several technical barriers which result in substantially lower actual capacities and poor capacity retention. The first is a mechanical concern. The sulfur cathode is liable to an 80% volume change during discharge.[37] Large volume changes are a common problem in conversion devices and can have a deleterious impact on capacity retention. For example, large expansion can cause swelling and cracking of the material as well as instability in the solid electrolyte interphase (SEI).[38] Moreover, Li-S devices

often suffer capacity losses due to under-utilization of active material or unfavorable side reactions in the electrolyte phase.[39] Mitigating these issues is an area of active research. For example, organometallic redox mediators may be used to provide better utilization of Li_2S.[40] However, two primary barriers to implementation of Li-S technologies have not yet been discussed. First, polysulfide shuttling leads to substantial self-discharge. Second, the fully lithiated and delithiated phases, Li_2S and S_8, do not demonstrate appreciable electrical conductivity. Fortunately, both of these deficiencies can be treated by the same strategy, namely, encapsulation within a conductive framework.[41] Accordingly, a number of carbonaceous frameworks and synthesis procedures have been proposed, including a precipitation technique to load sulfur into the large pore of a multi-walled carbon nanotube (MWCNT).[42] Alternatively, additives such as P_2S_5[43] or electrocatalysts[44] may be used to reduce polysulfide shuttling. Yet, despite recent progress in commercialization,[45] these systems still face several challenges[46-49] and it is worthwhile to discuss some other traditional and non-traditional electrode chemistries.

Recently, rapid progress has been made in the preparation of state-of-the-art anode materials. One particularly attractive chemistry are Si anodes, which exhibit a large specific capacity of 3350 ± 200 mAh/g for lithiation in the amorphous phase up to $Li_{15}S_4$[50] and up to 4200 mAh/g for fully lithiated $Li_{22}S_5$.[51] Note that a crystalline phase transition is encountered at the $Li_{15}S_4$ stoichiometry, as is expected,[52] but crystalline $Li_{15}S_4$ can be avoided if the potential of the electrode is kept above 70 mV during cycling.[50] In practice, Li atoms are injected into the lattice via a two phase mechanism that weakens the Si-Si bonds of the pristine Si anode to form lithiated amorphous Si.[53] This constitutes an alloying process and is accompanied by a large anisotropic volume expansion up to ~300% which can result in fracture and delamination.[54] These issues are often addressed through the geometric designs discussed earlier in this section.[51]

Alternatively, Li metal anodes demonstrate a similarly attractive theoretical specific capacity of 3860 mAh/g, coupled with a low density of 0.59 g/cm^3, and the lowest achievable negative electrochemical potential of -3.040 V vs. the standard hydrogen electrode.[55] Unfortunately, this material is prone to several shortcomings including volume expansion, capacity fading, increased overpotential, and potential safety hazards. Within these concerns, two commonly discussed are dendritic formation and low Coulombic efficiency. The latter is attributed to inactive, unreacted metallic Li[56] while the former is the subject of a common misconception. Figure 6-9 depicts a range of dendritic growth. As Fig. 6-9A suggests, researchers frequently worry that dendrite growth will occur perpendicular to the separator, thus piercing it and creating a hazardous short circuit.[14] However, the growth in Fig. 6-9A was observed in a beaker cell which is not representative of more standard designs. Instead, whisker-like Li deposits are preferentially formed, Fig. 6-9B. Due to the inherently heterogeneous structure of SEI layers, these formations tend to grow parallel to the separator and may possess large granular size when formed in the presence of advanced electrolytes, Fig. 6-9C. Indeed, the hypothesis of dendritic growth leading to internal short circuits has been further refuted by scanning electron microscopy measurements collected on cross sections of cycled Li anodes.[57] For that reason, dendritic growth is now considered to primarily disadvantage Li anodes by contributing to sharp increases in surface area and volume, but not by directly causing a short circuit.[56]

At present, the outlook for Li metal anodes is promising due to many technological advances, but it is not the most common anode material for LIBs, that distinction belongs jointly to graphite and lithium alloyed metal anodes.[58] Concerning the former, the lithiation mechanism in graphite-based electrodes is intercalation of Li into the layered structure. Full lithation leads to the LiC_6 structure with a theoretical capacity of 372 mAh/g.[59] This capacity is satisfactory for

the majority of applications, but is too restrictive for particularly high-energy consuming applications.[60] Nevertheless, graphite electrodes are favorable due to high Coulombic efficiency[61] and their capacity and capacity retention may be improved by microstructural design[62] of the electrode and selective pairing with doped or surface coated positive electrodes, respectively. However, the insertion of lithium into the layered structure of graphite expands the van der Waals gap and requires energy that often must be provided by charge transfer, as may be provided by the redox of most cathode materials. At this point, it is appropriate to segue and discuss the cathode chemistries which are the subject of intensive modern research.

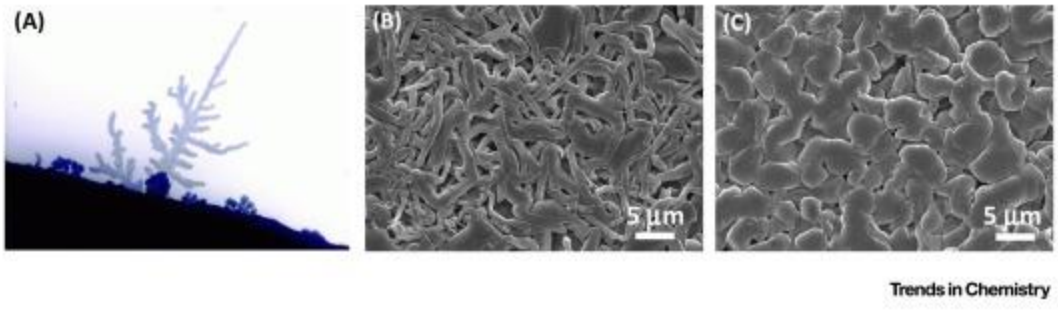

Fig. 6-9: Reproduced from Fang.[56] (A) Optical microscope image of Li dendrites in a beaker cell as reported by Xu *et al.*[55] (B) Whisker-like Li deposited during cycling with a mix of standard solvents, electrolytes, and additives. (C) Chunky Li deposited during cycling with a high-concentration ether-based electrolyte.

The optimization of cathode materials has remained the subject of intensive research over the last several decades. For that reason, a complete discussion would cover a wide range of enabling historical and economic achievements, myriad chemistries, and proposed methodologies for next-generation cathodes. Such discussions are well-justified and reviews have been presented by many researchers, including Whittingham.[63, 64] Other reviews devote considerable attention to the current state of cathode technologies, such as the review by

Bensalah and Dawoud which includes a particularly useful table summarizing the dominant performance metrics, preferred synthesis procedures, and publication of origin of nearly every cathode material currently available.[65] Much of modern research into cathode materials for rechargeable LIBs originated from studies of layered dichalcogenides. This began in the 1970s when researchers demonstrated ions and other species could be intercalated into these systems.[66] Titanium disulfide quickly gained interest[67, 68] due to its light weight, identity as a semi-metal[69] negating the need for a conductive diluent, and a single phase throughout the range of lithiation.[70] Years later, it was recognized that Li_xCoO_2 possesses a structure similar to the dichalcogenides and can be electrochemically cycled.[71] This technology was then paired with a carbon electrode to produce a commercializable technology.[72]

Eventually, it was deemed beneficial to employ a mixture of transition metals in the layered oxide structure rather than strictly Co. First, this allows fine-tuning of the mixture to achieve improved performance metrics as desired for the application of interest, see Fig. 6-10. Second, this reduces the amount of Co required for the application.[64] This last point is particularly important as Co is not only costly and scarce, but is also predominantly mined in the Democratic Republic of Congo. Beyond constituting a vulnerable supply chain, these mining operations are largely unregulated and environmentally harmful.[73] In addition, these operations are rife with human rights abuses and harmful to vulnerable communities via oxidative DNA damage and exposure to heavy metals.[74] Nevertheless, steady progress has been made in the performance of standard LIB cathode chemistries since commercialization, including many incremental increases in energy due to variations in cathode composition, Fig. 6-11. At present, several cathode chemistries exist, see Fig. 6-12 which compares many popular LIB cathode materials as well as several proposed cathode materials for sodiation. Note that, for reference,

the $LiNi_{0.8}Co_{0.15}Al_{0.05}O_2$ has a capacity of ~180 mAh/g,[64] and the layered transition metal oxide cathodes which are a blend of Ni, Mn, and Co are sometimes referred to as NMC cathodes. Yet, despite the wide range of technologies currently available, higher performance is always desirable. For that reason, a few popular candidates for next-generation cathode materials are discussed here.

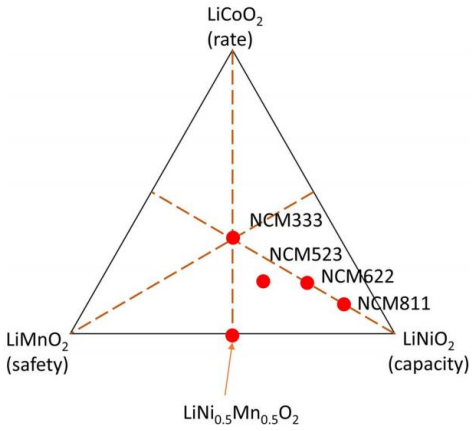

Fig. 6-10: Reproduced from Schipper.[75] Phase diagram representing the ternary system between three transition metal oxide species along with example compositions and considerations.

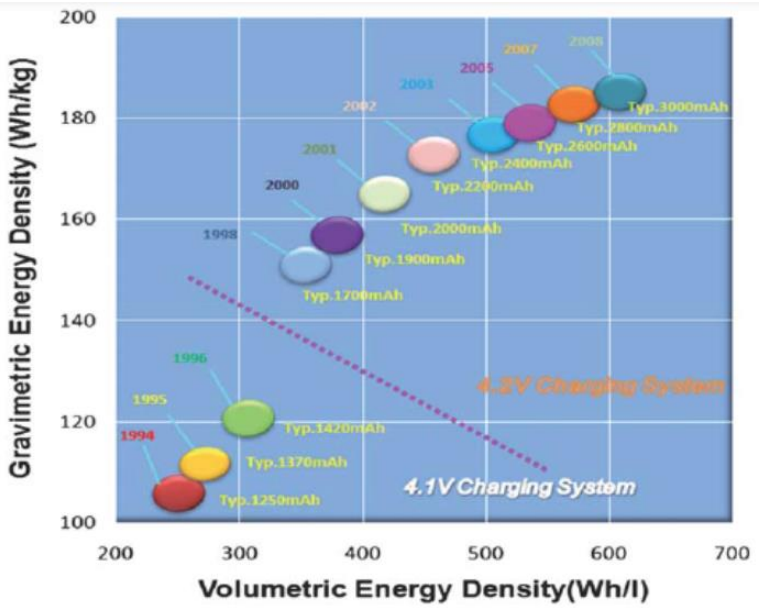

Fig. 6-11: Reproduced from Jeong.[76] Chronological energy densities of cylindrical-18650 LIBs.

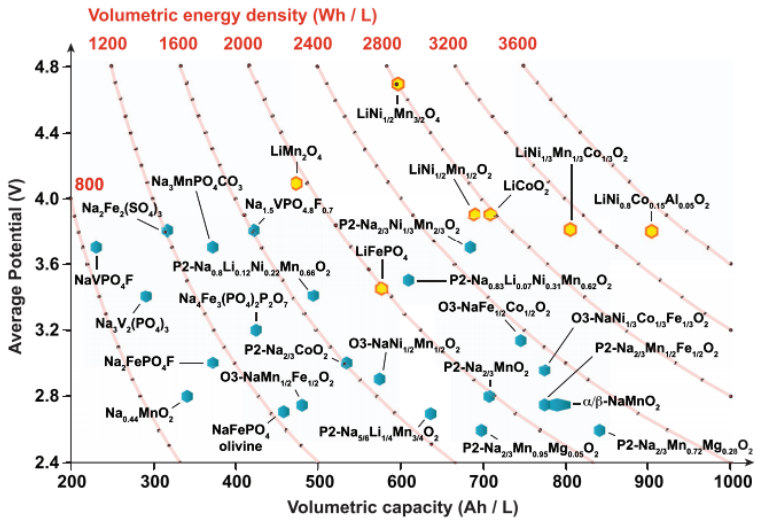

Fig. 6-12: Reproduced from Clément.[77] Average discharge potential and volumetric energy density vs. volumetric capacity of selected cathode materials for lithiation or sodiation.

Two dominant strategies for developing next-generation cathode materials are to select a material that can either be operated at higher potentials, or else a material that can accommodate intercalation of a multivalent ion or multiple Li-ions per redox active site. This first category

includes Ni-rich NMC materials. Here, the discharge capacity is improved at the cost of diminished thermal stability, see Fig. 6-13. The underlying mechanism for thermal instability in these systems is thought to be the formation of unstable, reactive Ni^{4+} ions which favor relaxation to the NiO rocksalt structure.[78] This process is accompanied by substantial oxygen evolution and has been studied by a combination of *in situ* time-resolved XRD and mass spectroscopy, Fig. 6-14. Alternatively, numerous researchers have directed their efforts toward improving cathode performance by pursuing the intercalation of multivalent ions. Typically, candidates offer high capacities, but suffer from poor ion mobility.[79] Yet another concern can play a significant role, see Fig. 6-15. As can be seen, these materials often exhibit complex ion-pairing behavior in solution, which necessarily requires varying degrees of stripping these ligand or hydration spheres upon insertion into a host lattice. In lieu of multivalent ions, a cathode material which permits the storage of multiple Li-ions permit per redox site. Several such cathode materials exist, including VSe_2[80], layered oxides such as $LiNi_{0.5}Mn_{0.5}O_2$,[64] and $VOPO_4$.[81] Of these, only $VOPO_4$ has both redox potentials at potentials useful for energy storage. Recently, ample progress has been made in achieving this material's relatively high theoretical capacity of 305 mAh/g.[82] This material exhibits several favorable characteristics that qualify it as a candidate material for the next-generation of cathode materials for LIBs. Future materials research campaigns will greatly benefit from the guidance of emerging *ab initio* studies which predict the performance metrics of large suites of viable electrode materials. See Fig. 6-16 for an example.

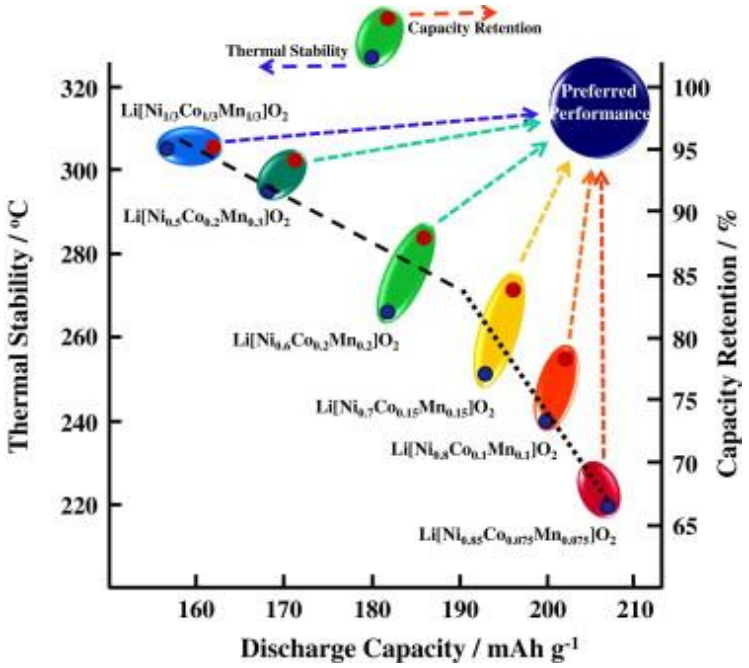

Fig. 6-13: Reproduced from Noh.[78] Trend in discharge capacity, thermal stability, and capacity retention as a function of Ni concentration in Ni-rich NMC cathode materials.

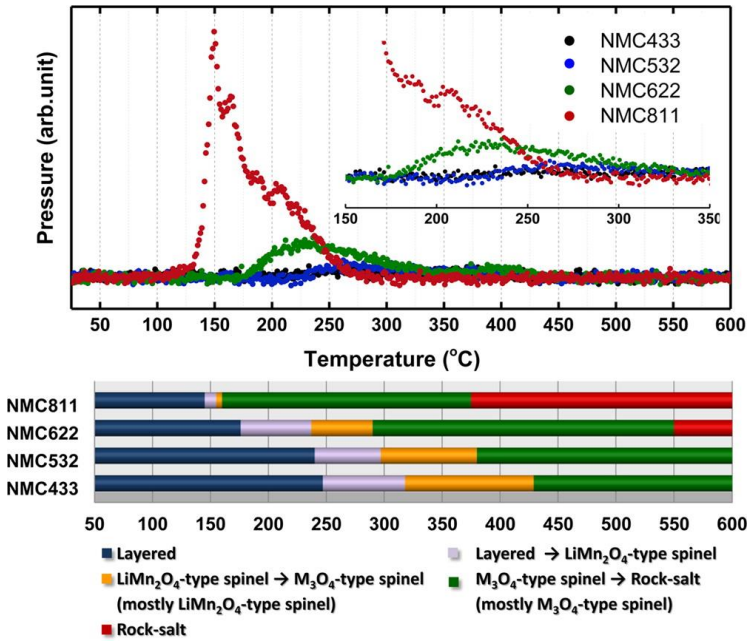

Fig. 6-14: Reproduced from Bak.[83] Mass spectroscopy results for oxygen as a function of temperature (top) compared with the materials' phase as determined by *in situ* XRD.

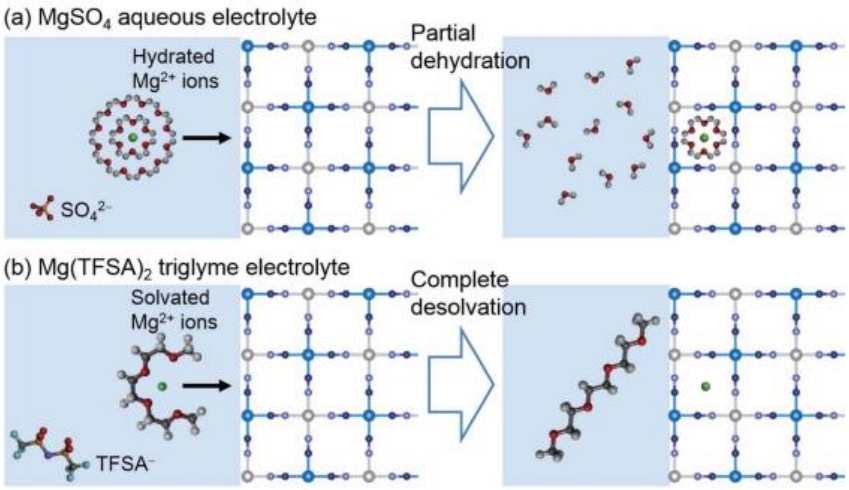

Fig. 6-15: Reproduced from Yagi.[83] Insertion of Mg^{2+} from an aqueous or triglyme electrolyte into a host lattice.

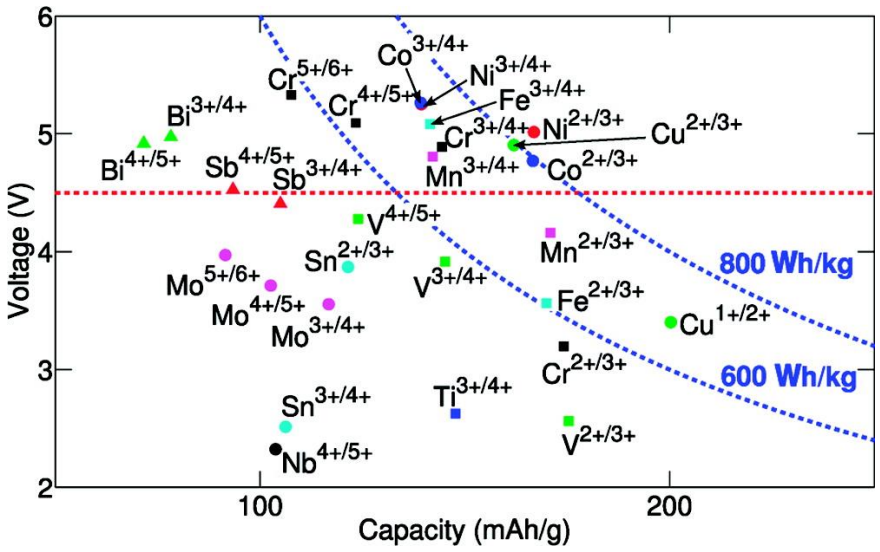

Fig. 6-16: Reproduced from Hautier.[84] Average voltage of select phosphates versus achievable capacity. Each redox couple is designated by a marker unique to the given element. The red dashed line represents an upper voltage beyond which decomposition of the electrolyte may occur.

3. Summary of Recent X-ray Spectroscopy Investigations of Energy Storage Materials

As evidenced by much of the above discussion, much of modern energy storage research is concerned with furthering the capacity and capacity retention of viable devices. For that reason, diagnostic tools which can provide insights into the mechanisms concerning redox and cell failure are highly valuable. For that reason, advanced X-ray spectroscopies are often advocated as methods to ascertain the state-of-health and state-of-charge of a battery.[85] In particular, X-ray emission spectroscopy (XES) and X-ray absorption fine structure (XAFS) analyses are able to interrogate the electronic, and atomic in the case of the latter, structure of novel energy materials in an element-specific manner.[86, 87] In recent years, such studies have resulted in considerable impact. Benerjee *et al.* combined Mn K-edge XANES with other techniques to identify Mn^{3+} rather than Mn^{2+} as the primary soluble species in $LiPF_6$ electrolyte solution.[62] Likewise, Kim *et al.* applied Extended X-ray Absorption Fine Structure (EXAFS), the long-range complement to XANES, to reveal that the Ni-O and Co-O distances change irreversibly and reversibly, respectively, during the first cycle of a NMC lithium ion battery, despite the redox reversibility of the Ni, Mn, and Co.[88] Similarly, Luo *et al.* reported a XANES analysis of previously inaccessible information on the oxidation of O_2^{2-} and oxygen loss in $LiMn_xNi_yO_2$ cathode, arguing that the electron-hole states coordinate to Mn^{4+} rather than Ni^{4+}.[89] Many other notable examples exist, including several spectro-microscopy studies to better understand species inhomogeneities across single active material particles. This includes a recent study by Mao *et al.* which explored degradation mechanisms leading to cracking in Ni-rich NMCs operated at especially high voltages[30] and a rapid mapping study concerning lithiation dynamics and degradation during overcharge of nickel cobalt aluminum oxide (NCA).[90] Finally, full speciation distribution analyses have been employed for the purpose of hypothesis testing. This includes a

study by Cuisinier which performed linear combination analysis on *operando* S K-edge XANES to determine the distribution of materials present, Fig. 6-16.[39] These results allowed them to evaluate two competing hypotheses for the diminished capacity of their cell, namely under-utilization of active material and the formation of deleterious side products. A further discussion of X-ray spectroscopy studies is provided by Jahrman *et al.* with special attention paid to studies on NMC materials and laboratory-based studies.[91]

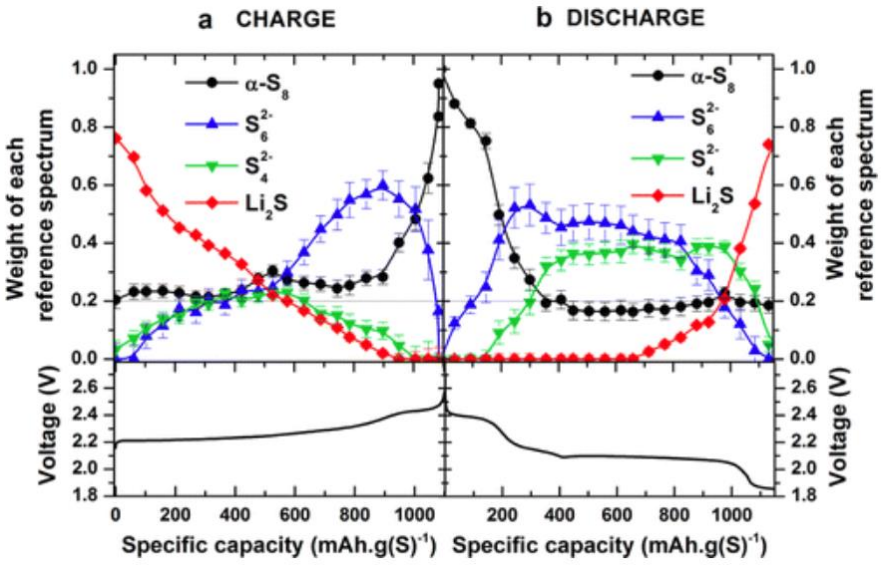

Fig. 6-17: Reproduced from Cuisinier.[84] Speciation distribution analysis results based on linear combination analysis of S K-edge XANES results upon cycling of a Li-S battery at a C/10 rate. Spectra are fit to a linear combination of four reference compounds: S_8, S_6^{2-}, S_4^{2-}, and Li_2S.

4. References

1. B. Obama, Science **355** (6321), 126 (2017).
2. Council of Economic Advisers, in *"Economic report of the President"* (Council of Economic Advisers, White House, Washington, DC, 2017), pp. 423-484.
3. BW Research Partnership, in *"U.S. energy and employment report"* (DOE, Washington, DC, 2017).
4. Department of Energy, in *"Revolution…Now: The future arrives for five clean energy technologies - 2016 Update"* (DOE, Washington, DC, 2016).

5. United Nations Framework Convention on Climate Change, in *"Marrakech action proclamation for our climate and sustainable development"* (UNFCCC, 2016).
6. M. A. Green, Y. Hishikawa, E. D. Dunlop, D. H. Levi, J. Hohl-Ebinger, M. Yoshita and A. W. Y. Ho-Baillie, Progress in Photovoltaics: Research and Applications **27** (1), 3-12 (2019).
7. California Independent System Operator Corporation, in *"What the duck curve tells us about managing a green grid"* (CISO Corp., Folsom, CA, 2016).
8. M. L. Perry and A. Z. Weber, Journal of The Electrochemical Society **163** (1), A5064-A5067 (2016).
9. Y. K. Zeng, T. S. Zhao, L. An, X. L. Zhou and L. Wei, Journal of Power Sources **300**, 438-443 (2015).
10. H. Chen, G. Cong and Y.-C. Lu, Journal of Energy Chemistry **27** (5), 1304-1325 (2018).
11. C. H. Hesse, M. Schimpe, D. Kucevic and A. Jossen, Energies **10** (12), 2107 (2017).
12. J. Lopez, M. Gonzalez, J. C. Viera and C. Blanco, presented at the INTELEC 2004. 26th Annual International Telecommunications Energy Conference, 2004 (unpublished).
13. A. Eftekhari, ACS Sustain Chem Eng **7** (6), 5602-5613 (2019).
14. J. M. Tarascon and M. Armand, Nature **414** (6861), 359-367 (2001).
15. Bloomberg New Energy Finance, in "Electric buses in cities: Driving towards cleaner air and lower CO_2" (BNEF, 2018).
16. P. Arora and Z. Zhang, Chemical Reviews **104** (10), 4419-4462 (2004).
17. S. Choudhury, M. Azizi, I. Raguzin, M. Göbel, S. Michel, F. Simon, A. Willomitzer, V. Mechtcherine, M. Stamm and L. Ionov, Physical Chemistry Chemical Physics **19** (18), 11239-11248 (2017).
18. L. Zolin, M. Destro, D. Chaussy, N. Penazzi, C. Gerbaldi and D. Beneventi, Journal of Materials Chemistry A **3** (28), 14894-14901 (2015).
19. D. R. Rajagopalan Kannan, P. K. Terala, P. L. Moss and M. H. Weatherspoon, International Journal of Electrochemistry **2018**, 7 (2018).
20. D. Deng, Energy Science & Engineering **3** (5), 385-418 (2015).
21. J. Kasnatscheew, R. Wagner, M. Winter and I. Cekic-Laskovic, Topics in Current Chemistry **376** (3), 16 (2018).
22. T. Jaumann, J. Balach, U. Langklotz, V. Sauchuk, M. Fritsch, A. Michaelis, V. Teltevskij, D. Mikhailova, S. Oswald, M. Klose, G. Stephani, R. Hauser, J. Eckert and L. Giebeler, Energy Storage Materials **6**, 26-35 (2017).
23. R. Schröder, M. Aydemir and G. Seliger, Procedia Manufacturing **8**, 104-111 (2017).
24. F. Croce, G. B. Appetecchi, L. Persi and B. Scrosati, Nature **394** (6692), 456-458 (1998).
25. M. H. Braga, C. M Subramaniyam, A. J. Murchison and J. B. Goodenough, J Am Chem Soc **140** (20), 6343-6352 (2018).
26. J. B. Goodenough and K.-S. Park, J Am Chem Soc **135** (4), 1167-1176 (2013).
27. M. Sternad, M. Forster and M. Wilkening, Scientific Reports **6**, 31712 (2016).
28. H. Wu and Y. Cui, Nano Today **7** (5), 414-429 (2012).
29. G. Fredi, S. Jeschke, A. Boulaoued, J. Wallenstein, M. Rashidi, F. Liu, R. Harnden, D. Zenkert, J. Hagberg, G. Lindbergh, P. Johansson, L. Stievano and L. E. Asp, Graphitic microstructure and performance of carbon fibre Li-ion structural battery electrodes **1** (1), 015003 (2018).

30. Y. Mao, X. Wang, S. Xia, K. Zhang, C. Wei, S. Bak, Z. Shadike, X. Liu, Y. Yang, R. Xu, P. Pianetta, S. Ermon, E. Stavitski, K. Zhao, Z. Xu, F. Lin, X.-Q. Yang, E. Hu and Y. Liu, Advanced Functional Materials **29** (18), 1900247 (2019).
31. A. J. Ilott, M. Mohammadi, H. J. Chang, C. P. Grey and A. Jerschow, Proceedings of the National Academy of Sciences **113** (39), 10779 (2016).
32. Y. Wen, D. Xiao, X. Liu and L. Gu, Npg Asia Materials **9**, e360 (2017).
33. Z. Du, D. L. Wood, C. Daniel, S. Kalnaus and J. Li, Journal of Applied Electrochemistry **47** (3), 405-415 (2017).
34. B.-S. Lee, Z. Wu, V. Petrova, X. Xing, H.-D. Lim, H. Liu and P. Liu, Journal of The Electrochemical Society **165** (3), A525-A533 (2018).
35. P. G. Bruce, S. A. Freunberger, L. J. Hardwick and J.-M. Tarascon, Nature Materials **11**, 19 (2011).
36. Y. Wang, E. Sahadeo, G. Rubloff, C.-F. Lin and S. B. Lee, Journal of Materials Science **54** (5), 3671-3693 (2019).
37. X. Liang, C. Hart, Q. Pang, A. Garsuch, T. Weiss and L. F. Nazar, Nature Communications **6**, 5682 (2015).
38. J. Ma, J. Sung, J. Hong, S. Chae, N. Kim, S.-H. Choi, G. Nam, Y. Son, S. Y. Kim, M. Ko and J. Cho, Nature communications **10** (1), 475-475 (2019).
39. M. Cuisinier, P. E. Cabelguen, S. Evers, G. He, M. Kolbeck, A. Garsuch, T. Bolin, M. Balasubramanian and L. F. Nazar, J Phys Chem Lett **4** (19), 3227-3232 (2013).
40. S. Meini, R. Elazari, A. Rosenman, A. Garsuch and D. Aurbach, The Journal of Physical Chemistry Letters **5** (5), 915-918 (2014).
41. S. Evers and L. F. Nazar, Accounts of Chemical Research **46** (5), 1135-1143 (2013).
42. W. Ahn, K.-B. Kim, K.-N. Jung, K.-H. Shin and C.-S. Jin, Journal of Power Sources **202**, 394-399 (2012).
43. Z. Lin, Z. Liu, W. Fu, N. J. Dudney and C. Liang, Advanced Functional Materials **23** (8), 1064-1069 (2013).
44. J. He and A. Manthiram, Energy Storage Materials **20**, 55-70 (2019).
45. A. Scott, Chemical & Engineering News **97** (24) (2019).
46. T. Cleaver, P. Kovacik, M. Marinescu, T. Zhang and G. Offer, Journal of The Electrochemical Society **165** (1), A6029-A6033 (2018).
47. J. Lochala, D. Liu, B. Wu, C. Robinson and J. Xiao, ACS Applied Materials & Interfaces **9** (29), 24407-24421 (2017).
48. A. Manthiram, Y. Fu and Y.-S. Su, Accounts of Chemical Research **46** (5), 1125-1134 (2013).
49. Q. Zhang, F. Li, J.-Q. Huang and H. Li, Advanced Functional Materials **28** (38), 1804589 (2018).
50. J. Li and J. R. Dahn, Journal of The Electrochemical Society **154** (3), A156-A161 (2007).
51. X.-y. Zhang, W.-L. Song, Z. Liu, H.-S. Chen, T. Li, Y. Wei and D.-n. Fang, Journal of Materials Chemistry A **5** (25), 12793-12802 (2017).
52. Z. Zeng, Q. Zeng, N. Liu, A. R. Oganov, Q. Zeng, Y. Cui and W. L. Mao, Advanced Energy Materials **5** (12), 1500214 (2015).
53. M. N. Obrovac and V. L. Chevrier, Chemical Reviews **114** (23), 11444-11502 (2014).

54. M. T. McDowell, S. W. Lee, W. D. Nix and Y. Cui, Advanced Materials **25** (36), 4966-4985 (2013).
55. W. Xu, J. Wang, F. Ding, X. Chen, E. Nasybulin, Y. Zhang and J.-G. Zhang, Energy & Environmental Science **7** (2), 513-537 (2014).
56. C. Fang, X. Wang and Y. S. Meng, Trends in Chemistry **1** (2), 152-158 (2019).
57. D. Lu, Y. Shao, T. Lozano, W. D. Bennett, G. L. Graff, B. Polzin, J. Zhang, M. H. Engelhard, N. T. Saenz, W. A. Henderson, P. Bhattacharya, J. Liu and J. Xiao, Advanced Energy Materials **5** (3), 1400993 (2015).
58. Y. Mekonnen, A. Sundararajan and A. I. Sarwat, presented at the SoutheastCon 2016, 2016 (unpublished).
59. B. Writer, in *Lithium-Ion Batteries: A Machine-Generated Summary of Current Research*, edited by B. Writer (Springer International Publishing, Cham, 2019), pp. 1-71.
60. Z. Jiao, R. Gao, H. Tao, S. Yuan, L. Xu, S. Xia and H. Zhang, Journal of Nanoparticle Research **18** (10), 307 (2016).
61. R. M. Humana, M. G. Ortiz, J. E. Thomas, S. G. Real, M. Sedlarikova, J. Vondrák and A. Visintin, ECS Transactions **63** (1), 91-97 (2014).
62. A. Banerjee, Y. Shilina, B. Ziv, J. M. Ziegelbauer, S. Luski, D. Aurbach and I. C. Halalay, J Am Chem Soc **139** (5), 1738-1741 (2017).
63. M. S. Whittingham, Chemical Reviews **104** (10), 4271-4302 (2004).
64. M. S. Whittingham, Chemical Reviews **114** (23), 11414-11443 (2014).
65. N. Bensalah and H. Dawoud, Journal of Material Science & Engineering **5** (2016).
66. F. R. Gamble, J. H. Osiecki, M. Cais, R. Pisharody, F. J. DiSalvo and T. H. Geballe, Science **174** (4008), 493 (1971).
67. M. S. Whittingham, Science **192** (4244), 1126 (1976).
68. G. L. Holleck and J. R. Driscoll, Electrochimica Acta **22** (6), 647-655 (1977).
69. A. H. Thompson, Phys Rev Lett **35** (26), 1786-1789 (1975).
70. M. S. Whittingham, Journal of The Electrochemical Society **123** (3), 315-320 (1976).
71. K. Mizushima, P. C. Jones, P. J. Wiseman and J. B. Goodenough, Materials Research Bulletin **15** (6), 783-789 (1980).
72. K. Ozawa, Solid State Ionics **69** (3), 212-221 (1994).
73. K. Shedd, E. McCullough and D. Bleiwas, Mining Engineering **69** (12), 37-42 (2017).
74. C. Banza Lubaba Nkulu, L. Casas, V. Haufroid, T. De Putter, N. D. Saenen, T. Kayembe-Kitenge, P. Musa Obadia, D. Kyanika Wa Mukoma, J.-M. Lunda Ilunga, T. S. Nawrot, O. Luboya Numbi, E. Smolders and B. Nemery, Nature Sustainability **1** (9), 495-504 (2018).
75. F. Schipper, E. M. Erickson, C. Erk, J.-Y. Shin, F. F. Chesneau and D. Aurbach, Journal of The Electrochemical Society **164** (1), A6220-A6228 (2017).
76. G. Jeong, Y.-U. Kim, H. Kim, Y. Kim and H.-J. Sohn, Energy Environ. Sci. **4**, 1986-2002 (2011).
77. R. J. Clément, P. G. Bruce and C. P. Grey, Journal of The Electrochemical Society **162** (14), A2589-A2604 (2015).
78. H.-J. Noh, S. Youn, C. S. Yoon and Y.-K. Sun, Journal of Power Sources **233**, 121-130 (2013).
79. Z. Rong, R. Malik, P. Canepa, G. Sai Gautam, M. Liu, A. Jain, K. Persson and G. Ceder, Chem Mater **27** (17), 6016-6021 (2015).

80. M. S. Whittingham, Materials Research Bulletin **13** (9), 959-965 (1978).
81. Y. Song, P. Y. Zavalij and M. S. Whittingham, Journal of The Electrochemical Society **152** (4), A721-A728 (2005).
82. C. Siu, I. D. Seymour, S. Britto, H. Zhang, J. Rana, J. Feng, F. O. Omenya, H. Zhou, N. A. Chernova, G. Zhou, C. P. Grey, L. F. J. Piper and M. S. Whittingham, Chemical Communications **54** (56), 7802-7805 (2018).
83. S.-M. Bak, E. Hu, Y. Zhou, X. Yu, S. D. Senanayake, S.-J. Cho, K.-B. Kim, K. Y. Chung, X.-Q. Yang and K.-W. Nam, ACS Applied Materials & Interfaces **6** (24), 22594-22601 (2014).
84. G. Hautier, A. Jain, S. P. Ong, B. Kang, C. Moore, R. Doe and G. Ceder, Chem Mater **23** (15), 3495-3508 (2011).
85. E. Talaie, P. Bonnick, X. Q. Sun, Q. Pang, X. Liang and L. F. Nazar, Chem Mater **29** (1), 90-105 (2017).
86. A. Gaur and B. D. Shrivastava, Review Journal of Chemistry **5** (4), 361-398 (2015).
87. P. Glatzel and U. Bergmann, Coordin Chem Rev **249** (1-2), 65-95 (2005).
88. T. Kim, B. Song, A. J. G. Lunt, G. Cibin, A. J. Dent, L. Lu and A. M. Korsunsky, Chem Mater **28** (12), 4191-4203 (2016).
89. K. Luo, M. R. Roberts, N. Guerrini, N. Tapia-Ruiz, R. Hao, F. Massel, D. M. Pickup, S. Ramos, Y.-S. Liu, J. Guo, A. V. Chadwick, L. C. Duda and P. G. Bruce, J Am Chem Soc **138** (35), 11211-11218 (2016).
90. L. Nowack, D. Grolimund, V. Samson, F. Marone and V. Wood, Scientific Reports **6** (2016).
91. E. P. Jahrman, L. A. Pellerin, A. S. Ditter, L. R. Bradshaw, T. T. Fister, B. J. Polzin, S. E. Trask, A. R. Dunlop and G. T. Seidler, Journal of The Electrochemical Society **166** (12), A2549-A2555 (2019).

Chapter 7. A Mail-in and User Facility for X-ray Absorption Near Edge Structure: The CEI-XANES laboratory x-ray spectrometer at the University of Washington

Submitted for publication: A. S. Ditter, E. P. Jahrman, L. R. Bradshaw, X. Xia, P. J. Pauzauskie and G. T. Seidler. Journal of Synchrotron Radiation (2019). E. P. Jahrman assisted assembly of the spectrometer and testing of equipment. E.P. Jahrman also planned and performed the study on energy storage materials.

There are more than 100 beamlines or endstations worldwide that frequently support x-ray absorption fine structure (XAFS) measurements, thus providing critical enabling capability for research across numerous scientific disciplines. However, the absence of a supporting tier of more readily accessible, lower-performing options has caused systemic inefficiencies, resulting in high oversubscription and the omission of many scientifically and socially valuable XAFS applications that are incompatible with the synchrotron access model. To this end, we describe the design, performance, and uses of the Clean Energy Institute x-ray absorption near edge structure (CEI-XANES) laboratory spectrometer and its use as both a user-present and mail-in facility. Such new additions to the XAFS infrastructure landscape raise important questions about the most productive interactions between synchrotron and lab-based capabilities. We propose that this can be discussed in the framework of five categories, only one of which is competitive. The categories are: independent operation on independent problems, use dictated by convenience, pre-synchrotron preparatory use of lab capability, post-synchrotron follow-up use of lab capability, and parallel use of both synchrotron and laboratory systems.

1. Introduction

X-ray absorption spectroscopies (XAS) exhibit a global intellectual reach, with more than 100 endstations or beamlines at synchrotron or free electron laser facilities world-wide. This has led to continuing scientific impact across numerous disciplines[1,2], with XAS playing an especially central role in research in catalysis[3,4], electrical energy storage[5–8], environmental science[9], fundamental chemistry and physics[10], biochemistry[11–13], and heavy-element chemistry[14,15]. Much of the highest profile contemporary research does require the full brilliance, time resolution, or other extreme performance metric of these light sources, but a considerable fraction of ongoing excellent work does not. Hence, while the history of XAS at synchrotron facilities is an undisputed scientific success, the recent reinvigoration of laboratory based XAS after several quiescent decades has been spawned by four observations: (1) the improved spectrometer performance seen with modern components; (2) the fact that the synchrotron facilities cannot support the full range of existing demand for XAS; (3) light source operations could benefit from a supporting tier of higher-access, if lower-performing, XAS capability; and (4) drawing analogy to x-ray diffraction, there is a large range of 'routine analytical' use of XAS that is largely incompatible with synchrotron facility priorities.

The observation of the possible synergies and mutual benefits from the coexistence of synchrotron facilities and laboratory-based systems is not new, and was recently summarized by Seidler, et al.[16] Key unmet opportunities include: the broad inclusion of XAS in education, sample validation prior to synchrotron beamtime, decreased synchrotron oversubscription by providing an alternative venue for experiments not requiring the full beamline performance (e.g., many transmission mode studies), rapid-turnaround studies for iterative improvement of new materials synthesis or for industrial process control, and even regulatory applications.

We discuss here a staffed, modern laboratory spectrometer facility for x-ray absorption near edge structure (XANES) studies in the hard x-ray range. This Clean Energy Institute X-ray Absorption Near-Edge Structure (CEI-XANES) facility is located in the Molecular Analysis Facility (MAF) at the University of Washington (https://www.moles.washington.edu/maf). CEI-XANES supports education and academic research at the University Washington in addition to accepting outside in-person users and providing mail-in measurement service for academic, national lab, and industrial studies. Placing this XANES capability in the MAF leads to interesting multi-mode characterization via the other capabilities in the MAF, such as x-ray diffraction, various static and dynamic optical wavelength spectroscopies, and surface characterization techniques.

An outline of the CEI-XANES technical design was presented a few years ago[17] and the system has been operating since 2016. However, with the full opening of CEI-XANES to outside in-person and mail-in users, we take this opportunity to give a more detailed technical description, to present representative results, and to seed a broad discussion of the evolving XAFS infrastructure landscape. Specifically, with the growing number of investigator-owned laboratory spectrometers and also systems run as user facilities, it is time to categorize the different interactions between synchrotron and lab-based capabilities. This discussion finds that competition between the two modes is minimal, and that the most prominent interaction between synchrotron and lab-based x-ray spectroscopy will likely be disjoint, independent use or else truly synergistic benefits from use of both.

2. Instrument Design and Operation

The CEI-XANES spectrometer utilizes a Rowland circle monochromator with a fixed source, i.e., the so-called 'linear spectrometer' design, well known in the 1970's[18], to produce the tunable monochromatic x-rays needed for XANES measurements. A similar design has recently

been implemented in Helsinki[19], and has seen good use for studies of actinide compounds[20] and for a demonstration study for *in situ* catalysis investigations[21]. The relative positioning of key components, i.e., source, analyzer, and detector, is shown in Figure 7-1. The description of the spectrometer then requires two paths: the key components themselves and the supporting components used for motion control. We begin with the former.

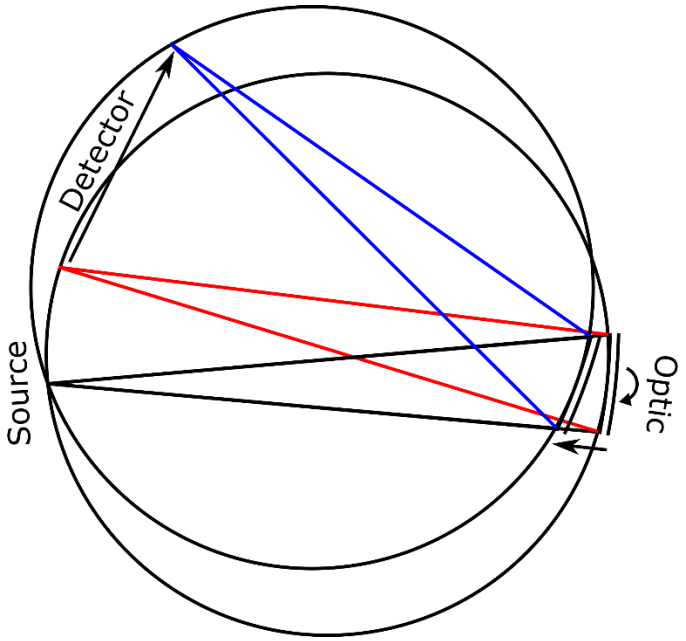

Fig. 7-1: Diagram showing the movement of the Detector and the SBCA in a fixed-source Rowland circle in the direction of low (red) to high (blue) energy. Note that both the source position and the direction from the source to the optic are fixed due to the stationary source.

The computer aided design (CAD) rendering in Figure 7-2 now provides important context. The x-ray source used in CEI-XANES is re-purposed from a powder x-ray diffractometer. Specifically, it is a Siemens XFFAg4k system capable of using either a 1.5kW Ag-anode tube or a 3 kW W-anode tube, just as are used in many powder or single crystal diffractometers. Two different anode materials are needed to avoid strong fluorescence line contamination such as occurs with the unfortunate position of the W Lα2 (8335 eV) emission line in the XANES of Ni

(K-edge 8333 eV). The x-ray tubes are used in 'point focus' configuration with a ~ 0.5 mm (vertical) x 1 mm (in-Rowland-plane) size at a median 6° angle take-off angle. The combination of limited shutter dimension and stronger absorption inside the anode at lower take-off angles results in a beam that slightly 'underfills' the horizontal extent of the spherically bent crystal analyzers (SBCA's, from XRS Tech or else home-made[22]), which have the required 1-m radius of curvature in the Johann geometry and whose constituent diffracting wafers have 10-cm diameter. A welded aluminum helium space with polyimide windows reduces air absorption on the transit from source to SBCA, and from SBCA to detector. A lead-covered, aluminum divider inside the helium box helps to further reduce stray scatter into the line of sight of the detector.

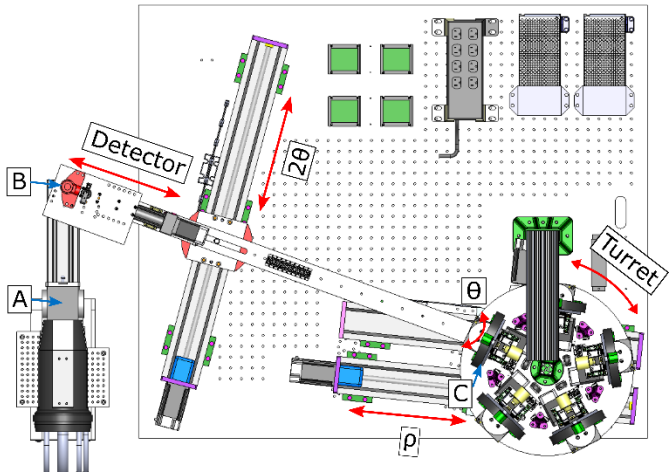

Fig. 7-2: CAD Rendering of CEI-XANES (top view). Labelled with red arrows are the 4 motors used in a scan (Detector, θ, 2θ, and ρ), and the turret motor which switches between optics. The key components are labelled with blue arrows and letters: A) the x-ray source, B) the detector, and C) the optic. Not shown is the helium box to reduce air absorption.

The choice of detector poses particular problems for this generation of high-powered laboratory XAFS system. First, the peak flux on a sufficiently tall detector can reach 500,000/s to 10^6/s and, depending on the choice of SBCA crystal and (hkl) orientation, can be accompanied by

strong, unwanted harmonics. Second, while toroidal optics useful for lab-based XAFS have recently been demonstrated[22], we still use (spherical) SBCA's whose sagittal focusing errors result in vertical stretching of the analyzed beam to 25 mm at a Bragg angle of 70 degrees. Hence, a relatively large detector with good energy resolution and high saturation rates would be ideal. We primarily use a silicon drift detector (SDD, Amptek Inc. with XIA Mercury digital processing hardware). Our SDD has an energy resolution of about 150 eV which easily rejects any harmonics and most background fluorescence, a necessary property to get an accurate measurement. However, the SDD has a collimated area which is just 17 mm^2 and is unable to capture the whole vertical extent of the analyzed beam at lower Bragg angles. In addition, the saturation of this SDD above a few hundred thousand counts per second (broadband) sometimes requires beam attenuation to avoid saturation on analyser harmonics. These limitations could be improved upon with use of larger, commercially available SDD, and also with use of the latest generation of very high speed processing electronics. All results reported here use the Amptek SDD. We have also investigated use of a gas proportional counter (GPC, from LND, Inc.). The GPC has a large active area (1.5 cm x 4 cm) but an energy resolution $\Delta E \sim 2$ keV at E = 7 keV and so must only be used with low-symmetry optics where the harmonics are well separated, and also requires much greater care in rejecting stray scatter and, e.g., fluorescence from the radiation enclosure walls. Using the GPC typically adds to the measurement overhead, as it requires additional background scans with the spectrometer slightly mis-tuned. We note that Hokannen *et al.*[19] found similar concerns when using a large scintillation detector in their spectrometer.

The final important component of the CEI-XANES instrument is the radiation enclosure. This was fabricated from a welded aluminum frame with leaded-plywood walls. The total dimensions of the radiation enclosure are quite large (2.5 m x 1.2 m) to allocate space to use the

second, opposite shutter on the x-ray tube source for a duplicate but independent spectrometer[17]. While the 'B-side' spectrometer is assembled, we have not yet commissioned it for operations.

Regarding spectrometer motions, a total of four motorized degrees of freedom are needed for energy scanning. We note that we use the 'clock angle' orientation scheme of Mortensen[23] to remove the need for motorizing the SBCA tilt perpendicular to the Rowland plane; that tilt axis is instead adjusted manually *once* with a micrometer and a diverging laser, then is unchanged for any and all SBCA installed onto that apparatus. The remaining four degrees of freedom are the scattering angle of the analyzer as seen by the source (θ, Velmex B59 rotary stage, equipped with a 10:1 gear reducer), the distance from the source to the analyzer (ρ, Velmex tandem BiSlide), a linear translation of the detector assembly to put the detector into the specular reflection condition from the analyzer (2θ, Velmex BiSlide), and a final stage immediately underneath the detector + sample sub-assembly (detector, Velmex XSlide) that moves the sample onto the focal point of the monochromatized radiation. Including the effect of the reducing gearbox for the "θ" motor, a single full motor step of the stepper motor results in an angular rotation of 0.004°. For example, near the iron K edge at 7112 eV using a Ge 620 optic, the minimum step size is approximately 0.1eV. While microstepping would, in principal, be able to achieve the same performance, in practice this is not the case: microsteps are highly reproducible across full step cycles but have irregular spacing within the full-step. In addition to energy scanning, the SBCA turret (see Fig. 7-2) requires an additional motorized degree of freedom. This turret was included in the 2016 design to allow rapid change of energy ranges.

Measurements in CEI-XANES are performed by scanning the monochromator over a range of Bragg angles twice, once with the sample in the beam (measuring the transmitted flux) and once without the sample in the beam (measuring the incident flux). The absorption is then calculated

according to the Beer-Lambert Law. The x-ray tube is set to 20 kV accelerating potential and the current is varied (up to 50 mA) so that the flux on the detector is kept near 50,000 counts per second to avoid detector dead time. Data collected here are processed by subtracting a polynomial fit to the pre-edge of the data and normalizing the edge-step to 1 using the Demeter package[24].

3. Experimental

Lepidocrocite and abiotic magnetite samples were ground to fine powders using a mortar and pestle and then spread over 25-μm thick polyimide tape. This tape was layered 8 times, resulting in a sample with an absorption edge step of approximately 0.5. Synchrotron measurements were performed at beamline 20-BM of the Advanced Photon Source. The spectra were calibrated to an iron foil (EXAFS Materials Inc.). The vanadium reference foil was also from EXAFS Materials Inc.

Single layer xx3450 pouch cell batteries were manufactured at the Cell Analysis, Modeling, and Prototyping (CAMP) Facility at Argonne National Laboratory. The anode used in these cells was Superior Graphite SCL1506T (graphite) and the cathode used was Toda NCM-04ST ($Li(Ni_{0.5}Mn_{0.3}Co_{0.2})O_2$ or NMC532). The anode was coated onto a 10-μm thick copper foil for a final electrode loading of 6.38 mg/cm^2 (coating only). The cathode was coated onto a 20-μm thick aluminum foil for a final electrode loading of 11.40 mg/cm^2 (coating only). Other standard pouch cell components included the separator (Celgard 2320), the pouch material (Cellpack-153PL from Youlchon Chemical), and the electrolyte and solvent (1.2M $LiPF_6$ in EC/EMC 3:7 wt%, respectively). Wetting and formation cycles were performed prior to x-ray analysis. The cell exhibited a nominal capacity of 20 mAh. Further cell details can be found in an upcoming manuscript[25].

Yb_2O_3 was purchased from Sigma Aldrich. This powders were mixed with BN powder (boron nitride, Alfa Aesar) and ground in a mortar and pestle, then packed into an aluminum washer between two layers of 25-μm thick polymide tape. Bulk Yb:$LiYF_4$ was synthesized by the Czochralski process at the University of New Mexico. A piece of a large single crystal was broken off, ground into a fine powder and used to fill the same type of sample holder. Nano-phase Yb:$LiYF_4$ was synthesized at the University of Washington using previously described methods[26]. The resulting solid was mixed with BN and ground in a mortar and pestle and again put into the same type of sample holder as for the other two Yb-rich samples.

4. Results

Here we describe measurements on several transition metal and rare-earth compounds to demonstrate the utility of CEI-XANES as a user facility. These measurements show both that CEI-XANES is able to reproduce synchrotron results and illustrate several "typical" use-cases for measurements.

To make a direct comparison with synchrotron data, lepidocrocite and aboitic magnetite were measured in transmission mode at both CEI-XANES and beamline 20-BM of the Advanced Photon Source (APS), shown in Figure 7-3. The CEI-XANES measurements were performed at 20 kV and 10 mA tube power for approximately two hours each using a Ge (620) optic. Measurement time would have been proportionally increased with higher tube current (we used only ~20% of maximum power) but we wished to avoid detector saturation. We can see that CEI-XANES reproduces the synchrotron results well, with no discernible difference between the spectra, showing that CEI-XANES is capable of producing sufficient quality spectra for many applications. Similar results for Rowland circle spectrometers using SBCA have been reported elsewhere.[16,19,27]

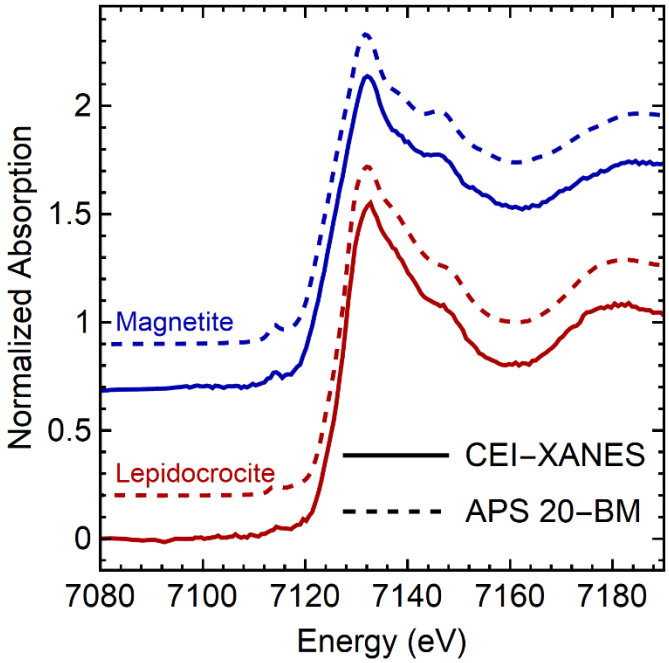

Fig. 7-3: Comparison of CEI-XANES (solid) and synchrotron (dashed, collected at APS 20-BM) data for both abiotic magnetite (blue) and lepidocrocite (red). Spectra are offset for clarity.

Figure 7-4 shows the measurement of an V foil as well as comparison with data taken at Beamline 13-ID of APS, as per an online XAFS database[28]. In this figure, the APS spectrum is shown both as measured and convolved with a Gaussian with FWHM of 0.8 eV. The broadening of 0.8 eV matches the CEI spectrum, so taking into account the energy resolution of the initial spectrum (0.6 eV), we estimate the energy resolution of CEI-XANES at the Fe K-edge to be 1.0 eV. This is similar to previous instruments[27], and given that the 1s core-hole lifetime broadening for transition metals is on the order of 1 eV, this energy resolution is sufficient for many applications. The broadening is likely dominated by the source size in the Rowland plane.

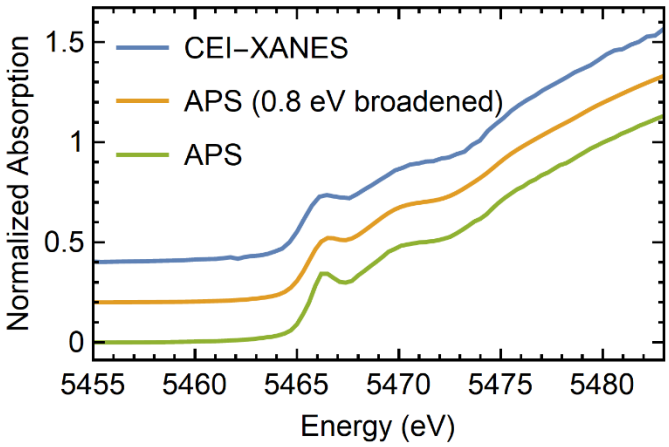

Fig. 7-4: Comparison of V Foil XANES spectra taken with CEI-XANES (blue) and at APS (green). Broadening the APS spectrum by 0.8 eV (orange) aligns it well with the CEI-XANES spectrum. Assuming an energy resolution 0.6 eV for the APS data, we estimate an energy resolution of 1.0 eV for CEI-XANES at the V k-edge. Spectra are offset for clarity.

CEI-XANES has its highest flux between 5-11 keV, so quick measurements of ideal samples at these x-ray energies are possible. We demonstrate this here with a few 2-minute scans of the Ni K-edge XANES scans of a NMC pouch cell battery, see Figure 7-5. A careful I_0 scan was taken before the study and a longer transmission scan (30 minutes) was used to normalize the edge step for the quicker 2-minute scans. These results will be expanded upon elsewhere in a complete *in operando* study of pouch cell charging and discharging.[25]

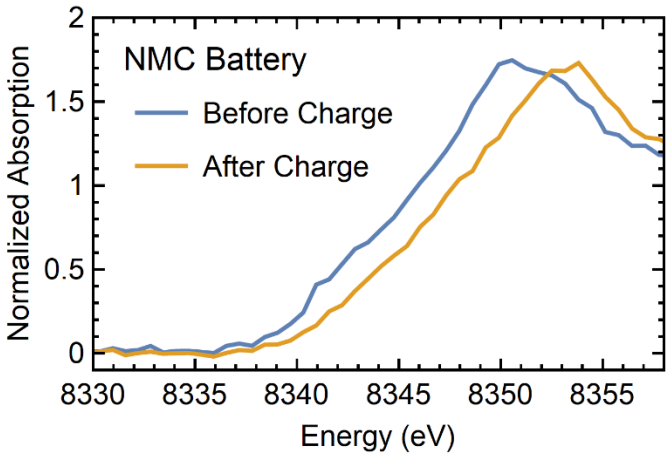

Fig. 7-5: Ni XANES spectra of an NMC pouch cell battery before and after charging. Not shown is a scan over a longer range used to normalize these data. Measurement time was 2 minutes for each spectrum. See the text for discussion.

Finally, we report on a 'routine' material characterization example. Ytterbium doped $LiYF_4$ is an important laser cooling material[29], however, when using the Czochralski synthesis, some product crystals could not be cooled upon laser excitation, generating heat instead. One hypothesis is some Yb atoms are reduced to the 2+ oxidation state due to the inclusion of HF in the synthesis, where the strong background absorption by Yb(II) causes the failure of laser cooling. Hence, it is important to learn whether the hydrothermally synthesized, nanophase Yb:$LiYF_4$, in which no HF is used, contains Yb(II).

In Figure 7-6, bulk and nano-phase Yb:$LiYF_4$ were measured alongside a Yb_2O_3 standard, and are presented alongside a previously measured Yb doped CaF_2 crystal[30]. Previous XANES studies have shown that Yb impurities in calcite and fluorite crystals can be partially in the 2+ oxidation state, and when they are, a pre-edge peak at 8040 eV is present.[30–34] This peak is not present for Yb in the 3+ oxidation state and so the absence of these peaks in both the bulk and nanocrystals indicate Yb is solely in the 3+ oxidation state. This type of routine oxidation-state

identification is a common use-case for the CEI-XANES facility, and one that can be easily performed without the brilliance of a synchrotron beamline.

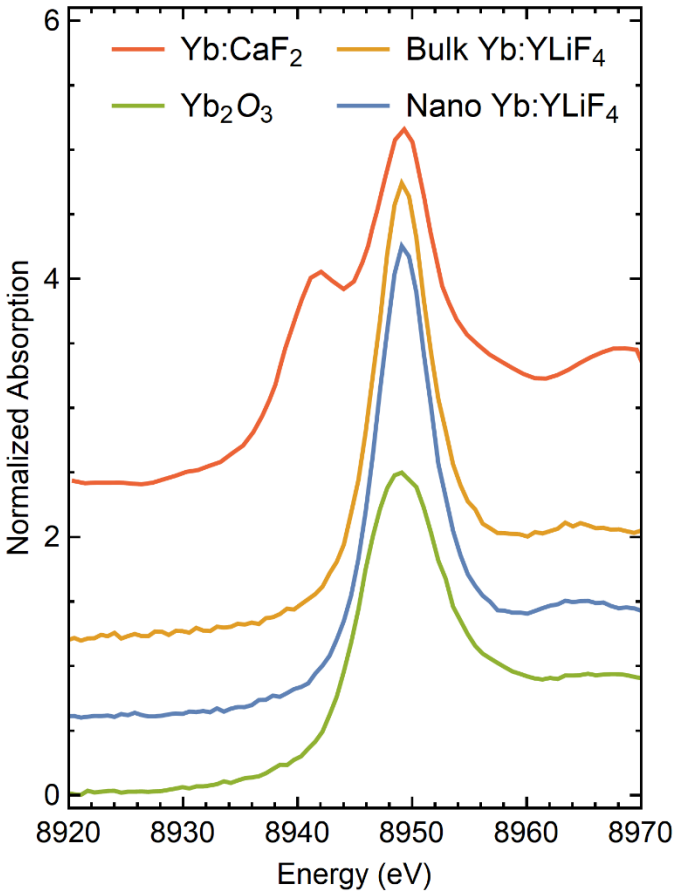

Fig. 7-6: Comparison of Nano Yb:$YLiF_4$ crystals (blue) with bulk crystals (yellow), and Yb^{III} standard Yb_2O_3 (green) measured at UW and $Yb^{II/III}$ mixed-valent Yb:CaF_2 (red) reproduced from Yoshida, et al (2005). Spectra offset for clarity.

5. Use Landscapes in a Future with Ubiquitous Laboratory XAFS and XES

In addition to the present work, there is a growing body of laboratory spectrometers for XAFS and XES in the hard x-ray[16,18,27,35,36,36–46] and tender x-ray ranges[47–54]. These systems have seen quite varied use, showing an impressive flexibility to address problems in many different fields. For example, the previously mentioned tender x-ray spectrometers have been used to

characterize the phosphorous oxidation state in InP quantum dots[55] and to look at sulfur speciation in biochars[56]. The various hard x-ray instruments have been used to look at oxygen vacancies in V_2O_5[57], to work towards creating a standardized regulatory measurement for Cr oxidation state[58], to look at actinide oxidation state[20], and for a long-duration study of Co/TiO_2 catalysts[21].

These earliest uses in what appears to be an ongoing rebirth of lab XAFS together with the rapidly growing number of lab XAFS systems causes us to wonder about the future. We can realistically imagine a time, perhaps 10 years hence, when the availability of lab XAFS and XES compared to synchrotron XAS has reached a 'sensible' level similar to the relative availabilities of, e.g., lab-based x-ray diffraction (XRD) compared to synchrotron XRD. In such a world, how should we think about the interplay between lab-based and synchrotron capabilities and facilities? Will they compete, be disconnected, or be synergistic? Will the synchrotron XAFS demand decrease because of lab-based capability, or will it instead greatly increase due to a likely new inclusion of XAFS in University education, with possible discovery of new research applications of XAFS?

While any detailed answers to the above questions would be speculative, we can still identify several important categories of interaction between lab and synchrotron XAS, and give exemplars for each. Hence, in Figure 7-7, we present five schema, which we now discuss in order. First, there is the situation of Fig. 7-7(a) where the two access paths are fully independent. Independence of lab XAS from the synchrotron is not due to any lack of technical capability at the synchrotron but is instead due to a fundamental mismatch between the character of the desired study and the scientific mission of the synchrotron light sources. Rapid feedback studies during new materials synthesis[55] and, more hypothetically, industrial quality control testing of, e.g., Li-ion battery transition metal oxide electrodes simply do not fit the synchrotron access model: they

require a high level of on-demand measurement. On the other hand, the extreme performance characteristics of synchrotron beamlines support a plethora of studies that are impractical or impossible in the laboratory.

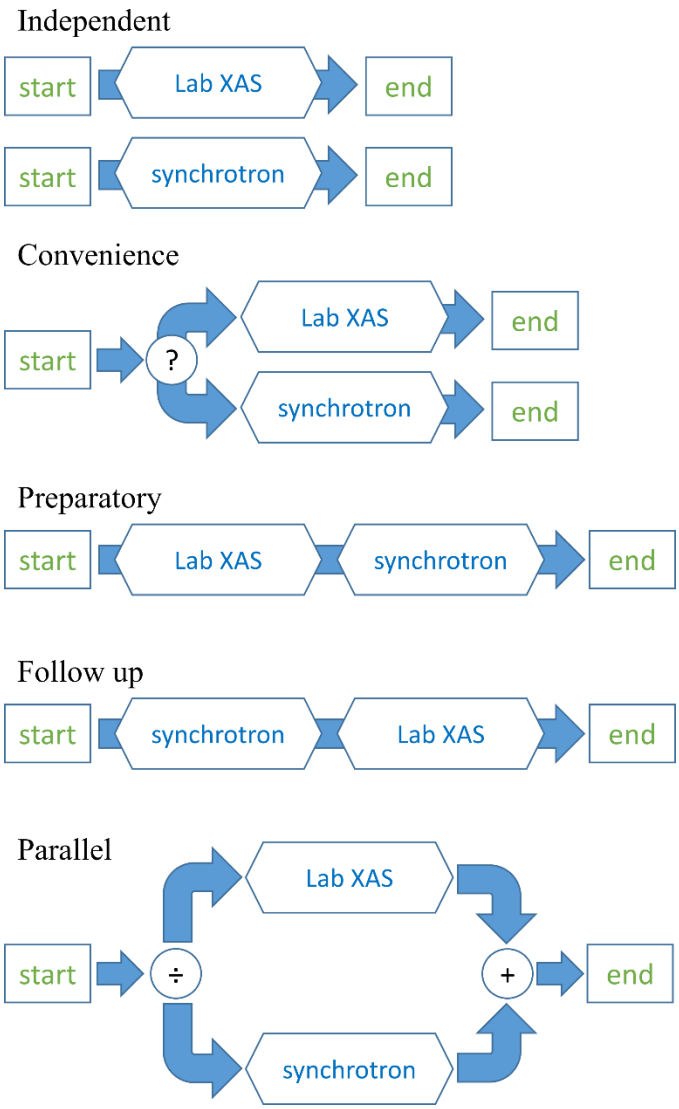

Fig. 7-7: Schema outlining the different ways that synchrotron and laboratory XAS interact. See text for further details.

Second, there is the category of user convenience, as in Fig. 7-7(b). It is only in this access pattern that there is competition between laboratory and synchrotron facilities. The user in this case has a project that meets the scientific standards of the synchrotron so as to pass, for example,

peer review by a general user proposal review panel, but the study could be successfully be performed with a laboratory spectrometer. At present, the question is one of convenience. As modern laboratory XAS systems and lab XAS user and mail-in facilities become more common, it is fair to ask whether the 'question' of operation in this use case may not be in the control of the user, but instead in the hands of the synchrotron review panel. Some years hence, if there is generically high access to lab XAS then it is fair to expect that synchrotron facilities might be able to decline studies that could be performed with lab-based systems.

Third, there are clear benefits from decreasing some of the common inefficiencies ubiquitous in synchrotron XAS beamtime usage. Education of new users is an obvious starting point. Although tutorials and workshops have undeniable value, hands-on lab-based measurement with iteration in demonstration or pedagogical studies would give a rich training that would immediately increase efficiency for future synchrotron beamtime. Further, even experienced users often spend a nontrivial fraction of beamtime refining their sample preparation. Much of this work can be done in the lab, or at least users can become very highly expert in calculating and executing sample preparation outside of beamtime. Finally, the issue of sample and/or experiment design validation must be considered distinct from sample preparation. By validation, we mean any of: at least qualitative confirmation of the synthesis of the desired phase; supporting evidence that the intended physical phenomena will indeed have an effect on the to-be measured spectrum; determination of the efficacy of special sample containers for, e.g., air-sensitive samples; or evaluation of signal levels to better estimate final beamtime needs. This latter case where one seeks more accurate estimation of beamtime needs is one where there is considerable ongoing effort [59].

Fourth, during post-synchrotron beamtime data analysis, users frequently find that some modest additional work would greatly benefit the project, if not in fact be necessary for its

completion. If the measurement demands synchrotron flux or brilliance, then there is no alternative but to wait for repeat beamtime. However, there are at least two obvious cases where lab XAS can serve in this regard. First, when XAFS data on additional reference standards is needed, the studies can typically be performed on concentrated samples. Second, XES can often serve to provide added context to aid with interpretation of XANES, in particular. This same synergy plays a likely role below, in the final use case.

Finally, there are likely cases where lab-based spectroscopy will strictly enhance synchrotron work at an equal level of scientific merit, rather than merely augmenting in support. The most obvious example is using lab-based nonresonant XES to provide direct context for better interpretations of synchrotron-based XANES results. Valence-to-core XES can clearly improve understanding of bonding character without need to address the subtleties of core-hole effects, and Kα XES can sometimes give a cleaner fingerprint of classical oxidation state of the species of interest than can XANES, as the former is less sensitive to local environment than the latter.[56]

6. Conclusion

We have demonstrated the capabilities of the CEI-XANES instrument as the first mail-in XANES user facility using lab-based instrumentation, and shown the capability to produce synchrotron-quality spectra in the 5-11 keV range. We have also outlined a number of ways that laboratory systems interact with synchrotron x-ray spectroscopies, and argue that laboratory spectrometers are best seen not as a direct competitor with synchrotron operations, but rather as an expansion of the existing XAFS access landscape to become more similar to those of the overwhelming majority of other analytical method. This will expand the user base especially in the emerging field of 'analytical' applications of XAFS but will also lead to better prepared and, we can hope, high impact synchrotron XAFS studies in disciplines where XAFS has not yet made entry. Therefore, the continuing development of laboratory instruments, including user-facility

class instruments like the one described here are a promising sign for increased access and an expansion in the utilization of x-ray absorption spectroscopy.

7. Acknowledgements

We gratefully acknowledge the help of Maxim I. Boyanov and Kenneth M. Kemmer in providing the iron reference standards and synchrotron measurements at APS 20-ID. We would also like to thank Bryant J. Polzin, Steven E. Trask, and Allison R. Dunlop of Argonne for helping to produce the NMC battery.

8. Funding Information

This material is based in part upon work supported by the State of Washington through the University of Washington Clean Energy Institute and via funding from the Washington Research Foundation. EPJ was supported in part by the Joint Center for Energy Storage Research (JCESR), an Energy Innovation Hub funded by the U.S. Department of Energy, Office of Science, and Basic Energy Sciences. Part of this work was conducted at the Molecular Analysis Facility, a National Nanotechnology Coordinated Infrastructure site at the University of Washington which is supported in part by the National Science Foundation (grant NNCI-1542101), the University of Washington, the Molecular Engineering & Sciences Institute, and the Clean Energy Institute. X.X., and P.J.P. gratefully acknowledge financial support from the MURI:MARBLe project under the auspices of the Air Force Office of Scientific Research (Award No. FA9550-16-1-0362). This research used resources of the Advanced Photon Source, an Office of Science User Facility operated for the U.S. Department of Energy (DOE) Office of Science by Argonne National Laboratory, and was supported by the U.S. DOE under Contract No. DE-AC02-06CH11357, and the Canadian Light Source and its funding partners.

9. References

1. Bunker, G. *Introduction to XAFS*. (Cambridge University Press, 2010).

doi:10.1017/CBO9780511809194
2. de Groot, F., Kotani, A. & Kotani, A. *Core Level Spectroscopy of Solids*. (CRC Press, 2008). doi:10.1201/9781420008425
3. Caudillo-Flores, U., Muñoz-Batista, M. J., Kubacka, A. & Fernández-García, M. Operando Spectroscopy in Photocatalysis. *ChemPhotoChem* **2**, 777–785 (2018).
4. John Meurig Thomas*, †,‡ and & Gopinathan Sankar*, †. The Role of Synchrotron-Based Studies in the Elucidation and Design of Active Sites in Titanium−Silica Epoxidation Catalysts. (2001). doi:10.1021/AR010003W
5. McBreen, J., O'Grady, W. E. & Pandya, K. I. EXAFS: A new tool for the study of battery and fuel cell materials. *J. Power Sources* (1988). doi:10.1016/0378-7753(88)80027-2
6. McBreen, J. The application of synchrotron techniques to the study of lithium-ion batteries. *J. Solid State Electrochem.* **13**, 1051–1061 (2009).
7. Cheng, H. *et al.* Synchrotron radiation X-ray powder diffraction techniques applied in hydrogen storage materials - A review. *Prog. Nat. Sci. Mater. Int.* **27**, 66–73 (2017).
8. Li, W. *et al.* Synchrotron-Based X-ray Absorption Fine Structures, X-ray Diffraction, and X-ray Microscopy Techniques Applied in the Study of Lithium Secondary Batteries. *Small Methods* **2**, 1700341 (2018).
9. Ma, B., Charlet, L., Fernandez-Martinez, A., Kang, M. & Madé, B. A review of the retention mechanisms of redox-sensitive radionuclides in multi-barrier systems. *Appl. Geochemistry* **100**, 414–431 (2019).
10. Young, N. A. The application of synchrotron radiation and in particular X-ray absorption spectroscopy to matrix isolated species. *Coord. Chem. Rev.* **277**–**278**, 224–274 (2014).
11. Sarangi, R. X-ray absorption near-edge spectroscopy in bioinorganic chemistry: Application to M–O2 systems. *Coord. Chem. Rev.* **257**, 459–472 (2013).
12. Porcaro, F., Roudeau, S., Carmona, A. & Ortega, R. Advances in element speciation analysis of biomedical samples using synchrotron-based techniques. *TrAC Trends Anal. Chem.* **104**, 22–41 (2018).
13. Kowalska, J. & DeBeer, S. The role of X-ray spectroscopy in understanding the geometric and electronic structure of nitrogenase. *Biochim. Biophys. Acta - Mol. Cell Res.* **1853**, 1406–1415 (2015).
14. Kosog, B., La Pierre, H. S., Denecke, M. A., Heinemann, F. W. & Meyer, K. Oxidation State Delineation via U L_{III}-Edge XANES in a Series of Isostructural Uranium Coordination Complexes. *Inorg. Chem.* **51**, 7940–7944 (2012).
15. Shi, W.-Q. *et al.* Exploring Actinide Materials Through Synchrotron Radiation Techniques. *Adv. Mater.* **26**, 7807–7848 (2014).
16. Seidler, G. T. *et al.* A laboratory-based hard x-ray monochromator for high-resolution x-ray emission spectroscopy and x-ray absorption near edge structure measurements. *Rev. Sci. Instrum.* **85**, 113906 (2014).
17. Seidler, G., Mortensen, D., Ditter, A., Ball, N. & Remesnik, A. A Modern Laboratory XAFS Cookbook. *J. Phys. Conf. Ser.* **712**, 012015 (2016).
18. Knapp, G. S., Chen, H. & Klippert, T. E. Development of a laboratory EXAFS facility. *Rev. Sci. Instrum.* **49**, 1658–1666 (1978).
19. Honkanen, A.-P. *et al.* Johann-type laboratory-scale x-ray absorption spectrometer with versatile detection modes. *Rev. Sci. Instrum.* **90**, 033107 (2019).
20. Bès, R. *et al.* Laboratory-scale X-ray absorption spectroscopy approach for actinide research: Experiment at the uranium L3-edge. *J. Nucl. Mater.* **507**, 50–53 (2018).

21. Moya-Cancino, J. G. *et al. In-situ* X-Ray Absorption Near Edge Structure Spectroscopy of a Solid Catalyst using a Laboratory-Based Set-up. *ChemCatChem* **11**, 1039–1044 (2019).
22. Jahrman, E. P. *et al.* Vacuum formed temporary spherically and toroidally bent crystal analyzers for x-ray absorption and x-ray emission spectroscopy. *Rev. Sci. Instrum.* **90**, 013106 (2019).
23. Mortensen, D. R. & Seidler, G. T. Robust optic alignment in a tilt-free implementation of the Rowland circle spectrometer. *J. Electron Spectros. Relat. Phenomena* **215**, 8–15 (2017).
24. Ravel, B. & Newville, M. ATHENA , ARTEMIS , HEPHAESTUS : data analysis for X-ray absorption spectroscopy using IFEFFIT. *J. Synchrotron Radiat.* **12**, 537–541 (2005).
25. E. P. Jahrman, L. A. Pellerin, A. S. Ditter, L. R. Bradshaw, T. T. Fister, B. J. Polzin, S. E. Trask, A. R. Dunlop and G. T. Seidler, Journal of The Electrochemical Society **166** (12), A2549-A2555 (2019).
26. Roder, P. B., Smith, B. E., Zhou, X., Crane, M. J. & Pauzauskie, P. J. Laser refrigeration of hydrothermal nanocrystals in physiological media. *Proc. Natl. Acad. Sci. U. S. A.* **112**, 15024–9 (2015).
27. Jahrman, E. P. *et al.* An improved laboratory-based x-ray absorption fine structure and x-ray emission spectrometer for analytical applications in materials chemistry research. *Rev. Sci. Instrum.* **90**, 024106 (2019).
28. GSE-CARS XAFS Spectra Library (beta). Available at: http://cars.uchicago.edu/xaslib/search. (Accessed: 28th May 2019)
29. Cittadino, G., Volpi, A., Di Lieto, A. & Tonelli, M. Co-doping of $LiYF_4$ crystal: a virtuous effect of cooling efficiency. *J. Phys. D. Appl. Phys.* **51**, 145302 (2018).
30. Yoshida, T., Kagi, H., Tsuno, H., Ohta, A. & Nomura, M. Oxidation States of Ytterbium Incorporated in Calcium Carbonate and Calcium Fluoride. *Chem. Lett.* **34**, 852–853 (2005).
31. Iyer, A. K. & Peter, S. C. EuLiGe2 and YbLiGe2 - A Divalent and an Intermediate-Valent Compound with CaLiSi2-Type Structures. *Eur. J. Inorg. Chem.* **2012**, 1790–1794 (2012).
32. Peter, S. C., Disseler, S. M., Niclas Svensson, J., Carretta, P. & Graf, M. J. Yb4LiGe4 – A Yb mixed valent Zintl phase with strong electronic correlations. *J. Alloys Compd.* **516**, 126–133 (2012).
33. Rao, C. N. R. *et al.* Valence fluctuation in some Yb intermetallics by X-ray photoemission and X-ray absorption. *Chem. Phys. Lett.* **76**, 413–415 (1980).
34. Hatwar, T. K. *et al.* X-ray absorption spectroscopic study of mixed valence systems EuCu2Si2, YbCu2Si2 and Sm4Bi3. *Solid State Commun.* **34**, 617–620 (1980).
35. Hoszowska, J., Dousse, J.-C., Kern, J. & Rhême, C. High-resolution von Hamos crystal X-ray spectrometer. *Nucl. Instruments Methods Phys. Res. Sect. A Accel. Spectrometers, Detect. Assoc. Equip.* **376**, 129–138 (1996).
36. Németh, Z., Szlachetko, J., Bajnóczi, É. G. & Vankó, G. Laboratory von Hámos X-ray spectroscopy for routine sample characterization. *Rev. Sci. Instrum.* **87**, 103105 (2016).
37. Kayser, Y. *et al.* Laboratory-based micro-X-ray fluorescence setup using a von Hamos crystal spectrometer and a focused beam X-ray tube. *Rev. Sci. Instrum.* **85**, 043101 (2014).
38. Malzer, W. *et al.* A laboratory spectrometer for high throughput X-ray emission spectroscopy in catalysis research. *Rev. Sci. Instrum.* **89**, 113111 (2018).
39. Schlesiger, C., Anklamm, L., Stiel, H., Malzer, W. & Kanngießer, B. XAFS spectroscopy by an X-ray tube based spectrometer using a novel type of HOPG mosaic crystal and optimized image processing. *J. Anal. At. Spectrom.* **30**, 1080–1085 (2015).
40. Szlachetko, M., Berset, M., Dousse, J.-C., Hoszowska, J. & Szlachetko, J. High-

resolution Laue-type DuMond curved crystal spectrometer. *Rev. Sci. Instrum.* **84**, 093104 (2013).
41. Cohen, G. G., Fischer, D. A., Colbert, J. & Shevchik, N. J. Tunable laboratory extended x-ray absorption fine structure system. *Rev. Sci. Instrum.* **51**, 273–277 (1980).
42. Thulke, W., Haensel, R. & Rabe, P. Versatile curved crystal spectrometer for laboratory extended x-ray absorption fine structure measurements. *Rev. Sci. Instrum.* **54**, 277–283 (1983).
43. Tohji, K., Udagawa, Y., Kawasaki, T. & Masuda, K. Laboratory EXAFS spectrometer with a bent crystal, a solid-state detector, and a fast detection system. *Rev. Sci. Instrum.* **54**, 1482–1487 (1983).
44. Williams, A. Laboratory x-ray spectrometer for EXAFS and XANES measurements. *Rev. Sci. Instrum.* **54**, 193–197 (1983).
45. Yuryev, Y. N. *et al.* Variable Rowland radius laboratory vacuum surface-sensitive x-ray absorption fine structure spectrometer. *Rev. Sci. Instrum.* **78**, 025108 (2007).
46. Anklamm, L. *et al.* A novel von Hamos spectrometer for efficient X-ray emission spectroscopy in the laboratory. *Rev. Sci. Instrum.* **85**, 053110 (2014).
47. Dolgih, V. E. *et al.* X-ray fluorescent spectrometer with linear position sensitive detector. *Nucl. Instruments Methods Phys. Res.* **224**, 117–119 (1984).
48. Yarmoshenko, Y. M. *et al.* Possibility of sulphur-oxygen substitution in YBa2Cu3O6+xSy analyzed by means of X-ray emission spectroscopy. *J. Phys. Chem. Solids* **54**, 1211–1214 (1993).
49. Yarmoshenko, Y. M., Trofimova, V. A., Kurmaev, E. Z., Slater, P. R. & Greaves, C. X-ray emission spectra of YSr2Cu3O7−δ containing sulphate and phosphate groups. *Phys. C Supercond.* **224**, 317–320 (1994).
50. Yarmoshenko, Y. M. *et al.* X-ray emission spectra and valence state of sulphur atoms of $YBa_2((CuO)_{1-x}(NiS)_x)_3O_{4-delta}$. *J. Phys. Condens. Matter* **7**, 213–218 (1995).
51. Sugiura, C., Gohshi, Y. & Suzuki, I. Sulfur K β x-ray emission spectra and electronic structures of some metal sulfides. *Phys. Rev. B* **10**, 338–343 (1974).
52. Sugiura, C., Gohshi, Y. & Suzuki, I. Kβ Emission and *K* Absorption Spectra of Sulfur in MnS. *Jpn. J. Appl. Phys.* **11**, 911–912 (1972).
53. Kavčič, M. *et al.* Design and performance of a versatile curved-crystal spectrometer for high-resolution spectroscopy in the tender x-ray range. *Rev. Sci. Instrum.* **83**, (2012).
54. Holden, W. M. *et al.* A compact dispersive refocusing Rowland circle X-ray emission spectrometer for laboratory, synchrotron, and XFEL applications. *Rev. Sci. Instrum.* **88**, 073904 (2017).
55. Stein, J. L. *et al.* Probing Surface Defects of InP Quantum Dots Using Phosphorus Kα and Kβ X-ray Emission Spectroscopy. *Chem. Mater.* **30**, 6377–6388 (2018).
56. Holden, W. M., Seidler, G. T. & Cheah, S. Sulfur Speciation in Biochars by Very High Resolution Benchtop Kα X-ray Emission Spectroscopy. *J. Phys. Chem. A* **122**, 5153–5161 (2018).
57. Bi, W. *et al.* Tailoring Energy and Power Density through Controlling the Concentration of Oxygen Vacancies in V_2O_5/PEDOT Nanocable-Based Supercapacitors. *ACS Appl. Mater. Interfaces* **11**, 16647–16655 (2019).
58. Jahrman, E. P., Seidler, G. T. & Sieber, J. R. Determination of Hexavalent Chromium Fractions in Plastics Using Laboratory-Based, High-Resolution X-ray Emission Spectroscopy. *Anal. Chem.* **90**, 6587–6593 (2018).
59. Abe, H. *et al.* Improving the quality of XAFS data. *J. Synchrotron Radiat.* **25**, 972–980 (2018).

Chapter 8. Laboratory-based X-ray Absorption Spectroscopy on a Working Pouch Cell Battery at Industrially-Relevant Charging Rates

Originally published as: E. P. Jahrman, L. A. Pellerin, A. S. Ditter, L. R. Bradshaw, T. T. Fister, B. J. Polzin, S. E. Trask, A. R. Dunlop, and G. T. Seidler. Journal of The Electrochemical Society **166** (12), A2549-A2555 (2019). This chapter represents a significant portion of this dissertation and the effort was led by the candidate.

Li-ion battery (LIB) research has continuing importance for the entire range of applications from consumer products to vehicle electrification and grid stabilization. In many cases, standard electrochemical methods only provide an overall voltage or specific capacity, giving an inadequate description of parallel redox processes or chemical gradients at the particle and pack level. X-ray absorption fine structure (XAFS) is frequently used to augment bulk electrochemical data, as it provides element-specific changes in oxidation state and local atomic structure. Such microscopic descriptors are crucial for elucidating charge transfer and structural changes associated with bonding or site mixing, two key factors in evaluating state of charge and modes of cell failure. However, the impact of XAFS on LIB research has been significantly constrained by a logistical barrier: contemporary XAFS work is performed almost exclusively at synchrotron x-ray light sources, where beamtime is infrequent and experiment time-frames are limited. Here we show that modern laboratory-based XAFS can not only be applied to, e.g., characterization of ex situ LIB electrode materials, but can also be used for operando studies at industrially-relevant charging rates in a standard pouch cell preparation. Such capability enables accelerated discovery of new materials and improved operation modes for LIBs.

1. Introduction

Li-ion batteries (LIBs) serve diverse roles in the evolving modern energy landscape. This begins with small, consumer-level products,[1, 2] continues to vehicle electrification,[3] and ends at several grid-level venues.[4] While typical LIB applications require high energy density, a specification that is often achieved by developing cathode materials of high discharge capacity and high operating voltage,[5] recent industrial fast-charging ventures also demand improved power densities.[6] To meet these ends, there is strong evidence that the development of new battery chemistries and operation modes requires not just the usual bulk electrochemical characterization, but is instead strongly facilitated by studies using advanced x-ray spectroscopies. Specifically, x-ray absorption fine structure (XAFS) provides element-specific changes in local atomic structure (whether crystalline or disordered), bond lengths, and redox state.

It is useful to provide a brief synopsis of recent utilizations of XAFS in LIB research to showcase the utility of these measurements and the information attainable from them, especially in cases where multiple transition metals are included in the electrode chemistry. Of particular relevance to the present work, Mao et al.[7] paired XAFS with other x-ray techniques to investigate the fatigue of an Ni-rich Ni-Mn-Co (NMC) LIB material. Ni-rich NMC LIBs garner significant interest by extending the capacity accessible at reasonable voltage cutoffs.[8] The utility of these systems is, however, hindered by instabilities due to oxygen evolution during phase transitions and concomitant redox chemistry changes in the constituent transition metals.[8-10] These researchers found high-voltage charging did not result in obvious lattice changes or oxygen evolution, contrary to previous reports. Rather, increased disorder is found around the Ni sites and the oxidation state of the Ni atoms is highly heterogeneous, thus leading to high

mechanical strain and micro-cracks. Note that this study was not an isolated effort in the literature. Indeed, the oxidation state of Ni-rich NMC materials has also been analyzed with XAFS by Tian et al.[11] and Bak et al.[9] Similarly, XAFS has been applied to the study of related materials. Aryal et al. examined all of the transition metals in a Li-rich Mn-Ni-Fe oxide cathode to reveal reduction of Mn and an irreversible loss of nearby oxygen atoms after cycling, while the Ni and Fe experienced little change in environment.[12] XAFS has also played a crucial role toward confirming charge transfer in analogous multivalent cathodes,[13, 14] which are often difficult to analyze electrochemically due side reactions.[15] Furthermore, Kim et al. presented a wavelet transform analysis of Extended X-ray Absorption Fine Structure (EXAFS) measurements to reveal the Ni-O and Co-O distances change irreversibly and reversibly, respectively, during the first cycle of a NMC lithium ion battery, despite the redox reversibility of the Ni, Mn, and Co.[16]

The case of NMC batteries and the other mixed-metal systems, above, illustrate a common theme: The structural and speciation characterizations accessible by x-ray absorption spectroscopy are critical in developing new energy storage technologies, yet, until recently, this technique has been performed almost exclusively at synchrotron light sources and therefore subject to necessarily restrictive access models. This availability constraint is problematic for LIB research and development efforts. It limits the application of these techniques as valuable diagnostic tools in emerging battery materials requiring rapid feedback for further development, and it also hinders long-term studies, i.e., for degradation mechanisms, that require regular and extended access. Here, we show how the growing renaissance of lab-based, advanced x-ray spectroscopies can enable rapid and routine *operando* analyses of energy storage materials.

Some prior studies have used earlier generations of laboratory-based XAFS in energy storage research, this includes *ex situ* studies of Fe-substituted $LiCoO_2$ electrodes[17, 18] as well as *ex situ* studies of Fe-substituted Li_2MnO_3[19] and an *in situ* study of Fe-substituted $LiMn_2O_4$ charged at a rate of C/10.[20] However, *operando* x-ray analysis is widely believed to be a vital tool for monitoring element-specific oxidation in an inherently non-equilibrium process.[21] Fortunately, the field of laboratory-based x-ray absorption spectroscopy has seen rapid improvement in the quality of instruments based on both von Hamos[22-24] and Rowland[25-29] geometries. Indeed, these technologies are now being suggested as tools to address the development of nuclear fuels and disposal of subsequent waste,[30] as a platform for catalysis research,[31-33] and as a viable option for applying advanced x-ray spectroscopies to regulatory compliance testing.[34]

Here, making use of a high-powered laboratory XAFS user facility at the University of Washington (i.e., more than 1000 km from the nearest synchrotron x-ray light source), the X-ray Absorption Near Edge Structure (XANES) spectrum of Co, Mn, and Ni are measured at their respective K-edges in a working Ni-rich NMC battery during charging and discharging. All elements were measured at a rate of C/5 and we assess the redox behavior of each metal, but the Ni K-edge was also measured at faster rates, up to a maximum of 3C to establish the feasibility of laboratory-based *operando* studies at industrially relevant fast charge rates. Indeed, the x-ray intensities provided by the present spectrometer permit the pouch cell to be studied without modification, which ensures the electrochemical behavior of the cell has not been perturbed.[35] Taken *en masse*, these results demonstrate a high potential for modern lab-based XAFS to impact LIB research and development.

2. Experimental Details

Single layer xx3450 pouch cell batteries were manufactured at the Cell Analysis, Modeling, and Prototyping (CAMP) Facility at Argonne National Laboratory. The anode used in these cells was Superior Graphite SCL1506T (graphite) and the cathode used was Toda NCM-04ST ($Li(Ni_{0.5}Mn_{0.3}Co_{0.2})O_2$ or NMC532). The composition of the anode electrode was 91.83 wt% graphite, 2 wt% Timcal C45 carbon black, 6 wt% Kureha 9300 (PVDF binder) and 0.17 wt% Oxalic acid. This electrode was coated onto a 10-µm thick copper foil. The electrode loading was 6.38 mg/cm^2 (coating only), electrode porosity was 37.4% and the electrode density was 1.36 g/cm^3 (no foil). The composition of the cathode electrode was 90 wt% NMC532, 5 wt% Timcal C45 carbon black and 5 wt% Solvay 5130 (PVDF binder). This electrode was coated onto a 20-µm thick aluminum foil. The electrode loading was 11.40 mg/cm^2 (coating only), electrode porosity was 33.1% and the electrode density was 2.71 g/cm^3 (no foil). Based upon anode and cathode loadings of the electrodes, the n:p ratio of the full cells is between 1.1 and 1.2, making this couple a balanced pairing.

After the electrodes were made, individual anode and cathode electrodes were punched to be made into the cells. The anode electrode size is ~32.4 mm x 46 mm and has an area of 14.9 cm^2. The cathode electrode size is ~31.3 mm x 45 mm and has an area of 14.1 cm^2. The anode is always slightly oversized to the cathode to prevent shorting between layers in a multilayer pouch cell. Tabs were ultrasonically welded to the electrodes and assembled in a wrap of Celgard 2320 separator (PP/PE/PP tri layer). A pouch was formed with pouch material from Youlchon Chemical (Cellpack-153PL) and the electrode assembly was placed in the pouch. A heat sealer was used to seal three sides of the cells. A quantity of (500 microliters) of 1.2 M $LiPF_6$ in (EC/EMC 3:7 wt%) was added to the pouch to serve as the electrolyte and solvent.

Several shallow vacuum cycles were pulled to fully wet the cells before the final seal under vacuum was done. Formation cycles were performed at a C/10 rate, the cells were then degassed and resealed. The final cell dimensions were 48 mm wide by 75 mm tall (including tab length) and the cell exhibited a nominal capacity of 20 mAh.

During XANES measurements, all charging and discharging was performed with a LAND Battery Testing System, model CT2001A 5V1A, from Wuhan LAND Electronics Co., Ltd. C/5 rates were performed at the Ni, Co, and Mn K-edges via a nominal 4 mA current. For the Ni K-edge, cycles were also performed at rates of C/2.5, C, 2C, and 3C. Nominal charge rates were calculated assuming the ideal capacity of 20 mAh. In all XANES experiments, the cycle began with a rest period of approximately 10 minutes, a discharge at C/5 to 3.0 V, a 20 second pause, a charge at the appropriate rate to 4.1 V, a 20 second pause, discharge at the appropriate rate to 3.0 V, followed by another rest period of approximately 10 minutes. An applied voltage was not maintained during any rest periods. All measurements were performed on the same cell.

XANES measurements were performed at the University of Washington using the Clean Energy Institute X-ray Absorption Near Edge Structure (CEI-XANES) laboratory-based spectrometer. This general theory of operation of this instrument has been described in Seidler et al.,[28] and detailed descriptions of this particular implementation have also been presented.[27, 36] Briefly, measurements were performed using a (Siemens XFFAg4k) x-ray tube source operated with an accelerating potential of 20 kV and a tube current of 5-10 mA for I_0 and of 50 mA for I_T of the pouch cell. The x-ray analyzers are various spherically-bent crystal analyzers with 1-m radius of curvature and 10-cm diameter (XRSTech). A small SDD (active area 25 mm^2, Amptek) was used to detect the x-rays in I_0 scans or after transmission through the pouch. Following our standard practice,[26, 28] I_0 scans are performed before or after the actual

transmission-mode measurement; tube stability is sufficient to allow for this deviation from common methodology at synchrotron light sources. In addition, a comparison of the current spectrometer's energy and temporal resolution to what is attainable at a synchrotron beamline merits some mention. A synchrotron light source offers a considerably larger monochromatic flux than an x-ray tube source, and, as a result, synchrotron beamlines are capable of much finer temporal resolution. Often, this resolution is limited by overhead constraints, including the time required for motor movements, however these can be substantially mitigated in quick-XAS[37, 38] or dispersive configurations.[39, 40] Even with significantly less modification, temporal resolutions enabling 30 C battery studies are readily achievable.[41] Furthermore, laboratory-based spectrometers routinely offer energy resolutions that are only slightly diminished compared to synchrotron beamlines.[26, 36] Such performance is more than capable of enabling studies of chemical speciation, as is the case here.

All spectra were energy corrected by aligning the spectrum of an appropriate metal foil (Ni, Mn, or Co from EXAFS Materials, LLC.) to standards from `Hephaestus`.[42] All spectra were deadtime corrected. As the same location of the cell was probed for a set of measurements, the same pre- and post-edge lineshapes were applied to all spectra of the cell for a given element. For each K-edge, these lineshapes were acquired by fitting a spectrum collected on the battery under steady-state conditions and spanning several hundred eV. Spectra were then normalized according to the methods employed by `Athena` and `SIXPack`.[42, 43] Each XANES spectrum is then synchronized with the electrochemical characteristics (the voltage, capacity, and state of charge) measured at the start of its acquisition period. The Co K-edge was probed over several hundred eV. The Co and Mn K-edges were rebinned to provide satisfactory statistics using a floating summation of four or three subsequent scans, respectively. In order to extract the edge

position for each spectrum, the data between approximately one quarter and three quarters of the white line intensity were first fit to a linear relation. The edge position was then chosen as the energy at which this function reached one half of the white line intensity. This is in general agreement with methods reported elsewhere.[44] In order to convert the XAFS spectra to photoelectron energy, each spectrum was shifted by its corresponding edge position. The position of the most distant scattering peak was then determined by assessing the mean of the photoelectron kinetic energy between 55 and 75 eV as weighted by the normalized absorption at each point.

3. Results and Discussion

The capacity and voltage values depicted as a function of time in Fig. 8-1 demonstrate healthy cycling performance for the selected battery. Several anticipated trends were observed, including a decreasing specific capacity at high charge rates coinciding with reduced Coulombic efficiency. In addition, the voltage profile exhibits sharp curves at the highest and lowest potentials, as is consistent with diffusion and polarization limitations. Furthermore, the plateau at intermediate potentials embodies significant structure as the thermodynamic availability of lithiation sites varies. Nonetheless, the charging potential was constrained to not exceed 4.1 V to avoid irreversible NiO formation due to oxygen evolution. As the present study encompassed several subsequent charging rates and edges, the present charging scheme was selected to avoid the degradation and irreversible phase transitions which have been previously reported.[45-47] The start of each XAS scan is also specified. The number of scans range between 38 during the C/5 charge and 10 in the discharge at 3C. In all cases, the number of scans acquired during a cycle was sufficient to provide insight into the electronic structure of the battery without substantial evolution of the sample between successive scans.

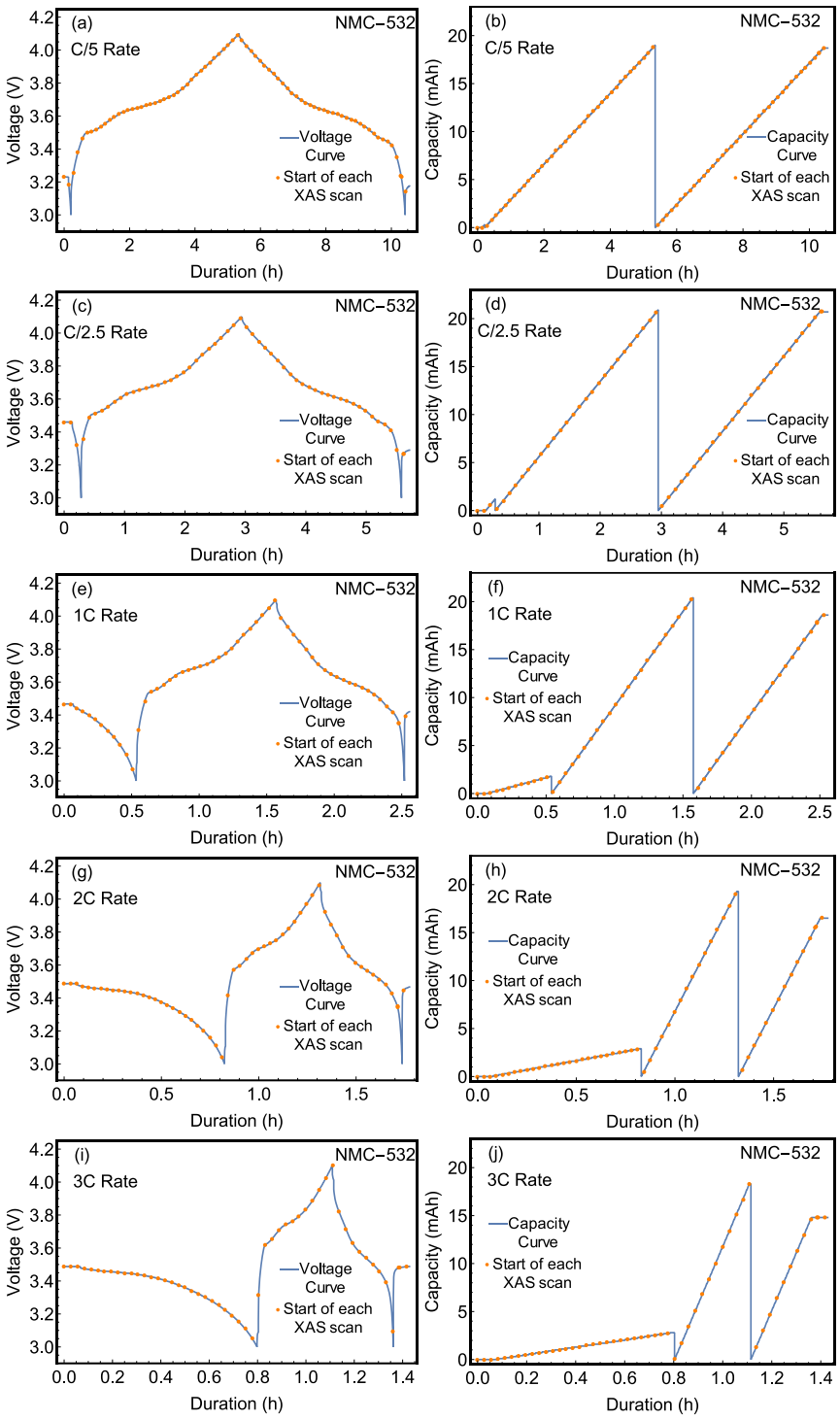

Fig. 8-1: Measured voltage and capacity for the battery cell as a function of time from the start of the experiment. A series of dots designate the start of each XAS scan. Curves are shown for all cycles for which the cell was studied via XANES measurements at the Ni K-edge.

Beginning with Ni, we show the XANES spectra at the Ni K-edge in Fig. 8-2 as a function of charge state of the battery. For conciseness, we show only the C/5, C, and 3C charge rates. At each current, the Ni K-edge is observed to shift to higher photon energies as the battery is charged, and to lower photon energies as the battery is discharged. This behavior is consistent with the intercalation of Li^+ ions, as Ni is known to be the primary agent in charge compensation for similar materials.[48] By tracking the redox behavior of the Ni atoms, the state-of-charge of the battery may be directly assessed and, if desired, be constrained to a range which avoids the formation of undesirable Ni species. In the present instance, comparison to previously reported empirical standards[7, 49, 50] suggest that the present Ni oxidation state is between +2 and +3 in the discharged state and between +3 and +4 at full charge. Moreover, a strictly lateral displacement devoid of any isosbestic points suggests that the entirety of the Ni atoms evolve in concert rather than forming a linear combination, indicating a solid solution behavior rather than a mixed-phase behavior. This is significant for several reasons. Ni-rich NMC cathodes are liable to oxidation state heterogeneity across its constituent clusters of active material.[7] The lack of clear shoulders on the rising edge constrains the non-uniformity of the Ni oxidation state, while the lack of isosbestic points suggests that further redox activity does not strongly prefer Ni atoms of a given oxidation state. This provides further evidence for the healthy functioning of our cell as a dominant decay mechanism in Ni-rich NMC cathodes is deactivation by segregation of metal cations, irreversible structural changes, and isolation from the conductive notework.[51, 52] The linearity of the redox-dependent edge shift was further analyzed as in Fig. 8-3. A smooth and monotonic relationship between the edge position and stored charge was observed at each charge/discharge rate indicating the Ni is consistently redox-active throughout the charge cycle. This relationship is definitively linear, possessing a R^2 of at least 0.992 in all cases. Moreover,

the roughly parallel nature of, e.g., the 3C and 1C charge rates coupled with the lack of points at diminished charge storage suggests that the reduced Coulombic efficiency is the result of incomplete conversion of Ni atoms back to their initial oxidation state.

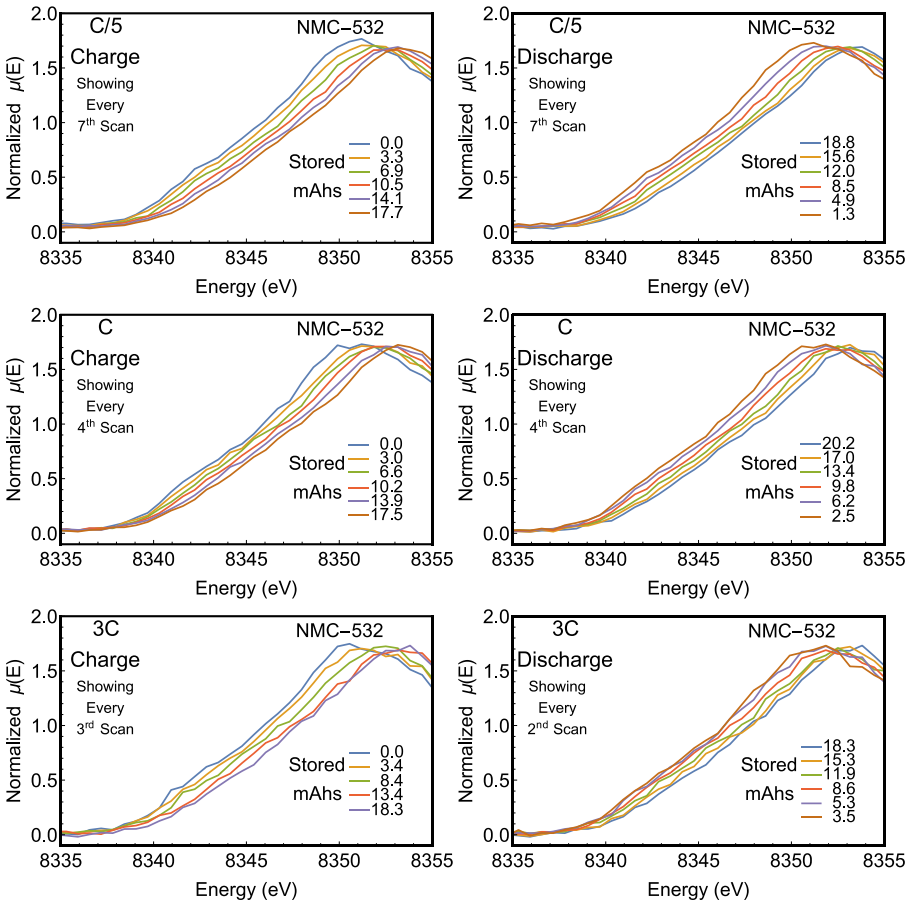

Fig. 8-2: Ni K-edge XANES of the LIB at different degrees of lithiation. The state of charge at the start of each scan is provided in each figure. Only scans at specified intervals were provided for clarity. Spectra corresponding to a C/5 rate were truncated from scans extending over several hundred eV.

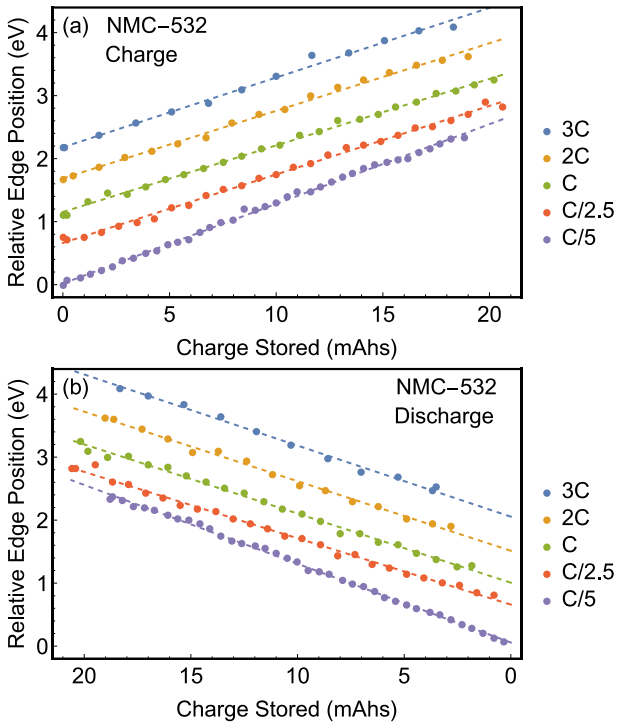

Fig. 8-3: The Ni K-edge of each spectrum given as a function of state of charge at each cycle rate. Data taken faster than C/5 are offset successively by 0.5 eV.

Finally, the C/5 and C/2.5 rates were sufficiently slow to allow the Ni K-edge to be scanned over a more extended energy range. In these cases, a peak was observed due to the outgoing photoelectron scattering off nearby oxygen atoms. By shifting each spectrum by its edge position, the fine structure modulating μ can be plotted as a function of the energy above the K-edge, i.e., the kinetic energy of the photoelectron (ΔE) for comparison, see Fig. 8-4. While the actual extended fine structure is difficult to extract over this limited energy range, the first peak is easily resolved. This peak shifts to higher energies as the state of charge increases, indicating a decrease in the Ni-O bond distance as is consistent with reports on similar systems.[53] The peak monotonically shifts to higher energies at the C/5 and C/2.5 rates, however it begins to plateau at higher states of charge for the faster charge rate. In addition, the photoelectron energy of the scattering peak reaches higher values at the end of discharge than the start of the charge cycle.

This is likely to be a result of the asymmetric condition caused by the applied voltage during use. Similar analyses relating the position of a scattering peak to a bond length have been pursued by other authors, especially in the field of actinide chemistry.[54, 55]

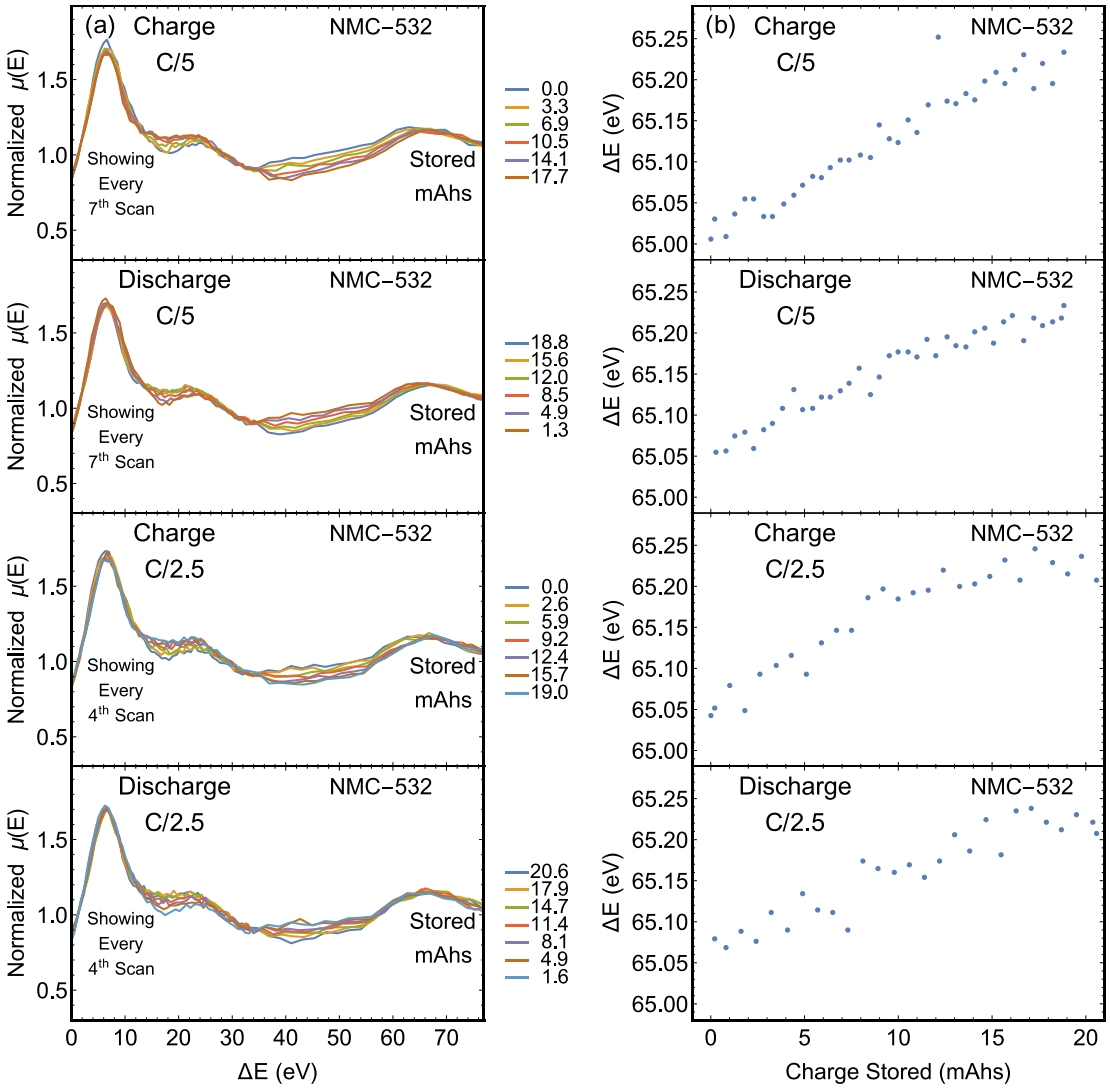

Fig. 8-4: Ni K-edge XAFS of the LIB at different degrees of lithiation for the C/5 and C/2.5 cycle rates. The state of charge at the start of each scan is provided in each figure. The horizontal axis has been converted from energy to outgoing photoelectron kinetic energy, i.e., the energy above the edge position. The peak related to scattering from the neighboring oxygen atoms is centered approximately 67 eV above the edge.

In addition to the electronic structure of Ni, the Mn and Co atoms were probed via *operando* XANES measurements at a C/5 cycle rate. The electrochemical measurements for both experiments are presented in Fig. 8-5. Spectra for Co were collected over several hundred eV and the most significant evolution was observed in the immediate vicinity of the K-edge, which is reported in Fig. 8-6. Here, two isosbestic points are observed on the rising edge of the Mn XANES spectra and one on the rising edge of the Co XANES spectra. For the Mn K-edge, the order of each spectrum between the isosbestic points is reversed outside of the isosbestic points. This behavior is consistent with the involvement of some Mn atoms in a disproportionation reaction, as has been proposed in other Li-ion systems.[56-58] However, the total lateral deviation is fairly minimal and the spectra are dominated by the +4 oxidation in all cases. Therefore, the rising-edge behavior may be due to subtler effects, including smaller changes in covalency. In contrast, only modest differences are observed in the rising edge of the Co XANES spectra. A departure from this trend is observed past the isosbestic point, where the white line feature shows significant sensitivity to the charge state and, as with the Mn spectra, the white line feature is seen to shift to higher energies upon charge and to lower energies upon discharge. Yet in the case of lithiated cobalt oxides, the effect of oxidation on the edge position is known to be fairly muted. Here, the observed behavior is similar to previous observations of the Co K-edge in Li_xCoO_2, Li_xNiO_2 with partial substitution of Ni by Co, and NMC-333 systems which often support conflicting hypotheses.[59-63] Some authors interpret such spectra to mean the Co oxidation state does not vary upon charge, while others assert the changes are due to oxidation of the Co or formation of oxygen holes on the oxygen ions neighboring the cobalt ions depending on the cell's state of charge. Finally, the above trends in the Mn, Co, and Ni K-edges are in

agreement with previous measurements conducted on NMC-333 by Bak et al.[60] and Petersburg et al.[63]

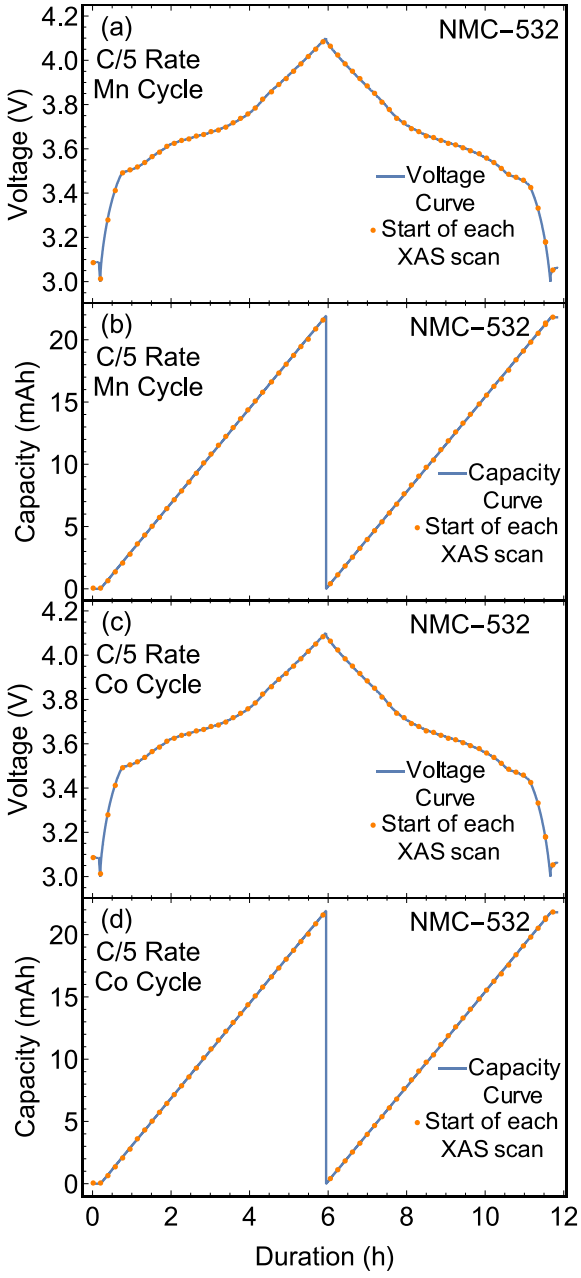

Fig. 8-5: Measured voltage and capacity for the battery cell as a function of elapsed time. A series of dots designate the start of each XAS scan. Curves are shown for one full cycle during which XANES measurements were carried out at the Mn or Co K-edge.

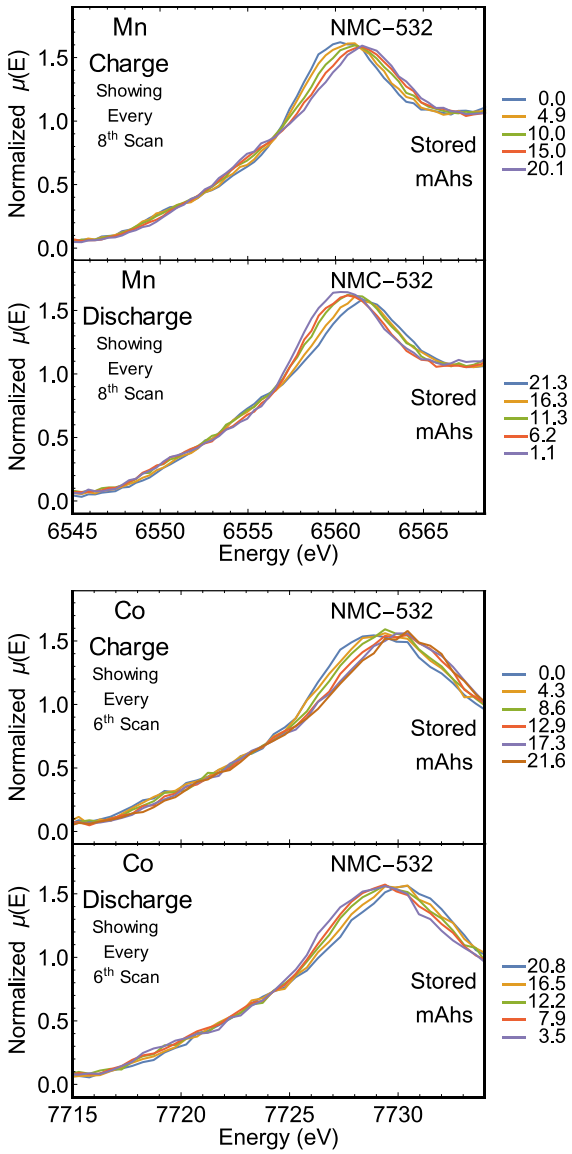

Fig. 8-6: Mn and Co K-edge XANES of the LIB at different degrees of lithiation. The state of charge at the start of each scan is provided in each figure. Only scans at specified intervals were provided for clarity.

4. Conclusion

Variation in the oxidation state of Ni was observed at elevated charge rates of an NMC battery. This was observed via *operando* XANES measurements in a laboratory setting and

supports the utility of modern laboratory-based instrumentation in energy storage research, even to the point of fast-charging studies. Indeed, present instrumentation can perform these analyses *in situ* without modification of the pouch cell and with time resolution relevant to fast charging applications. These instruments can be used to assess the state-of-charge and state-of-health in prototype systems that require faster feedback than conventionally available at synchrotron light sources. Similar measurements could be particularly informative for next generation energy storage materials, such as batteries with multivalent charge carriers[64] or anion redox mechanisms,[65] where the charge transfer site can be ambiguous. As a future direction, this laboratory-based paradigm can serve as a useful model for studies of degradation mechanisms which require frequent and long-term access.

5. Acknowledgments

EPJ and TTF were supported in part by the Joint Center for Energy Storage Research (JCESR), an Energy Innovation Hub funded by the U.S. Department of Energy, Office of Science, and Basic Energy Sciences. EPJ was also supported by a subcontract from the National Institute of Standards and Technology. Opinions, recommendations, findings, and conclusions presented in this manuscript and associated materials does not necessarily reflect the views or policies of NIST or the United States Government. Part of this work was conducted at the Molecular Analysis Facility, a National Nanotechnology Coordinated Infrastructure site at the University of Washington which is supported in part by the National Science Foundation (grant NNCI-1542101), the University of Washington, the Molecular Engineering & Sciences Institute, and the Clean Energy Institute. This material is based in part upon work supported by the State of Washington through the University of Washington Clean Energy Institute. For the cells produced by the CAMP Facility in this study, we gratefully acknowledge support from the U. S. Department of Energy (DOE), Office of Energy Efficiency and Renewable Energy, Vehicle

Technologies Office. Argonne National Laboratory is operated for DOE Office of Science by UChicago Argonne, LLC, under contract number DE-AC02-06CH11357.

6. References

1. D. Deng, *Energy Science & Engineering*, **3**, 385 (2015).
2. J. Lopez, M. Gonzalez, J. C. Viera and C. Blanco, in *INTELEC 2004. 26th Annual International Telecommunications Energy Conference*, p. 19 (2004).
3. A. Eftekhari, *ACS Sustainable Chemistry & Engineering*, **7**, 5602 (2019).
4. C. H. Hesse, M. Schimpe, D. Kucevic and A. Jossen, *Energies*, **10**, 2107 (2017).
5. W. Zhao, J. Zheng, L. Zou, H. Jia, B. Liu, H. Wang, M. H. Engelhard, C. Wang, W. Xu, Y. Yang and J.-G. Zhang, *Advanced Energy Materials*, **8**, 1800297 (2018).
6. X.-G. Yang, G. Zhang, S. Ge and C.-Y. Wang, *Proceedings of the National Academy of Sciences*, **115**, 7266 (2018).
7. Y. Mao, X. Wang, S. Xia, K. Zhang, C. Wei, S. Bak, Z. Shadike, X. Liu, Y. Yang, R. Xu, P. Pianetta, S. Ermon, E. Stavitski, K. Zhao, Z. Xu, F. Lin, X.-Q. Yang, E. Hu and Y. Liu, *Advanced Functional Materials*, **29**, 1900247 (2019).
8. R. Jung, M. Metzger, F. Maglia, C. Stinner and H. A. Gasteiger, *Journal of The Electrochemical Society*, **164**, A1361 (2017).
9. S.-M. Bak, E. Hu, Y. Zhou, X. Yu, S. D. Senanayake, S.-J. Cho, K.-B. Kim, K. Y. Chung, X.-Q. Yang and K.-W. Nam, *ACS Applied Materials & Interfaces*, **6**, 22594 (2014).
10. J. Zheng, T. Liu, Z. Hu, Y. Wei, X. Song, Y. Ren, W. Wang, M. Rao, Y. Lin, Z. Chen, J. Lu, C. Wang, K. Amine and F. Pan, *Journal of the American Chemical Society*, **138**, 13326 (2016).
11. C. Tian, Y. Xu, D. Nordlund, F. Lin, J. Liu, Z. Sun, Y. Liu and M. Doeff, *Joule*, **2**, 464 (2018).
12. S. Aryal, E. V. Timofeeva and C. U. Segre, *Journal of The Electrochemical Society*, **165**, A71 (2018).
13. A. L. Lipson, S. Kim, B. Pan, C. Liao, T. T. Fister and B. J. Ingram, *Journal of Power Sources*, **369**, 133 (2017).
14. P. Senguttuvan, S.-D. Han, S. Kim, A. L. Lipson, S. Tepavcevic, T. T. Fister, I. D. Bloom, A. K. Burrell and C. S. Johnson, *Advanced Energy Materials*, **6**, 1600826 (2016).
15. A. L. Lipson, D. L. Proffit, B. Pan, T. T. Fister, C. Liao, A. K. Burrell, J. T. Vaughey and B. J. Ingram, *Journal of The Electrochemical Society*, **162**, A1574 (2015).
16. T. Kim, B. Song, A. J. G. Lunt, G. Cibin, A. J. Dent, L. Lu and A. M. Korsunsky, *Chemistry of Materials*, **28**, 4191 (2016).
17. H. Kageyama, H. Shigemura, M. Tabuchi, K. Ado and H. Kobayashi, *Journal of Synchrotron Radiation*, **8**, 863 (2001).
18. V. L. McLaren, A. R. West, M. Tabuchi, A. Nakashima, H. Takahara, H. Kobayashi, H. Sakaebe, H. Kageyama, A. Hirano and Y. Takeda, *Journal of The Electrochemical Society*, **151**, A672 (2004).
19. M. Tabuchi, A. Nakashima, H. Shigemura, K. Ado, H. Kobayashi, H. Sakaebe, H. Kageyama, T. Nakamura, M. Kohzaki, A. Hirano and R. Kanno, *Journal of The Electrochemical Society*, **149**, A509 (2002).
20. H. Shigemura, H. Sakaebe, H. Kageyama, H. Kobayashi, A. R. West, R. Kanno, S. Morimoto, S. Nasu and M. Tabuchi, *Journal of The Electrochemical Society*, **148**, A730 (2001).

21. E. Talaie, P. Bonnick, X. Q. Sun, Q. Pang, X. Liang and L. F. Nazar, *Chemistry of Materials*, **29**, 90 (2017).
22. L. Anklamm, C. Schlesiger, W. Malzer, D. Grötzsch, M. Neitzel and B. Kanngießer, *Review of Scientific Instruments*, **85**, 053110 (2014).
23. Y. Kayser, W. Błachucki, J. C. Dousse, J. Hoszowska, M. Neff and V. Romano, *Review of Scientific Instruments*, **85**, 043101 (2014).
24. Z. Németh, J. Szlachetko, É. G. Bajnóczi and G. Vankó, *Review of Scientific Instruments*, **87**, 103105 (2016).
25. A. P. Honkanen, S. Ollikkala, T. Ahopelto, A. J. Kallio, M. Blomber and S. Huotari, *Review of Scientific Instruments*, **90**, 033107 (2019).
26. E. P. Jahrman, W. M. Holden, A. S. Ditter, D. R. Mortensen, G. T. Seidler, T. T. Fister, S. A. Kozimor, L. F. J. Piper, J. Rana, N. C. Hyatt and M. C. Stennett, *Review of Scientific Instruments*, **90**, 024106 (2019).
27. G. T. Seidler, D. R. Mortensen, A. S. Ditter, N. A. Ball and A. J. Remesnik, *Journal of Physics: Conference Series*, **712**, 012015 (2016).
28. G. T. Seidler, D. R. Mortensen, A. J. Remesnik, J. I. Pacold, N. A. Ball, N. Barry, M. Styczinski and O. R. Hoidn, *Review of Scientific Instruments*, **85**, 113906 (2014).
29. D. R. Mortensen, G. T. Seidler, A. S. Ditter and P. Glatzel, *Journal of Physics: Conference Series*, **712**, 012036 (2016).
30. R. Bès, T. Ahopelto, A. P. Honkanen, S. Huotari, G. Leinders, J. Pakarinen and K. Kvashnina, *Journal of Nuclear Materials*, **507**, 50 (2018).
31. J. G. Moya-Cancino, A.-P. Honkanen, A. M. J. van der Eerden, H. Schaink, L. Folkertsma, M. Ghiasi, A. Longo, F. M. F. de Groot, F. Meirer, S. Huotari and B. M. Weckhuysen, *ChemCatChem*, **11**, 1039 (2019).
32. M. E. Mundy, D. Ung, N. L. Lai, E. P. Jahrman, G. T. Seidler and B. M. Cossairt, *Chemistry of Materials*, **30**, 5373 (2018).
33. S. K. Padamati, D. Angelone, A. Draksharapu, G. Primi, D. J. Martin, M. Tromp, M. Swart and W. R. Browne, *Journal of the American Chemical Society*, **139**, 8718 (2017).
34. E. P. Jahrman, G. T. Seidler and J. R. Sieber, *Analytical Chemistry*, **90**, 6587 (2018).
35. O. J. Borkiewicz, K. M. Wiaderek, P. J. Chupas and K. W. Chapman, *The Journal of Physical Chemistry Letters*, **6**, 2081 (2015).
36. A. S. Ditter, L. R. Bradshaw, E. P. Jahrman, X. Xia and G. T. Seidler, *In Preparation* (2019).
37. O. Muller, M. Nachtegaal, J. Just, D. Lutzenkirchen-Hecht and R. Frahm, *Journal of Synchrotron Radiation*, **23**, 260 (2016).
38. A. K. Poswal, A. Agrawal, D. Bhattachryya, S. N. Jha and N. K. Sahoo, *AIP Conference Proceedings*, **1665**, 060027 (2015).
39. R. Alonso-Mori, J. Kern, D. Sokaras, T.-C. Weng, D. Nordlund, R. Tran, P. Montanez, J. Delor, V. K. Yachandra, J. Yano and U. Bergmann, *The Review of scientific instruments*, **83**, 073114 (2012).
40. J. Szlachetko, M. Nachtegaal, D. Grolimund, G. Knopp, S. Peredkov, J. Czapla–Masztafiak and J. C. Milne, *Applied Sciences*, **7** (2017).
41. Y.-N. Zhou, J.-L. Yue, E. Hu, H. Li, L. Gu, K.-W. Nam, S.-M. Bak, X. Yu, J. Liu, J. Bai, E. Dooryhee, Z.-W. Fu and X.-Q. Yang, *Advanced Energy Materials*, **6**, 1600597 (2016).
42. B. Ravel and M. Newville, *Journal of Synchrotron Radiation*, **12**, 537 (2005).

43. S. M. Webb, *Physica Scripta*, **T115**, 1011 (2005).
44. G. Henderson, F. De Groot and B. Moulton, *Reviews in Mineralogy and Geochemistry*, **78**, 75 (2014).
45. S.-K. Jung, H. Gwon, J. Hong, K.-Y. Park, D.-H. Seo, H. Kim, J. Hyun, W. Yang and K. Kang, *Advanced Energy Materials*, **4**, 1300787 (2014).
46. J. Li, L. E. Downie, L. Ma, W. Qiu and J. R. Dahn, *Journal of The Electrochemical Society*, **162**, A1401 (2015).
47. F. Lin, I. M. Markus, D. Nordlund, T.-C. Weng, M. D. Asta, H. L. Xin and M. M. Doeff, *Nature Communications*, **5**, 3529 (2014).
48. W. E. Gent, Y. Li, S. Ahn, J. Lim, Y. Liu, A. M. Wise, C. B. Gopal, D. N. Mueller, R. Davis, J. N. Weker, J.-H. Park, S.-K. Doo and W. C. Chueh, *Advanced Materials*, **28**, 6631 (2016).
49. A. N. Mansour, J. McBreen and C. A. Melendres, *Journal of The Electrochemical Society*, **146**, 2799 (1999).
50. D. Wang, Q. Li, C. Han, Z. Xing and X. Yang, *ACS Central Science*, **4**, 112 (2018).
51. H.-H. Sun and A. Manthiram, *Chemistry of Materials*, **29**, 8486 (2017).
52. P. Yan, J. Zheng, M. Gu, J. Xiao, J.-G. Zhang and C.-M. Wang, *Nature Communications*, **8**, 14101 (2017).
53. Y. W. Tsai, B. J. Hwang, G. Ceder, H. S. Sheu, D. G. Liu and J. F. Lee, *Chemistry of Materials*, **17**, 3191 (2005).
54. T. Vitova, I. Pidchenko, D. Fellhauer, T. Pruessmann, S. Bahl, K. Dardenne, T. Yokosawa, B. Schimmelpfennig, M. Altmaier, M. Denecke, J. Rothe and H. Geckeis, *Chemical Communications*, **54**, 12824 (2018).
55. L. Zhang, J. Zhou, J. Zhang, J. Su, S. Zhang, N. Chen, Y. Jia, J. Li, Y. Wang and J.-Q. Wang, *Journal of Synchrotron Radiation*, **23**, 758 (2016).
56. A. Banerjee, Y. Shilina, B. Ziv, J. M. Ziegelbauer, S. Luski, D. Aurbach and I. C. Halalay, *Journal of the American Chemical Society*, **139**, 1738 (2017).
57. I. Buchberger, S. Seidlmayer, A. Pokharel, M. Piana, J. Hattendorff, P. Kudejova, R. Gilles and H. A. Gasteiger, *Journal of The Electrochemical Society*, **162**, A2737 (2015).
58. S. K. Martha, J. Nanda, Y. Kim, R. R. Unocic, S. Pannala and N. J. Dudney, *Journal of Materials Chemistry A*, **1**, 5587 (2013).
59. F. M. Alamgir, E. Strauss, M. denBoer, S. Greenbaum, J. F. Whitacre, C. C. Kao and S. Neih, *Journal of The Electrochemical Society*, **152**, A845 (2005).
60. S. M. Bak, Z. Shadike, R. Lin, X. Yu and X. Q. Yang, *NPG Asia Materials*, **10**, 563 (2018).
61. J. McBreen and M. Balasubramanian, *The Journal of The Minerals, Metals and Materials Society*, **54**, 25 (2002).
62. I. Nakai, K. Takahashi, Y. Shiraishi and T. Nakagome, *Journal De Physique IV Colloque*, **7**, 1243 (1997).
63. C. F. Petersburg, Z. Li, N. A. Chernova, M. S. Whittingham and F. M. Alamgir, *Journal of Materials Chemistry*, **22**, 19993 (2012).
64. L. F. Wan, J. Wright, B. R. Perdue, T. T. Fister, S. Kim, C. A. Apblett and D. Prendergast, *Physical Chemistry Chemical Physics*, **18**, 17326 (2016).
65. G. Assat, A. Iadecola, C. Delacourt, R. Dedryvère and J.-M. Tarascon, *Chemistry of Materials*, **29**, 9714 (2017).

Chapter 9. Valence-to-core X-ray Emission Spectroscopy of Vanadium Oxide and Lithiated Vanadyl Phosphate Materials

In preparation for publication: E. P. Jahrman, W. M. Holden, N. Govind, J. J. Kas, J. Rana, L. F. J. Piper, C. Siu, M. S. Whittingham, T. T. Fister, and G. T. Seidler, Chem. of Materials (2019). This chapter represents a significant portion of this dissertation and the effort was led by the candidate.

We report valence-to-core (VTC) X-ray emission spectroscopy (XES) measurements of the electrochemical sequence ε-VOPO4, ε-LiVOPO4, ε-Li2VOPO4 and the reference oxides V_2O_3, VO_2, and V_2O_5. Our results demonstrate laboratory-based X-ray spectroscopy instrumentation is a viable route for attaining well-resolved VTC-XES features, even for samples of limited quantity or suffering from sensitivity to the atmosphere. Moreover, an extremely efficient use of flux in the present configuration permitted these results to be captured within several hours. Thus, this study represents a framework for interrogating the molecular bonding structure of a wide range of systems with a technique which has garnered substantial interest in the subfield of catalysis employing metalloenzymes. The experimental results are in good agreement with results produced by real-space Green's function and time-dependent density functional theory (TDDFT) methods. In particular, the latter reproduces spectral features with high fidelity and at fluorescence energies which are consistent between each set of calculations. Furthermore, the TDDFT framework lends itself naturally to investigating the character of the molecular orbitals involved in each transition, as is explored in this work.

1. Introduction

Motivated by an overlap of four key motivations, this work reports valence-to-core (VTC) X-ray emission spectroscopy (XES) measurements from a suite of lithiated ε-phase vanadyl phosphate compounds and a suite of reference V oxides. First, from a materials perspective, lithitaion of vanadyl phosphates is an area of ongoing research due to its promise as a next-generation cathode material in lithium ion batteries (LIBs).[1, 2] Likewise, vanadium oxides are frequently recommended for societally-critical applications including memory and energy storage devices.[3-8] Second, from a spectroscopy-oriented perspective, VTC-XES is a powerful technique that has garnered substantial interest.[9-11] However, with a few notable exceptions,[12, 13] VTC-XES has primarily been applied to the study of metalloorganic complexes and catalysts.[14-16] In these instances, the feature most commonly analyzed is the cross-over peak due to its sensitivity to the identity of atomic ligands, particularly for differentiating between several light atoms.[10] However, VTC-XES also permits the element-specific interrogation of the behavior of the valence electrons directly involved in molecular bonding. Therefore, it is desirable to further establish this technique as a general tool for studying the behavior of valence electrons in a wide range of materials. Third, from a technological perspective on XES itself, the instrumentation necessary to perform VTC-XES studies is becoming more accessible. Rapid improvements have been made to laboratory-based X-ray spectroscopy instrumentation in recent years.[17-23] At present, these instruments constitute a viable route for access to VTC-XES while maintaining manageable measurement durations. Fourth, many of the vanadyl phosphates possess complex VTC-XES spectral features. Accordingly, the measurements reported here are excellent test cases to verify theoretical models which simulate the XES process. These include time-dependent density functional theory (TDDFT) and Green's function-based methods.

The materials studied here are of considerable contemporary scientific interest. They span all accessible oxidation states of vanadium oxides and vanadyl phosphates. In order, V_2O_3 has been proposed as a candidate material for energy storage applications.[6] VO_2 has been extensively studied in both pristine and doped conditions.[24-26] This material undergoes a metal-to-insulator phase transition at 341 K, not far above room temperature.[27] As a result, it is often a candidate switching material for memory storage devices.[5, 7, 8] V_2O_5 is frequently used in energy applications spanning a range of power and energy densities. On one end of this range of applications, V_2O_5 is an inexpensive and effective electrode material in supercapacitors.[4, 28-30] On the other end, V_2O_5 and its derivatives are candidate cathode materials both for lithium intercalation[31-33] and for magnesium ion batteries.[3, 34, 35] For the other classes of materials, vanadyl phosphates have been proposed as a candidate cathode material for lithium ion batteries, as noted above.[1, 2] The reason for its appeal is that it is able to accommodate multiple lithium ions for each vanadium host. Moreover, it is one of the few materials that can do this via an intercalation rather than a conversion process with redox potentials for both electrochemical conversions at relatively high potentials. As a result, its theoretical capacity is 305 mAh g^{-1} and significantly exceeds that of conventional, commercially available lithium ion batteries. Moreover, recent progress has been made in synthesizing the vanadyl phosphate cathode materials as well as achieving reversible cycling and capacities that are near the theoretical limit.[36-38] In summary, these are all interesting materials with electronic structures of great interest, however the atomic structures of these compounds are nontrivial and the analysis of their corresponding VTC-XES spectra is best aided with theoretical predictions.

VTC-XES is a subject of considerable recent research as it provides a direct, element-specific interrogation of the behavior of the electrons involved in molecular bonding. For example, many

researchers tried to elucidate the atomic identity of a light central atom in FeMoCo, the active site for binding and reduction in nitrogenase, reported by Einsle *et al.*,[39] but it was not until Lancaster *et al.* used Fe VTC XES that the atom was revealed to be carbon.[40] Similarly, these researchers applied Fe VTC XES to a number of doubly nitrogenous Fe compounds which spanned a range of N-N bond distances.[41] Pollock *et al.* found that the position of a feature corresponding to the $\sigma_{2s2s}{}^* \rightarrow \mathrm{Fe}_{1s}$ transition could be used to track the N-N bond distance and thus the degree of activation in Fe-based catalysts used for nitrogen reduction. Other notable examples in VTC-XES include the work of Pushkar *et al.* who utilized Mn VTC XES to interrogate the electronic structure of the Mn_4Ca cluster in the oxygen evolving complex of photosystem II. With VTC-XES, these researchers were able to detect oxygen ligation to the Mn_4Ca cluster. Coincidentally, the sensitivities of the cross-over peak have been well documented by a study spanning a collection of manganese oxides.[42] Beyond metalloenzyme research, the VTC-XES of numerous Cr compounds were analyzed by experimental and theoretical means and were found to exhibit considerable sensitivity to the particular coordination of the Cr atoms in the system.[43] Also, VTC-XES has been used to discriminate amongst members of a set of Mn^{IV} dimers with varying protonation states on bridging oxygen atoms.[44] Nevertheless, much work remains to be done in measuring, cataloguing, and calculating the VTC XES spectra of chemical species. For this application, laboratory-based X-ray spectrometers are particularly well-suited.

Recently, the capabilities, diversity of design, and operational energy ranges of laboratory-based instruments which perform XES have rapidly grown. The present discussion will proceed in order of ascending photon energy. Modern laboratory-based spectrometers can measure the S and P K emission lines (~ 2-2.5 keV) using double crystal monochromators,[45-47] dispersive

Rowland circle geometries,[48-51] or the von Hamos geometry.[52] Similarly, many existing von Hamos instruments operate in the ~3-12 keV range desired for studies of first row transition metals and lanthanides.[18, 53-55] For similar energies, Rowland circle-based configurations using spherically bent crystal analyzers (SBCAs) have been extensively developed by some of the present authors.[23, 56-61] Lastly, Laue-type spectrometers can access higher energies, including the Au Kβ (78 keV).[62] Often, these spectrometers use conventional X-ray tube sources which emit broadband radiation. For XES, this corresponds to incredibly efficient utilization of flux.[23] Consequently, these spectrometers yield count rates comparable to what could be achieved with an insertion device at a 3rd generation synchrotron light source. Moreover, these instruments employ an SBCA which yields excellent energy resolution. Thus, spectra are achieved without loss in instrumental resolution, but only with the limitation that the XES spectrum of a material must be measured nonresonantly, often with some effective broadening because of the lack of resonant narrowing of emission lineshapes.

Again, many recent advances have been made in the field of quantum chemical calculations that enable the present work. In particular, TDDFT has emerged as a favorable alternative to a simple, single-electron DFT framework.[63, 64] Formally, DFT is a ground state method intended for the calculation of ground state properties and not electronic excitations. In contrast, TDDFT permits the calculation of properties in the presence of external potentials, including those by time-varying electric fields. Indeed, electronic transitions arise naturally in this formalism as the roots of the Kohn-Sham response function. Moreover, these roots can receive contributions from many orbital pairs. This is a definite advantage over conventional DFT approaches, particularly for transition metals, which are notorious for possessing many states closely spaced in energy such that the promotion and pairing energy of valence electrons become of comparable size.

Furthermore, in the NWChem implementation[65] the calculated roots span electric dipole, electric quadrupole, and magnetic dipole contributions to the oscillator strength corresponding to the transition. These merits resulted in excellent spectral agreement between Zn VTC-XES calculations and experimental results for a variety of chemistries.[58] Furthermore, TDDFT has been used to accurately model the XANES and VTC-XES of many materials, including transition metal compounds.[66-71]

This study brings together advances in spectroscopy instrumentation and computational tools to interrogate the electronic structure of a suite of vanadium oxide and vanadyl phosphate compounds, thus adding to the body of literature supporting an emergent technique, VTC-XES.

2. Methodology

Compounds

All vanadium oxides were purchased from commercial vendors. The phase and speciation of each was confirmed by X-ray diffraction (XRD) and XANES, respectively. The former permitted the phases of each oxide to be confirmed by matching the measurements to experimental spectra from a commercially available database of the International Center for Diffraction Data (ICDD). The latter was done by comparison to literature spectra.[72-74] The ε-$VOPO_4$ and its lithiated phases were obtained from Binghamton University. The phases of ε-$VOPO_4$ and ε-$LiVOPO_4$ were again confirmed by matching the measurements to experimental XRD spectra from the ICDD database. An Li_2VOPO_4 entry could not be located in this same database. Rather, the structure reported by Bianchini *et al.*[75] was used to simulate an XRD spectrum using the `xrayutilies` package for Python and confirmed to match the spectrum measured for the ε-Li_2VOPO_4 measured here.

The following steps were taken to prepare samples for X-ray analysis. The lithiated vanadyl phosphates, which are known to be air sensitive, were placed in vials and shipped in sealed aluminum mylar bags flushed with inert gas. The vials were eventually opened in an Ar glovebox at the University of Washington. The material was spread into a thin layer and sealed between three layers of polyimide tape with a silicon-based adhesive. These materials were then placed into a vial and sealed with parafilm prior to removal from the glovebox. These vials were opened immediately prior to measurement. The VTC-XES results, coupled with a V $K\beta_{1,3}$ spectrum measured at the start of each VTC-XES scan, were monitored over numerous scans to confirm that no degradation occurred. The material was measured by XRD after XES acquisition had completed to confirm each phase. The pristine ε-$VOPO_4$ was dried in a vacuum oven overnight to remove any hydrated or hydroxide components from the material. This was confirmed by XRD and the ε-$VOPO_4$ was also sealed by polyimide tape.

XES Experiment

A laboratory-based spectrometer at the University of Washington was used for these experiments. The basic design of the instrument is described in Seidler *et al.*[23] and the advances of Jahrman *et al.*[22] were utilized. In addition, this study used a Ge(422) spherically bent crystal analyzer (SBCA) which was aligned according to the method of Mortensen *et al.*[60] The energy resolution and scale was maintained by a slit on the sample side[58, 59] which each sample was aligned behind. In addition to these details, the instrument configuration included a Varex VF80 X-ray tube source with a W anode and operating at a total tube power of 100 W. Also, a commercial SDD (Amptek X-123SDD) was employed and provided enough energy resolution to exclude much of the detected background fluorescence.

For the data collection and analysis, VTC-XES spectra were averaged over several scans spanning an energy range from 5390 to 5500 eV to capture both the V Kβ mainlines and V VTC-XES. The total integration time for each scan was approximately 3 minutes, while the total measurement time for a sample was typically around 2.5 hours. All spectra were deadtime corrected, background subtracted and integral normalized over the full range of the spectrum. To aid comparison to theory, the high energy tail from the V $K\beta_{1,3}$ of each sample was subtracted from its VTC-XES spectrum. In principle, this can be done by conventional peak-fitting methods. However, for XES features, this would require robust predictions of the presence and shape of radiative auger emission features[76] and multielectron excitation satellites.[56] Furthermore, it can be difficult to meaningfully constrain the physical parameters contributing to the shape of each feature. Finally, with many free parameters, it is difficult to obtain a unique fit to the experimental data. As an alternative, approximate parameters can be used to fit a set of Lorentzians to the slope on the low-energy side of the VTC-XES spectrum and also the tail on the high-energy side of the VTC. This shape may be subtracted from the experimental spectrum to produce a flattened spectrum that, while it may possess some inaccuracies in the intensity of features, is devoid of distortions that would manifest as additional VTC-XES features.

XES Theory

VTC-XES results were modeled using `NWChem`. The input geometric files were taken from experimental configurations which reproduced the XRD results. These structures were truncated to a convenient size and the resulting cluster was terminated by hydrogen atoms superimposed with point charges in an effort to reproduce the behavior of the bulk solid.[77-79] This was done according to previously reported methods.[58, 69] With an appropriate atomic input constructed, XES calculations were carried out in the three step method of Wadey and Besley.[80]

First a DFT calculation was performed on the ground state system. This included selection of the exchange correlation functional PBE0.[81] The following basis sets were used for the each element: H used LANL2DZ,[82] Li used 6-31G*,[83, 84] P and O used the effective core potential basis Stuttgart RLC ECP,[85] and V used the effective core potential basis LANL2DZ ECP[86] except on the photoexcited atom which used Sapporo TZP 2012.[87] The pentavalent vanadium complexes were treated as diamagnetic compounds while all others were modeled as high spin paramagnets. Second, the converged molecular orbital vectors were used as input for a full core hole calculation[88-90] to relax the electronic structure in the presence of the core hole subject to a maximum overlap condition.[91, 92] Third, This solution was then used as the input to the TDDFT calculation, which was performed in the Tamm-Dancoff approximation.[93, 94]

The above calculations provided oscillator strengths for a number of electronic transitions. Processing these into a meaningful spectrum required the following steps. The oscillator strengths in the channels corresponding to excitation of a spin-up or spin-down electron in the V_{1s} orbital were normalized to give equal weight to both channels subject to the assumption that ejection of either electron was equally probable and that excitation was the rate-limiting step in the photoexcitation process. Oscillator strengths were rescaled to probabilities according to the formulae given by Mukoyama.[95] Each transition line was convolved with a 2 eV full-width half-maximum (FWHM) Lorentzian and the sum of all Lorentzains was taken as the final spectrum. In order to characterize the contribution of a given atomic orbital-type to a transition, the corresponding oscillator strengths were scaled by the contributions of molecular orbital pairs involved in the corresponding root found by TDDFT. These molecular orbitals were then scaled according to the contributions of the ten most dominant atomic orbitals in each.

The FEFF9[96-98] real-space multiple-scattering code was used to calculate the vanadium Kβ emission as well as the angular momentum projected densities of states (LDOS) of each compound. The code treats XES in terms of matrix elements between the core-level and the Green's function, i.e.,

$$\sigma_{XES}(\omega) \propto \langle c|d^{*}G(\omega + E_c)d|c\rangle\theta(\mu - \omega + E_c), \quad (10\text{-}1)$$

where $|c\rangle$ denotes the single particle core-state, d is the transition operator (usually dominated by dipole transitions), E_c is the core-level energy, and G is the one electron Green's function. The unit step function $\theta(\mu - \omega + E_c)$ selects occupied levels below the chemical potential μ.

For these calculations, potentials and densities were calculated with the self-consistent field (SCF) approach with a SCF radius of 5.0 Å, leading to a cluster ranging from 40 to 60 atoms. A full multiple scattering radius of approximately 8.5 Å (a cluster of 200-300 atoms) was used in the calculation of the LDOS and the XES, and was sufficiently large to produce a converged spectrum. Core-hole effects were neglected, other than the core-hole lifetime broadening, which was introduced as a shift into the complex plane of the energy at which the Green's function is evaluated, and is equivalent to a Lorentzian broadening of 0.99 eV FWHM.

3. Results and Discussion

In the VTC-XES shown in Fig. 9-1, a Kβ'' feature, which corresponds to the "cross-over" transition from a molecular orbital of predominantly ligand character, is clearly visible in most spectra. The Kβ'' is of variable intensity and decreases in intensity as expected from the known changes in V-O bond distances.[99-101] The $K\beta_{2,5}$ position is also observed to be highly sensitively to oxidation state, with the more oxidized found at higher emission energies. Furthermore, a slight curvature is on the high energy side of the spectra in Fig. 9-1, this curvature is because the spectra are truncated along a multi-electron excitation feature which was not of interest to this

study. Finally, an interesting triple-peak structure is observed in the main VTC feature of all the vanadyl phosphates.

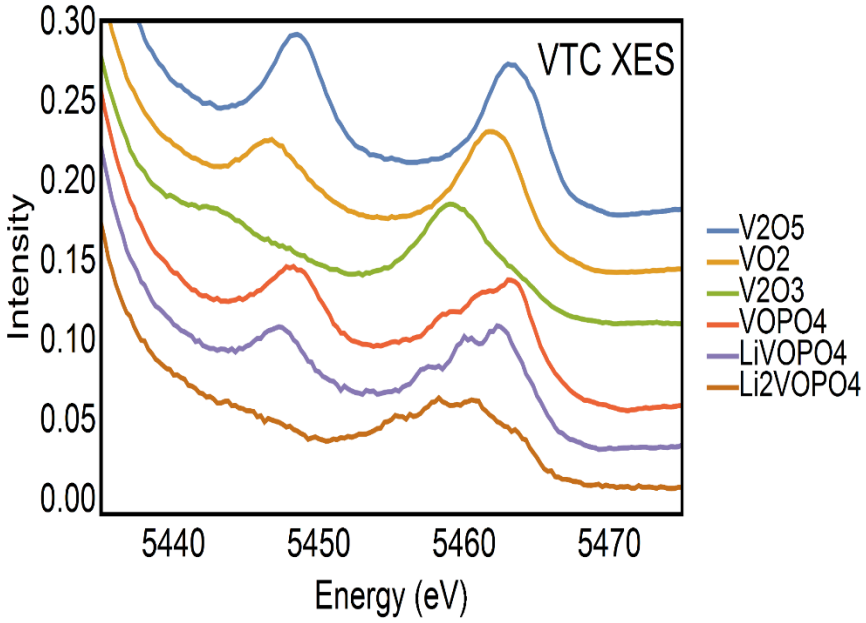

Fig. 9-1 Experimental V VTC-XES spectra of the set of V oxides and vanadyl phosphates. Spectra are shown after deadtime correction, constant background subtraction and integral normalization over the entire scan range.

In Fig. 9-2, a background and residual are shown for the fit of a representative VTC-XES spectrum. The fit is observed to agree well with the high-energy tail from the $K\beta_{1,3}$. The background stays below the VTC-XES features, and, likewise, does not exceed the majority of the multi-electron excitation feature around 5480 eV. Toward the highest energies, it can be seen that the fitted background is converging to the measured VTC-XES spectrum, as expected.

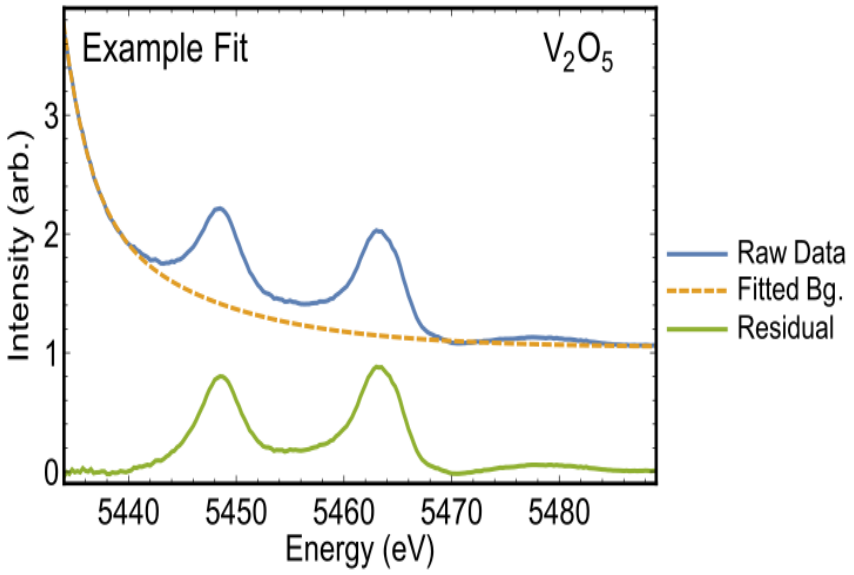

Fig. 9-2: Representative experimental V VTC-XES results are shown for V_2O_5 (blue) along with the background fit to the low- and high-energy ranges of the VTC (orange, dashed). These two spectra are shown offset from the residual (green). The residual represents the VTC-XES without the tail from the V $K\beta_{1,3}$.

In Fig. 9-3 and Fig. 9-4, theoretical Green's function and TDDFT calculations are shown relative to the measured experimental spectra. In all cases, the TDDFT calculations use a consistent energy shift of -29 eV to align with the experimental spectra. For the calculations performed in `FEFF9` all of the oxides required a uniform energy shift to align to experiment, while each of the vanadyl phosphates required a unique energy shift to achieve satisfactory alignment. Both theories qualitatively capture the spectral features in the VTC-XES, including the triple-peak structure of the $K\beta_{2,5}$ feature. For several compounds, including VO_2 and V_2O_3, TDDFT provides superior predictions for the energy spacing of the Kβ'' and $K\beta_{2,5}$ features, and also a more accurate prediction of the high-energy behavior of the $K\beta_{2,5}$ features around 5463 eV.

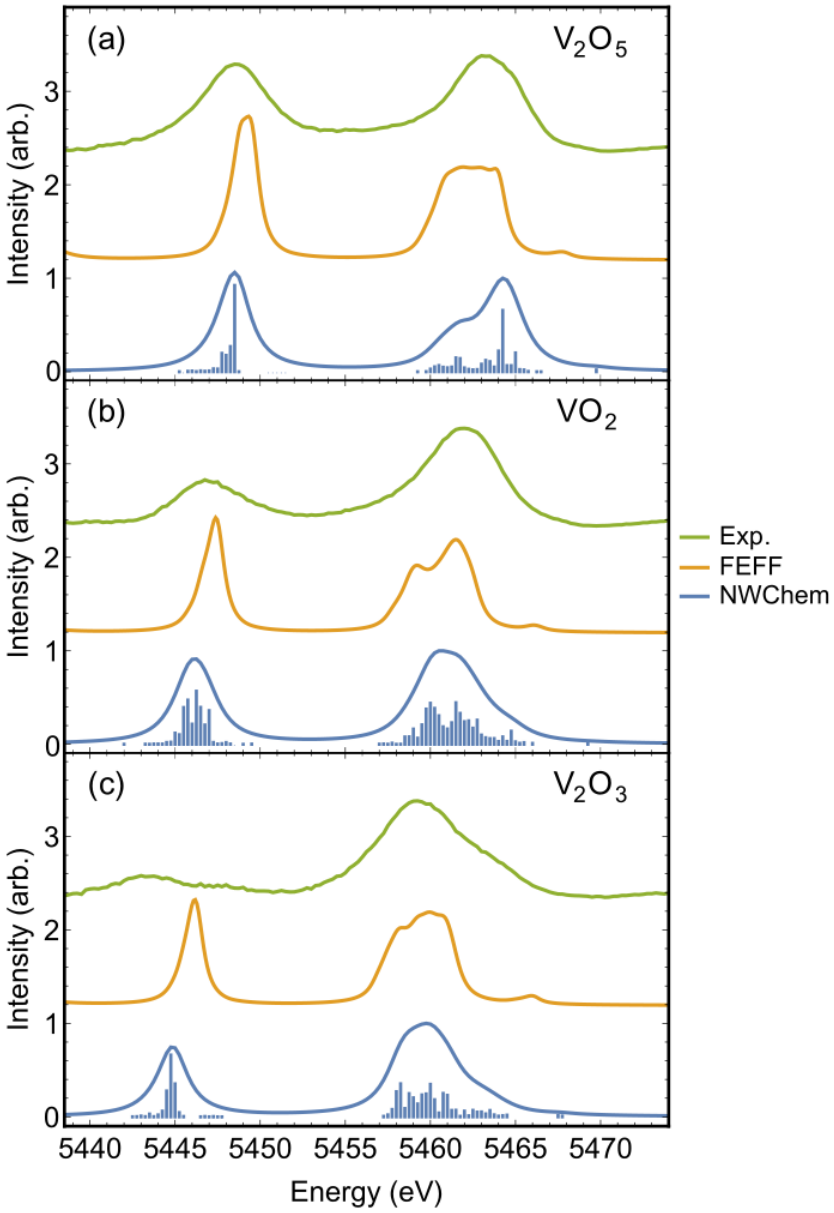

Fig. 9-3: V VTC-XES results for a suite of V oxides. The top spectrum in each frame is the experimental spectrum after correction for the tail from the V $K\beta_{1,3}$. The middle spectrum in each frame is the spectrum calculated by `FEFF9` using a Green's function approach. The bottom spectrum in each frame is the spectrum calculated by `NWChem` using a TDDFT approach. The sticks represent transition lines sorted into bins of 0.25 eV width. The sticks are subject to an arbitrary rescaling for clarity.

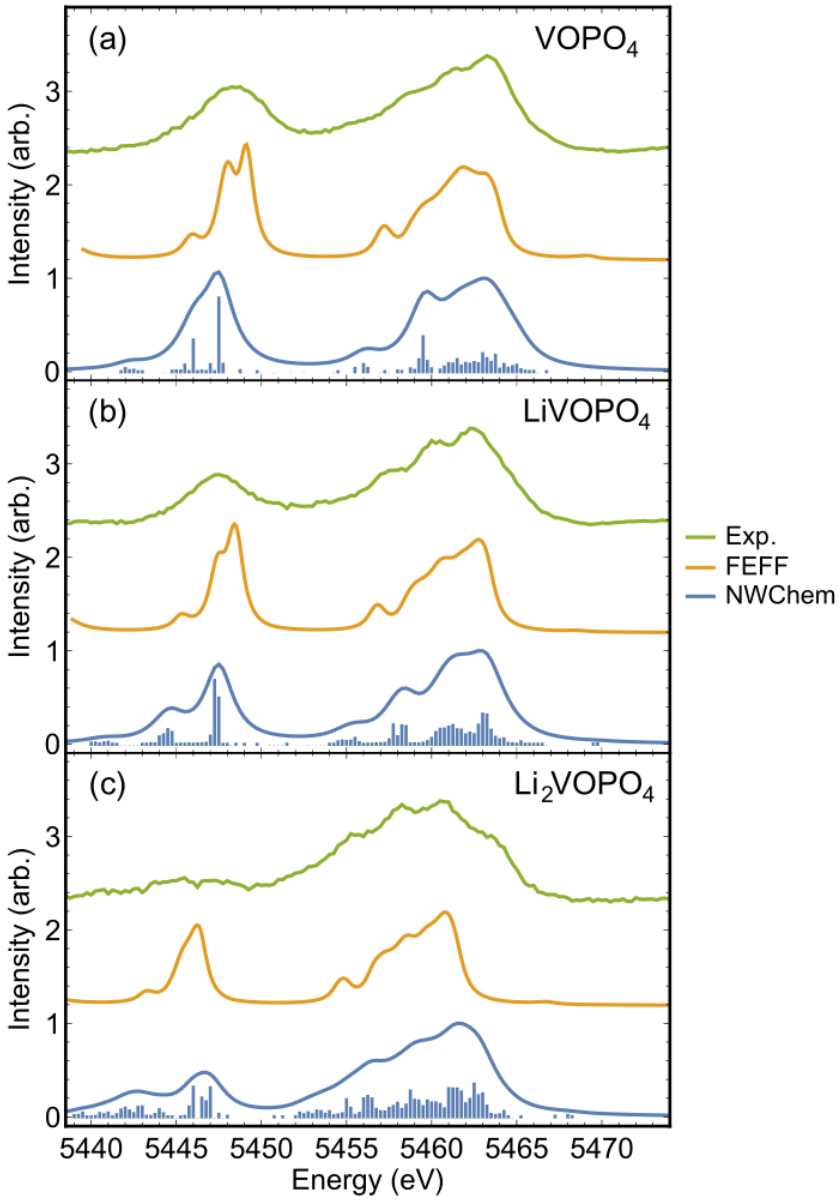

Fig. 9-4: V VTC-XES results for a suite of vanadyl phosphates. The top spectrum in each frame is the experimental spectrum after correction for the tail from the V $K\beta_{1,3}$. The middle spectrum in each frame is the spectrum calculated by `FEFF9` using a Green's function approach. The bottom spectrum in each frame is the spectrum calculated by `NWChem` using a TDDFT approach. The sticks represent transition lines sorted into bins of 0.25 eV in width. The sticks are subject to an arbitrary rescaling for clarity.

Both NWChem and FEFF9 offer some methods for assessing the character of the transitions. In FEFF9, this is accomplished by investigating various contributions to the system's density of states. In NWChem, the character of the orbital can be assessed by investigating the contribution of the atomic orbitals used in the calculation, see Fig. 9-5. In all regions, some V(s) character is observed. The Kβ'' was observed to be predominantly made of O(s) orbitals, in accordance with previously repeated VTC-XES results for transition metal compounds.[10, 11] Towards higher energies, the O(p) contributions increase, again as expected.[41] However, notable V(s) contributions are present, which are likely hybridized orbitals with traditionally dipole-allowed orbitals. Furthermore, a substantial degree of P(s), P(p), Li(s) and Li(p) are observed in different regions of the main VTC-XES feature. None of these atoms are directly associated with the absorbing V atom, and, therefore, reflect some degree of delocalization in the molecular orbitals. Further study into the theoretical results are ongoing for all the systems studied and will be reported in an upcoming publication.[102]

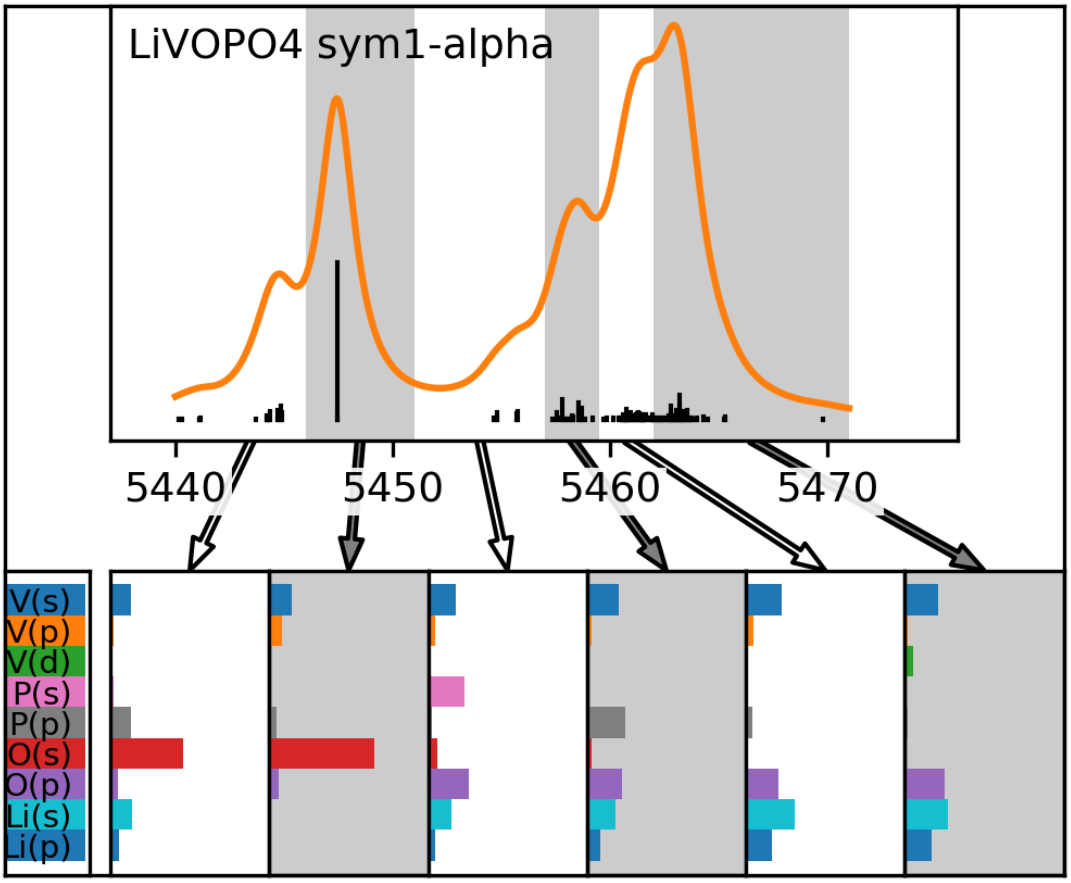

Fig. 9-5: Representative V VTC-XES TDDFT simulation. The relative contribution of each type of orbital to the transition lines occupying the corresponding region are shown in the histogram plot below the spectrum.

4. Conclusion

These results clearly demonstrate the utility of laboratory-based X-ray spectroscopy instrumentation for the measurement of VTC-XES of transition metal compounds. Here the VTC-XES of several compounds of societal and scientific relevance have been measured and presented with high-quality. The modern computational procedures used to simulate these results reproduced the experimental spectra with excellent agreement. Moreover, the third and

previously unreported triple feature structure in the vanadyl phosphate has been reported and modeled. This manuscript serves as a framework for future studies investigating the electronic structure of exotic materials by VTC-XES with laboratory-based X-ray spectroscopy instrumentation.

5. Acknowledgements

EPJ and TTF were supported in part by the Joint Center for Energy Storage Research (JCESR), an Energy Innovation Hub funded by the U.S. Department of Energy, Office of Science, and Basic Energy Sciences. EPJ was also supported by a subcontract from the National Institute of Standards and Technology. Opinions, recommendations, findings, and conclusions presented in this manuscript and associated materials does not necessarily reflect the views or policies of NIST or the United States Government. Part of this work was conducted at the Molecular Analysis Facility, a National Nanotechnology Coordinated Infrastructure site at the University of Washington which is supported in part by the National Science Foundation (grant NNCI- 1542101), the University of Washington, the Molecular Engineering & Sciences Institute, and the Clean Energy Institute. This material is based in part upon work supported by the State of Washington through the University of Washington Clean Energy Institute. The work of J. Rana, L. F. J. Piper, C. Siu, and M. S. Whittingham was supported as part of the NorthEast Center for Chemical Energy Storage (NECCES), and Energy Frontier Research Center funded by the U.S. Department of Energy, Office of Science, Basic Energy Sciences under Award No. DE-SC0012583.

6. References

1. M. S. Whittingham, Chemical Reviews **104** (10), 4271-4302 (2004).
2. M. S. Whittingham, Chemical Reviews **114** (23), 11414-11443 (2014).

3. J. L. Andrews, A. Mukherjee, H. D. Yoo, A. Parija, P. M. Marley, S. Fakra, D. Prendergast, J. Cabana, R. F. Klie and S. Banerjee, Chem **4** (3), 564-585 (2018).
4. W. Bi, E. Jahrman, G. Seidler, J. Wang, G. Gao, G. Wu, M. Atif, M. AlSalhi and G. Cao, ACS Applied Materials & Interfaces **11** (18), 16647-16655 (2019).
5. M. D. Goldflam, T. Driscoll, B. Chapler, O. Khatib, N. Marie Jokerst, S. Palit, D. R. Smith, B.-J. Kim, G. Seo, H.-T. Kim, M. D. Ventra and D. N. Basov, Applied Physics Letters **99** (4), 044103 (2011).
6. N. Hassan, J. Riaz, M. T. Qureshi, A. Razaq, M. Rahim, A. M. Toufiq and A. Shakoor, Journal of Materials Science: Materials in Electronics **29** (18), 16021-16026 (2018).
7. M. Son, J. Lee, J. Park, J. Shin, G. Choi, S. Jung, W. Lee, S. Kim, S. Park and H. Hwang, IEEE Electron Device Letters **32** (11), 1579-1581 (2011).
8. R. Xie, C. T. Bui, B. Varghese, Q. Zhang, C. H. Sow, B. Li and J. T. L. Thong, Advanced Functional Materials **21** (9), 1602-1607 (2011).
9. U. Bergmann and P. Glatzel, Photosynth Res **102** (2), 255 (2009).
10. E. Gallo and P. Glatzel, Advanced Materials **26** (46), 7730-7746 (2014).
11. P. Glatzel and U. Bergmann, Coordin Chem Rev **249** (1-2), 65-95 (2005).
12. S. G. Eeckhout, O. V. Safonova, G. Smolentsev, M. Biasioli, V. A. Safonov, L. N. Vykhodtseva, M. Sikora and P. Glatzel, Journal of Analytical Atomic Spectrometry **24** (2), 215-223 (2009).
13. C. Weis, G. Spiekermann, C. Sternemann, M. Harder, G. Vankó, V. Cerantola, C. J. Sahle, Y. Forov, R. Sakrowski, I. Kupenko, S. Petitgirard, H. Yavaş, C. Bressler, W. Gawelda, M. Tolan and M. Wilke, Journal of Analytical Atomic Spectrometry **34** (2), 384-393 (2019).
14. E. Gallo, C. Lamberti and P. Glatzel, Physical Chemistry Chemical Physics **13** (43), 19409-19419 (2011).
15. N. Lee, T. Petrenko, U. Bergmann, F. Neese and S. DeBeer, J Am Chem Soc **132** (28), 9715-9727 (2010).
16. J. C. Swarbrick, Y. Kvashnin, K. Schulte, K. Seenivasan, C. Lamberti and P. Glatzel, Inorg Chem **49** (18), 8323-8332 (2010).
17. W. Błachucki, J. Czapla-Masztafiak, J. Sá and J. Szlachetko, Journal of Analytical Atomic Spectrometry **34** (7), 1409-1415 (2019).
18. L. Anklamm, C. Schlesiger, W. Malzer, D. Grötzsch, M. Neitzel and B. Kanngießer, Review of Scientific Instruments **85** (5), 053110 (2014).
19. R. Bès, T. Ahopelto, A. P. Honkanen, S. Huotari, G. Leinders, J. Pakarinen and K. Kvashnina, Journal of Nuclear Materials **507**, 50-53 (2018).
20. A.-P. Honkanen, S. Ollikkala, T. Ahopelto, A.-J. Kallio, M. Blomberg and S. Huotari, Review of Scientific Instruments **90** (3), 033107 (2019).
21. W. M. Holden, O. R. Hoidn, A. S. Ditter, G. T. Seidler, J. Kas, J. L. Stein, B. M. Cossairt, S. A. Kozimor, J. Guo, Y. Ye, M. A. Marcus and S. Fakra, Review of Scientific Instruments **88** (7), 073904 (2017).
22. E. P. Jahrman, W. M. Holden, A. S. Ditter, D. R. Mortensen, G. T. Seidler, T. T. Fister, S. A. Kozimor, L. F. J. Piper, J. Rana, N. C. Hyatt and M. C. Stennett, Review of Scientific Instruments **90** (2), 024106 (2019).
23. G. T. Seidler, D. R. Mortensen, A. J. Remesnik, J. I. Pacold, N. A. Ball, N. Barry, M. Styczinski and O. R. Hoidn, Review of Scientific Instruments **85** (11), 113906 (2014).

24. A. Krammer, O. Bouvard and A. Schüler, Energy Procedia **122**, 745-750 (2017).
25. N. Wang, M. Duchamp, R. E. Dunin-Borkowski, S. Liu, X. Zeng, X. Cao and Y. Long, Langmuir **32** (3), 759-764 (2016).
26. L. Zhao, L. Miao, C. Liu, C. Li, T. Asaka, Y. Kang, Y. Iwamoto, S. Tanemura, H. Gu and H. Su, Scientific reports **4**, 7000 (2014).
27. J. Stajic, Science **362** (6418), 1014 (2018).
28. W. Bi, J. Huang, M. Wang, E. P. Jahrman, G. T. Seidler, J. Wang, Y. Wu, G. Gao, G. Wu and G. Cao, Journal of Materials Chemistry A **7** (30), 17966-17973 (2019).
29. W. Bi, J. Wang, E. P. Jahrman, G. T. Seidler, G. Gao, G. Wu and G. Cao, Small **0** (0), 1901747 (2019).
30. W. Bi, Y. Wu, C. Liu, J. Wang, Y. Du, G. Gao, G. Wu and G. Cao, ACS Applied Energy Materials **2** (1), 668-677 (2019).
31. J. S. Braithwaite, C. R. A. Catlow, J. D. Gale and J. H. Harding, Chem Mater **11** (8), 1990-1998 (1999).
32. R. Jourdani, L. Jadoual, M. Ait El Fqih, A. El Boujlaidi, H. Aouchiche and A. Kaddouri, Surf Interface Anal **50** (1), 52-58 (2018).
33. S. Nordlinder, L. Nyholm, T. Gustafsson and K. Edström, Chem Mater **18** (2), 495-503 (2006).
34. S.-C. Lim, J. Lee, H. H. Kwak, J. W. Heo, M. S. Chae, D. Ahn, Y. H. Jang, H. Lee and S.-T. Hong, Inorg Chem **56** (14), 7668-7678 (2017).
35. G. Sai Gautam, P. Canepa, A. Abdellahi, A. Urban, R. Malik and G. Ceder, Chem Mater **27** (10), 3733-3742 (2015).
36. Z. Chen, Q. Chen, L. Chen, R. Zhang, H. Zhou, N. A. Chernova and M. S. Whittingham, Journal of The Electrochemical Society **160** (10), A1777-A1780 (2013).
37. C. Siu, I. D. Seymour, S. Britto, H. Zhang, J. Rana, J. Feng, F. O. Omenya, H. Zhou, N. A. Chernova, G. Zhou, C. P. Grey, L. F. J. Piper and M. S. Whittingham, Chemical Communications **54** (56), 7802-7805 (2018).
38. Y. Song, P. Y. Zavalij and M. S. Whittingham, Journal of The Electrochemical Society **152** (4), A721-A728 (2005).
39. O. Einsle, F. A. Tezcan, S. L. A. Andrade, B. Schmid, M. Yoshida, J. B. Howard and D. C. Rees, Science **297** (5587), 1696 (2002).
40. K. M. Lancaster, M. Roemelt, P. Ettenhuber, Y. Hu, M. W. Ribbe, F. Neese, U. Bergmann and S. DeBeer, Science **334** (6058), 974 (2011).
41. C. J. Pollock, K. Grubel, P. L. Holland and S. DeBeer, J Am Chem Soc **135** (32), 11803-11808 (2013).
42. U. Bergmann, C. R. Horne, T. J. Collins, J. M. Workman and S. P. Cramer, Chem Phys Lett **302** (1), 119-124 (1999).
43. S. N. MacMillan, R. C. Walroth, D. M. Perry, T. J. Morsing and K. M. Lancaster, Inorg Chem **54** (1), 205-214 (2015).
44. B. Lassalle-Kaiser, T. T. Boron, 3rd, V. Krewald, J. Kern, M. A. Beckwith, M. U. Delgado-Jaime, H. Schroeder, R. Alonso-Mori, D. Nordlund, T.-C. Weng, D. Sokaras, F. Neese, U. Bergmann, V. K. Yachandra, S. DeBeer, V. L. Pecoraro and J. Yano, Inorg Chem **52** (22), 12915-12922 (2013).
45. C. Sugiura, Y. Gohshi and I. Suzuki, Physical Review B **10** (2), 338-343 (1974).

46. Y. Gohshi, Y. Hukao and K. Hori, Spectrochimica Acta Part B: Atomic Spectroscopy **27** (3), 135-142 (1972).
47. S. Chikara, G. Yohichi and S. Isao, Jpn J Appl Phys **11** (6), 911 (1972).
48. M. Y. Yu, V. A. Trofimova, V. E. Dolgih, M. A. Korotin, E. Z. Kurmaev, J. A. Aguiar, J. M. Ferreira and A. C. Pavao, Journal of Physics: Condensed Matter **7** (1), 213 (1995).
49. Y. M. Yarmoshenko, V. A. Trofimova, E. Z. Kurmaev, P. R. Slater and C. Greaves, Physica C: Superconductivity **224** (3), 317-320 (1994).
50. Y. M. Yarmoshenko, V. A. Trofimova, L. V. Elokhina, E. Z. Kurmaev, S. Butorin, R. Cloots, M. Ausloos, J. A. Aguiar and N. I. Lobatchevskaya, Journal of Physics and Chemistry of Solids **54** (10), 1211-1214 (1993).
51. V. E. Dolgih, V. M. Cherkashenko, E. Z. Kurmaev, D. A. Goganov, E. K. Ovchinnikov and Y. M. Yarmoshienko, Nuclear Instruments and Methods in Physics Research **224** (1), 117-119 (1984).
52. M. Kavčič, J. C. Dousse, J. Szlachetko and W. Cao, Nuclear Instruments and Methods in Physics Research Section B: Beam Interactions with Materials and Atoms **260** (2), 642-646 (2007).
53. Z. Németh, J. Szlachetko, É. G. Bajnóczi and G. Vankó, Review of Scientific Instruments **87** (10), 103105 (2016).
54. Y. Kayser, W. Błachucki, J. C. Dousse, J. Hoszowska, M. Neff and V. Romano, Review of Scientific Instruments **85** (4), 043101 (2014).
55. J. Hoszowska, J. C. Dousse, J. Kern and C. Rhême, Nuclear Instruments and Methods in Physics Research Section A: Accelerators, Spectrometers, Detectors and Associated Equipment **376** (1), 129-138 (1996).
56. R. A. Valenza, E. P. Jahrman, J. J. Kas and G. T. Seidler, Phys Rev A **96** (3), 032504 (2017).
57. G. T. Seidler, D. R. Mortensen, A. S. Ditter, N. A. Ball and A. J. Remesnik, Journal of Physics: Conference Series **712** (1), 012015 (2016).
58. D. R. Mortensen, G. T. Seidler, J. J. Kas, N. Govind, C. P. Schwartz, S. Pemmaraju and D. G. Prendergast, Physical Review B **96** (12), 125136 (2017).
59. D. R. Mortensen, G. T. Seidler, A. S. Ditter and P. Glatzel, Journal of Physics: Conference Series **712** (1), 012036 (2016).
60. D. R. Mortensen and G. T. Seidler, J Electron Spec **215**, 8-15 (2017).
61. E. P. Jahrman, G. T. Seidler and J. R. Sieber, Analytical Chemistry **90** (11), 6587 (2018).
62. M. Szlachetko, M. Berset, J. C. Dousse, J. Hoszowska and J. Szlachetko, Review of Scientific Instruments **84** (9), 093104 (2013).
63. O. Bunău and Y. Joly, Physical Review B **85** (15), 155121 (2012).
64. P. Elliott, F. Furche and K. Burke, Reviews in Computational Chemistry, 91-165 (2008).
65. M. Valiev, E. J. Bylaska, N. Govind, K. Kowalski, T. P. Straatsma, H. J. J. Van Dam, D. Wang, J. Nieplocha, E. Apra, T. L. Windus and W. A. de Jong, Computer Physics Communications **181** (9), 1477-1489 (2010).
66. L. Burkhardt, M. Holzwarth, B. Plietker and M. Bauer, Inorg Chem **56** (21), 13300-13310 (2017).
67. L. Burkhardt, C. Mueller, O. A. Groß, Y. Sun, H. Sitzmann and M. Bauer, Inorg Chem **58** (10), 6609-6618 (2019).

68. S. DeBeer George, T. Petrenko and F. Neese, Inorganica Chimica Acta **361** (4), 965-972 (2008).
69. N. Govind, K. Lopata, R. Rousseau, A. Andersen and K. Kowalski, The Journal of Physical Chemistry Letters **2** (21), 2696-2701 (2011).
70. P. J. Lestrange, P. D. Nguyen and X. Li, Journal of Chemical Theory and Computation **11** (7), 2994-2999 (2015).
71. Y. Zhang, S. Mukamel, M. Khalil and N. Govind, Journal of Chemical Theory and Computation **11** (12), 5804-5809 (2015).
72. M. J. Powell, I. J. Godfrey, R. Quesada-Cabrera, D. Malarde, D. Teixeira, H. Emerich, R. G. Palgrave, C. J. Carmalt, I. P. Parkin and G. Sankar, The Journal of Physical Chemistry C **121** (37), 20345-20352 (2017).
73. B. Ravel and M. Newville, Journal of Synchrotron Radiation **12** (4), 537-541 (2005).
74. C. M. Teodorescu, G. Socol, C. Negrila, D. Luca and D. Macovei, Journal of Experimental Nanoscience **5** (6), 509-526 (2010).
75. M. Bianchini, J. M. Ateba-Mba, P. Dagault, E. Bogdan, D. Carlier, E. Suard, C. Masquelier and L. Croguennec, Journal of Materials Chemistry A **2** (26), 10182-10192 (2014).
76. H. Enkisch, C. Sternemann, M. Paulus, M. Volmer and W. Schülke, Phys Rev A **70** (2), 022508 (2004).
77. M. Casarin, C. Maccato and A. Vittadini, The Journal of Physical Chemistry B **102** (52), 10745-10752 (1998).
78. M. L. Sushko, A. Y. Gal and A. L. Shluger, The Journal of Physical Chemistry B **110** (10), 4853-4862 (2006).
79. L.-W. Wang and J. Li, Physical Review B **69** (15), 153302 (2004).
80. J. D. Wadey and N. A. Besley, Journal of Chemical Theory and Computation **10** (10), 4557-4564 (2014).
81. C. Adamo and V. Barone, The Journal of Chemical Physics **110** (13), 6158-6170 (1999).
82. T. H. Dunning and P. J. Hay, in *Methods of Electronic Structure Theory*, edited by H. F. Schaefer (Springer US, Boston, MA, 1977), pp. 1-27.
83. J. D. Dill and J. A. Pople, The Journal of Chemical Physics **62** (7), 2921-2923 (1975).
84. V. A. Rassolov, J. A. Pople, M. A. Ratner and T. L. Windus, The Journal of Chemical Physics **109** (4), 1223-1229 (1998).
85. A. Bergner, M. Dolg, W. Küchle, H. Stoll and H. Preuß, Molecular Physics **80** (6), 1431-1441 (1993).
86. P. J. Hay and W. R. Wadt, The Journal of Chemical Physics **82** (1), 299-310 (1985).
87. T. Noro, M. Sekiya and T. Koga, Theoretical Chemistry Accounts **131** (2), 1124 (2012).
88. H. Ågren, V. Carravetta, O. Vahtras and L. G. M. Pettersson, Chem Phys Lett **222** (1), 75-81 (1994).
89. H. Ågren, V. Carravetta, O. Vahtras and L. G. M. Pettersson, Theoretical Chemistry Accounts **97** (1), 14-40 (1997).
90. W. J. Hunt and W. A. Goddard, Chem Phys Lett **3** (6), 414-418 (1969).
91. N. A. Besley, A. T. B. Gilbert and P. M. W. Gill, The Journal of Chemical Physics **130** (12), 124308 (2009).
92. A. T. B. Gilbert, N. A. Besley and P. M. W. Gill, The Journal of Physical Chemistry A **112** (50), 13164-13171 (2008).

93. S. Hirata and M. Head-Gordon, Chem Phys Lett **314** (3), 291-299 (1999).
94. I. P. E. Roper and N. A. Besley, The Journal of Chemical Physics **144** (11), 114104 (2016).
95. T. Mukoyama, Spectrochimica Acta Part B: Atomic Spectroscopy **59** (8), 1107-1115 (2004).
96. J. J. Rehr and R. C. Albers, Reviews of Modern Physics **72** (3), 621-654 (2000).
97. J. J. Rehr, J. J. Kas, M. P. Prange, A. P. Sorini, Y. Takimoto and F. Vila, Comptes Rendus Physique **10** (6), 548-559 (2009).
98. J. J. Rehr, J. J. Kas, F. D. Vila, M. P. Prange and K. Jorissen, Physical Chemistry Chemical Physics **12** (21), 5503-5513 (2010).
99. Y. Guo, S. J. Clark and J. Robertson, The Journal of Chemical Physics **140** (5), 054702 (2014).
100. A. Haras, M. Witko, D. R. Salahub, K. Hermann and R. Tokarz, Surf Sci **491** (1), 77-87 (2001).
101. F. D. Hardcastle and I. E. Wachs, The Journal of Physical Chemistry **95** (13), 5031-5041 (1991).
102. E. P. Jahrman, W. M. Holden, N. Govind, J. J. Kas, J. Rana, L. F. J. Piper, M. S. Whittingham, T. T. Fister and G. T. Seidler, Chem Mater (In preparation).

Chapter 10. Determination of Hexavalent Chromium Fractions in Plastics Using Laboratory-Based, High-Resolution X-Ray Emission Spectroscopy

Originally published as: E. P. Jahrman, G. T. Seidler, and J. R. Sieber. Analytical Chemistry **90** (11), 6587 (2018). This chapter represents a significant portion of this dissertation and the effort was led by the candidate. Among other details, the candidate performed all of the X-ray emission spectroscopy measurements and analysis, and also the X-ray absorption fine structure analysis.

Cr(VI) is a well-known human carcinogen with many water-soluble moieties. Its presence in both natural and man-made substances poses a risk to public health, especially when contamination of ground water is possible. This has led the European Union and other jurisdictions to include Cr(VI) in restriction of hazardous substances (RoHS) regulations. However, for several important industrial and commercial purposes, analytical capability to characterize Cr(VI) is known to be insufficient for regulatory purposes. For example, advanced X-ray spectroscopies, particularly synchrotron-based X-ray absorption fine structure (XAFS) studies, have shown that species interconversion and under-extraction can be difficult to prevent in many existing liquid extraction protocols when applied to plastics, mining ores and tailings, and paint sludges. Here, we report that wavelength dispersive X-ray fluorescence (WDXRF) spectroscopy taken at energy resolutions close to the theoretical limit imposed by the core-hole lifetime, generally called X-ray emission spectroscopy (XES) in the synchrotron community, can be used in the laboratory setting for non-invasive, analytical characterization of the Cr(VI)/Cr ratio in plastics. The selected samples have been part of ongoing efforts by standards development organizations to create improved Cr(VI)

testing protocols, and the present work provides a direct proof-of-principle for the use of such extremely high-resolution laboratory WDXRF as an alternative to liquid extraction methods for regulatory compliance testing of Cr(VI) content. As a practical application of this work, we report a value for the Cr(VI) mass fraction of the new NIST Standard Reference Material 2859 Restricted Elements in Polyvinyl Chloride.

1. Introduction

Chromium is an earth-abundant element whose toxicity, mobility, and bioavailability are all heavily dependent on its oxidation state within a given compound. The more harmful species, hexavalent Cr, i.e., Cr(VI), is known to be roughly one hundred times as hazardous as trivalent Cr(III) due to its carcinogenic properties.[1] It is therefore critical that test methods be in place to understand the speciation of Cr in our environment and in manufactured products. Indeed, the Cr(VI) concentration in the latter can be the result of unidentified precursors and subject to change following heat treatments or the incorporation of chemically-active agents during processing.[2] Consequently, standard protocols for Cr(VI) characterization have been developed by several international organizations with the goal of meeting restriction of hazardous substances (RoHS) guidelines mandating a maximum mass fraction of Cr(VI) of 0.1 % in materials used in consumer goods including plastics.[3] Further milestones have been set for the development of standard test materials and procedures for improved Cr(VI) detection with the goal of mitigating the risk of public exposure to Cr(VI) and a consequent reduction in adverse human health outcomes as motivated by established hazard control strategies.[4]

Methods capable of determining Cr(VI) content within a solid sample matrix currently exist but they suffer from systematic and pragmatic shortcomings. Many benchtop procedures require a chemical extraction process to separate Cr(VI) prior to colorimetric analysis by reaction

with diphenyl carbazide.[5] As a result, wet chemical methods are often criticized for susceptibility to species interconversion and incomplete extraction.

Indeed, a study by Malherbe *et al.*, demonstrated the tendency of EPA method 3060a to systematically underestimate the mass fraction of Cr(VI) in a series of reference soils.[6] This study implemented an X-ray spectroscopic technique, X-ray absorption fine structure (XAFS), that has the advantage of minimal sample preparation requirements so the electronic structure of a species may be interrogated in its native environment. In the case of Cr, the highly distinctive pre-edge feature is directly sensitive to the coordination and oxidation state of the metal within a given compound.[7] Moreover, XAFS is a robust methodology that has previously been applied to studies of Cr in glasses,[8] soils,[9] plastics,[10] coals,[11,12] chrome-tanned leathers,[13] and ultramafic rocks.[14] However to play a significant role in environmental and industrial regulatory monitoring and compliance verification, a technique must be highly accessible to its intended users. While there has been a resurgence of interest in laboratory-based XAFS,[15-19] at present XAFS analysis of extremely dilute samples is restricted to synchrotron light sources. Despite a growing number of beamlines serving industrial clients, synchrotron efforts are not currently a practical solution for high-throughput, fast turn-around, routine characterizations that are the workhorse needs of the broader analytical chemistry community.

However, there exist higher-access X-ray spectroscopic techniques having the same advantages of sensitivity to electronic structure, nondestructive measurement, and robustness to sample matrix. For example, X-ray photoelectron spectroscopy (XPS) is an established technique capable of speciation studies, yet is traditionally surface-sensitive and requires an ultra-high vacuum often incompatible with plastics, epoxies, and resins. On the other hand, X-ray fluorescence (XRF) spectroscopy, which examines the difference in screening between two core

holes, is widely implemented as a laboratory-based technique for elemental analysis. When equipped with sufficient energy resolution, such as in wavelength dispersive X-ray fluorescence (WDXRF) studies, measurements begin to demonstrate sensitivity to speciation. Numerous authors assert the viability of assigning coordination, and thus rudimentary speciation, according to the relative intensities of characteristic fluorescence lines.[20-22] In the case of Cr, branch-ratio analysis has been demonstrated to possess some limited utility in the detection of the hexavalent species.[23]

Further and more reliable determinations from WDXRF are pursued by instead investigating the fine shape of individual spectral features. Previously, Baydas *et al.*[24] reported the sensitivity of the Cr Kα fluorescence line to speciation via WDXRF, but while their results are promising, the utilized instrumentation possessed insufficient energy resolution to resolve peaks split due to spin-orbit coupling, let alone more subtle effects. A recent WDXRF study in the Kβ region satisfactorily resolved spectral features such that hexavalent and trivalent species were noticeably distinct, but suffered from limitations in energy range and energy resolution that complicated background subtractions and decreased the total information content of the spectra.[25]

The point of the present paper is to improve the performance of WDXRF speciation of Cr by refining the energy resolution of the measurements down to the intrinsic limit imposed by the core-hole lifetime of the principal 1*s* photoexcitation of the Cr ion. Such extremely high resolution WDXRF is typically called X-ray emission spectroscopy (XES) in the synchrotron community,[26] and it has demonstrated capability for ascertaining several categories of local electronic and structural information that is not available from studies having coarser energy resolution.[27-29] With growing frequency, XES is applied to studies of oxidation state, spin-state, covalency, or ligand environment, and like XAFS, XES is generally applicable to a range of sample environments.[30-32]

Accordingly, both experimental and theoretical works have investigated the viability of XES in the Kβ region as a tool for speciation studies of Cr in its native environment.[33,34]

While previous XES studies of Cr(VI)/Cr speciation were performed at synchrotron light sources, we show here that recent technical advances have made such extremely high resolution WDXRF studies of dilute samples accessible in a laboratory setting. For completeness, we note that there is a growing literature on lab-based XES instrumentation.[17,35-42] In this work, using a low-powered, lab-based X-ray emission spectrometer,[18] we perform Cr Kα XES in a broad survey of reference-standard plastics based on various polymer formulations, Cr mass fractions, and prepared Cr(VI) species fractions. Previous XES studies report the Cr Kβ lines' speciation dependence[25,33,34], but here we find that the fine spectral changes between various oxidation states of Cr are adequately resolved to serve as references when fitting the stronger Cr Kα spectrum of a plastic with unknown Cr content. This procedure yields quantitative results of the Cr(VI) species fraction consistent with a synchrotron XAFS study. Accordingly, we use the Kα lines as they are the most intense transition available and consequently decrease necessary integration times and increase our sensitivity. These results strongly support the accuracy of using Cr Kα for the purpose of determining the Cr(VI)/Cr ratio in plastics.

2. Methods

Materials and Preparation

This study investigates several certified reference materials and laboratory-prepared blends selected to span a range of plastic polymer formulations, total Cr mass fractions, Cr(VI) species fractions, and Cr starting materials. In particular, the range of total Cr and Cr(VI) mass fractions was selected to encompass the typical ranges found in plastics and the allowable levels listed in regulations, respectively. This information is summarized in Table 10-1 where sample notation

follows prior work or organizational convention.[43,44] Of note, polypropylene (PP) P106 was selected to demonstrate that Cr(VI) may be processed without reduction; conversely, Cr515 was chosen to assess the capability of XES for detecting the presence of strictly trivalent Cr. EC681k and CRM 8113a were included as representative plastics containing a mixture of hexavalent and trivalent Cr in polyethylene (PE) and acrylonitrile butadiene styrene (ABS), respectively. The remaining samples were included to assess the robustness of the method for the photosensitive case of polyvinyl chloride (PVC). An advantage of XES is that minimal sample preparation is required, nonetheless, some samples were sectioned to be more easily positioned in the instrument. IEC TC 111's E5 and F6 materials were received as flat sheets that were cut into disks. SRM 2859 and SRM 2861 were pressed into flat disks. P106 and Cr515 were provided as thick disks from which approximately rectangular strips were cut. EC681k and CRM 8113a were provided as thin pellets that could be conveniently measured without sectioning.

Table 10-1: Selected details of measured plastics. The samples contained various Cr compounds compounded in polymers: polypropylene (PP), polyethylene (PE), polyvinyl chloride (PVC), and acrylonitrile butadiene (ABS). The identity of the supplier, mass fraction and incorporated chromium compounds is also provided. For each Cr mass fraction value, the corresponding uncertainty is representative of a 95 % confidence interval. Materials, values, and uncertainty estimates are discussed in detail in the supplemental information.

Sample	Supplier[(a)]	Polymer	Cr Mass Fraction (mg/kg)	Cr(VI)/Cr from Preparation (%)	Cr(III) Source	Cr(VI) Source
P106[44]	CCQM	PP	252.5 ± 6.8	100	-	$BaCrO_4$/$PbCrO_4$
E5[43]	IEC TC111	PVC	1740 ± 350	100	-	$PbCrO_4$
F6[43]	IEC TC111	PVC	670 ± 130	100	-	$PbCrO_4$
SRM 2859[58]	NIST	PVC	716 ± 16	100	-	$Na_2Cr_2O_7$•$2H_2O$
SRM 2861[59]	NIST	PVC	50.4 ± 3.1	100	-	$Na_2Cr_2O_7$•$2H_2O$
EC681k[60]	IRMM	PE	100 ± 5	24.6	Cr_2O_3	$PbCrO_4$
CRM 8113a[61]	NMIJ	ABS	943.6 ± 18.0	25.1	Cr(III)-acetylacetonate	$PbCrO_4$
Cr515	NIST	PE	514.8 ± 2.2	0	Cr(III)-benzoylacetonate	-

[(a)] Organizations include the Inorganic Analytical Working Group of the Consultative Committee for Amount of Substance: Metrology in Chemistry and Biology (CCQM), the International Electrotechnical Commission Technical Committee 111 (IEC TC 111), the National Institute of Standards and Technology (NIST), the Institute for Reference Materials and Measurements (IRMM), and the National Metrology Institute of Japan (NMIJ).

XES Instrumentation and Methodology

The Seidler group at the University of Washington has recently developed laboratory-based (i.e., non-synchrotron) X-ray emission spectroscopy (XES) instrumentation that provides signal-to-noise, energy resolution, and stability fully comparable to synchrotron-based instrumentation.[16,18,45] These features make the instrument well-suited for studies of dilute samples. The technical design of the spectrometer is described in detail elsewhere.[18] The present implementation employed an X-ray tube (Moxtek Au anode) operated at 40 kV and 200 μA, i.e. only 8 W total tube power, a Ge (422) spherically bent crystal analyzer (SBCA) from XRS Tech, and an energy-dispersive silicon drift detector (Amptek SDD-X123), yielding exceptionally low backgrounds. In contrast to the prototype version of the instrument,[18] we replaced the 2-axis tilt, using instead the azimuthal orientation method of Mortensen *et al.*,[45] and we removed the translational stage beneath the optic in favor of a passive mechanical system coupling the source and SBCA to rest on the 1-m diameter Rowland circle.

All hexavalent and trivalent Cr compounds used in the production of the selected plastics were measured to acquire reference spectra. In addition, the Cr Kα spectrum of a 25 μm thick stainless-steel shim was frequently collected to ensure a consistent energy scale throughout the study and to aid in the alignment of the plastic samples. While alignment in the spectrometer is achieved by laterally translating the sample behind the entrance slit until a maximum count rate is reached, this procedure was not possible given the low Cr contents present in the plastic samples. Rather, the stainless-steel shim was first aligned and then replaced by the plastic sample with an appropriate adjustment for changes in sample thickness and attenuation length. Note that this alignment need not be especially precise, as has been documented in Mortensen *et al.*[16]

Further care was needed to determine the Cr(VI) species fraction for samples that exhibited radiation damage.[46,47] This was addressed in the standard way with a sample spinner to distribute the radiation dose over a larger sample area. Specifically, the spinner distributed the dose over an area approximately 28 times larger in size than that of the static sample. The scans averaged to represent the sample were then limited to those occurring before noticeable change in spectral shape or measured Cr(VI) content. The latter was assessed by examining the Cr(VI) fraction as a function of scan number and selecting consecutive points statistically consistent with no photo-induced reduction. As a result, the first eight scans were used for all PVC materials for which a quantitative result is reported.

XAFS Synchrotron Methods

Cr K-edge X-ray absorption fine structure (XAFS) was measured at beamline X23A2 at the National Synchrotron Light Source (NSLS). Cr XAFS spectra were collected in fluorescence mode using a four-element Si drift detector (Hitachi Vortex EX). The primary beam was monochromatized using a Si (311) double-crystal monochromator and was collimated to a line shape approximately 300 μm high and 9 mm wide. Each XAFS scan proceeded in 1 eV steps from 5889 eV to 5939 eV, 0.5 eV steps from 5939 eV to 5962 eV, 0.07 eV steps from 5962 to 6004 eV, 0.5 eV steps from 6004 eV to 6029 eV, and 2 eV from 6029 to 6338 eV with a 0.5 s dwell time at each point. Samples in powder form were prepared by cryogenic milling and mounted in a polyethylene sample cell between layers of 4 μm thick polypropylene film (Somar Spectrolene). Plastic disks were prepared by melt pressing. Temperatures for melt pressing were kept well below those used for extrusion or complete melting of the sample, rather, the employed temperature was the minimum required to fuse the materials with the aid of a hydraulic press. Each sample was

mounted on a spinner and rotated during measurements to overcome potential heterogeneity and to minimize potential beam damage. No evidence of beam damage was observed.

Fit Procedures

Determination of the Cr(VI) fraction by XES was accomplished via a least-squares regression analysis. First, the trivalent and hexavalent reference spectra were background corrected and normalized to the total number of counts in the integration range. The reference spectra were then fit to a pair of interpolating functions. Next, the spectrum of a sample with unknown chromium speciation was likewise background corrected and integral normalized. The portion of the unknown spectrum between 5400 eV and 5420 eV was fit by a linear combination of the interpolating functions representing the reference spectra. The fit was performed using the NonlinearModelFit function in Mathematica with the Cr(VI) species fraction as the optimization parameter, which was subsequently extracted along with its uncertainty.

Other sources of uncertainty affecting the fit were quantified, these include the particular choice of reference spectra and the variability in the XES energy scale upon sample exchange. The bias introduced with the choice of reference compound was estimated by performing fits with all possible combinations of references and calculating a corresponding uncertainty in the result. Additionally, the bias accompanying the imperfect reproducibility of the XES energy scale was estimated by sampling the maximal energy shifts introduced by sample exchange reported elsewhere.[16,48] This was done by displacing an employed reference spectrum 10 meV lower, not at all, or 10 meV higher in energy. Displacements were done to both the trivalent and hexavalent references, and after considering all nine possible permutations, the standard deviation of the resulting fit parameters was taken as the resulting uncertainty.

For the XAFS data, the Cr(VI) fraction was determined from the near-edge region by analysis with the ATHENA software, version 0.9.25.[49] After fitting the edge shape to an error function, the pre-edge features were fit to a set of three Lorentzian functions. The choice of three features is in accordance with previously reported spectra and fit procedures,[50-53] while the choice of Lorentzian functions is consistent with the work of Lytle *et al.*[54] and Calas *et al.*[55] The percentage of the hexavalent Cr species present in the plastic samples was related to the area of the Lorentzian of intermediate energy.[50,53,56]

The uncertainty in the XAFS fitting procedure's result was estimated from successive scans of each compound. In the trivalent and hexavalent cases, these spectra were merged prior to fitting. However, this was not done for the plastic compounds to minimize sensitivity to the precise background and normalization treatment applied to the necessarily dilute samples. Rather, all features were fit to a single scan before fixing all parameters, except the height of each feature. The regression analysis was then applied to the remaining scans and a result with a corresponding uncertainty obtained. This uncertainty was propagated with the error in the intensity of the Lorentzian representing 3d → 4p mixing in the hexavalent reference as obtained by the fitting procedure.

3. Results and Discussion

Reference compound spectra are presented in Fig. 10-1. Comparing the trivalent and hexavalent Cr compounds, differences in the spectral features are easily discernible with the current energy resolution and a determined instrumental sample-to-sample reproducibility of better than 20 meV. The trivalent species possess additional electron density in valence states, yielding additional screening of the nuclear potential and an increase in (2p,3d) exchange in the final electronic configuration. The spectral features of the trivalent species are consequently shifted to

higher energy and broadened with respect to the hexavalent species.[29] From Fig. 10-1, it is apparent the Kα emission probes an extremely local component of the electronic structure due to the involvement of only deeply bound orbitals. Nonetheless, minute differences are seen between the spectra of various species due to covalency and crystal field effects. For that reason, it is important to compare a spectrum of interest to that of reference compounds representative of the electronic structure of Cr(VI) and Cr(III) atoms in the sample and to assess possible systematic errors related to this choice. As a step in this direction, Figure S1 shows residual spectra within

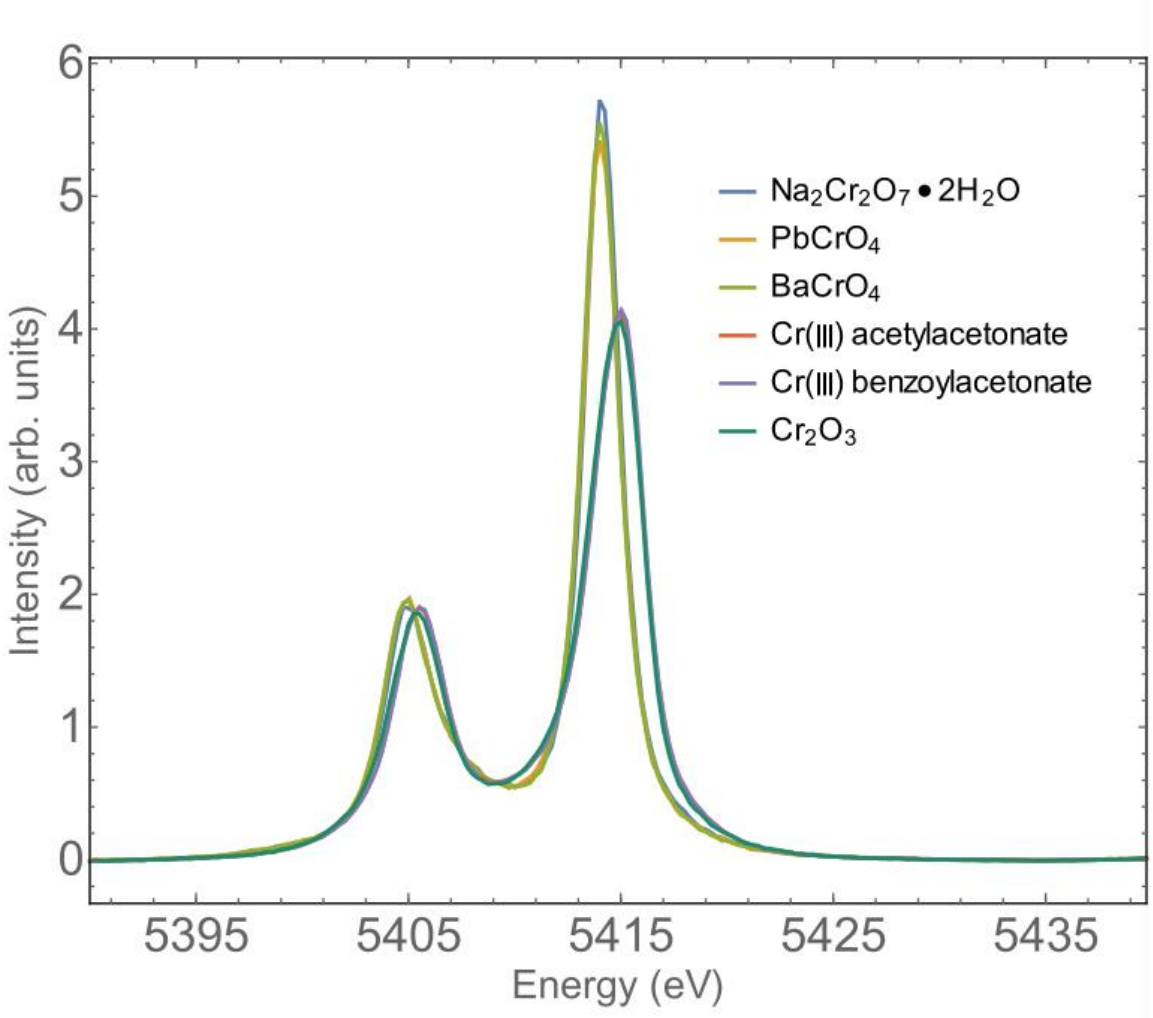

Fig. 10-1: Cr Kα XES of selected trivalent and hexavalent reference Cr compounds after background correction and integral normalization. Note, the spectrum of Cr(III) acetylacetonate is nearly identical to that of Cr(III) benzoylacetonate, and therefore hidden from view.

the families of Cr(III) and Cr(VI) reference materials, while Table S3 lists the position and intensity of the maxima of each reference material's Cr Kα emission lines.

The main results of the study are presented in Fig. 10-2 and Table 10-2. In Figure 10-2, we present the spectra collected from the reference plastics, least-squares fits to a linear

superposition of reference compound spectra, and labels indicating the inferred Cr(VI) fraction. For plastics other than PVC, the Cr sources used in the production process were selected as references with $PbCrO_4$ selected for the case of P106; however, fits to strictly $BaCrO_4$ (Cr(VI)) and Cr_2O_3 (Cr(III)) were employed in the PVC samples for convenience. Among other details, Table 10-2 presents the Cr(VI) species fractions determined by XES and their corresponding uncertainties. This final error estimate was calculated by propagating the magnitude of each source of bias reported in Table S1. Note that Table 10-2 also contains an estimate of the Cr(VI) mass fraction which was calculated from the estimated Cr(VI) species fraction and the total Cr mass fraction known from the preparation procedure or certified value for each material. When the Cr(VI) mass fraction is desired and the total Cr mass fraction is unavailable, this technique would require determination of total Cr by an appropriate method, such as XRF or inductively-coupled plasma optical emission spectrometry (ICP-OES).

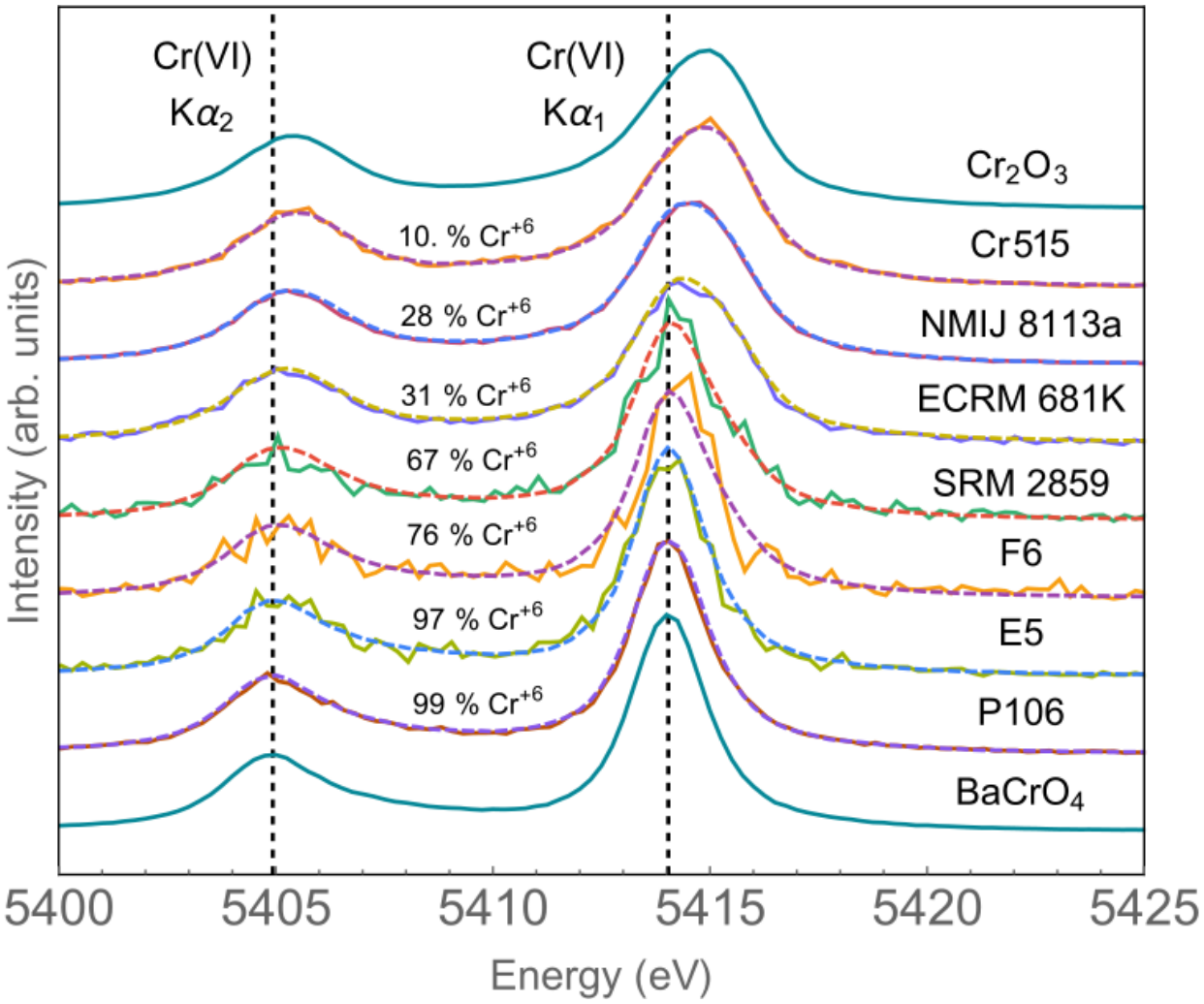

Fig. 10-2: Vertically offset Cr Kα XES spectra of plastics bracketed by compounds of pure-end member species (trivalent Cr_2O_3, top; hexavalent $BaCrO_4$, bottom). The measured spectrum for each plastic is shown along with the fit (dashed) provided by a least-squares regression analysis and the percent Cr(VI) determined from the fit. The first 10 eV and last 15 eV, which were collected to properly correct for background, are omitted. Note that all spectra are background corrected and integral normalized. For ease of reference, vertical dashed lines pass through the center of the Cr $K\alpha_1$ and $K\alpha_2$ peaks in $BaCrO_4$.

Table 10-2: The species fractions determined by XAFS and XES are presented along with total integration times for the latter. The Cr(VI) mass fraction was calculated from the Cr(VI) species fraction and total Cr mass fraction. In the case of E5 and F6, the results of an interlaboratory study facilitated by IEC TC 111 to determine the hexavalent chromium content via colorimetric analysis[43] are also included. Uncertainty estimates provided for the Cr(VI) mass fractions by XES are combined standard uncertainties including the uncertainty of the assigned total Cr value and the uncertainty of the found Cr(VI)/Cr ratio. All uncertainty values represent one standard deviation.

Sample	Cr(VI)/Cr from Preparation (%)[(b)]	Cr(VI)/Cr by Colorimetry (IEC 62321-7-2) (%)	Cr(VI)/Cr by XAFS (%)	Cr(VI)/Cr by XES (%)	Integration Time in XES (h)	Cr(VI) Mass Fraction by XES (mg/kg)
P106	100	-	100.0 ± 1.6	99.4 ± 2.5	86.1	250.9 ± 7.2
E5	100	73.6	-	96.8 ± 3.8	5.3	1680 ± 180
F6	100	63.	-	75.9 ± 6.6	5.3	508 ± 67
SRM 2859	100	-	-	67.0 ± 4.5	5.3	480. ± 33
EC681k	24.6	-	22.4 ± 1.8	30.5 ± 3.6	73.3	30.5 ± 3.7
CRM 8113a	25.1	-	30.3 ± 1.2	28.1 ± 3.5	44.4	265 ± 33
Cr515	0	-	3.1 ± 0.5	10.2 ± 4.3	30	52 ± 22
SRM 2861[(a)]	100	-	-	0		0

[(a)] See Supplemental Information for an explanation of this result.

[(b)] See text for discussion of interconversion during preparation.

The Cr(VI) species fractions measured by other spectroscopic techniques, including XAFS, are shown in Table 10-2. Furthermore, representative results of the fits in the near-edge region of

the XAFS spectra are shown in Figure 10-3, while the remaining fitted systems are presented in Figure S2. In general, the XAFS and XES methods are consistent with each other and with known preparation conditions. However, the XES results overestimate the Cr(VI) content with respect to XAFS in the limit of strictly trivalent Cr, as in Cr515. This can be explained by differences between the collected plastic sample's spectrum and that of the reference. The fit procedure is then unable to relax the fit onto the strictly trivalent case and consequently overestimates the present Cr(VI) content. This can be seen in greater detail in Table S2, which shows using Cr(III) benzoylacetonate as the trivalent fit component leads to a significantly larger estimation of the Cr(VI)/Cr species fraction than using Cr(III) oxide as the trivalent reference compound. On the other hand, iteratively displacing the position of the reference compound spectra, as in Table S1, leads to minimal changes in the resulting Cr(VI)/Cr species fraction. This suggests that either XES analysis does in fact overestimate Cr(VI) content in the strictly trivalent case or the electronic structure of the measured trivalent chromium is no longer well represented by Cr(III) benzoylacetonate.

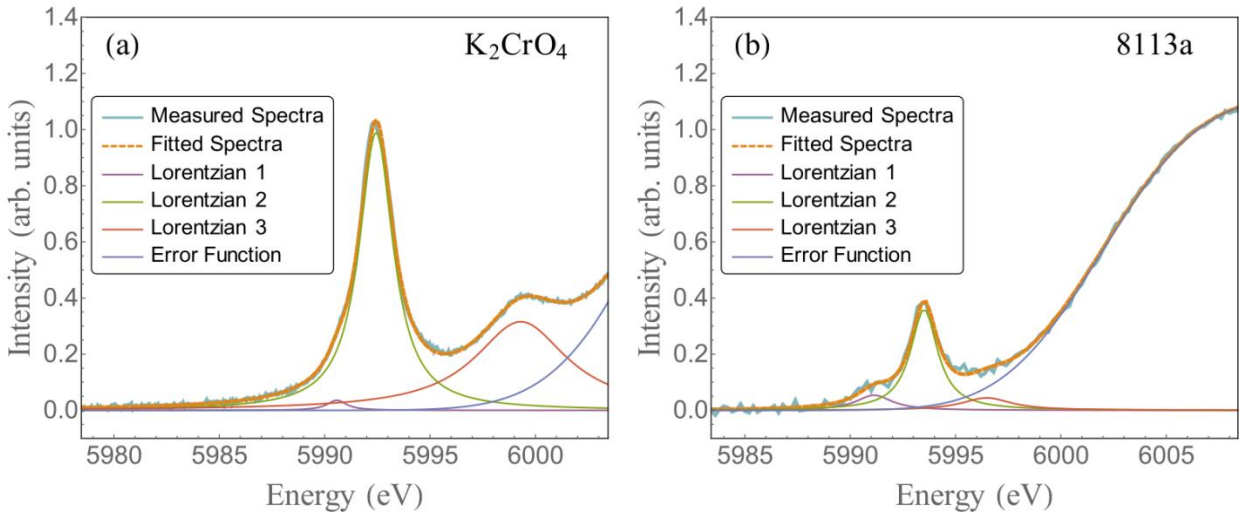

Fig. 10-3: The near-edge region of: (a) the XAFS spectra of the hexavalent reference, potassium chromate, and (b) CRM 8113a, a certified reference material developed for heavy metal analysis with respect to RoHS directives. Also shown are the acquired fits and their components.

A similar bias is observed at low Cr(VI) content in the XAFS results where the intensity of the peak nominally assigned to a 1s → 3d transition is related to the presence of Cr(VI). Additional peaks are present in the pre-edge region, including a peak on the low energy side of the transition of interest. As noted by Szulcewski *et al.*,[53] this peak becomes particularly noticeable in predominantly Cr(III) samples. Distinguishing these peaks, as well as reliably fitting a peak to a feature of now minimal intensity, thus complicates the fit procedure at low Cr(VI) content. Furthermore, strictly hexavalent Cr sources were employed in the production of materials E5, F6, SRM 2859, and SRM 2861, yet the XES measurements often reveal these materials to be reduced and to a lesser degree than reported by colorimetric analysis. Likely physical sources of reduction include processing and extrusion at 175 °C, the presence of Sb in F6 and SRM 2861, and the presence of stabilizer and plasticizer compounds in SRM 2859 and SRM 2861,[2,43] while species interconversion or incomplete extraction during preparation for colorimetric analysis can contribute to under-estimation of Cr(VI).

As a final point of data analysis, it is useful to evaluate the residuals of the fits, see Figure S3. The deviations from Poisson noise are minimal, and are of the same general scale as the intrafamily variations of the Cr(III) and Cr(VI) reference materials, presented in Fig. S1. Furthermore, Table S1 shows that, although the choice of reference is a significant contribution to the net error in an estimate of the hexavalent species fraction, it amounts to not more than 2 % to 4 % relative uncertainty. These results and the spectra shown in Fig. 1 provide evidence that Cr Kα emission is relatively insensitive to electronic structure differences among materials of the same oxidation state, as is required for robust species fractionation estimates.

The above results present a strong case in favor of Cr Kα XES as a potential standard test method for the determination of Cr(VI) species fractions in plastics. Several future directions are needed to assess the viability of this proposal and to potentially further improve on the current methodology. First, the Cr Kβ diagram line should be investigated at high energy resolution for the purpose of quantitatively analyzing the Cr(VI) content in the manner of Malherbe *et al.*[25] Second, efforts to extend the practical integration time for PVC materials should explore the use of larger sample areas, cryogenic temperatures, and replicates. Third, the required integration times listed in Table 10-2 are, at present, prohibitively long for some applications, yet measurements could be greatly accelerated in several ways. First, the tube was operated at only 8 W. It is nearly the *lowest* powered analytical XRF tube commercially available. Commercial XRF spectrometers come with tube power as high as 4 kW, and even standard 50 W and 100 W XRF-style tubes promise 5x to 10x improvements in measurement time that would suffice for greatly improved throughput. The measurements could be further expedited by increasing the collection solid angle by multiplexing several analyzers or by switching to newly-available 0.5 m spherical optics.[57]

4. Conclusion

The Cr(VI) species fraction has been measured via XES and XAFS analysis in a variety of plastic certified reference materials and research samples with at most 8.1 % disagreement between the methods. It was demonstrated that XES may be applied to plastics spanning a range of polymer formulations, Cr mass fractions, and Cr(VI) species fractions. The method is non-destructive, requires minimal sample prep, and may be performed with laboratory-based instrumentation. This technique provides quantitative measurements of the Cr(VI) species fraction with uncertainties sufficiently small to permit the application of this procedure toward regulatory compliance concerns. For the above reasons, laboratory-based Cr Kα XES measurements have the potential to become industrially relevant as a standard test method.

5. Acknowledgments

This material is based in part upon work supported by the State of Washington through the University of Washington Clean Energy Institute and by the U.S. Department of Energy through the Chemical Science and Engineering Division of Argonne National Laboratory.

Supporting Information Available: Photosensitivity analysis, uncertainty overview, depiction of instrumentation. All information is available from Analytical Chemistry.

Disclaimer: Certain commercial items are identified in this document to adequately specify experimental procedures. Such identification does not imply recommendation or endorsement by the National Institute of Standards and Technology, nor does it imply the materials or equipment identified are necessarily the best available for the purpose.

6. References

(1) Saha, R.; Nandi, R.; Saha, B. *J Coord Chem* **2011**, *64*, 1782-1806.
(2) Kim, Y. S.; Choi, Y. R.; Kim, J. S.; Ko, J. H.; Park, T. J.; Heo, S. B.; Lim, H. B. *Journal of Analytical Atomic Spectrometry* **2015**, *30*, 225-231.
(3) *Official Journal of the European Union* **2011**, *54*, 88-110.
(4) Schulte, P. A.; Rinehart, R.; Okun, A.; Geraci, C. L.; Heidel, D. S. *J Safety Res* **2008**, *39*, 115-121.
(5) Pflaum, R. T.; Howick, L. C. *J Am Chem Soc* **1956**, *78*, 4862-4866.
(6) Malherbe, J.; Isaure, M. P.; Seby, F.; Watson, R. P.; Rodriguez-Gonzalez, P.; Stutzman, P. E.; Davis, C. W.; Maurizio, C.; Unceta, N.; Sieber, J. R.; Long, S. E.; Donard, O. F. X. *Environ Sci Technol* **2011**, *45*, 10492-10500.
(7) Frommer, J.; Nachtegaal, M.; Czekaj, I.; Weng, T. C.; Kretzschmar, R. *J Phys Chem A* **2009**, *113*, 12171-12178.
(8) Farges, F. *Phys Chem Miner* **2009**, *36*, 463-481.
(9) Szulczewski, M. D.; Helmke, P. A.; Bleam, W. F. *Environ Sci Technol* **2001**, *35*, 1134-1141.
(10) Ohata, M.; Matsubayashi, N. *Spectrochim Acta B* **2014**, *93*, 14-19.
(11) Goodarzi, F.; Huggins, F. E. *Journal of Environmental Monitoring* **2001**, *3*, 1-6.
(12) Jiao, F.; Wijaya, N.; Zhang, L.; Ninomiya, Y.; Hocking, R. *Environ Sci Technol* **2011**, *45*, 6640-6646.
(13) Wells, H. C.; Sizeland, K. H.; Edmonds, R. L.; Aitkenhead, W.; Kappen, P.; Glover, C.; Johannessen, B.; Haverkamp, R. G. *Acs Sustain Chem Eng* **2014**, *2*, 1864-1870.
(14) Fandeur, D.; Juillot, F.; Morin, G.; Olivi, L.; Cognigni, A.; Webb, S. M.; Ambrosi, J. P.; Fritsch, E.; Guyot, F.; Brown, G. E. *Environ Sci Technol* **2009**, *43*, 7384-7390.
(15) Johnson, A. S.; Miseikis, L.; Wood, D. A.; Austin, D. R.; Brahms, C.; Jarosch, S.; Strüber, C. S.; Ye, P.; Marangos, J. P. *Structural Dynamics* **2016**, *3*, 062603.
(16) Mortensen, D. R.; Seidler, G. T.; Ditter, A. S.; Glatzel, P. *Journal of Physics: Conference Series* **2016**, *712*, 012036.
(17) Németh, Z.; Szlachetko, J.; Bajnóczi, É. G.; Vankó, G. *Review of Scientific Instruments* **2016**, *87*, 103105.
(18) Seidler, G. T.; Mortensen, D. R.; Remesnik, A. J.; Pacold, J. I.; Ball, N. A.; Barry, N.; Styczinski, M.; Hoidn, O. R. *Rev. Sci. Instrum.* **2014**, *85*, 113906.
(19) Seres, J.; Seres, E.; Landgraf, B.; Ecker, B.; Aurand, B.; Kuehl, T.; Spielmann, C. *Scientific Reports* **2014**, *4*, 4234.
(20) Kucukonder, A.; Sahin, Y.; Buyukkasap, E.; Kopya, A. *J Phys B-at Mol Opt* **1993**, *26*, 101-105.
(21) Mukoyama, T.; Taniguchi, K.; Adachi, H. *Physical Review B* **1986**, *34*, 3710-3716.
(22) Tamaki, Y. *X-Ray Spectrometry* **1995**, *24*, 235-240.
(23) de Oliveira, L.; Antunes, A. M.; Bueno, M. I. M. S. *X-Ray Spectrometry* **2010**, *39*, 279-284.
(24) Baydas, E.; Oz, E. *X-Ray Spectrometry* **2009**, *38*, 394-398.
(25) Malherbe, J.; Claverie, F. *Anal Chim Acta* **2013**, *773*, 37-44.
(26) de Groot, F. *Chemical Reviews* **2001**, *101*, 1779-1808.
(27) Bergmann, U.; Glatzel, P. *Photosynth Res* **2009**, *102*, 255-266.
(28) de Groot, F. *Coordin Chem Rev* **2005**, *249*, 31-63.
(29) Glatzel, P.; Bergmann, U. *Coordin Chem Rev* **2005**, *249*, 65-95.

(30) Ankudinov, A. L.; Elam, W. T.; Sieber, J. R.; Rehr, J. J. *X-Ray Spectrometry* **2006**, *35*, 312-318.
(31) March, A. M.; Assefa, T. A.; Bressler, C.; Doumy, G.; Galler, A.; Gawelda, W.; Kanter, E. P.; Németh, Z.; Pápai, M.; Southworth, S. H.; Young, L.; Vankó, G. *The Journal of Physical Chemistry C* **2015**, *119*, 14571-14578.
(32) Nilsson, A.; Pettersson, L. G. M. *Surface Science Reports* **2004**, *55*, 49-167.
(33) Deluigi, M. T.; de Groot, F. M. F.; Lopez-Diaz, G.; Tirao, G.; Stutz, G.; de la Vega, J. R. *J Phys Chem C* **2014**, *118*, 22202-22210.
(34) Deluigi, M. T.; Tirao, G.; Stutz, G.; Cusatis, C.; Riveros, J. A. *Chem Phys* **2006**, *325*, 477-484.
(35) Anklamm, L.; Schlesiger, C.; Malzer, W.; Grötzsch, D.; Neitzel, M.; Kanngießer, B. *Review of Scientific Instruments* **2014**, *85*, 053110.
(36) Dolgih, V. E.; Cherkashenko, V. M.; Kurmaev, E. Z.; Goganov, D. A.; Ovchinnikov, E. K.; Yarmoshienko, Y. M. *Nuclear Instruments and Methods in Physics Research* **1984**, *224*, 117-119.
(37) Hoszowska, J.; Dousse, J. C.; Kern, J.; Rhême, C. *Nuclear Instruments and Methods in Physics Research Section A: Accelerators, Spectrometers, Detectors and Associated Equipment* **1996**, *376*, 129-138.
(38) Kavčič, M.; Dousse, J. C.; Szlachetko, J.; Cao, W. *Nuclear Instruments and Methods in Physics Research Section B: Beam Interactions with Materials and Atoms* **2007**, *260*, 642-646.
(39) Kayser, Y.; Błachucki, W.; Dousse, J. C.; Hoszowska, J.; Neff, M.; Romano, V. *Review of Scientific Instruments* **2014**, *85*, 043101.
(40) Mantouvalou, I.; Witte, K.; Grötzsch, D.; Neitzel, M.; Günther, S.; Baumann, J.; Jung, R.; Stiel, H.; Kanngießer, B.; Sandner, W. *Review of Scientific Instruments* **2015**, *86*, 035116.
(41) Szlachetko, M.; Berset, M.; Dousse, J. C.; Hoszowska, J.; Szlachetko, J. *Review of Scientific Instruments* **2013**, *84*, 093104.
(42) Holden, W. M.; Hoidn, O. R.; Ditter, A. S.; Seidler, G. T.; Kas, J.; Stein, J. L.; Cossairt, B. M.; Kozimor, S. A.; Guo, J.; Ye, Y.; Marcus, M. A.; Fakra, S. *Review of Scientific Instruments* **2017**, *88*, 073904.
(43) *International Electrotechnical Commission* **2017**, Ed. 1. Report of the Fourth International Interlaboratory Study (IIS4). IEC 62321-7-2.
(44) Ma, L.; Feng, L.; Hioki, A.; Cho, K. H.; Vogl, J.; Berger, A.; Turk, G.; Macleod, S.; Labarraque, G.; Tong, W. F.; Schiel, D.; Yafa, C.; Valiente, L.; Konopelko, L. A.; Quetel, C.; Vermaercke, P.; Manzano, J. V. L.; Linsky, M.; Cort, E.; Tangpitayakul, S., et al. *Accreditation and Quality Assurance* **2010**, *15*, 39-44.
(45) Mortensen, D. R.; Seidler, G. T. *J Electron Spec* **2017**, *215*, 8-15.
(46) Engelhard, M.; Krishna, A.; Kulkarni, P.; Lee, C.-Y.; Baer, D. *Surface Science Spectra* **2003**, *10*, 57-66.
(47) Militello, M. C.; Gaarenstroom, S. W. *Surface Science Spectra* **2003**, *10*, 127-136.
(48) Mortensen, D. R.; Seidler, G. T.; Kas, J. J.; Govind, N.; Schwartz, C. P.; Pemmaraju, S.; Prendergast, D. G. *Physical Review B* **2017**, *96*, 125136.
(49) Ravel, B.; Newville, M. *Journal of Synchrotron Radiation* **2005**, *12*, 537-541.
(50) Bajt, S.; Clark, S. B.; Sutton, S. R.; Rivers, M. L.; Smith, J. V. *Analytical Chemistry* **1993**, *65*, 1800-1804.
(51) Lytle, F. W.; Greegor, R. B.; Bibbins, G. L.; Blohowiak, K. Y.; Smith, R. E.; Tuss, G. D. *Corrosion Science* **1995**, *37*, 349-369.

(52) Sutton, S. R.; Jones, K. W.; Gordon, B.; Rivers, M. L.; Bajt, S.; Smith, J. V. *Geochim Cosmochim Ac* **1993**, *57*, 461-468.
(53) Szulczewski, M. D.; Helmke, P. A.; Bleam, W. F. *Environ Sci Technol* **1997**, *31*, 2954-2959.
(54) Lytle, F. W.; Greegor, R. B.; Panson, A. J. *Phys Rev B* **1988**, *37*, 1550-1562.
(55) Calas, G.; Petiau, J. *Solid State Communications* **1983**, *48*, 625-629.
(56) Kendig, M. W.; Davenport, A. J.; Isaacs, H. S. *Corrosion Science* **1993**, *34*, 41-49.
(57) Rovezzi, M.; Lapras, C.; Manceau, A.; Glatzel, P.; Verbeni, R. *Review of Scientific Instruments* **2017**, *88*, 013108.
(58) Certificate of Analysis for SRM 2859; National Instite of Standards and Technology, Gaithersburg, MD; https://www-s.nist.gov/srmors/certificates/2859.pdf; accessed December 2017.
(59) Certificate of Analysis for SRM 2861; National Institute of Standards and Technology, Gaithersburg, MD; https://www-s.nist.gov/srmors/certificates/2861.pdf; accessed December 2017.
(60) *European Reference Materials* **2007**, *Report EUR 22784 EN*.
(61) Ohata, M.; Kurahashi , M.; Hioki, S. *Bunseki Kagaku* **2008**, *57*, 417-426.

Chapter 11. Double-Ionization Satellites in the X-ray Emission Spectrum of Ni Metal

Originally published as: R. A. Valenza, E. P. Jahrman, J. J. Kas, and G. T. Seidler. Phys Rev A **96** (3), 032504 (2017). Among other details, E. P. Jahrman designed the sample rotation stage, helped perform the X-ray measurements and analysis, collected a large portion of the necessary background information, and wrote a meaningful portion of the text.

We report measurements of the nonresonant x-ray emission spectroscopy (XES) from Ni metal in an energy range spanning the Kβ diagram line, valence-to-core emission, and double-ionization (DI) satellites that appear beyond the single-particle Fermi level. We make special use of a laboratory-based x-ray spectrometer capable of both x-ray emission and x-ray absorption measurements to accurately align the XES and x-ray absorption spectra to a common energy scale. The careful alignment of energy scales is requisite for correction of the strong sample absorption of DI fluorescence above the Ni K-edge energy. The successful correction of absorption effects allows a determination of the branching ratios for the [1s3d], [1s3p], [1s2p] and [1s2s] satellites with respect to their corresponding diagram lines. We compare our results with other work, finding good agreement with prior experiments and with theoretical calculations in the multi-configuration Dirac-Fock framework.

1. Introduction

Multi-electron transitions caused by the absorption of single x-ray photons were first observed a century ago by Siegbahn and Stenstrom[1] before further study by researchers including Richtmyer[2, 3] and Druyvesteyn[4]. Since then, a range of phenomena have been attributed to these processes, including numerous features in nonresonant x-ray emission spectroscopy (XES)[5-7], low energy satellites in x-ray photoelectron spectroscopy (XPS)[8-11], and discontinuities in x-ray absorption fine structure spectra[12].

The simplest model for multi-electron excitations employs the shake process within the sudden approximation. Within this model, the incident photon first induces the emission of a single photoelectron, causing all remaining electrons to subsequently experience a change in the central potential due to the reduction in screening accompanying the creation of a core hole. Second, the reduction in screening prompts the occupied orbitals to relax, yielding an imperfect overlap between the initial and final wavefunctions. Finally, this perturbation results in a nonzero probability that a second electron will undergo a monopole excitation to an unoccupied bound state (a shake-up process, 'SU') or to a continuum state (a shake-off process, 'SO'). An extensive record of theoretical studies of shake probabilities in the sudden approximation[13-17] was motivated by the 1941 observation of Migdal and Feinberg[18, 19] that the rapid change in nuclear potential following β decay results in an appreciable probability of ionization in each of the atom's occupied orbitals. Recently, *ab initio* relativistic Dirac-Fock multiplet calculations including configurations with spectator holes arising from shake processes have enabled the accurate reconstruction of the emission spectra of Cu, Sc, and Ti[20-22]. The best agreement with experiment is achieved in the multi-configuration framework advocated by Chantler, Lowe, and

Grant[23-25], implementing the procedure for transition probability calculations using nonorthogonal orbitals developed by Olsen *et al*[26].

Alternative models have been proposed to explain spectral features without the inclusion of shake effects. Of particular note are conduction-band collective excitations[27], exchange[28], surface plasmons[29], and the (e,2e)-like electron impact half collision knockout (KO) process[30]. As might be expected, progress toward understanding these spectral features has been incrementally provided by numerous experimental and theoretical studies. It is now known that the KO process, while measurable in many studies, becomes negligible at high energy excitations where photoabsorption approaches the asymptotic limit of shakeoff[31, 32], as is the case in this work. Also, the surface plasmon hypothesis has been called into question by Karis *et al*[33] in a careful XPS study of metallic Ni.

Irrespective of the microscopic description, double ionization (DI) is by far the most probable multi-electron transition[16] in typical experiments and, as a result, is the most commonly studied. More recently, a greater understanding of DI transitions has motivated several novel research directions including the emergence of the spin-flip forbidden $K\alpha_1^h$ ($^3P_1 \rightarrow {}^1S_0$) transition as a highly sensitive indicator of the transition from the LS coupling scheme to intermediacy[30, 34], experiments probing the variation of fundamental constants in space-time[35], and tests of the Breit interaction in quantum electrodynamics[36-38].

That said, much of the interest in multi-electron transitions stems from the observation that for weak interactions, such as those involving photoionization, the probability of DI events greatly exceeds predictions that treat both electrons as independent[39]. Consequently, the ejection of multiple electrons depends strongly on many-electron interactions[40] and can thus provide a

means to understand intra-atomic electron correlations and verify theoretical methods as they are developed.

It is important to note that the DI process is not restricted to the high energy isothermal region, but is also present in the adiabatic regime close to the double-ionization threshold. In this limit, the potential of the first photoelectron during the second ionization cannot be ignored and is addressed, for example, via time-dependent perturbation theory[41, 42]. The adiabatic regime, and especially the transition from adiabatic to isothermal regime, has benefitted from many outstanding experimental efforts[34, 43, 44]. In such studies, satellite intensities at various excitation energies are fit by optimizing the parameters required by the Thomas[41], Roy[45], Roy-2[46], or Vatai[47] model, with the Thomas model the most common of the four. Nevertheless, it should be noted that these models are not *ab inito* treatments[48]. For example, only the Vatai and Roy model incorporate the Coulomb interaction as the mechanism of excitation while the Thomas and Roy-2 models simply postulate that the time dependence is described by an analytic function and include the interaction Hamiltonian in a parameter representing the asymptotic value given by the sudden approximation.

In the present study, we investigate the DI x-ray emission satellites occurring above the single-electron Fermi level of Ni in the isothermal limit of high-energy excitation. The various DI XES peaks observed above the Fermi level are analyzed with an eye toward establishing a protocol for reliable determination of the branch ratio of DI features to their corresponding diagram line fluorescence. These branch ratios serve as a natural benchmark for comparison to theory. In addition, several aspects of our experimental approach may prove useful in the future, particularly a method to align XES and XAFS spectra to a common energy scale when using a laboratory-based spectrometer and a demonstration of the necessary corrections for the sample's

internal absorption that otherwise alter the intensity of DI XES features appearing above the single-particle Fermi level.

This manuscript continues as follows. First, in Section II, we describe the experimental details. This includes a description of instrumentation and data collection protocol, a detailed discussion of the energy-dependent correction for self-attenuation effects, and our method for obtaining absorption and emission spectra on the same energy scale. We argue that these latter two issues are critical for obtaining accurate estimates of the relative branch ratios of multi-electron satellites above the single-particle Fermi level. Next, in Section III, we present and discuss the results of the study. We give special attention to the energies and branch ratios of the several observed DI features and to their comparison with theory. Finally, in Section IV, we conclude.

2. Experimental Procedure

A. Laboratory spectrometer

Our group has recently developed laboratory-based (i.e., non-synchrotron) instrumentation for XES and x-ray absorption fine structure (XAFS) measurements[49-52]. Energy scanning, whether for XAFS or for XES, uses a scissors-style monochromator that symmetrically moves the source and detector while maintaining the delicate angular-orientation of the spherically bent crystal analyzer (SBCA) needed for alignment. The careful use of internal shielding together with the added rejection provided by the energy-dispersing silicon drift detector (Amptek SDD-123) results in exceptionally low backgrounds, allowing for clear observation of the DI features without use of any background subtraction in the measured XES spectra.

In the XAFS implementation of the instrument used here[52], photons from the x-ray tube source are monochromatized and refocused at the detector by a synchrotron-quality SBCA, providing useful flux for transmission-mode studies with 1-eV or finer energy resolution. The XES implementation benefits from the same inherent high resolution, but differs in that nonresonant excitation of a material is accomplished by direct illumination of the sample behind an entrance slit. The entrance slit, then, establishes an effective source on the Rowland circle and stabilizes instrument performance[50]. Additionally, direct illumination by the x-ray tube, whose output spectrum includes bremsstrahlung and characteristic fluorescence lines, is a highly efficient source of excitation as all photons above the Fermi level can create a core hole in the sample. While the x-ray tube (Moxtek Au anode) has 10 W maximum electron beam power, the close approach of the sample to the anode results in a core-hole generation rate that is intermediate between those of a monochromatized bending magnet and monochromatized insertion device beamline at a 3rd generation synchrotron[50, 52].

B. Implementation of a common energy scale for emission and absorption

In the section below (II.C), we describe a method to correct for the strong absorption of the above-Fermi level DI emission by the sample itself, *i.e.*, because this x-ray emission has intensity at and above the absorption edge. This method requires, however, that the XES and XANES spectra be reliably placed onto the same energy scale; otherwise the steep rise in absorption at the edge will not be properly located and result in systematic error. Fortunately, we can make use of a novel feature of our laboratory-based instrument; its ability to transition simply between XES and XANES measurements[52]. Typically, this transition involves a reconfiguration of components along the Rowland circle, which has the possibility of introducing a shift in energy scale due to imperfect rigidity of the support structure for the source stage and

especially the spectrometer entrance slit. We address this issue with a simple, localized procedure for energy alignment across the various measurements needed to correct XES spectra for the phenomenon of self-attenuation.

In Fig. 1 we demonstrate our procedure to obtain a XANES and XES spectrum on the same energy scale. In each subfigure, the SBCA is used for energy selection and focusing, and energy scanning is done by moving both the sample and detector symmetrically around the Rowland circle. First, in Fig. 1a, we show a typical XES geometry where the entire spectrum of the x-ray tube source illuminates the sample, causing it to fluoresce. Next, we place the sample in front of the detector and move the source onto the Rowland circle, as shown in Fig. 1b. for the XANES configuration. Here, we measure transmission through the sample to obtain the absorption cross section, μ, via the Beer-Lambert Law. The standard procedure is to then set the global energy scale by aligning the measured absorption edge to database values or XANES spectra recorded at a beamline or available in the HEPHAESTUS software package[53]. However, the finite rigidity of the spectrometer means that the reconfiguration of components can lead to a shift in energy scale between the XES and the XANES measurements.

Finally, an intermediate, hybrid configuration (Fig. 1c) helps resolve this difficulty by moving the sample to the opposite side of the Rowland circle so that it is in front of the source, but behind the entrance slit. As all components except the sample have been held fixed, we have high confidence that our energy scale has remained unaltered between the XAFS and hybrid configurations. The hybrid-configuration spectrum contains both an absorption edge (as we are measuring transmission through the sample) and emission peaks (as the sample is on the source side of the Rowland circle and is strongly excited by the x-ray tube in this geometry). The absorption edge can be aligned with the previously measured XANES spectrum, which is set to a

global energy scale, and the observed fluorescence peaks in the hybrid spectrum can be used to shift the XES spectrum from the configuration of Fig. 1a onto the necessary common energy scale.

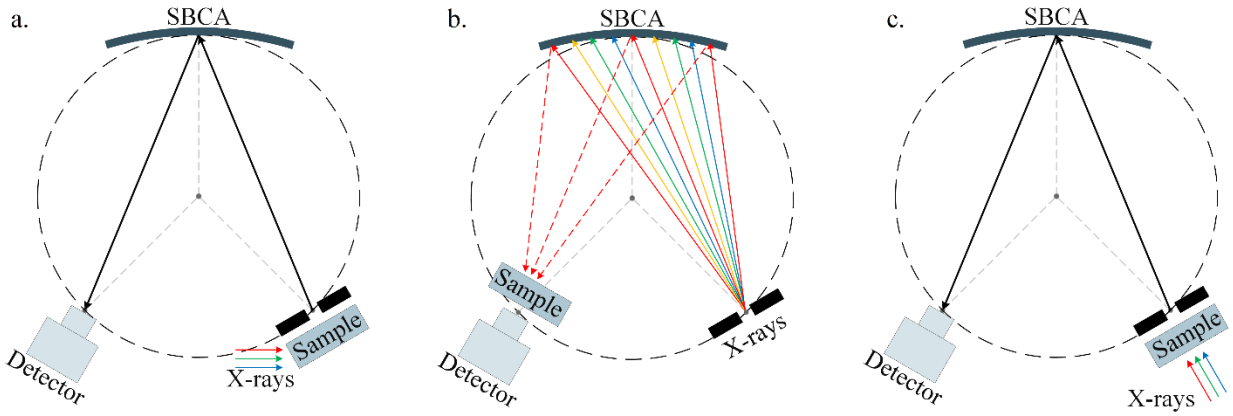

Fig. 11-1: Experimental Diagrams for Energy Scale Reproduction — Above are standard Rowland circle geometries used in (a) x-ray emission and (b) x-ray absorption fine structure measurements. An intermediate hybrid geometry, (c), is used to establish a common energy scale across measurements. This is necessary to correct for sample absorptive effects in XES measurements.

C. Correction for combined geometric and absorptive effects

In this subsection, we describe the correction for geometric and absorptive effects to the intensity of the above Fermi level DI XES relative to the usual single-excitation diagram lines. These absorptive effects are known to influence the shape of spectral features in XES[54]. Indeed, other authors have taken steps to correct for sample absorption, particularly when deemed as requisite for reporting a quantitative result, such as for measurements of the magnetic circular dichroism of Gd films measured via XES[55]. In the present case, the intensity of spectral features above the Fermi level is strongly suppressed by absorptive effects.

In Fig. 2, we show a typical sample geometry for XES. Incoming photons from the tube source travel a distance $z/\sin(\alpha)$ before being absorbed by the sample, causing the emission of photons of energy E_e to fill the core-hole. These emitted photons can then be reabsorbed by the sample during their exit path over the distance $z/\sin(\beta)$. When the parameter z is integrated over the sample thickness t, we obtain the form of the measured spectrum, $I(E_e)$,

$$I(E_e) = \frac{\Omega}{4\pi} I_o(E_i)\epsilon(E_e|E_i)\frac{\mu(E_i)}{\mu(E_i) + \mu(E_e)\frac{\sin(\alpha)}{\sin(\beta)}}\left(1 - \exp\left\{-t\left(\frac{\mu(E_i)}{\sin(\alpha)} + \frac{\mu(E_e)}{\sin(\beta)}\right)\right\}\right), \quad (1)$$

where μ is the attenuation coefficient, as measured via XANES, $I_o(E_i)$ is the intensity distribution of photons incident on the sample, Ω is the solid angle of the detector, and $\epsilon(E_e|E_i)$ is the ideal emission spectrum, representing the probability that an emission energy, E_e, is measured given an incident photon of energy, E_i. However, for nonresonant excitation, the emission spectrum is independent of the incident photon energy, *i.e.* $\epsilon(E_e|E_i) = \epsilon(E_e)$, allowing us to invert Eq. 1. to obtain an absorption-corrected spectrum,

$$\epsilon(E_e) \propto \frac{I(E_e)}{I_o(E_i)}\frac{\mu(E_i)\sin(\beta) + \mu(E_e)\sin(\alpha)}{\mu(E_i)\sin(\beta)}\left(1 - \exp\left\{-t\left(\frac{\mu(E_i)}{\sin(\alpha)} + \frac{\mu(E_e)}{\sin(\beta)}\right)\right\}\right)^{-1}. \quad (2)$$

The right-hand side may then be numerically integrated with respect to E_i across the range of incident photon energies. We found the result to be insensitive to integration bounds and consequently integrated from 8310 eV to 8370 eV for convenience.

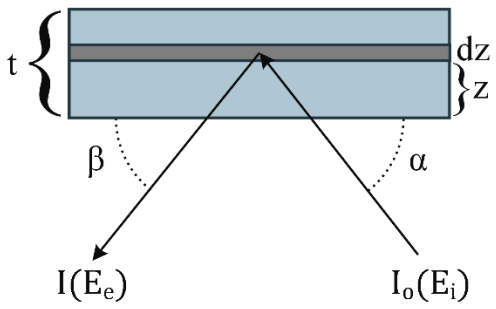

Fig. 11-2: Sample Geometry — X-ray photons of energy E_i from a source spectrum of intensity $I_o(E_i)$ are incident at an angle α relative to the face of the sample of thickness t. A detector, placed at an angle β from the sample's face, measures an emission spectrum $I(E_e)$.

D. Final Experimental Parameters

Following the above strategies, we collected XANES, XES, and hybrid-spectrum measurements from a 6-□m thick foil of Ni metal acquired from EXAFS Materials. The operating parameters of the x-ray tube source were 40 kV and 200 μA. The overwhelming majority of incident photons that excite Ni 1s electrons, including both the fluorescence lines from the Au anode and the relevant part of the bremsstrahlung spectrum, are high enough in energy that our results are overwhelmingly in the isothermal limit. A manual rotation stage was integrated into the sample mount design to allow us to control the independent variables α and β or, equivalently, the effective thickness of the sample.

XES spectra were collected at sample angles α of 44 deg and 64 deg. XAFS and hybrid measurements were conducted per the procedure outlined in Section II.B. All spectra were collected in 0.25-eV increments. Multiple scans for each category of measurement were summed to provide total integration times of: 150 s per step for measurement of the incident intensity (no sample, XANES configuration); 930 s and 310 s per step, respectively, for valence

XES with $\alpha = 44$ deg and $\alpha = 64$ deg; 620 s per step for the hybrid configuration; and 930 s per energy step for the XAFS configuration. To reduce overall measurement times, detailed valence XES scans spanned a range in energy from 8310 to 8380 eV and were later normalized to a single XES spectrum covering the full energy range from 8240 to 8380 eV.

E. Determination of Branch Ratios

Phenomenological fits were computed using the routines available in the *BlueprintXAS* software package[56, 57]. *BlueprintXAS* uses a Monte-Carlo search method to determine the starting points for the chosen evaluation model. Specifically, an array of parameter combinations spanned throughout the solution space is randomly generated, and the combination with the smallest sum of squared errors (SSE) is selected as input for the non-linear least-squares fitting procedure. This process is repeated multiple times to generate many independent fits. From this set, the fit with the smallest SSE is selected. While this process of parameter and fit selection does reduce user-bias, it can lead to large error estimates if the limits on the parameters are under-constrained. This was the case in this study, which involved several overlapping spectral features.

For the evaluation models, Pseudo-Voigt functions were used to fit the $K\beta_{1,3}$, $K\beta_{2,5}$, and multi-electron spectra, with Radiative Auger emission being accounted for by including an additional function as described by Enkisch *et al*[58]. The $K\beta_{1,3}$, which lies below the Ni absorption edge and thus does not require a self-attenuation correction, was used across measurements to preserve the overall intensity scale. Areas of the multi-electron peaks were then calculated and compared with relevant diagram lines to determine branching ratios. Estimating uncertainties in the branching ratio involved approximating the pseudo-Voigt integral per a method described by Lenz and Ayres[59].

3. Results and Discussion

The spectra collected via the energy alignment procedure outlined in Section II.B. are shown in Fig. 3. The resultant difference spectrum, which shares an energy scale with our XANES measurements, provides us with an emission peak with which we can align our XES spectra – thus ensuring a common energy scale across all our measurements. Here, we find that a one-time energy shift of ~8 eV is necessary. In Fig. 4, we show the Ni XES spectra measured at two different sample rotation angles together with the same spectra after correction for sample absorption effects using the method outlined in Section II.C., this results in as much as a factor-of-two correction to the measured spectra intensity above the Fermi level. The good agreement between the corrected results at the two different sample angles confirms the validity of our treatment of sample absorption effects.

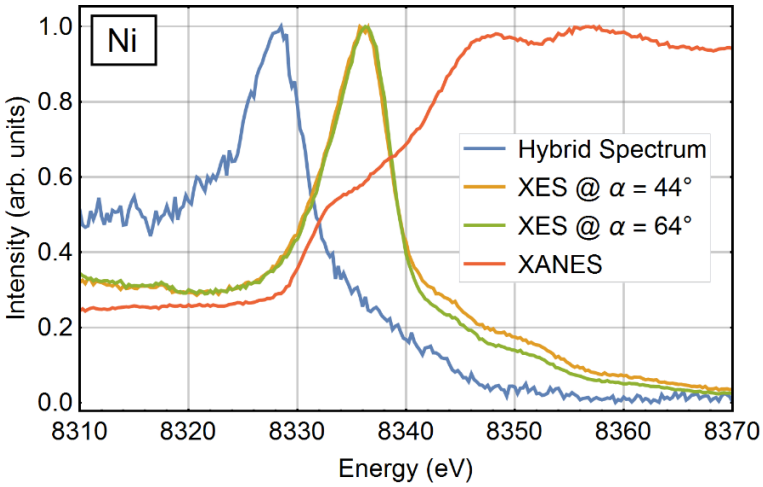

Fig. 11-3: Measured Spectra from Various Sample Geometries — Spectra from each of the three experimental configurations of Fig. 1 with the hybrid and XANES spectra energy corrected. An energy shift of 8.75 eV aligned the hybrid and XANES spectra to the energy scale established at the synchrotron. A comparable energy shift was also needed to align the XES data to the new, common energy scale.

The results in Fig. 4 show several clear satellites in the spectrum above the $K\beta_{2,5}$. We identify these peaks with the Z+1 model. The approach is an established tool for the treatment of multi-electron features in arenas such as L-edge EXAFS in rare-earth minerals[60], two- and three-electron excitations in Kr XANES[61-63], and emission spectroscopy of transition metals[20, 44, 58, 64]. Despite documented shortcomings[65], many of which it shares with multiplet calculations[8, 62], this approach typically predicts accurate values of excitation thresholds and emission satellites. Specifically, satellite energies are calculated with

$$E_{\gamma'} = E_{\gamma} + BE_{Z+1} - BE_{Z}, \qquad (3)$$

where $E_{\gamma'}$ is the energy of the satellite, E_{γ} is the energy of the diagram line, and BE_{Z+1} and BE_{Z} are the binding energies of the electrons emitted to form spectator holes in the fully screened Z and Z+1 systems, respectively. This process yields excellent agreement between the locations of

satellites predicted by the Z+1 model and the peak locations in Fig. 4-5. Having identified the various DI features, we then fit the corrected spectrum using the method described in Section II.E. We show the consequent fit in Fig. 5. A comparison between predicted and measured satellite positions is presented in Table 11-1 where a method, motivated by the convention of Druyvesteyn[4], was adopted for the [1snp] satellite by calculating the weighted average of the $np_{1/2}$ and $np_{3/2}$ binding energies according to population. The extracted branch ratios are presented, and compared with past experimental and theoretical results in Table 11-2. These literature values were reported as probabilities, which we converted to branching ratios by dividing the satellite probability by unity less the shake probability.

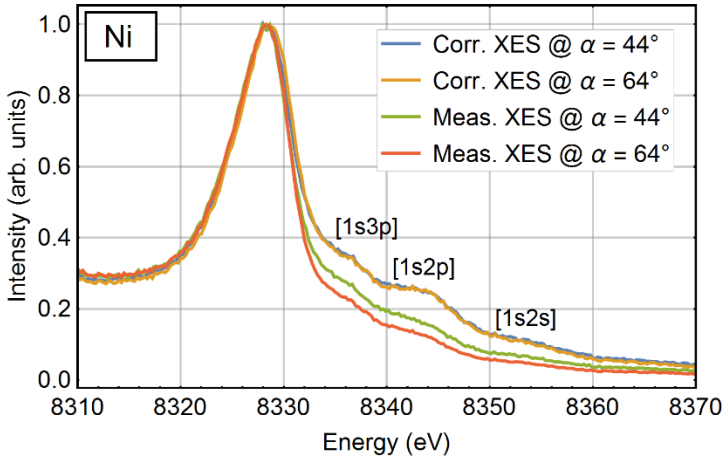

Fig. 11-4: Absorption-Corrected Nickel Valence Emission — This figure shows both the uncorrected and corrected spectra of Ni valence emission. Obtaining the correct intensity of multi-electron peaks, which are identified via the *Z*+1 approximation, is critical for theory comparison.

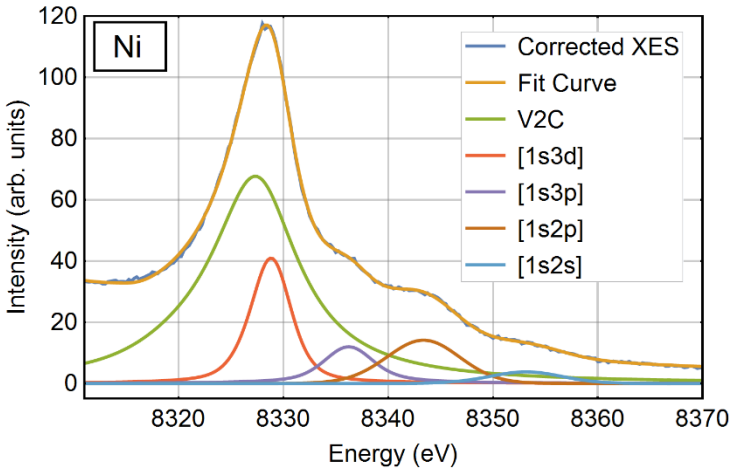

Fig. 11-5: Phenomenological Fits to Ni Multi-Electron Peaks — This figure shows the multiple pseudo-Voigt functions that were used to fit to each of the multi-electron emission peaks. These peaks' areas were used to determine the branching ratios given in Table 11-2. Not shown here are the fitted radiative Auger and $K\beta_{1,3}$ features, which also contribute to the determination of the final fit.

Table 11-1: Comparison between measured satellite energies and values predicted by the Z+1 model, referenced to the energy of the VTC diagram line.

Multi-electron Transition	Z+1 (eV)	Observed (eV)
[1s3p]	9.0	9.1 ± 0.5
[1s2p]	16.9	16.3 ± 0.5
[1s2s]	24.2	26.0 ± 0.5

Table 11-2: Comparison between experimental and predicted branching ratios (%) of the identified DI peaks and their corresponding diagram line intensity. Literature values were converted from probabilities to branching ratios following the procedure outlined in Section III.

DI Transition	Diagram Line	Mukoyama[17] (theory)	Hölzer[66] (exp.)	Ito[6] (exp.)	Lowe[24] (theory)	Kawatsura[67] (exp.)	Measured
[1s3p]	$K\beta_{2,5}$	3.19	-	-	-	-	9 ± 5
[1s2p]	$K\beta_{1,3}$	0.60	-	-	-	0.62	0.15 ± 0.05
[1s2s]	$K\beta_{1,3}$	0.12	-	-	-	-	0.041 ± 0.016
[1s3d]	$K\beta_{2,5}$	11.26	35	27	28	-	23. ± 10.

While few theoretical studies are as comprehensive as that of Mukoyama *et al*[17], there exist several additional theoretical and experimental measurements with which to compare our results. Our reported value of 23% for the branching ratio of the [1s3d] satellite is in good agreement with the work of Ito *et al*[6], but not with that of Mukoyama *et al.* Nonetheless, this has been similarly observed by other authors, who have reported analogous findings in studies of Cu[6, 20, 23], Ti[25], and Sc[21], suggesting a systematic underestimation in that particular study due to an incomplete treatment off the SO process. Despite the lack of agreement with Mukoyama's predictions, our reported values agree well with the theoretical work of Lowe *et al.* While both authors' calculations were atomic in nature, Lowe employed a multi-configurational framework that was inaccessible to the earlier, single-configurational calculation of Mukoyama, but is

necessary for modeling complex, open shell atoms. Furthermore, our measured branch ratio of the [1s2s] satellite is smaller than predicted by Mukoyama and the [1s3s] satellite is not present in our spectra. These observations can be explained by a suppression of the satellites by fast Coster Kronig transitions[21, 43, 48, 68]. Finally, the branching ratio of the [1s2p] we reported disagrees with the result of Mukoyama *et al* for the reasons previously discussed, but also disagree with the result of Kawatsura *et al*[43]. The latter study fit the intensity evolution of the satellite feature with the Thomas model and extracted the excitation probability from the corresponding fit parameter. The lack of agreement is then explained by the authors' own assertion that the Thomas model does not account well for the intensity evolution of SO from the 2p shell.

4. Conclusion

In conclusion, we report measurement of the x-ray emission spectrum for Ni in the regime near the Fermi level that includes both single-excitation, valence-to-core x-ray fluorescence and significant contributions from double-ionization. We have demonstrated a procedure for aligning to a universal energy scale and correcting for self-attenuation effects that is crucial when measuring features that lie beyond the single-particle Fermi level. Reported satellite positions are in good agreement with those predicted by the Z+1 approximation, and branching ratios agree well with prior experimental work for those satellites that have been previously reported. Errors associated with the branching ratios presented here are strongly influenced by the difficulty of fitting a spectrum to substantially overlapping peaks, specifically the [1s3d], which is nearly enveloped by the $K\beta_{2,5}$. Reliable, precise theoretical estimates of the satellite position and widths would allow the fit to be further constrained and lower the reported errors of the branching ratios. While the theoretical treatments discussed in this work are atomic in nature,

other authors have suggested a suppression of DI features due to charge transfer effects and an influence of speciation on the weight of contributing configurations and thus multiplet structure[69]. Future studies of the valence-to-core and DI region of various Ni compounds are likely warranted, and should benefit from the methodologies demonstrated here.

5. Acknowledgements

This work was supported by the United States Department of Energy, Office of Basic Energy Sciences, under grant DE-SC0002194 and also by the Office of Science, Fusion Energy Sciences, under grant DE-SC0016251. JJK was supported by DOE grant DE-FG02-97ER45623.

6. References

1. M. Siegbahn and W. Stenstrom, Phys Z **17**, 48-51 (1916).
2. F. K. Richtmyer and R. D. Richtmyer, Phys Rev **34** (4), 0574-0581 (1929).
3. F. K. Richtmyer, J Frankl Inst **208**, 325-361 (1929).
4. M. J. Druyvesteyn, *Het röntgenspectrum van de tweede soort*. (Rijks-Universiteit te Groningen., 1928).
5. Z. Horak, P Phys Soc Lond **77** (5), 980-986 (1961).
6. Y. Ito, T. Tochio, H. Oohashi and A. M. Vlaicu, Radiat Phys Chem **75** (11), 1534-1537 (2006).
7. M. Kavcic, M. Zitnik, D. Sokaras, T. C. Weng, R. Alonso-Mori, D. Nordlund, J. C. Dousse and J. Hoszowska, Phys Rev A **90** (2), 022513 (2014).
8. A. Bosch, H. Feil, G. A. Sawatzky and N. Martensson, Solid State Communications **41** (4), 355-357 (1982).
9. S. Hufner and G. K. Wertheim, Phys Lett A **51** (5), 299-300 (1975).
10. N. Martensson and B. Johansson, Phys Rev Lett **45** (6), 482-485 (1980).
11. D. A. Shirley, Physical Review B **5** (12), 4709-4714 (1972).
12. A. Filipponi and A. Dicicco, Phys Rev A **52** (2), 1072-1078 (1995).
13. T. Aberg, Phys Lett A **26** (10), 515-516 (1968).
14. T. A. Carlson, C. W. Nestor, T. C. Tucker and F. B. Malik, Phys Rev **169** (1), 27-36 (1968).
15. A. G. Kochur and V. A. Popov, Radiat Phys Chem **75** (11), 1525-1528 (2006).
16. A. G. Kochur and V. A. Popov, J Phys B - Ato. Mol. Opt. **39** (16), 3335-3344 (2006).
17. T. Mukoyama and K. Taniguchi, Phys Rev A **36** (2), 693-698 (1987).
18. A. Migdal, J Phys-Ussr **4** (1-6), 449-453 (1941).
19. E. L. Feinberg, J Phys-Ussr **4** (1-6), 423-438 (1941).

20. M. Deutsch, G. Holzer, J. Hartwig, J. Wolf, M. Fritsch and E. Forster, Phys Rev A **51** (1), 283-296 (1995).
21. D. F. Anagnostopoulos, R. Sharon, D. Gotta and M. Deutsch, Phys Rev A **60** (3), 2018-2033 (1999).
22. C. T. Chantler, J. A. Lowe and I. P. Grant, J Phys B - Ato. Mol. Opt. **46** (1), 015002 (2013).
23. C. T. Chantler, J. A. Lowe and I. P. Grant, Phys Rev A **82** (5), 052505 (2010).
24. J. A. Lowe, C. T. Chantler and I. P. Grant, Phys Rev A **83** (6), 060501 (2011).
25. J. A. Lowe, C. T. Chantler and I. P. Grant, Phys Lett A **374** (47), 4756-4760 (2010).
26. J. Olsen, M. R. Godefroid, P. Jonsson, P. A. Malmqvist and C. F. Fischer, Phys Rev E **52** (4), 4499-4508 (1995).
27. S. Doniach and M. Sunjic, J Phys Part C Solid **3** (2), 285-291 (1970).
28. A. Liebsch, Phys Rev Lett **43** (19), 1431-1434 (1979).
29. A. P. Grosvenor, M. C. Biesinger, R. S. Smart and N. S. McIntyre, Surf Sci **600** (9), 1771-1779 (2006).
30. J. Hoszowska, A. K. Kheifets, J. C. Dousse, M. Berset, I. Bray, W. Cao, K. Fennane, Y. Kayser, M. Kavcic, J. Szlachetko and M. Szlachetko, Phys Rev Lett **102** (7), 073006 (2009).
31. R. C. Forrey, H. R. Sadeghpour, J. D. Baker, J. D. Morgan and A. Dalgarno, Phys Rev A **51** (3), 2112-2116 (1995).
32. T. Pattard, T. Schneider and J. M. Rost, J Phys B - Ato. Mol. Opt. **36** (12), L189-L195 (2003).
33. O. Karis, S. Svensson, J. Rusz, P. M. Oppeneer, M. Gorgoi, F. Schafers, W. Braun, W. Eberhardt and N. Martensson, Physical Review B **78** (23), 233105 (2008).
34. R. Diamant, S. Huotari, K. Hamalainen, R. Sharon, C. C. Kao and M. Deutsch, Radiat Phys Chem **75** (11), 1434-1446 (2006).
35. V. A. Dzuba, V. V. Flambaum, M. G. Kozlov and M. Marchenko, Phys Rev A **66** (2), 022501 (2002).
36. C. T. Chantler, M. N. Kinnane, C. H. Su and J. A. Kimpton, Phys Rev A **73** (1), 012508 (2006).
37. C. T. Chantler, J. M. Laming, J. D. Silver, D. D. Dietrich, P. H. Mokler, E. C. Finch and S. D. Rosner, Phys Rev A **80** (2), 022508 (2009).
38. J. D. Gillaspy, C. T. Chantler, D. Paterson, L. T. Hudson, F. G. Serpa and E. Takacs, J Phys B - Ato. Mol. Opt. **43** (7), 074021 (2010).
39. J. P. Briand, P. Chevallier, A. Chetioui, J. P. Rozet, M. Tavernier and A. Touati, Phys Rev A **23** (1), 39-45 (1981).
40. J. Hoszowska, J. C. Dousse, W. Cao, K. Fennane, Y. Kayser, M. Szlachetko, J. Szlachetko and M. Kavcic, Phys Rev A **82** (6), 063408 (2010).
41. T. D. Thomas, Phys Rev Lett **52** (6), 417-420 (1984).
42. T. D. Thomas, J Electron Spec **40** (3), 259-269 (1986).
43. K. Kawatsura, T. Morikawa, K. Takahiro, M. Oura, H. Yamaoka, K. Maeda, S. Hayakawa, S. Ito, M. Terasawa and T. Mukoyama, J Phys B - Ato. Mol. Opt. **36** (20), 4065-4072 (2003).
44. C. Sternemann, A. Kaprolat, M. H. Krisch and W. Schulke, Phys Rev A **61** (2), 205011-205014 (2000).
45. M. Roy, J. D. Lindsay, S. Louch and S. J. Gurman, Journal of Synchrotron Radiation **8**, 1103-1108 (2001).

46. T. Mukoyama, M. Uda, L. Kover, Z. Berenyi, I. Cserny and W. Drube, X-Ray Spectrometry **38** (2), 138-143 (2009).
47. E. Vatai, Phys Rev A **38** (7), 3777-3780 (1988).
48. T. Mukoyama, M. Uda and L. Kover, X-Ray Spectrometry **38** (5), 406-409 (2009).
49. D. R. Mortensen and G. T. Seidler, J Electron Spectrosc **215**, 8-15 (2017).
50. D. R. Mortensen, G. T. Seidler, A. S. Ditter and P. Glatzel, Journal of Physics: Conference Series **712** (1), 012036 (2016).
51. G. T. Seidler, D. R. Mortensen, A. S. Ditter, N. A. Ball and A. J. Remesnik, Journal of Physics: Conference Series **712** (1), 012015 (2016).
52. G. T. Seidler, D. R. Mortensen, A. J. Remesnik, J. I. Pacold, N. A. Ball, N. Barry, M. Styczinski and O. R. Hoidn, Rev Sci Instrum **85** (11), 113906 (2014).
53. B. Ravel and M. Newville, Journal of Synchrotron Radiation **12** (4), 537-541 (2005).
54. M. Bianchini and P. Glatzel, Journal of Synchrotron Radiation **19**, 911-919 (2012).
55. Y. Takayama, T. Yoshida, S. Nakamura, N. Sasaki, H. Ishii and T. Miyahara, J Phys Soc Jpn **75** (12), 124709 (2006).
56. M. U. Delgado-Jaime, C. P. Mewis and P. Kennepohl, Journal of Synchrotron Radiation **17**, 132-137 (2010).
57. M. U. Delgado-Jaime and P. Kennepohl, Journal of Synchrotron Radiation **17**, 119-128 (2010).
58. H. Enkisch, C. Sternemann, M. Paulus, M. Volmer and W. Schulke, Phys Rev A **70** (2), 022508 (2004).
59. D. D. Lenz and T. R. Ayres, Publ Astron Soc Pac **104** (681), 1104-1106 (1992).
60. J. Chaboy, A. Marcelli and T. A. Tyson, Physical Review B **49** (17), 11652-11661 (1994).
61. S. J. Schaphorst, A. F. Kodre, J. Ruscheinski, B. Crasemann, T. Aberg, J. Tulkki, M. H. Chen, Y. Azuma and G. S. Brown, Phys Rev A **47** (3), 1953-1966 (1993).
62. M. Deutsch and M. Hart, Phys Rev Lett **57** (13), 1566-1569 (1986).
63. G. G. Li, F. Bridges and G. S. Brown, Phys Rev Lett **68** (10), 1609-1612 (1992).
64. S. Galambosi, H. Sutinen, A. Mattila, K. Hamalainen, R. Sharon, C. C. Kao and M. Deutsch, Phys Rev A **67** (2), 022510 (2003).
65. E. Chainet, M. Decrescenzi and J. Derrien, Physical Review B **31** (11), 7469-7471 (1985).
66. G. Holzer, M. Fritsch, M. Deutsch, J. Hartwig and E. Forster, Phys Rev A **56** (6), 4554-4568 (1997).
67. K. Kawatsura, T. Morikawa, K. Takahiro, M. Oura, H. Yamaoka, K. Maeda, S. Hayakawa, S. Ito, M. Terasawa and T. Mukoyama, J Phys B-at Mol Opt **36** (20), 4065-4072 (2003).
68. D. Coster and R. D. L. Kronig, Physica **2** (1), 13-24 (1935).
69. J. Kawai, M. Takami and C. Satoko, Phys Rev Lett **65** (17), 2193-2196 (1990).

VITA

Evan Jahrman was near Seattle Washington on Septermber 30th, 1991. In 2010, he graduated from Bainbridge Island High School. He then attended Gonzaga University, where he was taught by many exceptional professors, including Gergely Gidofalvi, who advised Evan Jahrman's undergraduate research in computational chemistry. In 2014, he graduated from Gonzaga University with a BS in physics and a minor in chemistry and enrolled in the PhD program in physics at the University of Washington. Here, he was a member of the Seidler lab, studying various X-ray spectrscopies and their associated instrumentation. In 2019, he graduated the University of Washington with a PhD in physics.